SCUOLA DI DOTTORATO
UNIVERSITÀ DEGLI STUDI DI MILANO-BICOCCA

Department of Earth and Environmental Sciences

PhD program in Chemical, Geological, and Environmental Sciences
XXXIV Cycle
Curriculum in Geological Sciences

# The subsurface urban heat island in Milan – Anthropogenic heat sources and city-scale modeling of present and future scenarios

Previati Alberto
Registration number 764521

Supervisor: Prof. Crosta Giovanni B.
Tutor: Prof. Frattini Paolo
Coordinator: Prof. Malusà Marco G.

**ACADEMIC YEAR 2020/2021**

# Abstract

Urban areas rely on subsurface resources to produce drinking water and extract low enthalpy geothermal energy. However, atmospheric and subsurface environment modifications by climate change and/or human activities affect the physical-chemical conditions such as the groundwater thermal regime. The subsurface urban heat island (SUHI) effect was documented in several cities worldwide with 2 to 8°C warmer temperatures than in suburban areas and warming trends were linked to global warming and urbanization. Highly developed cities are more impacted due to the superimposition of anthropogenic heat sources (e.g. building basements, asphalted surfaces, tunnels, geothermal installations), and positive (e.g. heating potential) and negative (e.g. thermal pollution) implications for groundwater uses exist. Thus, monitoring and modeling tools are mandatory to disentangle the complex superimposition of positive/negative heat flows from natural/anthropogenic sources and assess the future evolution.

Moreover, EU objectives on climate change mitigation are focused on the development of renewable energies to reduce greenhouse gas emissions. Low enthalpy geothermal energy is considered a valid alternative to common heating/cooling techniques as it is available almost everywhere and has a low carbon footprint, especially where thermal energy is supplied by fossil fuels.

The Milan city area (MCA) is one of the most densely populated and industrialized regions in Europe and, consequently, has a very high thermal power demand. Moreover, many activities related to urbanization contribute to modify the groundwater environment but their effects on the subsurface thermal status have never been assessed.

In the first part of this study, the low enthalpy geothermal potential of the shallow aquifers was assessed at regional scale. Advantageous hydrogeological characteristics (e.g. highly conductive aquifers) were mapped and different analytical solutions used to estimate the thermal potential of ground coupled (GCHP) and groundwater (GWHP) heat pumps. The potential of GCHP was estimated considering subsurface hydraulic/thermal parameters and temperature, climatic data and borehole characteristics. The potential of GWHP was

estimated considering the water drawdown and temperature drop allowed by regulation. The results were compared with heat demand rates on a municipal basis and the most profitable configuration was discussed.

Successively, the extent and intensity of the SUHI in the MCA was assessed. Natural and anthropogenic controls on groundwater temperatures were revealed analyzing head and temperature records, and the occurrence of an up to 3° C intense SUHI was demonstrated. Vertical heat fluxes to the aquifer are strongly related to the groundwater depth and density of surface structures/infrastructures. This heat accumulation is reflected by a constant warming trend between +0.1 and +0.4 °C/y leading up to a +25 MJ/m$^2$/y heat storage by densely distributed heat sources. Furthermore, the effects of urbanization, SUHI and physical-chemical conditions on the microbiological abundance were assessed by a flow cytometry analysis.

Finally, a holistic city-scale fluid flow and heat transport FEM model was developed focusing on (I) the reconstruction of large-scale aquifer heterogeneities to consider the advective dominated heat transport, (II) the definition of the upper thermal boundary by a coupled analytical solution and (III) the integration of natural and human-related fluid/heat sources as transient boundary conditions. A fluid/heat budget analysis revealed the heat flow from buildings, infrastructures and tunnels contributes to 85% of the net annual heat accumulation (1.4 PJ/y). The thermal potential was evaluated numerically, and it was demonstrated that future climate change and city expansion could lead to the highest subsurface warming compared to shallow geothermic development which, for this reason, should be highly supported and monitored.

# Riassunto

Le risorse sotterranee sono essenziali per l'approvvigionamento idrico ed energetico nelle aree urbane. Tuttavia, le attività umane modificano l'assetto naturale del sottosuolo alterandone le condizioni chimico-fisiche, tra cui il regime termico. L'effetto isola di calore nel sottosuolo (SUHI) è stato osservato in diverse città del mondo con temperature da 2 a 8°C più calde rispetto alle aree suburbane, spesso associato a trend di riscaldamento riconducibile al riscaldamento globale e all'urbanizzazione.

Infatti, le città ben sviluppate sono anche più colpite a causa della sovrapposizione di fonti di calore antropiche come i seminterrati degli edifici, le superfici asfaltate, i tunnel e gli impianti geotermici. Tale fenomeno ha implicazioni positive (es: maggior efficienza del riscaldamento con geotermia) e negative (es: l'inquinamento termico) sulle acque sotterranee, e l'integrazione di tecniche di monitoraggio e modellazione è fondamentale per quantificare i contributi di calore naturale/antropico in un ambiente complesso e valutarne l'evoluzione futura.

Inoltre, gli obiettivi dell'UE sulla mitigazione del cambiamento climatico si concentrano sullo sviluppo di energie rinnovabili per ridurre le emissioni di gas serra. Tra queste, l'energia geotermica superficiale è considerata una valida alternativa ai sistemi di condizionamento tradizionali in quanto è disponibile quasi ovunque ed ha un bassissimo impatto.

L'area metropolitana di Milano è una delle regioni maggiormente popolate d'Europa e ha una domanda energetica molto alta. Inoltre, molte attività legate all'urbanizzazione hanno contribuito ad alterarne la superficie e il sottosuolo, ma una valutazione dello stato termico tutt'ora non esiste.

Nella prima parte di questo studio, il potenziale geotermico a bassa entalpia è stato stimato a scala regionale integrando con un approccio GIS dati climatici e parametri idrogeologici e termici del sottosuolo. Tramite soluzioni analitiche si è calcolato il potenziale di impianti a circuito chiuso e aperto, considerando: per i primi, i parametri, la temperatura del sottosuolo, e le caratteristiche dello scambiatore, mentre per secondi, l'abbassamento piezometrico e il

salto di temperatura ammessi dalla normativa regionale. I risultati sono stati confrontati con gli usi energetici attuali su base comunale, suggerendo la configurazione più favorevole.

Nella seconda parte, si dimostra l'estensione dell'isola di calore sotterranea, di intensità fino a 3°C nella città di Milano. L'analisi spazio-temporale dei record di soggiacenza e temperatura ha permesso di individuare il ruolo dei principali fattori naturali e antropici: i flussi di calore verso l'acquifero sono più intensi dove la tavola d'acqua è superficiale e strutture/infrastrutture antropiche sono densamente distribuite. Questo accumulo di calore si riflette in un trend positivo tra +0.1 e +0.4 °C/a che porta fino a +25 MJ/m$^2$/a nel sottosuolo del centro città. Inoltre, sono anche stati osservati gli effetti dell'urbanizzazione sull'abbondanza microbiologica nella falda superficiale.

Infine, è stato sviluppato il primo modello numerico (FEM) di flusso e trasporto di calore alla scala urbana, focalizzandosi su (I) la ricostruzione delle eterogeneità del sottosuolo per simulare il trasporto di calore advettivo, (II) una soluzione analitica accoppiata per definire la condizione al contorno termica alla superficie e (III) l'integrazione di molteplici sorgenti di calore naturali/antropiche come condizioni al contorno. Dalla simulazione dello stato attuale emerge che il flusso di calore dagli edifici e dalle infrastrutture/gallerie contribuisce all'85% dell'accumulo di calore annuale (1.4 PJ). Inoltre, il potenziale termico è stato valutato anche numericamente, e si è dimostrato che l'aumento di calore sotterraneo dovuto allo sviluppo geotermico è ben inferiore ai possibili effetti del riscaldamento globale e dell'espansione urbana e quindi, per questo motivo, dovrebbe essere valorizzato.

# Table of contents

# List of abbreviations

BC ..... Boundary condition
BHE ..... Borehole heat exchanger
C (aquifer) ..... Confined
CCC ..... Cross-correlation coefficient
COP ..... Coefficient of performance
DO ..... Dissolved oxygen
EC ..... Electrical conductivity
EFLH ..... Equivalent full-load hours
FDM ..... Finite difference method
FEM ..... Finite element method
GCHP ..... Ground-coupled heat pumps
GHG ..... Greenhouse gases
GSHP ..... Ground source heat pumps
GW ..... Groundwater
GWHP ..... Groundwater heat pumps
MAE ..... Mean absolute error
MCA ..... Milan city area
ME ..... Mean error
ORP ..... Oxidation-reduction potential
OW ..... Observation well
P (aquifer) ..... Phreatic
PC ..... Principal component
PCA ..... Principal component analysis
PDE ..... Partial differential equation
PDF ..... Probability density function
REV ..... Representative elementary volume
RMSE ..... Root mean square error
SC (aquifer) ..... Semi-confined
SUHI ..... Subsurface urban heat island
TDS ..... Total dissolved solids
TRT ..... Thermal response test
UHI ..... Urban heat island

# List of figures

# List of tables

# List of equations

# 1. Introduction

In many big cities worldwide, groundwater bodies are essential to assure good quality drinking water and low enthalpy geothermal energy. In the last decades, it has been observed that the quality and the availability of these resources is jeopardized by their intense use as well as by local modifications of the surface and subsurface environment (e.g. Bayer et al., 2019; Foster, 2001; Herbert et al., 2013; Huggenberger and Epting, 2011; Sharp Jr et al., 2003). Several human activities, urbanization-related processes and climate change can alter the energy budget at the ground surface and the subsurface thermal regime in the vadose zone and groundwater is prone to be influenced. Among all, the most relevant disturbances are due to the high density of buildings, ground covering/sealing with asphalt and surface infrastructures, the shallow subsurface occupation by underground structures such as tunnels and building basements, and local thermal alterations induced by several kinds of shallow geothermal installations (e.g. borehole heat exchangers, geothermal wells, energetic foundation piles) for heating and cooling purposes. Recent studies worldwide (for a review, Bayer et al., 2019 and Zhu et al., 2011; Berlin, Cologne and Karlsruhe, Benz et al., 2016 and Menberg et al., 2013a; Basel, Epting and Huggenberger, 2013; Cardiff, Farr et al., 2017; Paris, Hemmerle et al., 2019; Munich, Frankfurt and Darmstadt, Menberg et al., 2013a; Tokyo, Seoul, Osaka and Bangkok, Taniguchi et al., 2007; Amsterdam, Visser et al., 2020;) documented the effect of these activities by diffusely elevated groundwater temperature in the city center with respect to the surrounding rural areas, referring to this phenomenon as the subsurface urban heat island (SUHI).

The impact SUHI may have on groundwater quality (e.g. biological, chemical and physical effects) and on the potential and sustainability of shallow geothermal systems is of increasing interest among drinking water suppliers and energy planners (Blum et al., 2021). On one side, the extensive warming of urban aquifers modifies the chemical-physical properties of groundwater and can affect the microfauna and living ecosystems that play an important role for groundwater quality (Brielmann et al., 2009; Koch et al., 2020). On the other hand, the SUHI contains an enormous amount of thermal energy and, consequently, represents an

attractive reservoir for shallow geothermal uses such as space heating and cooling (Arola and Korkka-Niemi, 2014; Zhu et al., 2011). It was demonstrated that the heating potential of SUHI in many urban areas exceeds the annual residential heating demand (Zhu et al., 2011), and extracting this amount of thermal energy by means of geothermal installations could reduce the emission of greenhouse gases due to conventional carbon-based heating systems (Bayer et al., 2012; Blum et al., 2010), which were identified as one of the most relevant pollution sources in urban areas and their replacement with "green" solutions is a primary challenge in today's society (EU DIRECTIVE 2018/2001; Solomon et al., 2007). However, the urban heat island (UHI) in the atmosphere reduces the heating demand and increases the cooling demand, and elevated groundwater temperatures beneath cities may restrict the use of the subsurface for cooling purposes (which is more needed in urban areas).

Thus, the quantification of the intensity and extent of the anthropogenic thermal pollution in the subsurface of big cities is a worldwide concern to preserve the groundwater quality status and support the installation of sustainable heating/cooling solutions such as shallow geothermal systems. A profound knowledge of the subsurface groundwater and thermal regimes based on monitoring data is fundamental to unravel the relevant heat sources and transport mechanisms at the city scale and the development and application of quantitative tools such as numerical modeling is mandatory to assess the present variability and future changes

The Milan city area (MCA), Northern Italy (Lombardy Region), is one of the most densely populated and industrialized regions in Italy (6,836 inhabitants/$km^2$ in the city of Milan) (ISTAT, 2019). It is characterized by a dense texture of structures and infrastructures that modify the water infiltration and groundwater flow processes, the heat transfer between the surface and the subsurface, and the heat transport in the shallow aquifer. Due to the exceptional urban density and the availability of enough long and spatially distributed groundwater monitoring data, the Milan city was selected for most of the investigations presented in this PhD thesis.

## 1.1. Aims and outline of the thesis

This PhD thesis aims to investigate the thermal status of the subsurface in the Milan city area, recognize the most relevant present and future thermal sources at the city scale, and evaluate the thermal potential of the alluvial-plain aquifer system at regional- and city-scale. The local thermal impact of various underground activities (e.g. heated basements, geothermal wells, and borehole heat exchangers) has been studied with analytical (Ferguson and Woodbury, 2004) and local-scale numerical modeling (Attard et al., 2016). However, the resulting groundwater thermal regime and the mechanisms establishing a diffused SUHI are yet mostly unexplored at the city-scale. The main objectives of this PhD thesis are the following:

**Assessment of the low enthalpy geothermal potential** (Chapter 6)

Shallow geothermal energy is a "green" alternative to common heating/cooling systems as it is available almost everywhere and has very low carbon footprint but information on the availability, extraction rates, costs and most suitable technology are mandatory to support the development of this technology. One of the best indicators of geothermal efficiency and suitability is the geothermal potential, which describes the capability to exchange heat with the ground/groundwater. In this thesis, the susceptibility to host different low enthalpy geothermal systems (closed- and open-loop) was evaluated at regional-scale and specific heat exchange rates were derived linking geological and hydrogeological information to climatic data through analytical equations and considering the existing technical, economic, and regulatory restrictions. This was achieved characterizing the spatial distribution of the hydraulic and thermal parameters of the aquifers as from borehole geological logs and estimating the aquifer temperature from groundwater and climatic data. The potential to fulfill the actual thermal demand was assessed on a municipality-based GIS approach and the best technology according to the hydrogeological framework and heat demand scenarios was evaluated.

**Characterization of the SUHI and its sources in the Milan city area** (Chapter 7)

Successively, the impact of human activities on the subsurface thermal regime in the Milan city area was investigated to unravel the complex thermal framework of the urban subsurface.

As part of this project, the high-resolution groundwater monitoring network active since 2016 was intensified reaching a total number of 61 monitored piezometers (22 out of 61 equipped with automatic devices). Descriptive/explorative spatial-temporal statistical techniques were used to investigate the relation between the groundwater thermal regime and many natural and anthropogenic possible heat sources. Finally, a comprehensive conceptual model for the thermal regime in the Milan city area was proposed considering the relevant heat sources and transport mechanisms.

**Effects of urbanization on groundwater chemistry and micro-fauna abundance** (Chapter 8)

The city-scale distribution of physical-chemical indicators and groundwater micro-fauna abundance in the shallow aquifer was measured and mapped. A bi-variate analysis between natural and human activities-influenced aquifer conditions such as the degree of groundwater-atmosphere interactions (controlled e.g. by the amount of green unsealed/natural areas and the percentage of fine deposits), temperature, pH, dissolved oxygen was carried out to disentangle their role on the bacterial activity described by the total cell count (TCC) and high-nucleic acid percentage (HNAP) indexes measured by a flow cytometry analysis.

**Modeling the SUHI present and future impact on the shallow aquifers** (Chapter 9)

Finally, a holistic 3D FEM groundwater flow and heat transport modeling approach is proposed to investigate the subsurface thermal regime in the Milan city area, quantify the thermal contribution of single heat sources, define the thermal potential based on the simulated thermal regime and assess the evolution of the thermal regime under future scenarios. New approaches were developed and combined with already existing techniques to improve the first city-scale FEM numerical model in the MCA focusing on:

i) the reconstruction of large-scale aquifer heterogeneities to consider the advective heat-transport by the 3D spatialization of hydrogeological properties from the classification in hydro- and thermo-facies of grain size-based borehole log information;
ii) a novel large-scale approach to define the upper thermal boundary upscaling and integrating the ground surface thermal characteristics from a high-resolution land use

map into a multilayer conductive heat transfer analytical solution coupled to the numerical solution;

iii) the integration of many relevant natural and anthropogenic fluid and heat sources as transient boundary conditions;

iv) a fluid and heat budget analysis on the most relevant sources at the city-scale to quantify and compare single contributions to the development of the SUHI;

v) the combination of modeling results to assess the geothermal potential, the groundwater flow and thermal regimes to support the subsurface thermal management;

vi) future predictions on the shallow aquifer warming due to climate and city size changes and development of geothermal installations.

# 2. Thermogeology

## 2.1. Origin of Earth's heat

Geothermal energy is the thermal energy stored in the Earth body. The Earth has a layered internal structure: at 6,000 km depth the inner core temperature is above 5,000 °C and the pressure is about 400 GPa, while the average temperature at the Earth's surface is about 14°C. This difference between the core and the surface is the driving force for the heat flow, which is generally directed from the core outwards. Typical values at the Earth's surface (**Figure 2.1**) range from 50 to 100 mW/m$^2$ in the continental crust and oceanic crust (Davies, 2013). The main heat sources from the Earth's interior are the heat losses from the inner core and the decay of radioactive elements in the crust, which on average contribute 38 and 62 % to the heat flux, respectively. Due to this heat flow, it was estimated a global neat heat loss of 1.4x10$^{12}$ W to the space from the Earth's surface (Clauser, 2009). On the other hand, about 170 W/m$^2$ of solar energy reaches the planet by solar radiation and balances with the internal heat flow to reach about 14°C on average at the Earth's surface. The related average vertical temperature gradient is about 0.03°C/m with local variations due to the geological settings.

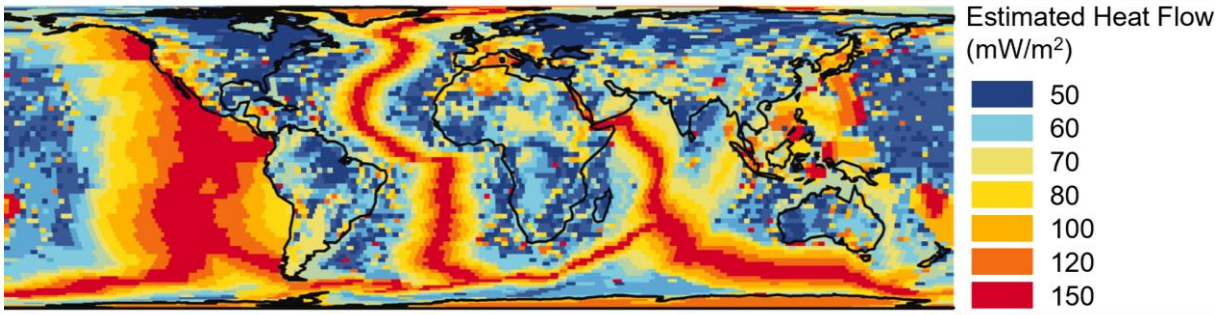


***Figure 2.1*** *– Map showing the heat flow distribution at world scale (from Davies, 2013)*

## 2.2. Heat transport mechanisms

The heat transport in aquifers is mainly a coupled process between heat conduction through the solid matrix (and water in its pores) and heat advection by moving groundwater. The fundamental empirical law of heat conduction states that heat flow in a continuous medium occurs because of temperature differences exists in the medium. The transfer of energy occurs

from zones of higher temperature to zones of lower temperature. The empirical heat conduction equation is called the Fourier's law from *Jean Baptiste Fourier (1768 – 1830)*:

$$h = -\lambda * \Delta T/\Delta \mathrm{x} \qquad \textit{(Eq. 2.1)}$$

Accordingly, the specific heat flow $h$ [W/m$^2$] along x direction is related to the temperature gradient $\Delta T/\Delta \mathrm{x}$ and is proportional to the thermal property of the medium (i.e. the thermal conductivity - $\lambda$ [W/mK]). The thermal conductivity describes the ability to transfer heat and, in geological materials, ranges from about 1 (e.g. basalt, gypsum) to 7 W/mK (e.g. quartz), whereas the typical conductivity of air is 0.02 W/mK and water 0.6 W/mK (VDI 4640/1, 2000). In a heterogeneous medium, such as alluvial deposits and rocks, the thermal conductivity is usually expressed through a bulk equivalent-value. The effective thermal conductivity of a multi-phase systems (e.g. sand with pores filled by air and water) ranges between the harmonic and arithmetic mean of the conductivities of the species for "in series" and "in parallel" arrangement of the phases respect to the heat flow direction (Woodside and Messmer, 1961). For a multi-phase random distribution, the volume-weighted geometric mean is a good estimate of the empirically determined bulk thermal conductivity ($\boldsymbol{\lambda}_{bulk}$) (Woodside and Messmer, 1961), which for a typical two-phase geological medium (e.g. dry or water-saturated sands) becomes:

$$\boldsymbol{\lambda}_{bulk} = \left(\boldsymbol{\lambda}_{fluid}\right)^{\varphi} * \left(\boldsymbol{\lambda}_{solid}\right)^{(1-\varphi)} \qquad \textit{(Eq. 2.2)}$$

where $\boldsymbol{\lambda}_{fluid}$ and $\boldsymbol{\lambda}_{solid}$ are the thermal conductivity of the fluid and solid phase of the system and $\varphi$ is the porosity. The amount of heat that can be accumulated or released by a volume unit is described by the volumetric heat capacity ($S$) [J/m$^3$K], obtained as the product between the specific heat capacity ($C$) and the specific mass ($\rho$):

$$S = C * \rho = \left(\frac{1}{M} * \frac{\Delta Q}{\Delta T}\right) * \rho \qquad \textit{(Eq. 2.3)}$$

where $\Delta Q$ represents the amount of heat needed to uniformly raise the temperature of the sample by the increment $\Delta \mathrm{T}$. In a multi-phase system, the bulk $S$ is given by the volume-weighted arithmetic mean of the capacities of the species (Eq. 2.4):

$$s_{bulk} = \rho c_{bulk} = \varphi * \rho c_{fluid} + (1 - \varphi) * \rho c_{solid} \qquad \textit{(Eq. 2.4)}$$

**Table 2.1** shows typical values of thermal properties for different geological media according to the German guidelines for the thermal use of the underground (VDI 4640/1, 2000).

***Table 2.1*** *– Examples of thermal conductivity and volumetric heat capacity of geological media (from VDI 4640/1, 2000)*

| Rock/Material | Thermal conductivity (W/mK) | | Volumetric heat capacity (MJ/m$^3$K) |
|---|---|---|---|
| | ***range*** | ***typical*** | ***range*** |
| | | **Magmatic rocks** | |
| Basalt | 1.3 – 2.3 | 1.7 | 2.3 – 2.6 |
| Diorite | 2.0 – 2.9 | 2.6 | 2.9 |
| Gabbro | 1.7 – 2.5 | 1.9 | 2.6 |
| Granite | 2.1 – 4.1 | 3.4 | 2.1 – 3.0 |
| Peridotite | 3.8 – 5.3 | 4.0 | 2.7 |
| Rhyolite | 3.1 – 3.4 | 3.3 | 2.1 |
| | | **Metamorphous rocks** | |
| Gneiss | 1.9 – 4.0 | 2.9 | 1.8 – 2.4 |
| Marble | 1.3 – 3.1 | 2.1 | 2.0 |
| Metaquartzite | approx. 5.8 | 5.8 | 2.1 |
| Micaschists | 1.5 – 3.1 | 2.0 | 2.2 |
| Argillaceous schists | 1.5 – 2.6 | 2.1 | 2.2 – 2.5 |
| | | **Sedimentary rocks** | |
| Limestone | 2.5 – 4.0 | 2.8 | 2.1 – 2.4 |
| Marl | 1.5 – 3.5 | 2.1 | 2.2 – 2.3 |
| Quartzite | 3.6 – 6.6 | 6.0 | 2.1 – 2.2 |
| Salt | 5.3 – 6.4 | 5.4 | 1.2 |
| Sandstone | 1.3 – 5.1 | 2.3 | 1.6 – 2.8 |
| | | **Unconsolidated rocks** | |
| Gravel, dry | 0.4 – 0.5 | 0.4 | 1.4 – 1.6 |
| Gravel, watersaturated | approx. 1.8 | 1.8 | approx. 2.4 |
| Moraine | 1.0 – 2.5 | 2.0 | 1.5 – 2.5 |
| Sand, dry | 0.3 – 0.8 | 0.4 | 1.3 – 1.6 |
| Sand, watersaturated | 1.7 – 5.0 | 2.4 | 2.2 – 2.9 |
| Clay/silt, dry | 0.4 – 1.0 | 0.5 | 1.5 – 1.6 |
| Clay/silt, watersaturated | 0.9 – 2.3 | 1.7 | 1.6 – 3.4 |
| Peat | 0.2 – 0.7 | 0.4 | 0.5 – 3.8 |
| | | **Other** | |
| Ice | 2.32 | | 1.87 |
| Water | 0.59 | | 4.18 |
| Air | 0.02 | | 0.0012 |
| Steel | 60 | | 3.12 |
| Concrete | 0.9 – 2.0 | | approx. 1.8 |

Considering the time dependency, the rate of heat transferred by conduction from the hot to the cold end of a material is expressed by the thermal diffusivity [m$^2$/s] as the ratio between the thermal conductivity and the volumetric specific heat capacity:

$$\alpha = \frac{\boldsymbol{\lambda}_{bulk}}{\rho c_{bulk}} \qquad \textit{(Eq. 2.5)}$$

The heat advection is referred to as the movement of heat from one place to another due to a moving fluid mass (e.g. the water flow in pores). Thus, the direction of the specific heat flow by advection ($h$) depends essentially on the direction and velocity of the fluid flow and it is described by the following equation:

$$h = \mathrm{q} * \rho c_{fluid} * \Delta T \qquad \textit{(Eq. 2.6)}$$

where q is the Darcy flow velocity [m/s] and $\Delta T$ is the temperature change of the volume unit. Thus, to describe the heat flow by advection in a porous medium, the fluid flow must be characterized. The Darcy equation, from *Henry Darcy (1803 – 1858)*, describes the relationship between the specific fluid discharge (q) through a unit area (also referred to as the Darcy flow velocity) and the pressure gradient for a linear flow:

$$\mathrm{q} = -\frac{k}{\mu}\left(\nabla P + \rho_f g \nabla Z\right) \qquad \textit{(Eq. 2.7)}$$

where $k$ is the intrinsic permeability (i.e. the ability of a porous material to allow fluids to move through it), $\rho_f$ and $\mu$ are the density and dynamic viscosity of water (respectively 0.99987 g/cm$^3$ and 1.0016 mP), $g$ is the gravity, $P$ is the pore-water pressure and $Z$ is the elevation. The product $\frac{k*\rho_f g}{\mu}$ is commonly referred to as the hydraulic conductivity (K) which in surface hydrogeological systems is usually assumed constant (at ambient temperature).

In a complex system, the relevance between the advective and the conductive heat transport depends on the hydrogeological and thermal properties of the medium and it is described by the dimensionless Péclet number given by:

$$Pe = \frac{\rho c_{fluid}\, \boldsymbol{q}\, L}{\boldsymbol{\lambda}_{bulk}} \qquad \textit{(Eq. 2.8)}$$

where $L$ is the characteristic length [m] that, for unconsolidated deposits, is usually replaced by the median grain-size ($d_{50}$) of the porous medium. $Pe > 1$ indicates that thermal energy is mainly transported by advection and, vice versa, for $Pe < 1$ the conduction is more relevant.

Generally, the heat conduction dominates within the lithosphere, however, if the flow rate and the porosity are sufficiently high (c.a. $K > 10^{-7}$ m/s) the heat advection can be equally or even more efficient with respect to the conductive heat transfer (Clauser, 2009). This can occur both in free convection, i.e. under density gradient, (e.g. along mid-oceanic ridges; Clauser, 2009) and in forced convection or advective systems, i.e. under hydraulic gradient. This is the case of all sedimentary basins, where the hydraulic gradient drives the water flow through the pores and the associated heat.

Furthermore, similarly to mass transport, the heat transport by advection in porous media is subject to mechanical dispersion. This effect causes less steep thermal gradients at the advection front due to microscale inhomogeneities such as pore directions not parallel to flow and delays the thermal perturbation front with respect to the advection front. The longitudinal ($D_L$) and transverse ($D_T$) dispersivity account for the dispersion parallel and perpendicular to the groundwater flow, and their effects will be discussed in section 4.2.

## 2.3. Thermal regime of shallow aquifers

The thermal regime of the shallow subsurface is governed by the heat flow from the Earth's interior and the temperature at the surface. Normally, the temperature increases with depth according to the vertical temperature gradient. As said above, this is generally positive (i.e. the temperature increases with depth), also referred to as "normal", and has a typical value of 0.03 °C/m, but due to local conditions it can varies significantly or even be "negative". Higher values can be found close to mid-oceanic ridges and volcanic areas, while lower values are typically found within aquifer complexes where the fluid-mass movement can alter the normal conduction-related gradient. Inverse temperature gradients are mainly found near the surface where additional external heat sources are located (e.g. the heat released from anthropogenic activities located at the surface and in the shallow subsurface).

Approximately, the temperature of the shallow subsurface is close to the mean annual soil temperature, which is generally higher than the mean annual air temperature (Signorelli and Kohl, 2004). In general, the shallow soil temperature depends mainly on the climate (i.e. on the latitude, the elevation above sea level and the exposition), the groundwater flow and the local geothermal heat flow. Thus, thermal signals from air temperature variations at the

surface penetrate through the unsaturated zone mainly by heat conduction and can perturb the temperature distribution in the deeper subsurface. Due to the high thermal resistance of the unsaturated zone (the pores are filled mainly with air, which has an extremely low thermal conductivity compared to rock materials), diurnal temperature fluctuations will typically be seen at less than 1 m depth in dry soil, but seasonal fluctuations may be detectable at depths of 10 m or more (Taylor and Stefan, 2009) (i.e. generally to a depth of about 10 m below the ground surface the amplitude of the temperature fluctuations is reduced by a factor of about 10). Below this depth, the thermal regime is highly dampened and more stable, and is influenced mainly by long-term conditions. **Figure 2.2a** shows a typical annual envelope of monthly temperature-depth profiles in the subsurface where the transition between the "seasonal fluctuations" and the "stable" zone is clearly visible. Note that, due to the thermal diffusivity (α) of the shallow subsurface, the temperature signal from the surface is also delayed in time with increasing depth (**Figure 2.2b**). According to the geological and hydrogeological settings the phase shift of the temperature signal in the subsurface can even be higher than one year.

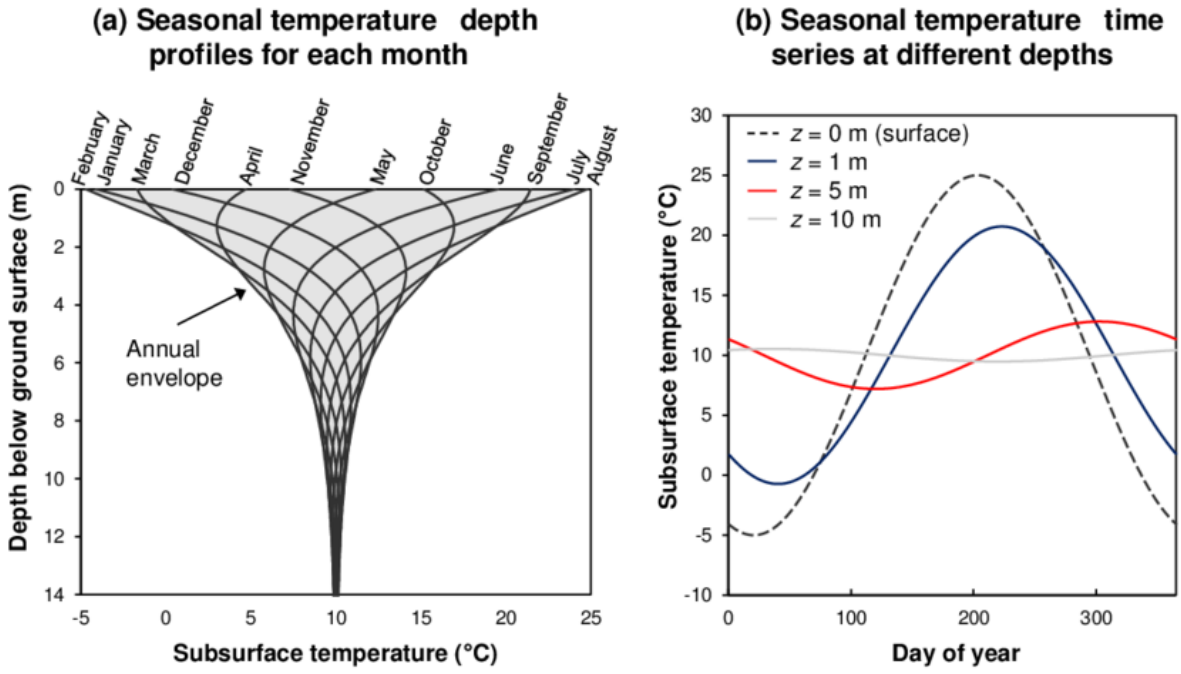


***Figure 2.2*** *– (a) Typical temperature-depth profiles in the shallow subsurface for one year showing the dampening of the seasonal fluctuations with depth. (b) Temperature time-series at different depths below the ground surface showing the phase shifting between the signals.*

## 2.4. Geothermal energy

Geothermal energy is the thermal energy stored in the Earth's body. This amount of energy is increasingly used to produce electricity and thermal energy as it is extremely abundant ($8.6*10^{20}$ J according to Clauser, 2006), relatively cheap (Blum et al., 2011; Kavanaugh and Rafferty, 2014) and has a low impact on the environment (Blum et al., 2010; Fridleifsson et al., 2008; Saner et al., 2010).

Geothermal reservoirs can be subdivided according to the thermodynamic potential enthalpy (i.e. the heat content per mass unit). The enthalpy (H) reflects the heat content of a geological medium, depending not only on the temperature, but also on the pressure and the available volume. Generally, geothermal reservoirs are subdivided in three main categories:

- High Enthalpy T>150°C
- Medium Enthalpy T>90°C
- Low Enthalpy T<90°C

High and medium enthalpy reservoirs are generally used to produce electricity. The process of energy conversion, from thermal to electrical, is similar to the conventional fossil fuel-fired power plants which use steam turbines. The main difference is the lack of a manmade boiler as the heat is directly taken from the underground. Therefore, geothermal power plants release a significant lower amount of carbon dioxide in the atmosphere compared to conventional ones (Stober and Butcher, 2017). In addition, geothermal energy production can be considered a renewable energy as the amount of thermal energy stored in the Earth's body is extremely higher (Clauser, 2006) than the chemical energy stored within oil reservoirs, which is well known it will be depleted in the next hundreds of years (Shafiee and Topal, 2009). The main limit of this technique is the non-ubiquity of high and medium enthalpy reservoirs in the world or the poorly profitable payback for very deep and non-conventional installations. Consequently, the most efficient power plants are developed in high geothermal heat flux regions (**Figure 2.1**) such as mid-oceanic ridges (e.g. Iceland), convergent plate margins and volcanic areas (e.g. Larderello, Italy)(Davies, 2013).

The thermal energy in lower enthalpy reservoirs is mainly used directly (e.g. for domestic hot water, thermal baths, district heating). Very low enthalpy reservoirs have near ambient

temperature and are suitable to exchange or store heat. This is the case of the shallow subsurface where ground source heat pumps (GSHP) are commonly used to extract or release heat in the underground through a heat pump system. Common applications of geothermal energy are shown in the Lindal's diagram (**Figure 2.3**).

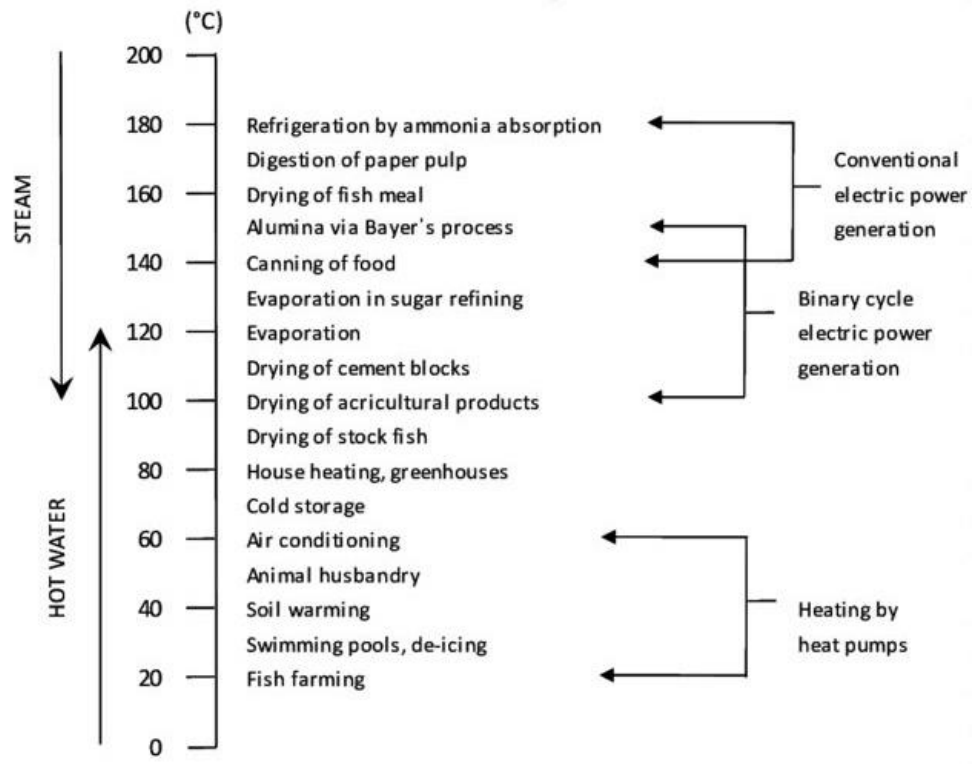


***Figure 2.3*** *– The Lindal's diagram: industrial and other applications of geothermal energy depending on the temperature of the reservoir (from Lindal, 1973)*

Another common distinction between geothermal applications is based on their depth. This is related to a combination between the location of the target reservoir and the potential profit (e.g. money or CO2 savings) compared to drilling and maintenance costs. Near-surface geothermal applications (< 400 m) are mainly heat-exchangers through heat pumps or direct geothermal heat applications. At depth greater than 400 m the drilling costs usually hamper direct heat applications (except for very large heat production plants) and the power generation is the main application. **Figure 2.4** illustrates possible geothermal applications depending on the depth.

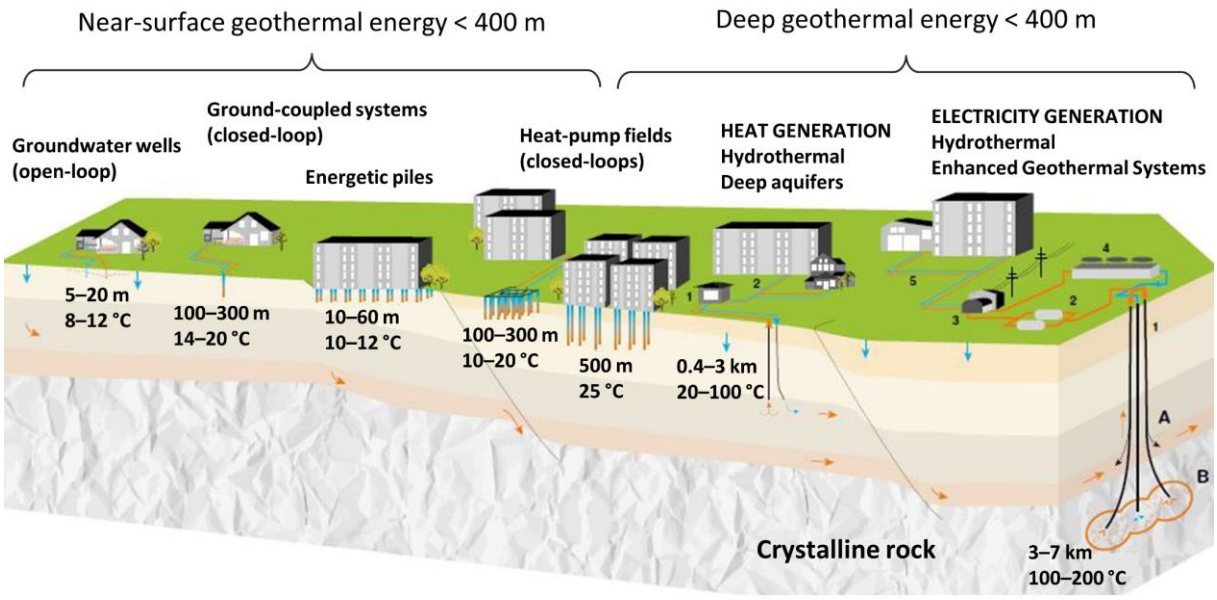


***Figure 2.4*** *– Diagram showing the most common geothermal applications based on their depth (redrawn from www.geothermie.ch)*

## 2.5. Shallow geothermal installations

Low enthalpy geothermal resources are abundant and available in most locations around the world. The use of such thermal energy is relatively simple because the depth is generally small and, thus, the drilling and installation costs are relatively small. For this reason, low enthalpy shallow geothermal energy is considered a valid alternative to common carbon-based heating/cooling techniques (e.g. fossil fuel burners, air-coupled heat pumps) (Lund and Boyd, 2016). Even though shallow geothermal systems require electricity to extract heat from the ground, a significantly lower amount of electrical power is required and lower volumes of greenhouse gases (GHGs) are emitted compared to conventional heating/cooling systems (Bayer et al., 2012; Blum et al., 2010). It has been demonstrated that the use of geothermal energy in common residential and commercial buildings in Europe can reduce the emission of GHGs, such as $CO_2$, between 31% and 88% (depending on the source of the supplied electricity and the efficiency of the installation) compared to conventional heating systems such as oil and gas fired boilers and air-coupled heat pumps (Saner et al., 2010). Moreover, it was demonstrated that low enthalpy geothermal systems are the best cost-effective space conditioning solution for a wide range of buildings, notwithstanding the high initial investment costs (Self et al., 2013).

The principle of shallow geothermal energy installations is based on the heat exchange with the subsurface by means of a heat pump. Such systems use a little amount of electricity to move the heat from/to the subsurface to/from the end user and, thus, can be used both for heating and cooling. The operation of a heat pump is based on the principle of refrigerating machines, where electrical energy is used to perform mechanical work by powering a compressor to move heat from a cold to a hot place. In detail, a heat pump is based on four main components (**Figure 2.5**):

1. Evaporator
2. Compressor
3. Condenser
4. Expansion valve

The heat pump circuit is filled with a refrigerant fluid of specifically designed boiling and freezing points (e.g. a mix of water, antifreeze such as Propylene Glycol and a refrigerant such as Freon) such that it boils at a temperature ($\theta_A$) enough lower than the heat source temperature ($\theta_{in}$) (as it boils, it absorbs a large amount of latent heat). The refrigerant fluid at temperature ($\theta_D$) passes through a heat exchanger (evaporator) where absorbs heat from the heat source ($\theta_{in}$) until it evaporates. Now vapor, it passes through a compressor, powered by the electrical energy and, by reducing the volume, the temperature rises again ($\theta_B$). Then the refrigerant fluid passes through the second heat exchanger (condenser) where releases heat to the end user (e.g. a space conditioning system or a domestic water boiler) which has a lower temperature ($\theta_{out} < \theta_B$). In the condenser, the refrigerant condenses back to a liquid shedding latent heat to the heat sink. Finally, the refrigerant completes the cycle by passing through an expansion valve and losing more heat until it reaches the final temperature ($\theta_D$) and the cycle repeats. To gain and release heat at specific temperature values, the two subsections of the heat pump (i.e. evaporator and condenser) has to be kept at different pressures ($P_A < P_B$). Usually, a reversing valve allows to switch the process by gaining heat from the right-hand side and releasing it to the left-end side. This is often used to reverse the operating mode of a GSHP system from heating to cooling.

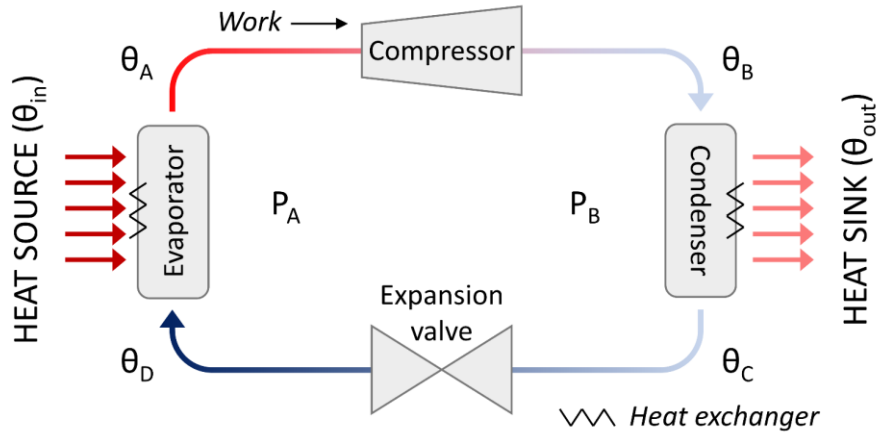


***Figure 2.5*** *– Diagram showing the components and operation of a heat pump.*

The efficiency of a heat pump is defined as the ratio between the heat delivered to- (H) or removed from (C) the end user, and the work performed by the compressor (E). This is expressed by the coefficient of performance for heating ($COP_H$) and colling ($COP_C$) mode:

$$COP_H = \frac{H}{E} \; ; \; COP_C = \frac{C}{E} \qquad \textit{(Eq. 2.9)}$$

H and C are also referred to as the "total heating and cooling loads" and are obtained as:

$$H = G_H + E \qquad \textit{(Eq. 2.10)}$$

$$C = G_C - E \qquad \textit{(Eq. 2.11)}$$

where $G_H$ is the heat extracted from the subsurface in heating mode and $G_C$ is the heat released in cooling mode. Since during cooling mode, the compressor increases the temperature of the refrigerant fluid to favor an efficient heat transfer into the subsurface, an additional heat is introduced into the system. Therefore, the "total cooling load" is given by the difference between the heat injected into the ground and the electrical energy (E) used by the compressor (which is used to increase the temperature of the system and, for this reason, has opposite sign than $G_C$, the heat released into the ground). Thus, the COP of a GSHP in cooling mode is always lower than the heating COP of the same system.

Low enthalpy shallow geothermal systems (also called generally GSHP) can be subdivided into two main categories depending on how the heat exchange between the heat-pump and the subsurface takes place (**Figure 2.6**):

- **Groundwater heat pumps (GWHP – Open-Loops):** the heat exchange is obtained by directly passing the groundwater (pumped from a groundwater well) through the heat exchanger of the heat pump. After the heat exchange the groundwater is given back to the aquifer or released into surface water bodies.
- **Ground-coupled heat pumps (GCHP – Closed-Loops):** the heat exchange between the subsurface and the heat-pump is obtained through an additional circuit where a refrigerant circulates in a loop (pipes) placed in the ground with which it has no direct contact. The heat transfer with the ground occurs through the piping material.

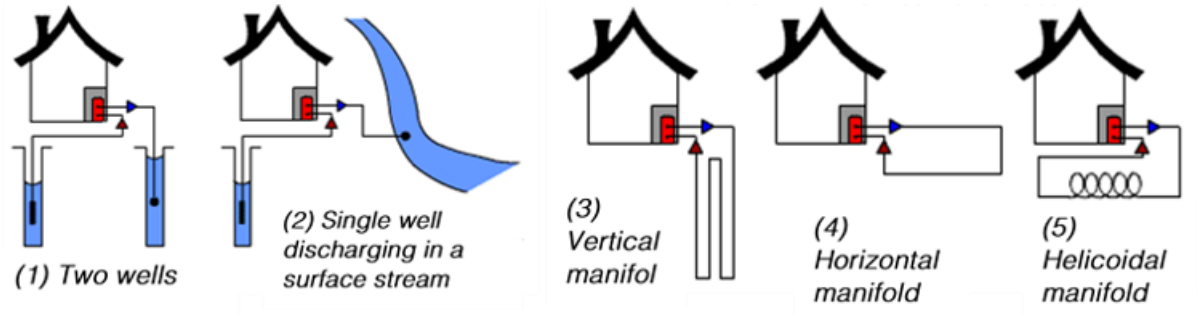


***Figure 2.6*** *– Schematic representation of different configurations of shallow geothermal systems: 1 and 2 – GWHP; 3, 4 and 5 – GCHP*

### 2.5.1. GWHP

Open-loop systems interact directly with the ground as they use groundwater as a direct heat transfer medium. The groundwater is pumped from an aquifer, passed through the heat exchanger of the heat-pump, and then discharged back to the source or into secondary water collection systems such as surface water bodies (e.g. rivers or man-made canals). The discharge in surface water bodies is the simplest and cheapest discharge mode for a GWHP system. In fact, it avoids the drilling costs of reinjection wells, the thermal alteration of the groundwater and the occurrence of thermal short-circuit (Casasso and Sethi, 2016a). However, at long term this method can lead the depletion of groundwater resources and the impact on the water balance of the exploited aquifers has to be assessed. Thus, GWHP systems with reinjection wells (**Figure 2.7**) are the most used since they do not require near surface water bodies and the fluid budget is always preserved.

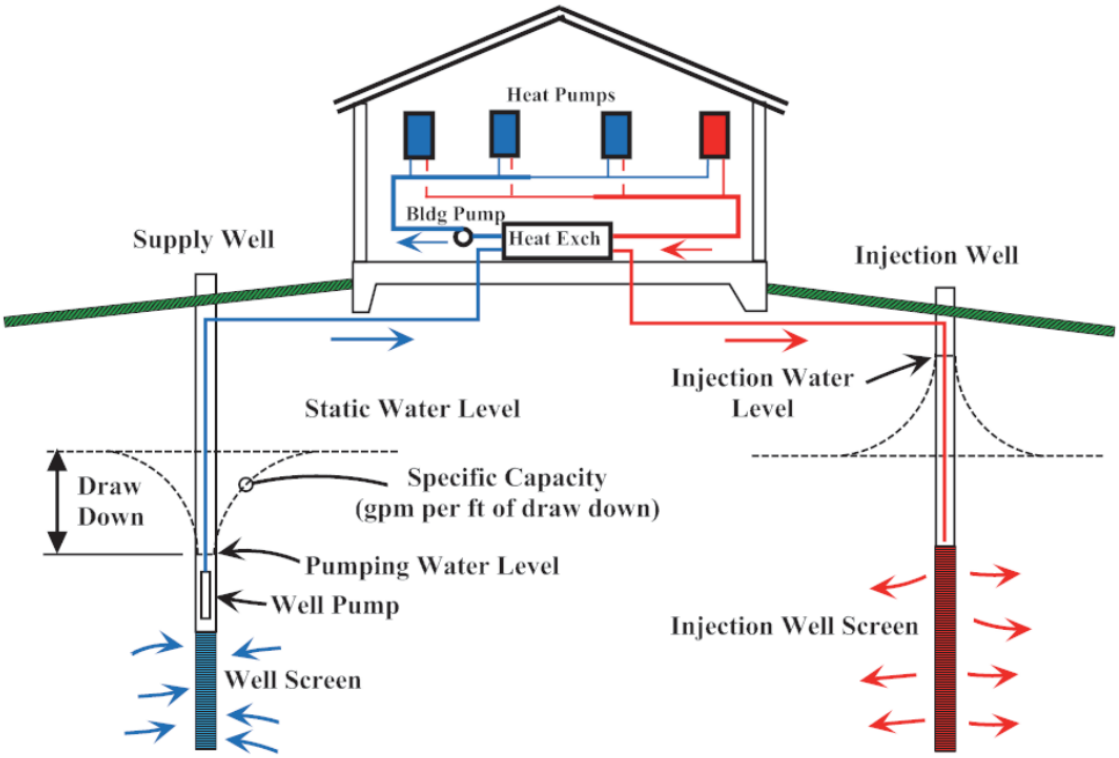


***Figure 2.7*** *– Schematic configuration of a groundwater heat pump (GWHP) (from* Kavanaugh and Rafferty, 2014)

The main advantage of GWHP is that the groundwater temperature is almost constant throughout the year, and it is close to the mean annual ambient temperature which makes this technology attractive for both heating and cooling. Moreover, the length to be drilled for open-loop configurations is usually less than vertical closed-loops with the same thermal output, and the associated initial costs compared to GCHPs is generally lower. The main disadvantage with respect to closed-loop systems is the higher cost of groundwater pumping that makes GWHPs attractive only for high thermal load installations where the pumping costs are compensated by the obtained thermal energy. For smaller installations such as single buildings, the more attractive solution is given by GCHPs.

#### *2.5.1.1. Sizing methods*

The amount of heat (P) that can be extracted from/released to the groundwater is given by:

$$P = \rho c_w * Q * \Delta T_w \qquad \textit{(Eq. 2.12)}$$

where $Q$ is the well discharge [$m^3/s$], $\Delta T_w$ is the water temperature variation due to the heat exchanger (drop or rise for heating and cooling mode, respectively), and $\rho c_w$ is the volumetric specific heat capacity of water (4.18 $MJ/m^3K$). The volume of water that can be extracted and

the temperature change are usually limited by local regulations on the protection of the quantity and quality of the groundwater resource. Thus, known the requested thermal power and the maximum allowable temperature change, extraction and reinjection wells has to be dimensioned according to aquifer properties and the groundwater regulation. Multiple wells (well fields) can be adopted for large power installations or low transmissivity aquifers.

### 2.5.2. GCHP

In closed-loop systems the heat exchange between the heat-pump and the subsurface is obtained by circulating a heat carrier fluid in an underground loop. The fluid has no direct contact with the subsurface and the heat exchange occurs through the piping material. GSHP systems can be divided in two configurations:

- Direct circulation: the heat-pump refrigerant fluid flows directly throughout the subsurface in a pipe which is the evaporator of the heat pump. With this configuration there is one single loop.
- Indirect circulation: an additional carrier fluid circulates in a secondary pipe loop placed in the subsurface. This additional loop is in contact both with the subsurface (through a borehole) and with the evaporator of the heat pump (through an additional the heat exchanger between the ground heat exchanger and the heat pump).

Closed-loop pipes can be coupled to the ground vertically, horizontally, or inside foundation piles. Horizontal GCHP are the cheapest solution and can be easily installed by means of a mechanical excavator. Usually the horizontal pipes are installed in trenches at depth from 1 to 3 m in a parallel or helicoidal configuration. Although horizontal arrangement is the cheapest solution among GCHPs, the total thermal power is relatively low due to the interference of relatively close coils and the higher seasonal temperature fluctuations in the very shallow subsurface. Hence, most of the GCHPs installations use vertical heat exchangers to improve the performance of the system. In fact, even if higher initial costs of vertical GCHPs are higher due to drilling operations, the more stable ground temperature at deeper locations and the lower interference between the pipes (less space is required) ensure better

performance and many authors agree that these systems are more efficient (Hepbasli, 2006; Viesi *et al.*, 2016).

A solution of water and antifreeze (if the loop is expected to reach temperatures below 0°C) is typically used as the heat "carrier" fluid (refrigerant). Antifreeze can be ethylene glycol, propylene glycol, methanol, ethanol, or sodium chloride (freezing points between -10 and -20 ° C are typical values for these solutions). The flow rate and the pipe internal diameter are properly regulated in order to:

- Reach turbulent flow conditions inside the pipes to improve the heat exchange between the ground and the carrier fluid;
- Avoid excessive hydraulic head losses in the pipes to reduce excessive power consumption;
- Maintain the flow rate in the heat pump to meet the power demand of the system.

The borehole depth typically ranges between 50 and 100 m for residential and over 150 m for larger industrial applications. Borehole depth higher than 200 m are generally avoided due to the drilling costs and generally a "borehole field" configuration is preferred. The borehole spacing has to be assessed through analytical and numerical solutions to prevent the thermal interaction between the pipes (Al-Khoury, 2012). Typical pipes configurations are (**Figure 2.8**):

- U-tubes: one (single U) or more (double U) pipes are arranged with the inlet pipe (that comes out from the heat pump) parallel to outlet pipe (that comes back from the ground to the heat pump), separated by specific grout;
- Coaxial: concentric pipes configuration where the inlet pipe is included with the outlet pipe (annular configuration – CXA), or vice versa (centered configuration (CXC).

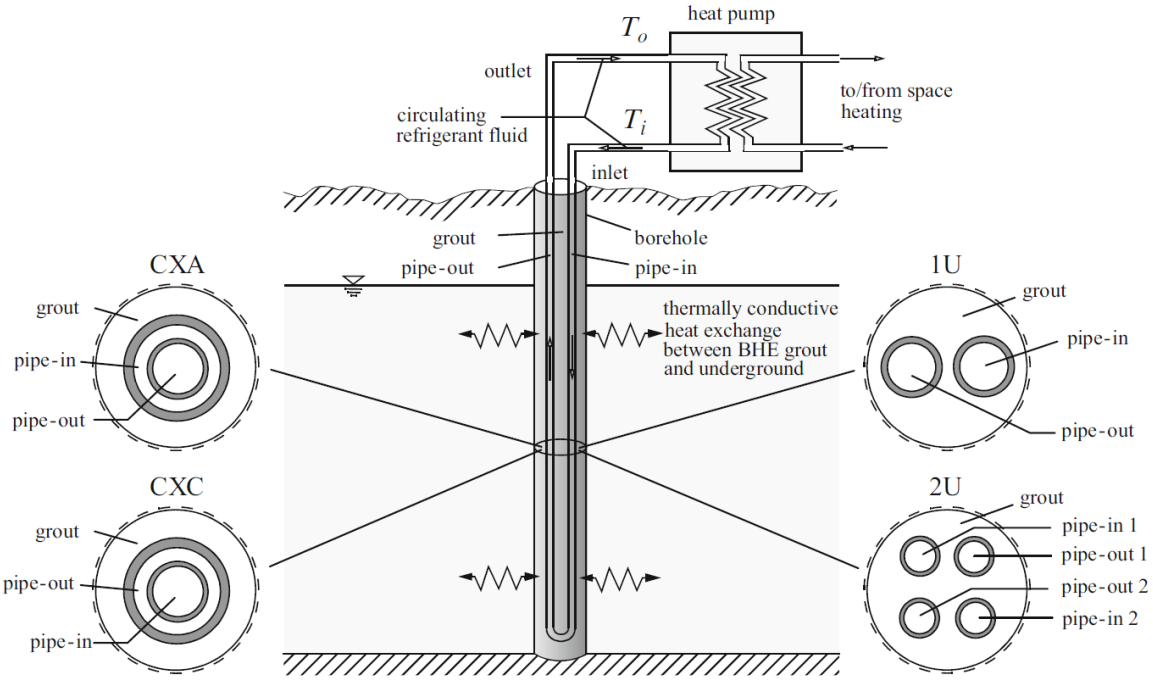


***Figure 2.8*** *– GCHP pipes configuration schemes: single U-shape (1U), double U-shape (2U), coaxial with annular inlet (CXA) and coaxial with centered inlet (CXC) pipes. From Diersch (2014).*

#### *2.5.2.1. Sizing methods*

Many installers use rules of thumb based on subsurface lithology to roughly assess of the thermal output of a GSHP system. As an example, the German guidelines on the thermal use of the underground (VDI 4640/2, 2001) provide tables and nomograms on the specific thermal power (i.e. the thermal output per length unit of installed BHE) according to the lithology, the type of installation and the yearly operating hours. These tables are generally obtained by comparing the effective thermal power of installed GSHP and can be very useful to derive preliminary estimates on the total required length and, thus, on the installation costs. Typically, horizontal installations tolerate specific extraction rates between 10 to 30 W/m, whereas vertical ones range from 25 to 100 W/m, depending on the ground properties (VDI 4640/2, 2001).

Sizing methods based on analytical equations (e.g. the ASHRAE method by Kavanaugh and Rafferty, 2014; the G.POT method by Casasso and Sethi, 2016b) can give more precise estimates on the thermal output according to the local undisturbed ground temperature, thermal diffusivity and the thermal resistance of the borehole. Analytical methods allow the estimation of the geothermal potential with an explicit correlation, which can be easily

implemented in a GIS environment or in electronic spreadsheets. An exhaustive explanation of the ASHRAE method (Kavanaugh and Rafferty, 2014) is given in section 6.3 and the geothermal potential of a reference GSHP system is estimated by this method in section 6.4.

Finally, the global thermal response of the coupled borehole-ground system is usually verified by means of an in-situ thermal response test (TRT). After drilling and installing a first exploratory borehole heat exchanger, the test is performed by injecting a constant thermal power in the loop (e.g. water at constant temperature) and measuring the temperature evolution during time at the end of the loop. Since the thermal resistance of the pipes is known from their material and geometry, the thermal response depends essentially on the underground temperature, which is measured in advance, and on the thermal properties of the ground, which are obtained. The infinite line source method by Ingersoll et al. (1954) was implemented by Carslaw and Jaeger (1959) to obtain the equation for the temperature field as a function of time ($t$) and radius ($r$) around a line source with constant heat injection rate ($q$) which can be used to derive the thermal properties of the ground during a TRT:

$$T(t) = T_0 + qR_b + \frac{q}{4\pi\lambda}\left[\ln\left(\alpha\frac{4\,t}{r_b^2}\right) - 0.5772\right] \qquad \textit{(Eq. 2.13)}$$

where $R_b$ and $r_b$ are the borehole thermal resistance and radius, $T_0$ is the undisturbed initial ground temperature, $\lambda$ and $\alpha$ are the ground thermal conductivity and diffusivity.

## 2.6. Geothermal potential

A common obstacle to shallow geothermal development is the lack of knowledge of the potential of heating and cooling techniques, and about the sites where geothermal installations could be more efficient and easily to installed. The geothermal potential is an indicator to describe and compare the efficiency and suitability of specific locations to host geothermal installations, i.e. describes the ability to exchange heat with the ground or groundwater. Even though it is not uniquely defined (Bayer et al., 2019), this is commonly obtained through analytical equations or by a combination of positive and negative scores based on local characteristics to obtain a general GIS-based comparative mark.

Bayer *et al.* (2019) reviewed the most relevant works on geothermal potential assessment introducing the distinction between the theoretical potential (i.e. the total energy stored in a reservoir or the amount of exchangeable heat based only on hydrogeological and thermal properties of the aquifers) and the technical potential (i.e. the fraction of the theoretical potential that can be used by a specific technology) (**Figure 2.9**). In practice, only a fraction of the total theoretical potential can be exploited depending on technical restrictions, and on existing regulations about the conservation of the groundwater resource and the protection of the thermal status of the aquifers (acceptable potential). The fraction of the technical potential that can cost-effectively be used is typically defined as the economic potential.

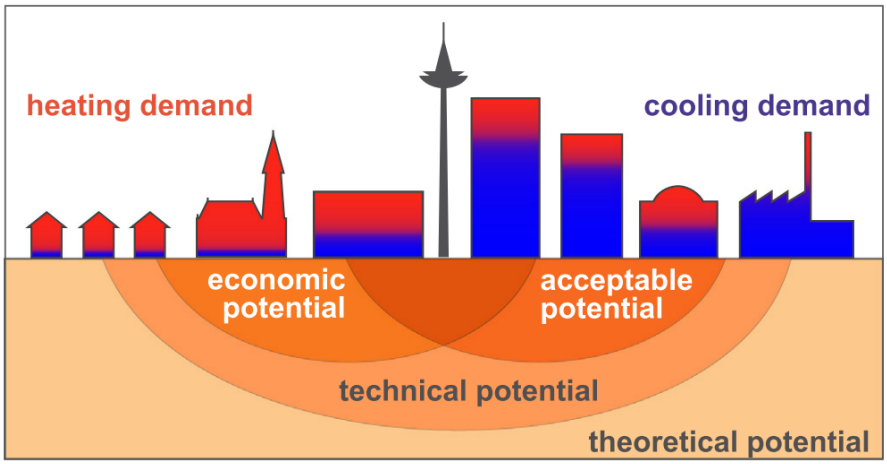


***Figure 2.9*** *– Illustration on the hierarchical distinction of the geothermal potential proposed by* Bayer et al. (2019)

Thus, hydrogeological and thermal settings (i.e. the hydraulic and thermal properties of each unit and the present thermal regime) as wells as restrictions imposed by local regulations and cost-benefit (payback) assessments have to be considered to obtain a comprehensive assessment of the effective technical thermal potential. Many authors mapped the technical geothermal potential of GCHPs and GWHPs by combining climatic and thermo-geological information through theoretical physical equations (García-Gil et al., 2015; Zhu et al., 2011) or empirical equations (Böttcher et al., 2019; Casasso and Sethi, 2016b; Galgaro et al., 2015; Viesi et al., 2018) and derived techno-economic indicators such as the investment cost and payback times (Perego et al., 2019). At the city scale Epting *et al.* (2018) and Mueller et al. (2018) evaluated the amount of extractable heat through numerical modeling techniques. These methods are very precise tools for city-scale geothermal potential assessment and thermal management of local aquifers but are computationally expensive for regional-scale

geothermal mapping. **Figure 2.10** shows the workflow adopted by *Casasso et al. (2017)* to derive the geothermal potential of GCHP for the Cuneo province (Northern Italy) combining geological, hydrogeological and climatic data into their G.POT method.

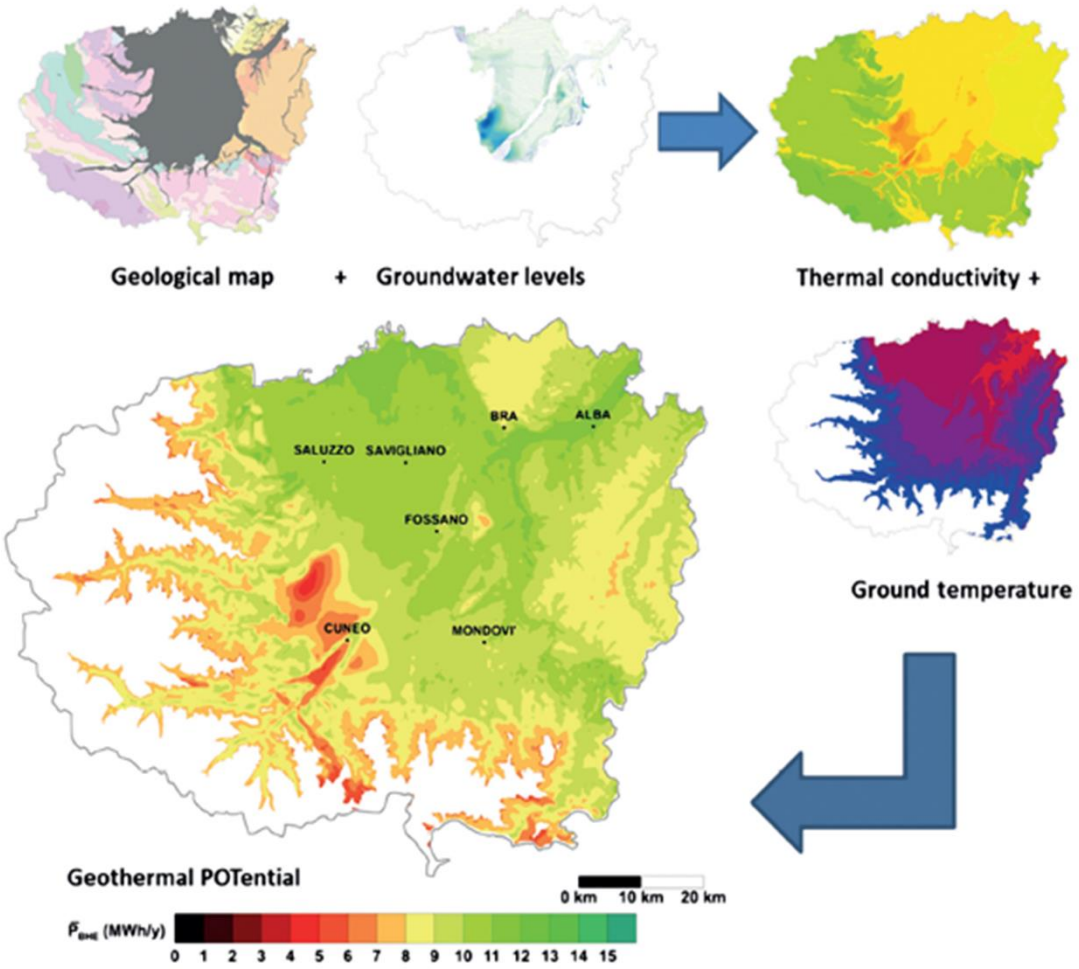


***Figure 2.10*** *– Typical workflow to derive the shallow geothermal potential from geological, hydrogeological and climatic data. (modified from* Casasso et al., 2017)

# 3. Human impact on subsurface temperatures

Recent studies on the climate, based on past meteorological records and modeling of future scenarios show a worldwide dramatic warming trend (Solomon et al., 2007). This temperature increase is and will be more extreme in most big cities around the world due to the urban heat island (UHI) effect (Oke, 1973). The UHI is defined as the positive air temperature anomaly in the city center respect to the surrounding rural areas due to modifications of the natural surface energy budget caused by human-related changes of the urban environment. Oke (1973) demonstrated that the size and intensity of the UHI it is positively correlated to the population density and city size. This phenomenon is well known in the atmosphere and, recently, was investigated also in the subsurface environment of many cities worldwide (for a review, Bayer et al., 2019 and Zhu et al., 2011; Berlin, Cologne and Karlsruhe, Benz et al., 2016 and Menberg et al., 2013a; Basel, Epting and Huggenberger, 2013; Cardiff, Farr et al., 2017; Paris, Hemmerle et al., 2019; Munich, Frankfurt and Darmstadt, Menberg et al., 2013a; Tokyo, Seoul, Osaka and Bangkok, Taniguchi et al., 2007; Amsterdam, Visser et al., 2020;). The UHI is often documented in densely populated and highly developed cities as its formation is related to the modifications of the environment due to urbanization, such as land artificial covering/sealing with buildings, asphalt and surface infrastructures, and heat losses from anthropogenic sources. Such factors modify the solar radiation balance and the energy balance at the earth's surface, leading to the local warming of the air and the ground temperature. The development of subsurface urban heat islands (SUHI) is related to human modifications of the surface (e.g. density of buildings and asphalted/concrete infrastructures) and subsurface (e.g. foundations, tunnels and shallow geothermal uses) settings (**Figure 3.1**).

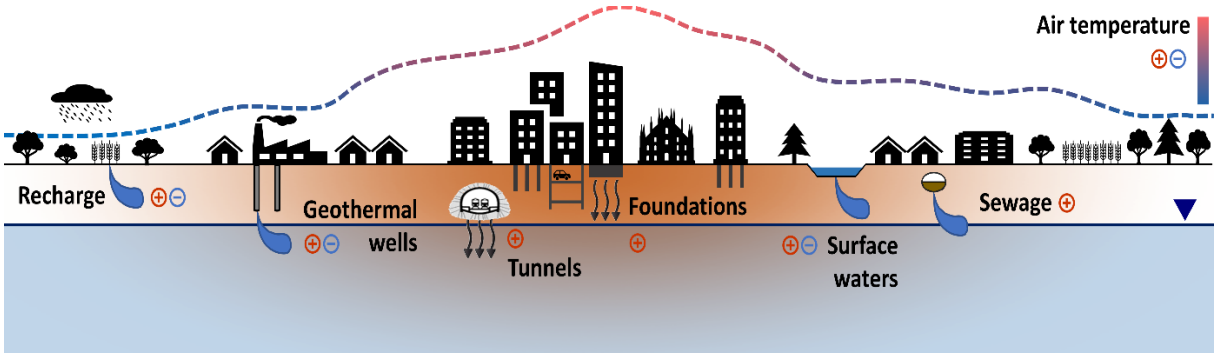


***Figure 3.1*** *– Schematic representation of the heat sources in the subsurface of urban areas*

For the above mentioned city sites, the shallow mean annual groundwater temperature is 2 to 8 °C warmer than in suburban areas and, for some of them, a warming trend was recognized due to global warming and urbanization effects. Benz et al. (2015) evaluated the thermal contribution of various anthropogenic heat sources for two European cities revealing the building basements and the elevated ground surface temperatures as the dominant heat sources on a citywide scale.

SUHIs were documented as an environmental issue since elevated temperatures can affect the groundwater quality in terms of chemical, physical and biological conditions (Blum et al., 2021) and living ecosystems (Brielmann et al., 2009). However, elevated groundwater temperatures may also represent an opportunity in areas with high energy demand since the thermal energy stored in the aquifers can be exploited by shallow geothermal systems (Arola and Korkka-Niemi, 2014; Bayer et al., 2019). This, besides recovering part of the energy released by human activities and stored in the subsurface, might control the size and the intensity of the SUHI in large cities (and the above-mentioned side effects). Thus, the analysis of the thermal regime is essential to the sustainable management of the subsurface thermal resources in order to reach, by a cautious usage, a balance between the heat released by anthropogenic pollution and the heat extracted by geothermal installations. As an example, Zhu et al. (2011) estimated the thermal potential of SUHIs in several big cities due to elevated groundwater temperatures to be always higher than the total annual city heating demand.

## 3.1. Investigation methods

Define the spatial distribution of natural variables in complex systems, such as the temperature distribution in urban groundwater bodies, is a tough issue and appropriate monitoring, descriptive techniques and spatialization methods are necessary. First, the heat sources in the urban subsurface are typically arranged in some isolated spots (e.g. specific structures, wells) whose thermal perturbation has a finite spatial extent (Attard et al., 2016), but in high urban density areas these contributions mix together to obtain a diffuse thermally altered zone (SUHI). Secondly, groundwater chemical-physical parameters can only be measured directly by means of piezometers (**Figure 3.2a**), which represent a punctual or at most linear (vertical) information. Thus, the robustness of investigations on the subsurface thermal regime depends not only on the adopted techniques but mostly on the spatial density and the appropriate choice of monitoring locations. As a general rule, the more information may have, the better, but the location of groundwater monitoring wells is not secondary. In fact, city-scale and regional investigations rely on information which are not too close to specific heat sources to catch the general behavior of the system. Anyway, measurements close to specific sources can improve the understanding of single phenomena, which may be useful to delineate the general framework, but have to be considered carefully to avoid misinterpretations of the whole system.

The most and easily adopted groundwater temperature monitoring techniques are:

- Temperature-depth profiles (**Figure 3.2b**): point-in-time measurements of the groundwater temperature at different depth levels. This is usually done by moving a probe inside the piezometer to record the temperature with a given vertical spacing;
- Temperature time-series (**Figure 3.2c**): time distributed measurements of the groundwater temperature at a specific depth in a piezometer. This is usually performed by automatic sensors/data loggers placed at specific depth inside a piezometer.
- Combined (distributed): time distributed measurements of the groundwater temperature along the vertical extension of a piezometer. This is usually done by placing a series of automatic sensors at different depth levels or by distributed fiber optic technique.

Temperature depth profiles are useful to derive vertical and horizontal flow patterns inside an aquifer from the analysis of the profile shape (e.g. Anderson, 2005; Taniguchi et al., 1999). They also contain information on the depth of the seasonal fluctuation zone and the shallow thermal gradient, which is regulated by the surface thermal regime and, thus, can be used to obtain information on the thermal perturbations from the surface (e.g. Taniguchi et al., 1999). Temperature time-series are useful to assess the degree of thermal interactions with the surface and to derive thermal properties and hydrogeological settings of the subsurface (e.g. Smerdon et al., 2006; Taylor and Stefan, 2009), as well as to evaluate the temporal trend of the groundwater temperature related to climate change and urbanization (e.g. Menberg et al., 2014; Taylor and Stefan, 2009).

Thus, to define the extent and the intensity of the SUHI and to derive information on the main controlling factors, different spatialization and statistical techniques have been adopted. Usually, spatial interpolation of groundwater temperature is performed only with very highly distributed data and attention must be paid in complex urban settings. Point representation is usually preferred and the correlation with natural and anthropogenic heat sources can be resolved by statistical techniques such as bi- and multi-variate statistics. In complex systems, the number of variables relatable to thermal pollution can be very high and the principal component analysis (PCA) can be used to reduce their dimensionality.

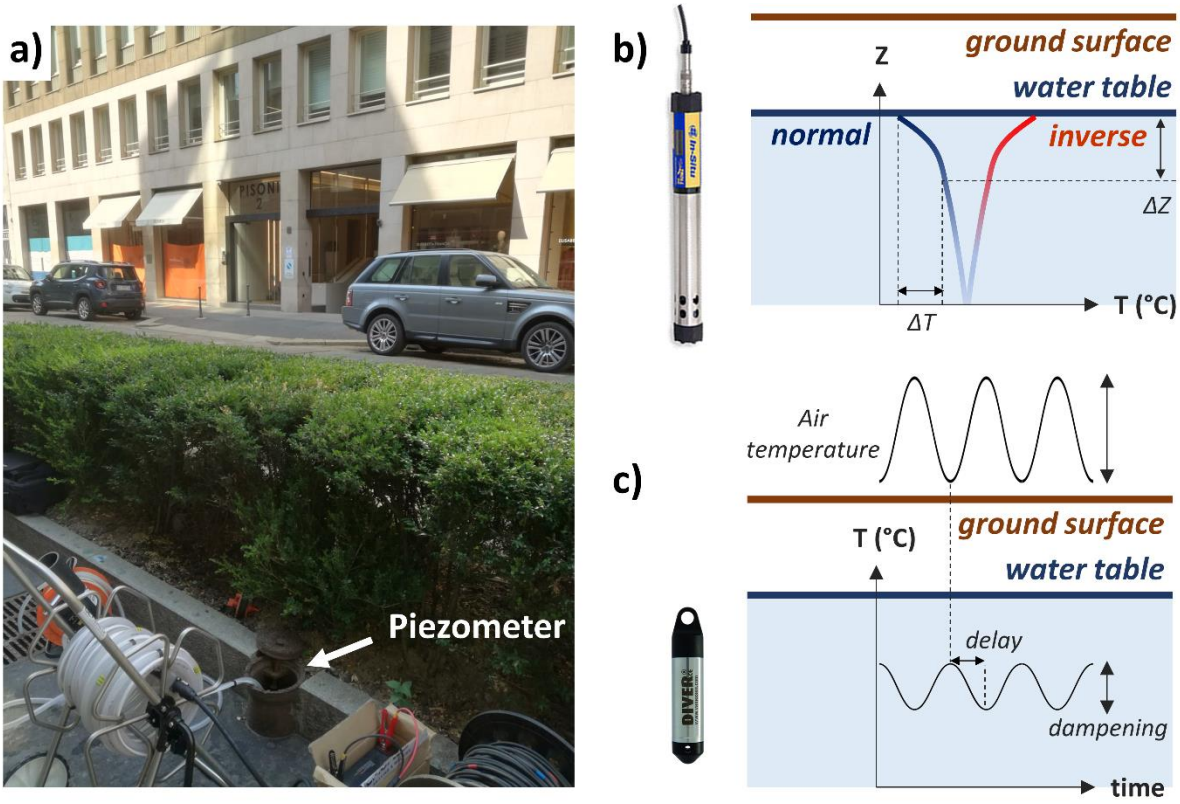


***Figure 3.2*** *– (a) Example of groundwater temperature monitoring in urban areas: (b) temperature-depth profiles by manual vertical logging and (c) automatic recording of temperature time-series.*

# 4. Geological and fluid-flow/heat-transport 3D modeling of shallow aquifers

Over the last 40 years, several methods based on experimental data and mathematical approaches have been developed to study coupled fluid flow and transport processes in complex natural porous systems, such as aquifers (Bundschuh and Suarez Arriaga, 2010). Among the mathematical methods, analytical methods were initially used, followed by analog models and, most recently numerical models. One of the main problems is the difficulty to accurately represent the dimensions and the spatial distribution of randomly distributed natural geological features (e.g. the grain size distribution of shallow aquifer bodies, fractures of rock masses) and their relative hydrogeological and thermal properties (e.g. hydraulic conductivity and thermal diffusivity). The mathematical model and its associated numerical code can be used to combine several complex hypotheses and to verify them against observed facts and data. Thus, physical processes-based numerical modeling is a unique tool for the quantitative analysis and synthesis of the subsurface, as it can reproduce large scale physical processes of natural systems which cannot be made in the laboratory. A full digital twin is reached when all the information on the subsurface, relevant at the scale of analysis, are integrated in the model as material properties and dynamic boundary conditions. A digital twin has the ‘‘pre-diction’’ and ‘‘retro-diction’’ capacities and allows the quantitative estimation of future behaviors that are yet to be observed, as well as the estimation of processes that are no longer observed. In addition, the cost of a numerical model is considerably lower compared to any other techniques.

## 4.1. Subsurface geological modeling

“Hydrogeology” is the combination of “hydraulics” and “geology” (De Marsily et al., 2005): somehow, hydraulics can be considered a relatively simple science as it is based on equations that can be solved, analytically or numerically, given the geometry of the system, boundary conditions, etc.; geology is much more complex as the description of a natural system and the

spatialization of hydraulic and thermal properties is based only on few spots at which they were measured (e.g. borehole logs, pumping tests) or indirectly estimated from the response of the subsurface to a related property (e.g. porosity or water content from resistivity). Thus, aquifer heterogeneity is a key matter in subsurface modeling as it controls the fluid flow and solute/heat transport in highly conductive aquifers (De Marsily et al., 2005). The heterogeneity of aquifer systems exists at different scales (Bersezio et al., 1999): from fine scale (e.g. small lenticular structures) to large scale (e.g. fining/coarsening sequences, alternance of different grain-size layers). Modeling the effects of fine scale heterogeneities on large scale fluid flow and heat transport is impossible due to the lack of spatially distributed information and the highly computational costs of a large, highly detailed model. Therefore, the fine scale heterogeneity is usually upscaled and averaged by identifying homogeneous portions, whose equivalent parameters (e.g. volume averaged) allow to reproduce the average flow regime at larger scale throughout the real heterogeneous sedimentary structures (**Figure 4.1**).

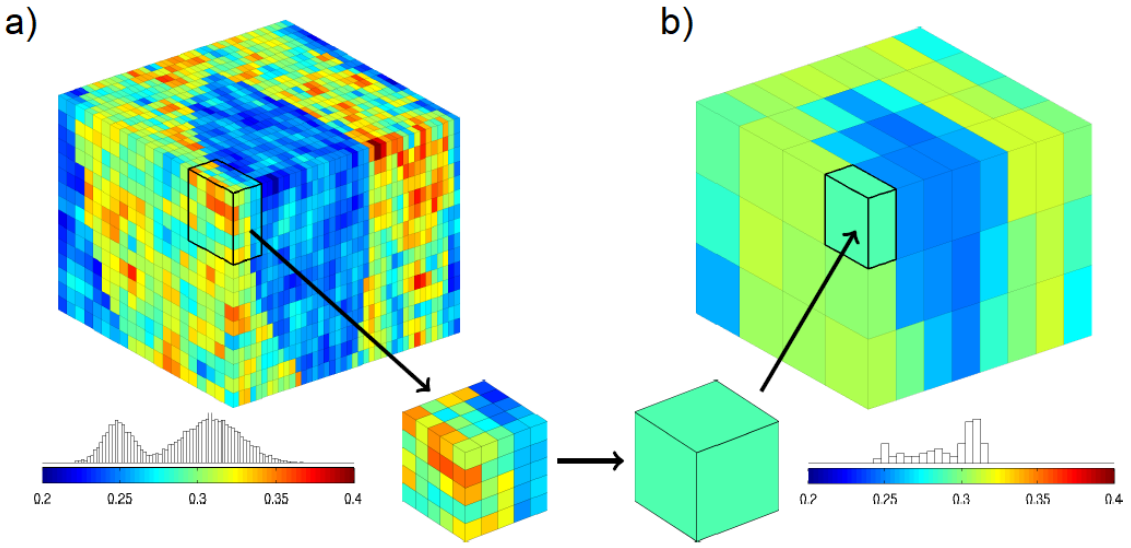


***Figure 4.1*** *– Example of upscaling of geological properties considering the volume weighted average of parameters described by (a) over the blocks in (b).*

According to the scale of the investigated phenomenon, thus on the data spatial density and size of the systems, different degree of heterogeneities upscaling can be adopted. A common approach in subsurface flow modeling is based on the subdivision of the subsurface according to geological bodies (i.e. sedimentary units) or to the grain-size distribution (i.e. litho-facies and hydro-facies) of the deposits. The second approach is more appropriate to the mentioned

aims as the flow and transport processes are related to hydraulic and thermal parameters which, for shallow unconsolidated aquifers, depend mainly on the grain size distribution.

### 4.1.1. Model types

Subsurface geological modeling to support flow and transport simulations in heterogeneous porous media is a longstanding challenge and many methods were developed since the '60. Large-, medium- and fine-scale subsurface heterogeneities are only recognized at few spots and adequately characterized along the vertical direction (e.g. core samples, lithologic borehole logs), but the horizontal connectivity of different units between two points where they have been recognized has to be assessed by interpolation techniques. As reviewed in several books and review articles (e.g. Davis and Sampson, 1986; de Marsily et al., 2005; De Marsily et al., 1998; Journel and Huijbregts, 1976) geostatistical methods have been extensively used to characterize the subsurface heterogeneities, in terms of facies or parameter spatial distribution, and associated uncertainty. They are mainly divided into continuous properties (e.g. gaussian distributed natural variables such as the hydraulic conductivity, porosity, percentage of a specific grain-size class) or discrete features/indicators (e.g. sedimentary facies) interpolators. Another main distinction exists between deterministic (a unique solution is obtained, which is the best estimate) and stochastic (give the probability that a certain value/property is encountered in a certain portion of the domain) methods.

The Kriging method is a deterministic geostatistical method to interpolate continuous natural variables such as geological properties (Journel and Huijbregts, 1976). It is based on the definition of a variogram (**Figure 4.2a**), where the variance of each pair of data is evaluated according to the mutual distance. Thus, if the data are spatially correlated, the semi-variance increases with distance until a horizontal plateau is reached around the mean variance of the dataset. Finally, the Kriging estimate is given by a weighting function according to the distance of the surrounding information and the defined variogram model. 3D Kriging is often used in the parametrization of numerical models (e.g. Ouellon et al., 2008) due its simplicity, but it is less adequate to reproduce the exact shape sedimentary bodies. As an example, sharp contacts between facies (as in the "real" subsurface) are not well represented and the connectivity between very high/low layers can be hampered. This approach was implemented

to improve the subsurface facies reconstruction by applying different layers of gaussian distributions (e.g. the percentage of fine sediments together with the size of gravels in alluvial plain deposits) and truncating the distribution to derive the facies structure from a related property. Recently, multiple-point variogram techniques (Strebelle, 2002) were developed to characterize the connectivity of curvilinear geometries that cannot be modeled with traditional two-point variograms.

Indicator interpolators describe the occurrence of a certain facies at each location in the model by means of a Boolean indicator (e.g. assign 1 if class *n* occurs at location x, and 0 if doesn't occur). Thus, the facies are mutually exclusive and their occurrence can be defined e.g. by Indicator Kriging and Markov Chain (Fogg, 1996) methods. The first is still based on a binary variogram (i.e. it evaluates the distance at which the probability to find a specific facies becomes equal to the probability to don't find it), while the second is based on the definition of the spatial structure of categorical data (i.e. facies) according to transition probability laws between each combination of facies (**Figure 4.2b**). The main advantage of these methods is that they incorporate geological information such as mean lengths and directional orientation of lithofacies and, thus, better honor the sedimentary structures. However, their shape and mutual relations can be hard to assess in areas with low spatial density of data and their implementation into a numerical model often requires an upscaling procedure.

**Figure 4.2** illustrates the main characteristics of the variogram (Kriging) and transition probability (Markov Chain) models together with an example of typical results.

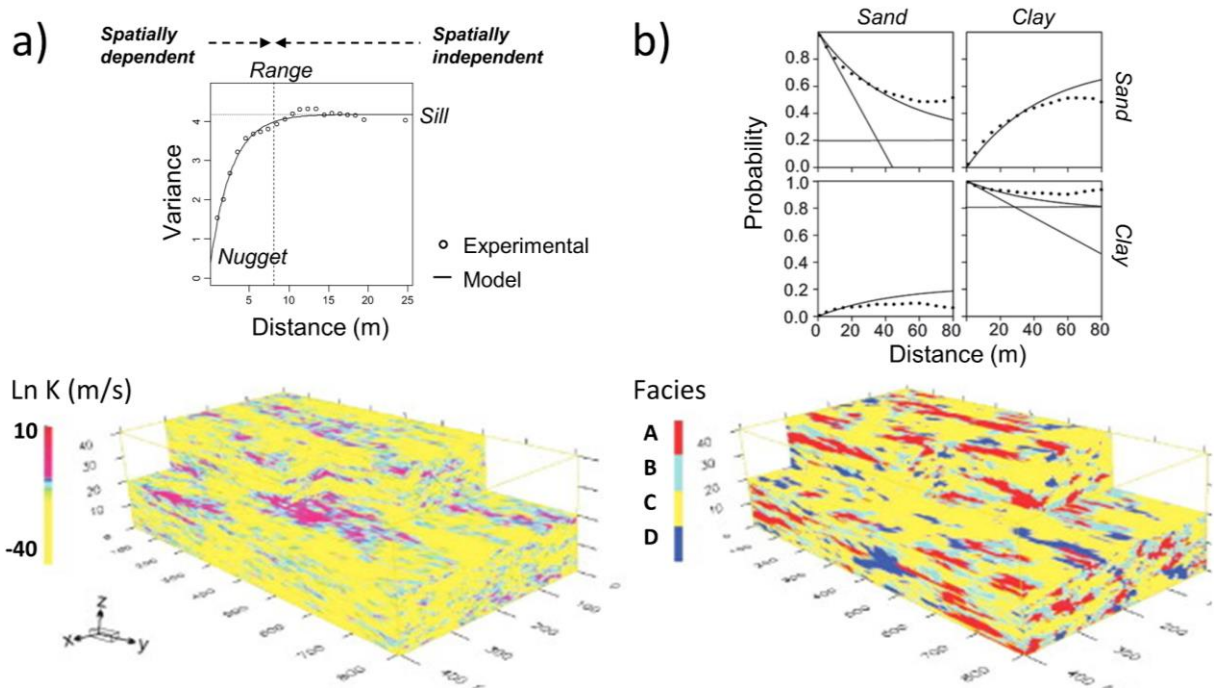


***Figure 4.2*** *– (a) Variogram model characteristics and typical spatial distribution of the logarithmic hydraulic conductivity obtained from a Kriging solution. (b) Transition probability model for a two facies system and typical spatial distribution of discrete facies obtained from a Markov Chain solution. Redrawn from* (Lee et al., 2007).

## 4.2. Numerical modeling

A numerical model is used to describe in space and time natural processes, such as groundwater flow and heat transport in porous media, by solving partial differential equations (PDE) of flow and transport physical processes, based on initial and boundary conditions. Unlike few special idealized cases with very simple geometry, finding analytical solutions to describe complex spatially distributed (random) natural phenomena is too tough. Numerical techniques allow finding solutions in irregularly bounded areas or when boundary conditions vary in time and space. The main distinction between numerical codes is based on how PDE describing the system are solved. The main ones are the finite difference method (FDM) and the finite element method (FEM) (**Figure 4.3**). Each method leads to a set of algebraic equations in which the unknows are the hydraulic head and/or temperature at a finite number of nodal points (Wang and Anderson, 1995). The FDM consists of replacing differential expressions by quotients of differences that include the values of the unknowns (Smith et al., 1985). Thus, the solution of PDE is performed by means of a system of algebraic equations that can be solved using different techniques. The FEM is a method for solving PDE by

approximating continuous quantities as a set of quantities solved by an integral approach (instead of a differential approach for the FDM) at discrete points (nodes). The domain is decomposed into a set of sub-regions (elements) were quantities are defined by interpolation functions between the nodes (Zienkiewicz et al., 1977). The FDM is usually implemented with rectangular cells, while the FEM is implemented with a variety of element types such as triangles, tetrahedra and hexahedra. The use of interpolation functions to define the solution throughout the problem domain is an important concept that distinguishes the FEM from FDM models. The FDM is a classic numerical solution technique, which despite its geometric limitations is still widely used in modeling groundwater and geothermal systems due to its simplicity and consequent easiness in programming. FEM models can be adapted to problems of great complexity and unusual geometry, and they are extremely powerful to solve complex fluid flow and transport processes.

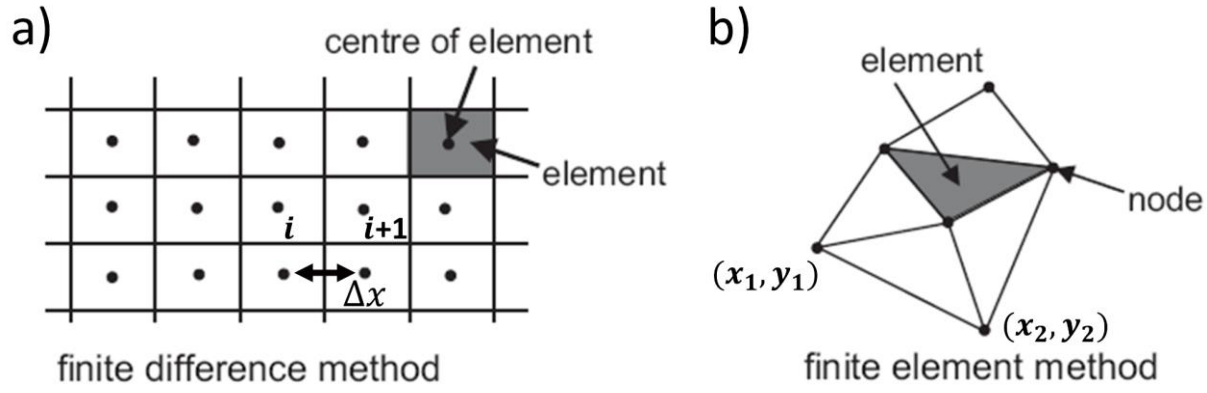


***Figure 4.3*** *– Schematic representation of the distinction between (a) the finite difference method (FDM) and (b) the finite element method (FEM).*

According to Bundschuh and Suarez Arriaga (2010), the main steps in numerical modeling of subsurface groundwater flow and heat transport are: (1) the elaboration of an accurate conceptual model, (2) the selection of the appropriate code suitable for the elaborated conceptual model, (3) the discretization of the model area in space and time, (4) the correct calibration and validation of the model by selecting the appropriate calibration and validation parameters, and (5) the correct evaluation of the simulation results and reliability considering the model uncertainties, that are related to the uncertainty of the data used to test the selected conceptual model.

### 4.2.1. The conceptual model

The conceptual model of a system is a schematic representation of all the phenomena contributing to control the investigated processes (i.e. groundwater flow and thermal regime) considering the scale of analysis. To delineate a conceptual model for regional scale fluid flow and heat transport analysis several data must be collected. Among these, direct (hard) and indirect (soft) geological data are useful to derive the structure of different geological units, their composition and limiting surfaces such as aquitards and aquicludes. Field groundwater head and temperature data and water balance schemes are useful to define the amount and location of the main fluid and heat sources and sinks in the modeling area (e.g. regional groundwater inflow/outflow, groundwater recharge from precipitation and surface water bodies, groundwater abstraction from drinking water and geothermal wells). Information on the location and depth of human structures and infrastructures as well as climatic data are useful to identify the main thermal sources and their spatial distribution. Generally, all the features introduced in the conceptual model must be addressed in the numerical model in terms of hydraulic/thermal parameters and boundary conditions.

### 4.2.2. The continuum approach

Since microscale characterization in large scale modeling is not practical and the necessary data spatial density for a fully representative parametrization is not available, an acceptable upscaling of the properties must be introduced. The most adopted assumption is that a porous granular medium, such as an aquifer, can be regarded as a continuum (e.g. Bear, 1972). The continuum assumption ignores the fact that a medium is made of discrete particles (i.e. grains) tighten each other with voids filled by fluids (e.g. air or water). Instead, variables such as temperature and pressure are assumed to be well-defined at infinitely small scale, and they vary continuously from point to point. When considering groundwater flow and transport in porous media, only the interconnected pore space needs to be considered, whereas the solid matrix can participate in the heat transport. By definition, a continuum can be defined at every point within the domain, which is not possible for a porous medium since it is composed of at least two phases and sharp contacts of grains, characterized by different variables. This is overcome by smoothing the real scale variability with a continuum equivalent medium

assumption considering the principle of the representative elementary volume (REV) (Bear, 1972). The REV is the minimum volume at which a given parameter measurement becomes independent to the size of the sample (**Figure 4.4**). In other words, the REV corresponds to the minimum volume of the porous media to obtain non-random estimates of the parameters describing the solid, the void space, and fluid phases at any point in the porous medium domain. At this scale, the estimated parameters behave as a continuous homogeneous medium. Thus, each element dividing the model domain must be greater than the REV for the investigated parameters and physical quantities.

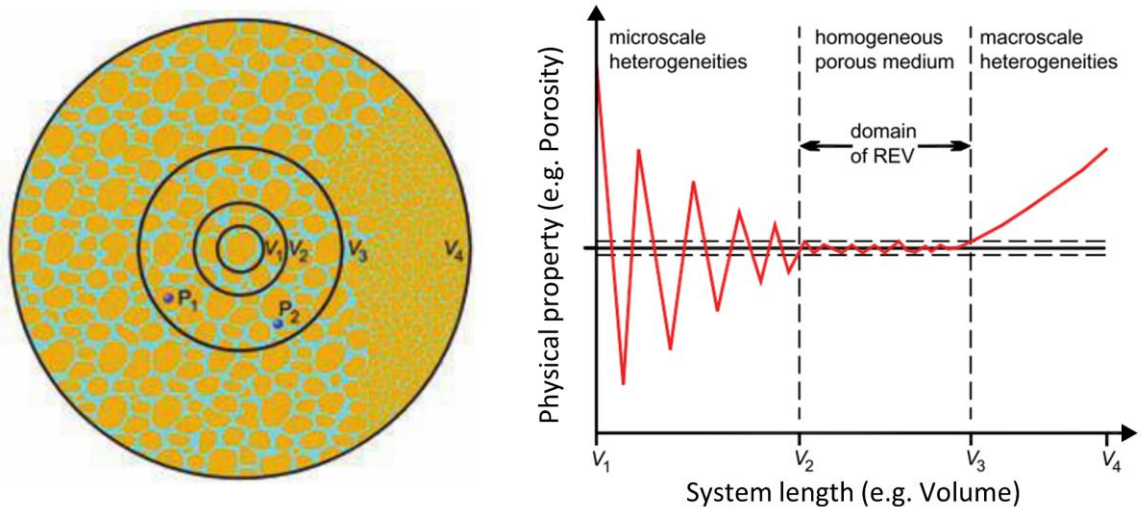


***Figure 4.4*** *– Representative elementary volume (REV) approach: the medium properties becomes homogeneous at a volume larger than $V_2$, where microscale heterogeneities have no more effect on the measured property. For volume higher than $V_4$, macroscopic aquifer heterogeneity becomes relevant.*

### 4.2.3. Governing equations

The global governing equations at the macroscale are obtained by linking single constitutive relations, e.g. the Darcy's and Fourier's law, of the investigated processes in a multiple phases (solid, fluids, gases) system represented by equivalent properties of a continuum. The set of governing equations for the fluid flow (Eq. 2.7) are coupled to the equations for heat transfer (Eq. 2.1) and transport (Eq. 2.6) by considering the fluid mass and thermal energy balance to obtain the set of simultaneous equations needed to solve the problem (Diersch, 2014). Thus, the fluid flow in transient conditions is described by (Eq. 4.1) which combines the Darcy's law and the continuity equation for the mass conservation for a single elementary portion of the continuum (e.g. a cell or element):

$$-\nabla \cdot (-\boldsymbol{K}\, \nabla h) + w = S_s \frac{\partial \boldsymbol{h}}{\partial t} \qquad \textit{(Eq. 4.1)}$$

where $\boldsymbol{K}$ [m s$^{-1}$] and $S_s$ [m$^{-1}$] are the equivalent hydraulic conductivity and the specific storage of the porous medium, $h$ [m] is the hydraulic head and $w$ [m$^3$ s$^{-1}$] represents the fluid sources/sinks.

Similarly, (Eq. 4.2) describes the "global problem" of the subsurface for the thermal energy balance in transient conditions:

$$\boldsymbol{q}\, \rho c_{fluid} \cdot \nabla T - \boldsymbol{\lambda}_{bulk} \cdot \nabla^2 T + \rho c_{bulk} \frac{\partial T}{\partial t} - s = 0 \qquad \textit{(Eq. 4.2)}$$

where $\boldsymbol{q}$ [m s$^{-1}$] is Darcy's flow velocity, $\rho$ [kg m$^{-3}$] the specific mass, $c$ [J kg$^{-1}$ K$^{-1}$] the specific heat capacity, $\rho c_{bulk} = \varphi * \rho c_{fluid} + (1-\varphi) * \rho c_{solid}$ [J m$^{-3}$ K$^{-1}$] the bulk volumetric heat capacity (*svc*), where $\varphi$ is the porosity, $T$ [K] is the average element temperature, $\boldsymbol{\lambda}_{bulk} = \left(\boldsymbol{\lambda}_{fluid}\right)^{\varphi} * (\boldsymbol{\lambda}_{solid})^{(1-\varphi)}$ [W m$^{-1}$ K$^{-1}$] is the bulk thermal conductivity obtained as the geometric mean between the solid ($\boldsymbol{\lambda}_{solid}$) and the fluid ($\boldsymbol{\lambda}_{fluid}$) thermal conductivity (Woodside and Messmer, 1961), and $s$ [W m$^{-3}$] is the heat source/sink term.

The first term of (Eq. 4.2) denotes the amount of heat transported by advection (i.e., by the movement of the fluid mass), the second term denotes the conductive heat flux (i.e., due to a temperature gradient), the third term represents the heat released/stored due to a temperature variation and the last term the heat gained/lost by external sources/sinks. The relevance of the advection versus the conduction process is governed by the hydrogeological and thermal properties of the medium and is described by the dimensionless Péclet number given by (Eq. 2.8). In numerical analysis, this is also used to assess the stability of coupled advection-dispersion processes. The Péclet-grid number depends also on the size of the elementary volume (i.e. mesh element) and is evaluated for a specific computational mesh through the following equation (Eq. 4.3):

$$Pe = \frac{\boldsymbol{q}\, L}{D^t} \qquad \textit{(Eq. 4.3)}$$

where the characteristic length $L$ [m] is determined according to the element size in the flow direction and $D^t$ is the thermal dispersion coefficient that includes both thermal diffusion ($\lambda/\rho c$) and mechanical dispersion effects described by the longitudinal ($D_L$) and transverse

($D_T$) dispersivity (Diersch, 2014). To avoid numerical instability and artifacts the Péclet-grid number which should not exceed a value of 2.

### 4.2.4. Geometry, parameters, and boundary conditions

The model domain is a simplified representation of the investigated portion of the subsurface (e.g. an aquifer). It is bounded horizontally (at the top surface and at the bottom) and vertically by lines/surfaces of known head/temperature (i.e. equipotential lines in 2D or surfaces in 3D) or fluid/heat flux (i.e. flow lines in 2D or faces in 3D) which can be easily implemented as boundary conditions (BC). Typical horizontal boundaries are the top (ground surface) and the bottom (no flow boundary) of the aquifer system, while vertical lateral boundaries can be regional groundwater flow lines, rivers and lakes or impervious features such as units with significantly lower conductivity with respect to the investigated aquifers. Moreover, the numerical solution of flow/transport equations requires the discretization of the model volume. This is obtained by constructing a computational mesh made of a web of lines defining 3D cells (or elements) and intersecting at points called nodes. The elements can be triangular or of polygonal shape in two dimensions, and tetrahedral or prismatic in three dimensions. Volumetric quantities such as temperature or pressure are defined at the centroids of the elements or at nodes according to the model type (FDM or FEM). For numerical accuracy, a grid or a mesh is refined around wells with significant discharge or near features where large gradients in the hydraulic heads and temperature, or rock properties, are observed or expected. Thus, the size of the elements should be fine enough to avoid numerical errors close to large gradient zones, but coarse enough to meet the REV size.

The structure and geometry of different geological layers or units such as aquifers, aquitards, and semipermeable layers, must be determined before developing the mesh structure. The volume-equivalent hydrogeological and thermal properties of each modeled geological unit, with their spatial variation, heterogeneity and anisotropy must be evaluated in horizontal and vertical directions to obtain a parametrization of the domain. As mentioned above, the heterogeneity of the aquifers must be evaluated in order to define zones with uniform values (e.g. typically an element or a group of elements).

Additional parameters are used for specific applications, e.g. to consider the fluid or heat exchanges between the surface and surface water bodies, and the groundwater. A list of the main parameters required by a fluid flow and heat transport numerical analysis is shown in **Table 4.1**. What information is necessary and what can be neglected depends to a large degree on the objectives of the numerical model and hence, must be assessed by the modeler.

***Table 4.1*** *– Hydraulic and thermal parameters adopted in a fluid flow and heat transport numerical model.*

| *Parameter* | *Symbol* | *Unit* | *Description* |
|---|---|---|---|
| ***Hydraulic properties*** | | | |
| Horizontal and vertical hydraulic conductivity | $K_h$ , $K_v$ | m/s | describes the ease with which water can move through a saturated porous medium |
| Effective porosity | $n_e$ | - | ratio between the interconnected pore volume (that contributes to fluid flow) and the total volume |
| Specific yield | $S_y$ | - | fraction of the bulk volume that can be drained by gravity (unconfined aquifers) |
| Specific storage | $S_S$ | 1/m | amount of water that a confined aquifer releases from storage per unit change in the hydraulic head (remaining fully saturated) |
| Fluid transfer rate | - | 1/s | fluid inflow/outflow at transfer boundary conditions calculated from the relevant area, the transfer rate, and the difference between reference and groundwater head |
| ***Thermal properties*** | | | |
| Thermal conductivity | λ | W/mK | ability of a material to transfer heat by conduction |
| Volumetric heat capacity | svc | $J/m^3K$ | amount of thermal energy required by one volume unit of the medium to change by one unit of temperature |
| Total porosity | n | - | ratio between the total pore volume in the medium and the total volume |
| Heat Transfer rate | - | $W/m^2K$ | heat inflow/outflow at heat transfer boundary conditions calculated from the relevant area, the transfer rate, and the difference between reference and groundwater temperature |
| Longitudinal and transversal dispersivity | $D_L$ , $D_T$ | m | consider the effects on heat transport due to heterogeneities not represented by bulk equivalent properties such as thermal retardation due to diffusion and mechanical dispersion (it depends on the grain size and the scale of the problem) |

Practically, a first estimate of the values of hydrogeological and thermal parameters to adopt in the model types may for example be obtained from: (I) literature values, (II) empirical equations based on grain size distributions data (e.g. hydraulic conductivity), (III) field investigation methods such as pumping tests (e.g. hydraulic conductivity and transmissivity from the aquifer response to well pumping) and thermal response tests (e.g. thermal conductivity from the response of the medium to a heat injection).

The solve the numerical problem of groundwater flow and heat transport by means of differential equations, initial and boundary conditions are required. Boundary conditions represent particular zones inside and at the boundary of the model where physical processes have been recognized and quantified, e.g. in the conceptual model. The BC can be punctual (at nodes) and linear (along mesh edges) or volumetric (related to elements) as sink/source terms. In other words, BC give the solution of the partial differential equations at specific locations in the model and are used to solve the problem in the rest of the domain. The mathematical distinction between the three types of boundary conditions is given in **Table 4.2**, together with examples of possible application for fluid flow and heat transport problems.

***Table 4.2*** *– Types of boundary conditions (BC) and their application in a fluid flow and heat transport model.*

| BC Type | *Description* | **Fluid Flow** | **Heat Transport** |
|---|---|---|---|
| (I)<br>Dirichlet | Known head / temperature | Regional hydraulic head isolines<br>Rivers/lakes contact with GW<br>Phreatic springs | Known temperature (e.g. lake) |
| (II)<br>Neumann | known fluid /<br>heat flux | Regional GW flow lines<br>Rainfall infiltration<br>Discharge through a section | Geothermal heat flux<br>Heat injection/abstraction |
| (III)<br>Cauchy | Reference head/ temperature combined with a conductance parameter | Surface waters – groundwater interactions | Heat exchanges between surface, tunnels, foundations and GW through asphalt, walls |

Finally, transient fluid flow and heat transport simulations requires initial values of hydraulic head and temperature distributions. The hydraulic head initial distribution can be obtained from regional piezometric maps or from steady state solutions considering the fluid flow settings for the initial simulation time. The subsurface temperature distribution at a certain

time is the snapshot of the thermal equilibrium reached by the complex superimposition of positive/negative thermal perturbations that propagates with different velocities according to the bulk thermal diffusivity, the temperature gradient and the advective velocity. These perturbations occur at different time scales that could be significantly longer than the total simulation time. Thus, the definition of temperature initial conditions is essential to consider the thermal energy already stored during the past decades which is impossible to simulate with short simulation periods. For this reason, the initial temperature distribution can be estimated by means of interpolation of the mean annual groundwater temperature obtained from monitoring data (e.g. temperature-depth profiles) or by a steady state thermal simulation representing the average annual settings of the past years. Then, the thermal fingerprint of the shallow subsurface, i.e. where the seasonal fluctuations are relevant, can be obtained by adding 2-3 years before the target time span.

### 4.2.5. Calibration

The first estimate of the parameter values can be adjusted after comparing the agreement between the simulation results and measured values at specific locations (i.e. model error). The model error can be expressed in terms of the mean error (ME), mean absolute error (MAE) and root mean square error (RMSE) between the simulated head or temperature and all the available measured values at specific locations. Thus, (horizontally and vertically) densely spaced and long-term monitoring data are required to assess the goodness of the model results and parameters. Parameters can be changed considering their variability range due to uncertainties on the estimate and on the natural variability inside homogeneous zones of the model. The calibration can be achieved by manual “trial-and-error” procedures (e.g. changing manually the parameters until the accuracy of the model results satisfies the objective of the model) or by automated inversing algorithms such as PEST (Doherty et al., 1994).

The existence of multiple solutions of automated calibration techniques requires the most accurate field data as possible and expertise by the modeler to judge which is preferable considering sufficient accuracy (according to the modeling objectives) and checking the consistency of the solution with geological observations. Generally, the model error (i.e. difference between simulated and measured values) should be higher than the measuring

error and over fitting must be avoided. In other words, it is preferable a model a with higher error that satisfies geological assumptions on the subsurface than a highly parametrized model (thus with a lower error) that ignores assumptions from the conceptual model.

The computing time required by automated calibration depends on the number of parameters to be calibrated. In complex numerical models this can lead to very high computing times, which can be avoided by identifying the most relevant parameters (i.e. subspace regularization) affecting the behavior of the system by a linear sensitivity analysis (i.e. the sensitivity of the model results to the parameter change). In addition, the number of homogeneous zones to divide each parameter (i.e. structural regularization) can be adjusted to further reduce the calibration time. Subspace and structural regularization techniques are discussed in detail is section 9.4.5.

### 4.2.6. Validation

Finally, the retro- and pre-diction capability of a model must be assessed by analyzing the response during a period not included in the calibration procedure. This is usually done by previously splitting the groundwater head and temperature time-series for the calibration and validation of the model. If the groundwater head or temperature values are not accurately represented during the validation phase, some relevant processes were probably ignored and the conceptual model and the fluid and heat budgets over the modeling period have to be checked. Usually, the most misrepresented areas of the model during the validation phase can give important information about the quantities that have been ignored.

# 5. Study area

This thesis addresses several topics related to subsurface thermal management with different techniques and at different scales. In this chapter a global overview of the study area with the relevant geological and hydrogeological settings is presented. The location and extension of different dataset such as the hydrological and the groundwater monitoring network is presented in general and further details will be discussed in the following specific chapters.

The study area is located in the northern portion of the Po plain (northern Italy) and is bounded by the Adda, Ticino and Po rivers eastward, southward and westward, respectively, and by the alpine foothills to the north (**Figure 5.1**). The area covers 3,827 $km^2$ and is one of the most densely populated (about 5,351,148 inhabitants in 2019) and industrialized regions in Italy (mean population density: 1,398 inhabitants/$km^2$, max: 6,836 inhabitants/$km^2$ in the city of Milan) (ISTAT, 2019).

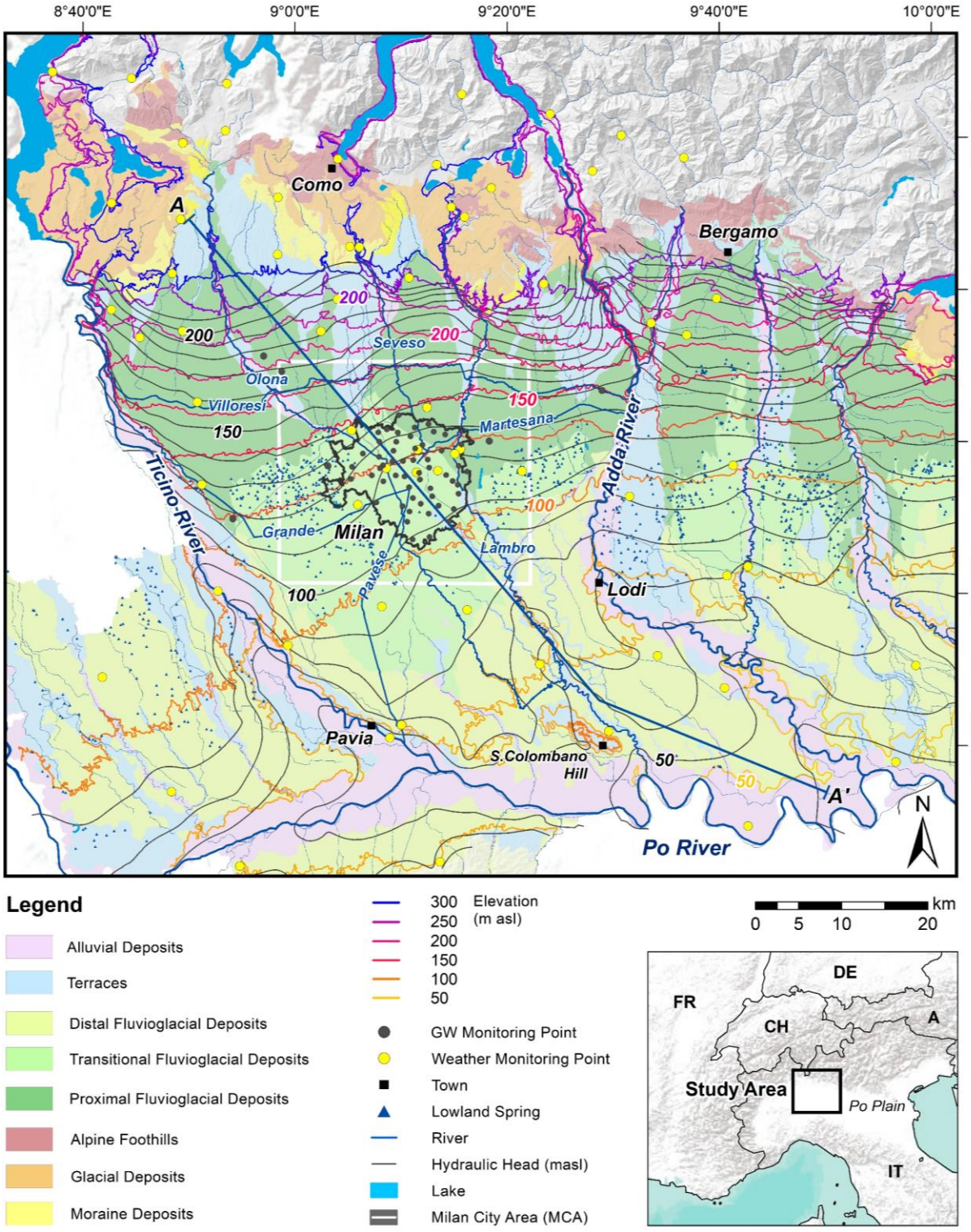


***Figure 5.1*** *– Map of the study area showing the spatial distribution of the shallow deposits, the elevation of the ground surface and the water table, the hydrological network (Po, Ticino, Adda, Lambro, Olona and Seveso Rivers; Martesana, Grande and Pavese man-made canals – "Navigli", and the Villoresi irrigation canal), the lowland springs ("Fontanili"), the weather and groundwater (GW) monitoring locations, and the Milan municipality. Section A-A' refers to* ***Figure 5.2****.*

## 5.1. Climate setting

The climate of the study area is overall homogeneous since the elevation ranges between 40 and 400 m above sea level. According to the Köppen-Geiger classification (Kottek et al., 2006; Peel et al., 2007) the climate regime falls between the Cfa (i.e. warm-temperate, humid with hot summers) and Csb classes (i.e. warm-temperate with warm and dry summers), and it is typically continental with moderately cold winters and hot muggy summers. The mean annual precipitation varies between 800 and 1,000 mm/yr (ARPA Lombardia, 2019). According to the meteorological records of the last 20 years, the mean annual air temperature is about 14.2 °C with a minimum mean daily temperature of -5.4 °C and a maximum mean daily temperature of +31 °C (ARPA Lombardia, 2019). These values are approximately constant in the whole study area, even if warmer conditions can be found in the Milan urban area due to the heat island effect (Pichierri et al., 2012). This phenomenon is reflected by a mean annual air temperature of about 15.7 °C recorded by the meteorological monitoring station located in the center of Milan (ARPA Lombardia, 2019) that is 2°C higher than the nearest available air temperature measurement outside the city (see also sections 7.3.1 and 9.4.1). Due to the mild continental climate, the buildings in the study area need both heating and cooling. The amount of thermal energy required for heating or cooling depends on the degree days. Degree days were estimated as the difference between the air temperature and the reference indoor temperature below (or above) which a building will require active heating (or cooling). Annual heating degree days in the study area range between 1800 and 2300, whereas cooling degree days range from 400 to 800 (see also section 6.3.1.3).

## 5.2. Geological and hydrogeological setting

The northern portion of the Po plain (the largest alluvial basin in Italy) is the foreland basin of the Alpine collisional belt (Southern Alps domain), and it was developed during the Pliocene in response to global climate change, forcing the sedimentation rate and Alpine uplift. At the southern Alps foothills, the occurrence of glacial amphitheaters (**Figure 5.1**) testifies the advance of glacial tongues along the main Alpine valleys during the last glaciation peak period (i.e. the Last Glacial Maximum, LGM, between 24 and 18 Ky BP). In the northern plain, below

the terrace units and moraine amphitheaters, the alluvial fans coalesce along mountain fronts forming a bajada (Guzzetti et al., 1997). The top of this unit, known as “Livello Fondamentale della Pianura (LFP)” (Petrucci and Tagliavini, 1969) presents a low slope related to the glacial conditions in the Alps during the last glacial maximum. The SSE dipping topographic surface of the area is characterized by large fan-shaped alluvial systems fed by the main valleys. According to Fontana et al. (2014) most of them are megafans, characterized by a clear longitudinal differentiation in the slope and grain-size of the deposits. The northern sector, i.e. the steep (topographic gradient of about 5‰) piedmont sector of the plain, consists of amalgamated gravels, while the distal portion has a gradient <2‰ and is dominated by fine sediments.

The recent knowledge of the Po Plain subsurface has been improved through high resolution seismic (Francese et al., 2005), electric borehole logs, and lithostratigraphic and petrographic analyses of 11 deep (>200 m) boreholes (Garzanti et al., 2011; Regione Lombardia and ENI, 2002; Scardia et al., 2006). The subsurface of the study area hosts a sequence of deposits up to 800 m thick characterized by deep marine sediments, covered by fluvioglacial sequences relative to the onset of major glaciations and by the progradation of laterally extensive alluvial sediments coming from the Alps (Garzanti et al., 2011; ISPRA and Regione Lombardia, 2016; Regione Lombardia and ENI, 2002). The various depositional events from early Pleistocene account for the creation of three main depositional sequences (**Figure 5.2**) which correspond to as many aquifer complexes (from top to bottom):

(A) Phreatic aquifer – P (Aquifer Group “A”, Regione Lombardia and ENI, 2002; “Acquifero tradizionale”, Martinis and Mazzarella, 1971): mainly consists of gravel with a sandy matrix. The sequence was formed during the Middle-Late Pleistocene and consists of proximal braid-plain deposits composed mainly of coarse, poorly sorted gravels. The aquifer, 20 - 50 m thick, overlays a clayey-silty regional aquitard (0.45 Ma) which shows a good continuity south of Milan, and disappears moving northward;

(B) Semi-confined aquifer – SC (“Aquifer Group B”, Regione Lombardia and ENI, 2002; “Acquifero tradizionale”, Martinis and Mazzarella, 1971): consists of sands and

sandy gravels with a thickness in the range between 50 m and 100 m. The major Pleistocene glaciations in the Alps produced a widespread sequence boundary in the basin at 0.87 Ma, which marks the synchronous and widespread progradation of the braid-plain sequences over the previous meandering river deposits. Thus, the lower portion of the aquifer consists of clay and silt layers, and locally of conglomeratic units (i.e. Ceppo formation);

(C) Deep confined aquifers – C (Aquifer Group "C", Regione Lombardia and ENI, 2002; "Acquifero profondo", Martinis and Mazzarella, 1971): a fining upward sequence of medium-fine sand layers interbedded with clay and silt representing the lower Pliocene continental-marine and meandering river plain facies. This sequence (1.4–0.87 Ma) mainly consists in meandering river plain deposits fed from the Western and Central Alps and prograding in low subsidence settings (Garzanti et al., 2011). The aquifer base consists of Pliocene continental-marine deposits.

To the South, in proximity of the San Colombano hill (**Figure 5.1**), the syndepositional tectonics related to the activity of an anticline ramp above the Apennine blind thrusts uplifted the Pliocene and the Lower Pleistocene basement (Bersezio et al., 2010). The occurrence of lowland springs (called "fontanili" – see **Figure 5.1** for their location) is observed across the entire Po Plain (E-W for about 800 km) in a 20-km-wide belt. These springs of phreatic water have been explained by the changes (from N to S) in both the ground surface slope gradient and the sediment grain size between the coarse-grained deposits of the high plain and finer deposits of the low plain (De Luca et al., 2014). Because of their constant flow rate and temperature (ca. 10 °C to 13 °C) the fontanili have been used for land reclamation, since the XII-XIII century, and for irrigation, since the XVI century, to keep fields unfrozen during winter (De Luca et al., 2014).

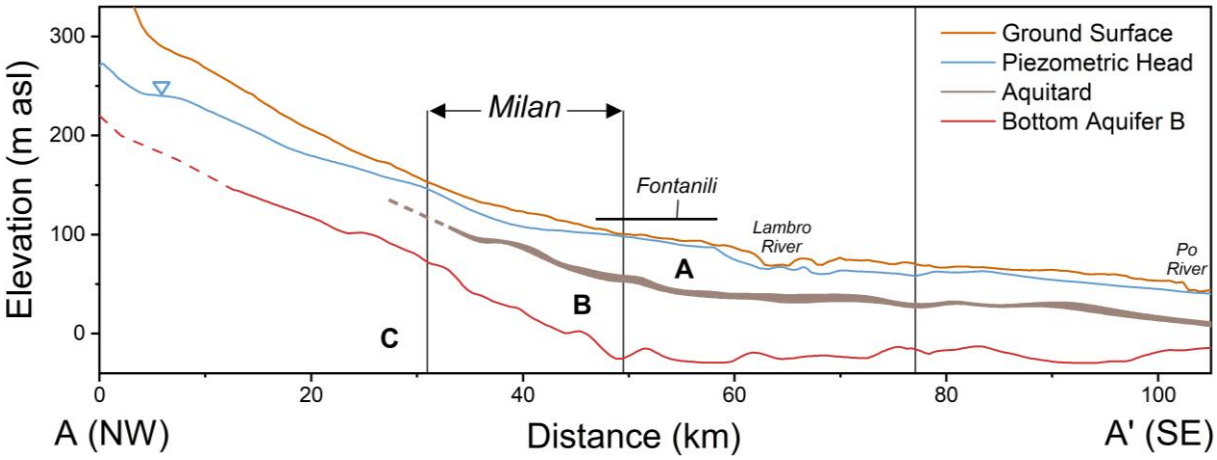


***Figure 5.2*** *– Simplified cross-section profile showing the boundary surfaces between the three main regional aquifers in the study area, from top to bottom: phreatic (A), semi-confined (B) and confined (C). The borders of the Milan city, the location of the lowland springs belt (Fontanili) and the intersections with Lambro and Po rivers is highlighted. See* ***Figure 5.1*** *for the section line A-A'.*

## 5.3. Hydrographic network

The study area is characterized by a complex hydrographic network made of rivers, minor streams, and irrigation man-made canals. The main ones are the Ticino (350 $m^3/s$) and Adda (190 $m^3/s$) rivers, which flow from the Maggiore and the Como Lake respectively, to the Po River (1,550 $m^3/s$) (**Figure 5.1**). The Adda and Ticino flow in valleys incised from 5 to 80 m below the local average ground elevation due to headward erosion and, thus, they are mostly connected to the groundwater (i.e. gaining rivers). The Lambro, Olona, Seveso and Lura rivers originate from the alpine foothills and converge in the Milan city area where they are partly culverted (**Figure 5.3**), except the Lambro River. These rivers have a relatively shallow riverbed (1 to 5 m below the local average ground elevation) and, thus, their interaction with the groundwater goes from losing conditions (i.e. the water level is above the groundwater level) in the northern sector, to gaining conditions (i.e. the water level is below or similar to the groundwater level) in the southern sector, according to the elevation of the water table.

In the Milan area, three main navigable canals were built since the 12$^{th}$ century. This canal network (i.e. the "Navigli" system) was created to connect the city of Milan with the nearby Adda and Ticino Rivers for commercial and irrigation purposes (**Figure 5.3b**). The Naviglio Grande flows from the Ticino River to Milan and feed the Naviglio Pavese which flow from Milan to Pavia. The Naviglio Martesana flows from the Adda River to Milan feeding a large

number of secondary irrigation canals. The Navigli are periodically maintained, and the flow rate can be totally or partially reduced. In the northern sector, the Villoresi main irrigation canal flows from the Ticino to the Adda river feeding a fully gravity-driven irrigation network of secondary and tertiary canals with a total length of about 3,000 km. **Figure 5.4** shows the water level and riverbed elevation profiles along the urban section of the three man-made canals (Navigli) flowing across the Milan city (note that the water coming from Naviglio Grande is discharged into Naviglio Pavese in the city center). The locations of low head dams are highlighted by ticks.

***Figure 5.3*** *[next page] – (a) Map showing the distribution of impervious and vegetated land cover, the hydrographic network (Rivers, Navigli, Irrigation canals and Springs) and the groundwater monitoring network (instrumented piezometers – Automatic, and manual measurements locations) in the Milan city area (MCA). See* ***Figure 5.1*** *for the extent of the map. (b) View of the "Naviglio Grande" man-made canal in the center of the Milan city. (c) View of a typical phreatic resurgence of groundwater at a lowland spring ("Fontanili").*

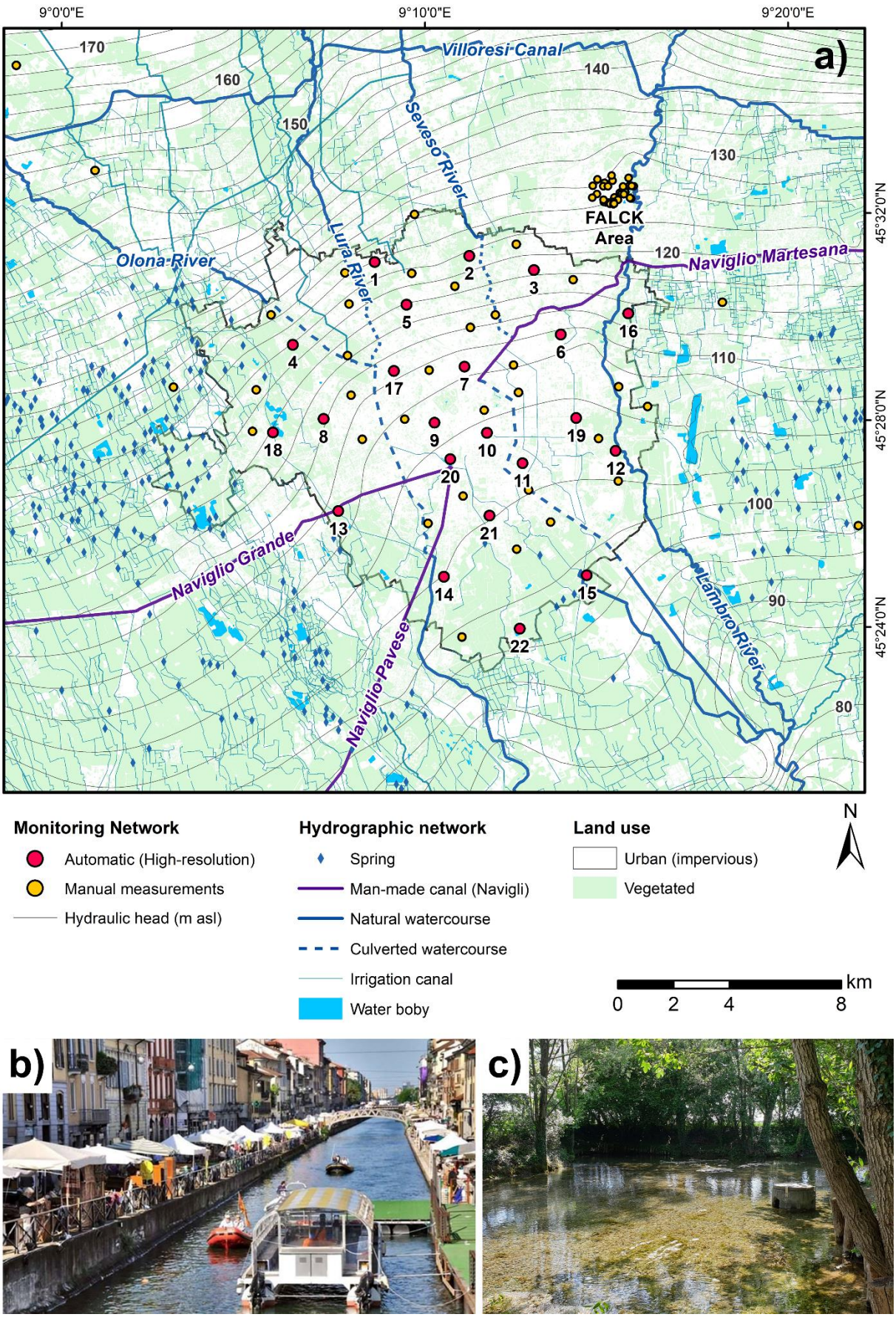
a)
9°0'0"E
9°10'0"E
9°20'0"E
45°32'0"N
45°28'0"N
45°24'0"N
Villoresi Canal
Seveso River
Olona River
Lura River
Naviglio Martesana
Naviglio Grande
Naviglio Pavese
Lambro River
FALCK Area
170
160
150
140
130
120
110
100
90
80
1
2
3
4
5
6
7
8
9
10
11
12
13
14
15
16
17
18
19
20
21
22
Monitoring Network
Automatic (High-resolution)
Manual measurements
Hydraulic head (m asl)
Hydrographic network
Spring
Man-made canal (Navigli)
Natural watercourse
Culverted watercourse
Irrigation canal
Water boby
Land use
Urban (impervious)
Vegetated
N
km
0
2
4
8


b)


c)

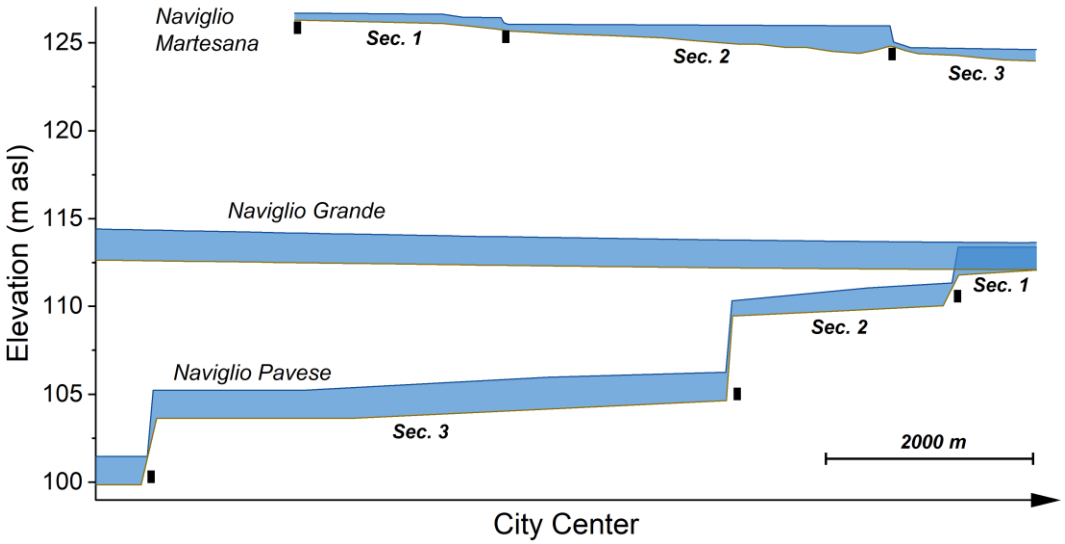


***Figure 5.4*** *– Water level and riverbed elevation profiles along the urban section of the three man-made canals (Navigli) flowing in the Milan city (note that the water coming from Naviglio Grande is discharged into Naviglio Pavese at the city center). Vertical ticks show the locations of low head dams.*

## 5.4. Present and historical groundwater levels

Groundwater levels in the study area are mainly related to the plain geomorphology and the hydrographic setting with local disturbances around urban areas. **Figure 5.1** shows the spatial distribution of groundwater levels in the study area in 2014 and **Figure 5.2** a north-south cross section. Regional piezometric map were retrieved from the regional geographic database (Regione Lombardia and PTUA, 2014). Depth of the water table and water table slope (i.e. the hydraulic gradient) range from about 30 m and 1% to 2-5 m and 0.05% moving from the high to the low plain. This can be explained by changing in the ground surface slope, the grain-size distribution of aquifer bodies and the groundwater budget (e.g. recharge contribution from irrigation). In the Milan area, a city-scale drawdown cone is caused by local changes in the groundwater budget due to superimposed effects of densely spaced shallow and deep groundwater wells. Thus, long-term groundwater fluctuations were linked to the socio-economic development of the area since the early ‘60s as urbanization/industrialization modify the groundwater withdrawals and land cover changing the groundwater budget (De Caro, 2018). In particular, in the MCA many industrial activities have flourished after the post-war reconstruction and during the “economic boom” (1950 – 1975) leading to intense groundwater exploitation. The total groundwater abstraction raised by 50% mainly due to

industrial uses, causing a general decrease of hydraulic head in the phreatic aquifer from 10 to 20 m. After 1975 (oil crisis) a sudden change in the groundwater regime was observed following the gradual decrease of groundwater abstraction rates during the EU monetary system crisis and the economic decline, mainly due to decommissioning of large industrial districts in the northern part of the Milan city (the water demand fell by 36%). Consequently, the groundwater levels started to rise since the '90s with a rising rate up to 1 m/y, reaching a local maximum in 2015 when the groundwater monitoring network in the Milan city was established by this Department. The gradual recovery of the water table after a prolonged period of artificially controlled drawdown such as high groundwater abstraction rates is referred to as the groundwater rebound phenomenon (Crosta and De Caro, 2018; Greswell et al., 1994). According to the evolution of groundwater levels and pumping rates in the MCA a groundwater rebound is clearly visible (**Figure 5.5**). Since many underground structures were built during the '60/'70s when the water table was significantly lower, flooding of non-impervious structures (e.g. tunnels, deep basements) or buoyancy of submerged elements became a major concern since 2014 in the MCA and many monitoring and mitigation approaches were studied and applied (Beretta et al., 2004; Colombo et al., 2018; De Caro et al., 2020a; Gattinoni and Scesi, 2017; Sartirana et al., 2020).

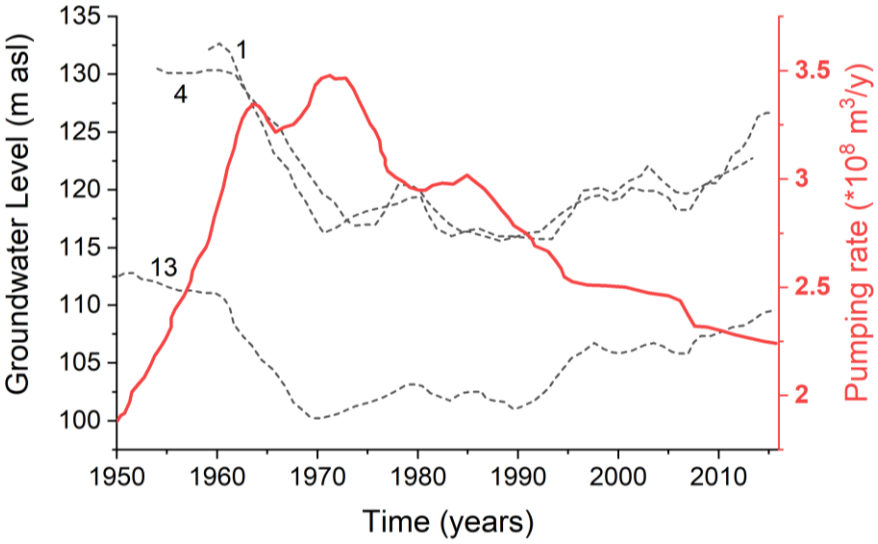


***Figure 5.5*** *– Historical groundwater level time series at three locations in the MCA (see* ***Figure 5.3*** *for their location) versus total annual abstraction rate from groundwater wells showing the groundwater rebound phenomenon (redrawn from* De Caro, 2018*).*

## 5.5. Shallow geothermal uses

The shallow geothermal uses in the study area are mainly to space conditioning (heating and cooling) of buildings such as houses and offices. Recent regulations on shallow geothermal installations in the Lombardy region (see section 5.4.1.) simplified and homogenized the management of the shallow geothermal resource. The management of GCHP and GWHP is in charge of different environmental authorities. For this reason, information on their location and installed power are not homogeneous in the study area. A spatial database for GCHP applications exists since 2010, whereas a comprehensive dataset on GWHP is still lacking and information are available only in the Milan metropolitan district (Provincia di Milano). In 2021 the total number of installed GCHPs in the study area was 1,668 (3,321 boreholes in total) with a total power of about 42 and 33 MW for heating and cooling, respectively. The mean power for a single system is about 40 kW for heating and 43 kW for cooling, and the average borehole length is about 105 m, ranging from 28 to 200 meters (**Figure 5.6**). According to the Lombardy Region database on closed-loop systems a constant increase in the installed GCHP exists since 2010 (**Figure 5.6d**) (geothermal systems installed earlier are not included in the regional database and are not considered in this analysis) (Regione Lombardia, 2021).

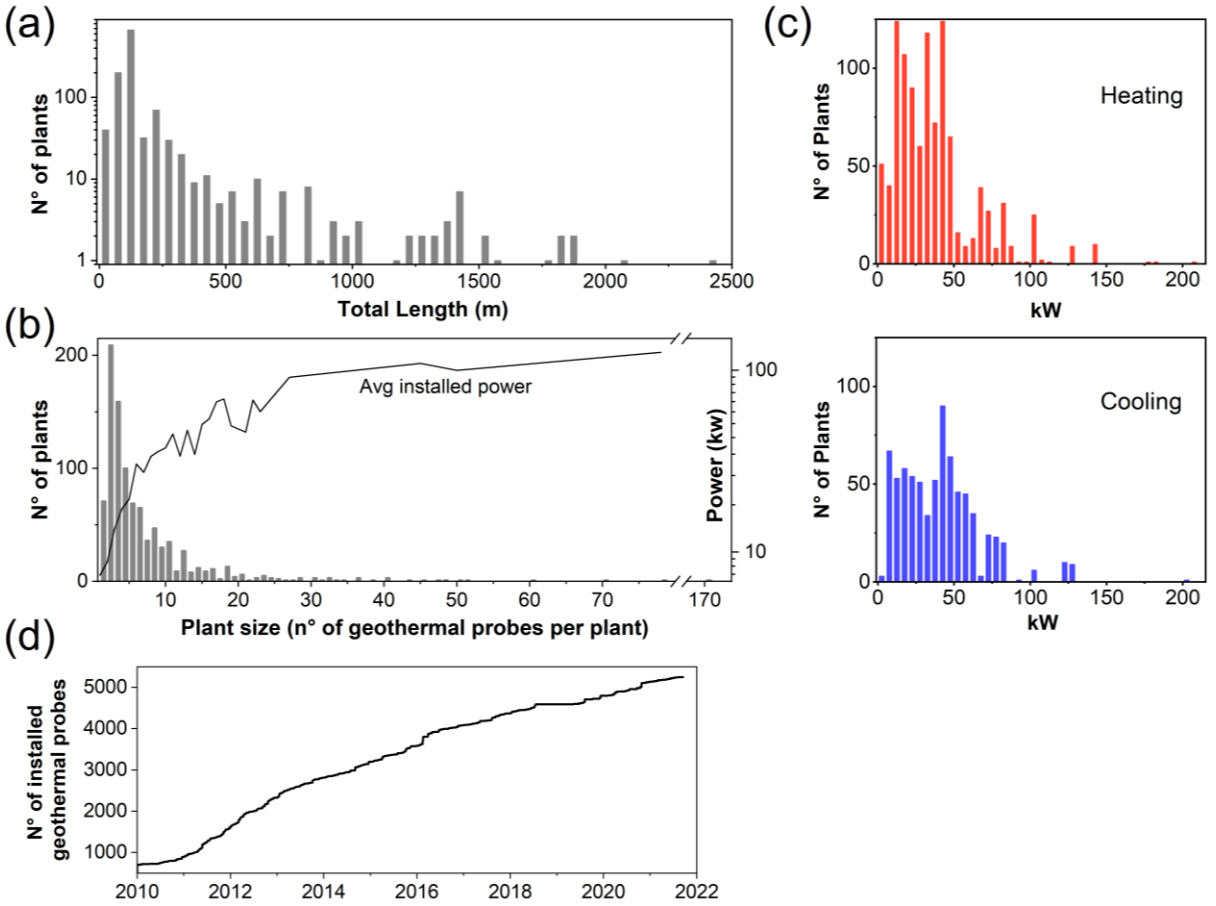


***Figure 5.6*** *– Statistics of the installed closed-loop systems in the study area as on 2021: (a) amount of systems per total drilled length class; (b) amount of systems per size class (i.e. number of geothermal probes per single installation) versus the average installed power; (c) amount of systems per power class for heating and cooling mode; (d) total cumulative installed geothermal probes (GCHP) since 2010 in the Lombardy Region.*

On the other hand, information about GWHPs are sparse and incomplete due to the fragmentation of local environmental management authorities. In this work we report only the 893 geothermal wells installed in the Milan metropolitan area (Provincia di Milano) that extract water from the shallow phreatic aquifer for geothermal application.

Even if the extent of the datasets is not comparable, **Figure 5.7** shows that open-loop systems tend to concentrate within the Milan city area where large power systems are more frequently installed due to the higher thermal demand of large buildings. In fact, this solution is generally more attractive (and sometimes the only feasible after a cost-benefit analysis) for large systems due to the higher costs of installation and maintenance (see also section 2.5). On the other hand, closed-loop systems are typically installed for smaller thermal power demand applications such as residential buildings. The northern portion of the study area shows the

highest number of GCHP installations. This is due to the higher population density (the thermal request is higher) and deeper location of the water table (GWHP solutions are less attractive where groundwater is deeper due to higher drilling and pumping costs).

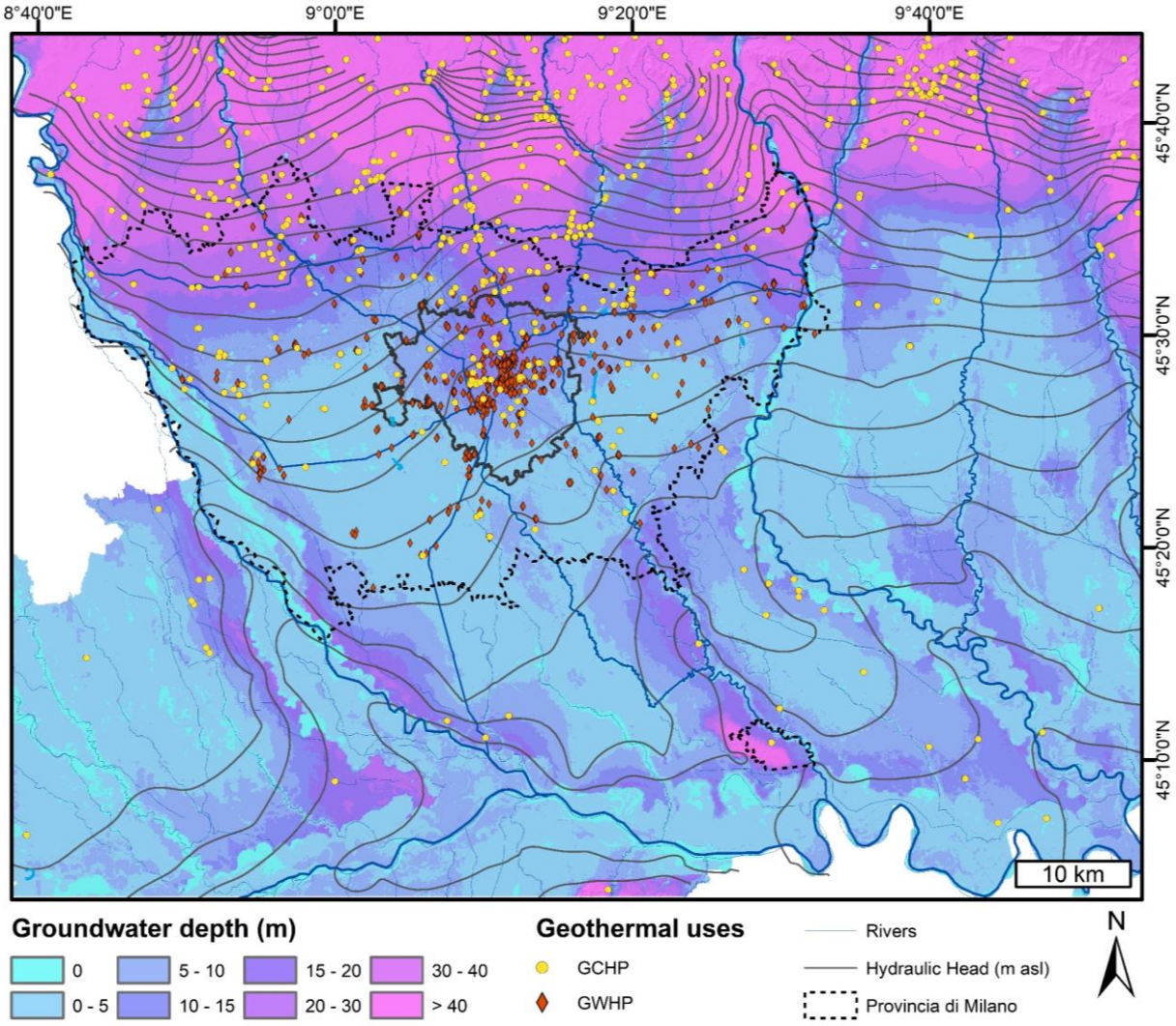


***Figure 5.7*** *– Map showing the spatial distribution of the geothermal installations in the study area and the depth of the water table. Data for GWHP are available only for the Milan metropolitan district (Provincia di Milano)*

### 5.5.1. Local regulation

Regulations and actions of European countries on the use and promotion of low enthalpy shallow geothermal energy are largely based on EU directives on the development of renewable sources to produce electricity and thermal energy such as directive 2009/28/CE. Recently, some Italian regulations on the use and management of the subsurface resources have acknowledged the EU directives by introducing specific indications and rules for shallow geothermal uses. Different regulations exist about GCHP and GWHP systems on a regional

basis and the legislative framework for the Lombardy Region, which encloses the study area, is here presented. The regional decree on "the prevention and reduction of atmospheric emissions to protect the health and environment" (L.R. n 24/2006, art. 10) promotes low enthalpy geothermal applications and defines simplified procedures for the installation and management of both geothermal probes (GCHP) and wells (GWHP).

**Closed-loops (GCHP)**

Based on the regional decrees "L.R. n 24/2006, art. 10" and "R.R. n 7/2010", the installation of geothermal probes (ground heat exchangers) is free, except for groundwater protection zones, and regulated according to the installed thermal power (P) as follows:

- Small plants (P ≤ 50 kW): ground thermal properties can be estimated from the available geological stratigraphy (obtained directly from surveys or from available geological information in the area) by means of literature values, e.g. from VDI 4640/2 (2001) or the Regional directive "D.G.R. 8/10965". If the heating and cooling thermal loads are highly unbalanced, a dynamic analysis of the systems based on ground thermal properties is required.
- Large plants (P > 50 kW): sizing of higher thermal power plants is subject to a direct estimation of the ground thermal properties with in-situ characterization. A thermal response test (TRT) is required to obtain the thermal resistance of the probes, the thermal conductivity of the ground and the mean temperature of the ground. Possible verification of the thermal alteration by means of numerical modeling and future monitoring can be requested by the local authorities for very large plants.

Another distinction is based on the depth reached by the probes: installations at depth greater than 150 m from the ground surface are subject to the authorization from the respective district environmental authorities ("Province"), whereas horizontal installations and vertical boreholes up to 150 m deep are free.

Environmental issues are addressed by the definition of the quality of the aquifers encountered by drillings to avoid the transport of pollutants from shallow to deeper aquifers and water is preferable as heat exchange fluid and certified non-toxic additives are permitted. According to the above-mentioned regional decrees, a unique database for the Lombardy

region on GCHP installations was developed in 2006. Information on the location, total thermal power (heating and cooling), number of probes, geometry and depth, and on the thermal properties of the ground (if requested) are stored in a public dataset (Regione Lombardia, 2021).

**Open-loops (GWHP)**

The use of the shallow groundwater for geothermal applications (GWHP) is regulated by the national law "D.Lgs. n 152/2006" and the regional directive "D.G.R. n 6203/2017". Due to environmental concerns, the re-injection of shallow groundwater after pumping is permitted only for shallow geothermal applications in the same geological unit where it has been extracted. Groundwater concessions for geothermal applications are regulated on a provincial basis according to the regional directives. The use of groundwater for heat exchange with heat pumps and the relative reinjection is permitted in the only phreatic shallow aquifer (P) and is subject to the preliminary assessment of the water quality and the thermal perturbation according to the mean daily extracted volume (Q):

- Category I ($Q \leq 5$ l/s): water quality analysis not requested. The hydrogeological report must contain hydrogeochemical values from the literature or nearby wells and must check the compatibility with groundwater protection and diffused contamination zones.
- Category II ($Q > 5$ l/s): additional water analysis are requested and the invariance of groundwater chemical parameters must be supported by a monitoring plan.

Thus, the license for groundwater extraction is obtained upon the payment of an annual fee based on the total annual extracted volume. An additional constrain is given to regulate the thermal status of the groundwater: as a general rule, the temperature difference (in cooling and heating mode) between reinjected water and the mean annual extracted water must not exceed 5°C. In addition, the temperature of the re-injected water must not exceed 21°C (except at locations where a well-documented natural geothermal anomaly exists). For very shallow groundwater (close to the ground surface), if seasonal thermal fluctuations are strong and without thermal retardation respect to the air, the maximum temperature threshold for groundwater reinjection is shifted to 23 °C. Finally, an environmental risk assessment

procedure ("VIA" described by D.Lgs. n 152/2006) is required for derivations larger than 50 l/s to meet the following conditions: (i) absence of chemical-bacteriological variation between pumped and reinjected water; (ii) absence of short- or long-term thermal short-circuiting; (iii) verification of the amplitude and extent of the thermal perturbation; (iv) assessment of the local distortion of the water table elevation and the influence on the nearby structures. According to the groundwater quantity protection principle, the reinjection of geothermal wastewaters into aquifers is preferred but some exceptions, such as the discharge in surface watercourses, are allowed upon environmental assessment. Due to the fragmentation of the regulation on the thermal use of groundwater, a database on the location and characteristics of the installed GWHP for the Lombardy region is still lacking.

## 5.6. Stratigraphic information

The subsurface of the study area was investigated by means of indirect and direct methods to define the main stratigraphic units described in section 5.2 (e.g. Regione Lombardia and ENI, 2002). Previous works by this department (De Caro, 2018; De Caro et al., 2020b) identified the boundaries between the three main aquifer groups (aquifers "A", "B" and "C" in section 5.2) from several borehole logs and, by means of Kriging interpolation, obtained the boundary surfaces between the units. These sequences are highly heterogeneous due to the natural random depositional processes that contributed to their formation such as fluvioglacial and alluvial. Large scale heterogeneities were investigated and implemented in this thesis by spatializing the geological information and associated parameters from the borehole logs.

The regional stratigraphic database (Regione Lombardia - CASPITA, 2019) collects the available borehole logs in the Lombardy-Po Plain area. The database contains information on the position, the elevation, the depth and the lithological description of the layers crossed by each borehole. **Figure 5.8** shows the spatial distribution and depth of the 8,854 borehole logs collected and stored in a georeferenced database in the scope of this work.

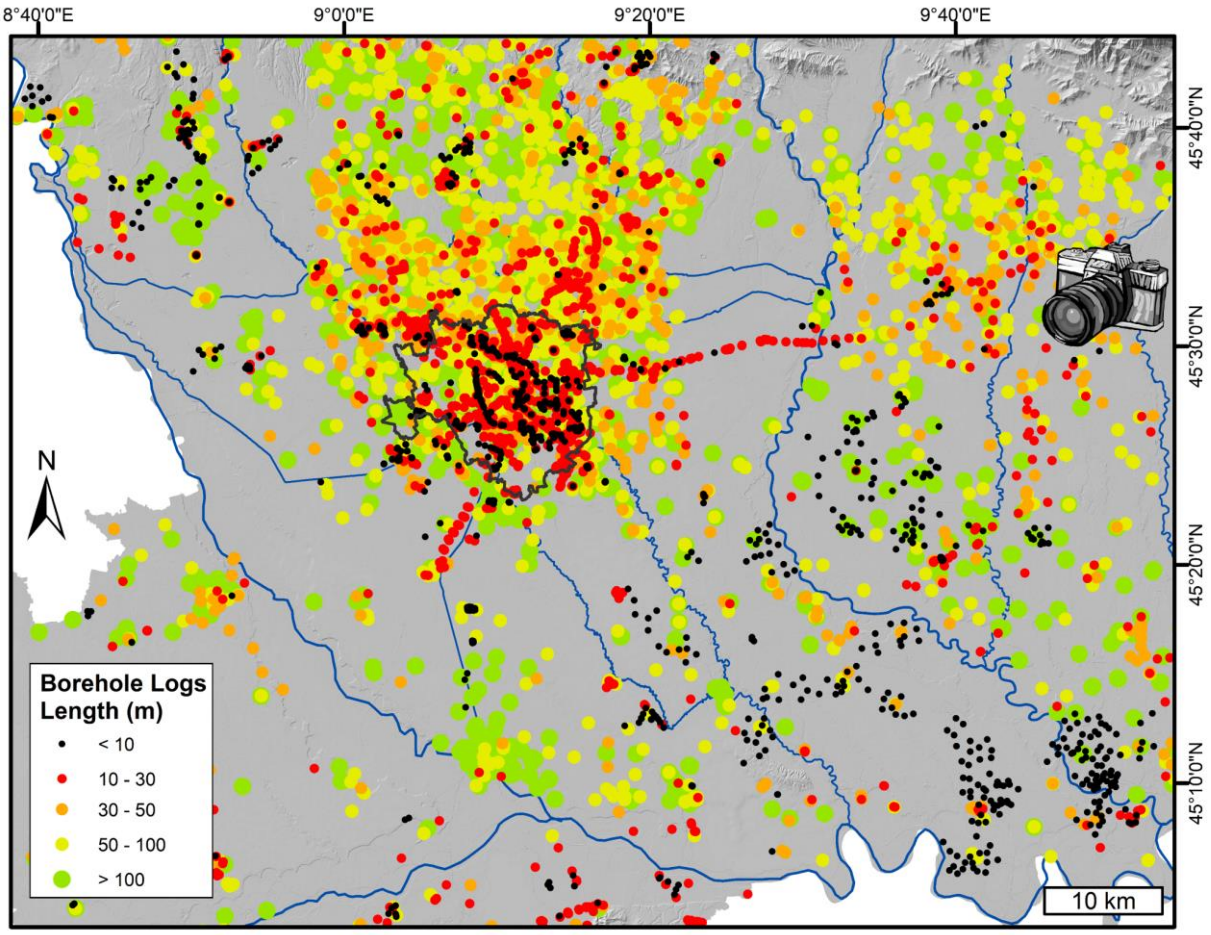


***Figure 5.8*** *– Map of the study area showing the spatial distribution of the available borehole logs with their depth. The camera shows the viewpoint and view direction adopted in the 3D representation (**Figure 5.10**)*

The stratigraphic units of each borehole log were classified according to the lithological descriptions in lithofacies and hydrofacies by De Caro et al. (2020b). Each stratigraphic layer description was codified with an uppercase and a lowercase alphabetical code, where the first indicate the prevailing texture (e.g. G for gravel, S for sand, M for silt and C for clay), and the latter the dominant grain size dimension (e.g. *c* for coarse, *m* for medium or *f* fine), to obtain a lithology codification. Then, a hierarchical classification of the lithologies was adopted to reclassify them into 29 lithofacies, 12 hydrofacies, and 5 aquifer groups. The hydraulic conductivity and porosity of each lithofacies in the study area was estimated by De Caro et al. (2020b) through empirical correlations with characteristic values of the grain-size distribution of specific units, such as the $d_{10}$ (effective diameter), the $C_u$ (uniformity coefficient), and the $d_{50}$ (median diameter) values. **Table 5.1** shows the hierarchical classification adopted in this thesis and the estimated hydraulic parameters (the lithology codification is not presented).

***Table 5.1*** *– Hydraulic conductivity and porosity values assigned to the 29 identified lithofacies. The following codification was adopted: G for gravel, S for sand, M for silt, C for clay, Ar for arenaceous rock units, Cong for conglomeratic units, P for peat and Landfill for shallow incoherent artificial deposits.*

| **Facies** | %. | **Hydrofacies** | %. | **Lithofacies** | %. | **Hydraulic Conductivity (m/s)** | **Total Porosity** |
|---|---|---|---|---|---|---|---|
| Gravel-Sand | 31.7 | G | 4.9 | G | 4.9 | 9.05E-02 | 0.26 |
| | | GS | 25.9 | GS | 21.7 | 2.40E-03 | 0.29 |
| | | | | GSC | 1.5 | 1.21E-03 | 0.29 |
| | | | | GSM | 2.7 | 1.50E-05 | 0.30 |
| | | G | 1.0 | *Landfill* | 1.0 | 9.05E-02 | 0.26 |
| Sand-Gravel | 30.5 | GC | 1.4 | GC | 1.4 | 6.68E-04 | 0.38 |
| | | GM | 0.3 | GM | 0.3 | 6.10E-04 | 0.34 |
| | | S | 8.2 | S | 8.2 | 5.80E-05 | 0.34 |
| | | SG | 20.6 | SG | 18.0 | 5.51E-04 | 0.31 |
| | | | | SGC | 0.6 | 2.81E-04 | 0.30 |
| | | | | SGM | 2.0 | 1.00E-05 | 0.30 |
| Partially Cemented | 4.6 | R | 4.6 | *Ar* | 1.0 | 3.63E-04 | 0.28 |
| | | | | *Cong* | 3.6 | 2.35E-02 | 0.29 |
| Aquitard | 14.1 | M | 3.2 | M | 1.8 | 9.00E-06 | 0.44 |
| | | | | MC | 0.6 | 8.00E-06 | 0.40 |
| | | | | MG | 0.1 | 7.00E-06 | 0.35 |
| | | | | MS | 0.7 | 6.00E-06 | 0.30 |
| | | SC | 6.0 | SC | 4.5 | 1.10E-05 | 0.32 |
| | | | | SCG | 1.5 | 1.60E-05 | 0.33 |
| | | SM | 5.0 | SM | 1.2 | 2.20E-05 | 0.34 |
| | | | | SMC | 0.6 | 4.00E-06 | 0.27 |
| | | | | SMG | 3.1 | 6.00E-06 | 0.33 |
| | | | | SP | 0.002 | 2.20E-05 | 0.34 |
| | | | | P | 0.1 | 2.20E-05 | 0.34 |
| Aquiclude | 19.1 | C | 19.1 | C | 12.1 | 5.00E-08 | 0.50 |
| | | | | CG | 0.6 | 3.00E-06 | 0.46 |
| | | | | CM | 0.9 | 1.20E-07 | 0.45 |
| | | | | CS | 4.1 | 5.00E-06 | 0.43 |
| | | | | CP | 1.4 | 8.00E-06 | 0.48 |

**Figure 5.9** shows the frequency (based on the length) of each lithofacies class and the percentage of facies (i.e. aquifers, aquitard and aquiclude) classes in the study area considering their relative proportions in the phreatic (A) and semi-confined (B) aquifer.

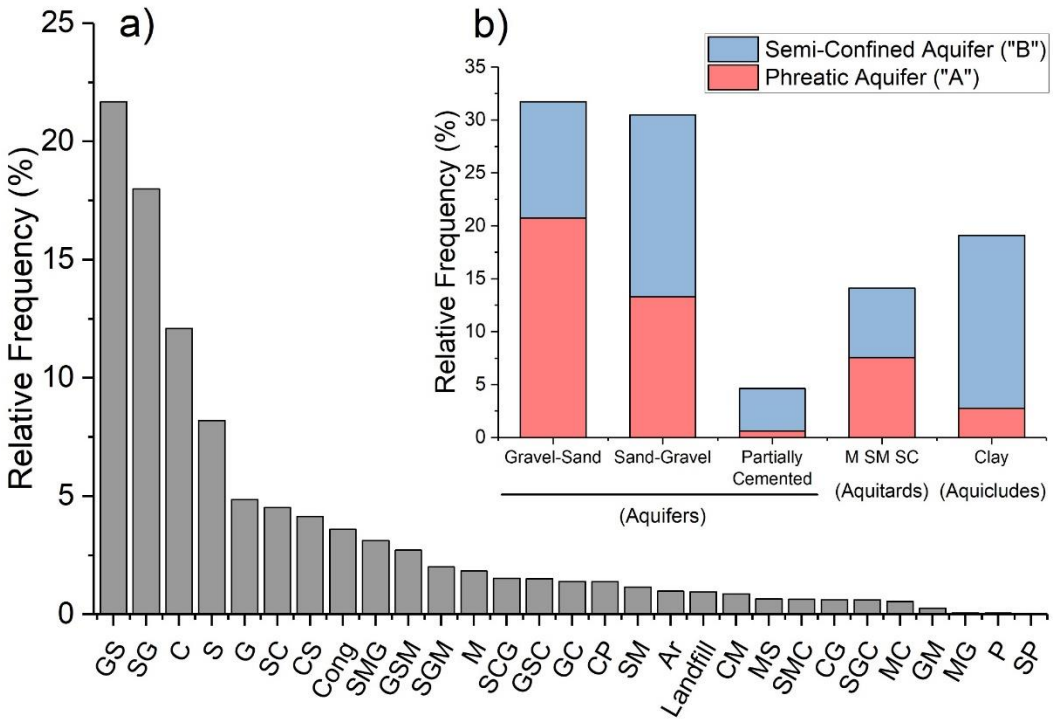


***Figure 5.9*** *– (a) Relative frequency of the lithofacies classes in the study area and (b) abundances of the facies classes and relative abundance in the phreatic and semi-confined aquifers.*

**Figure 5.10** shows a 3D view of the boundary surfaces between the phreatic (A), semi-confined (B) and confined (C) aquifers as from (De Caro et al., 2020b), and the available borehole logs in the study area covering mainly the first two shallow aquifers.

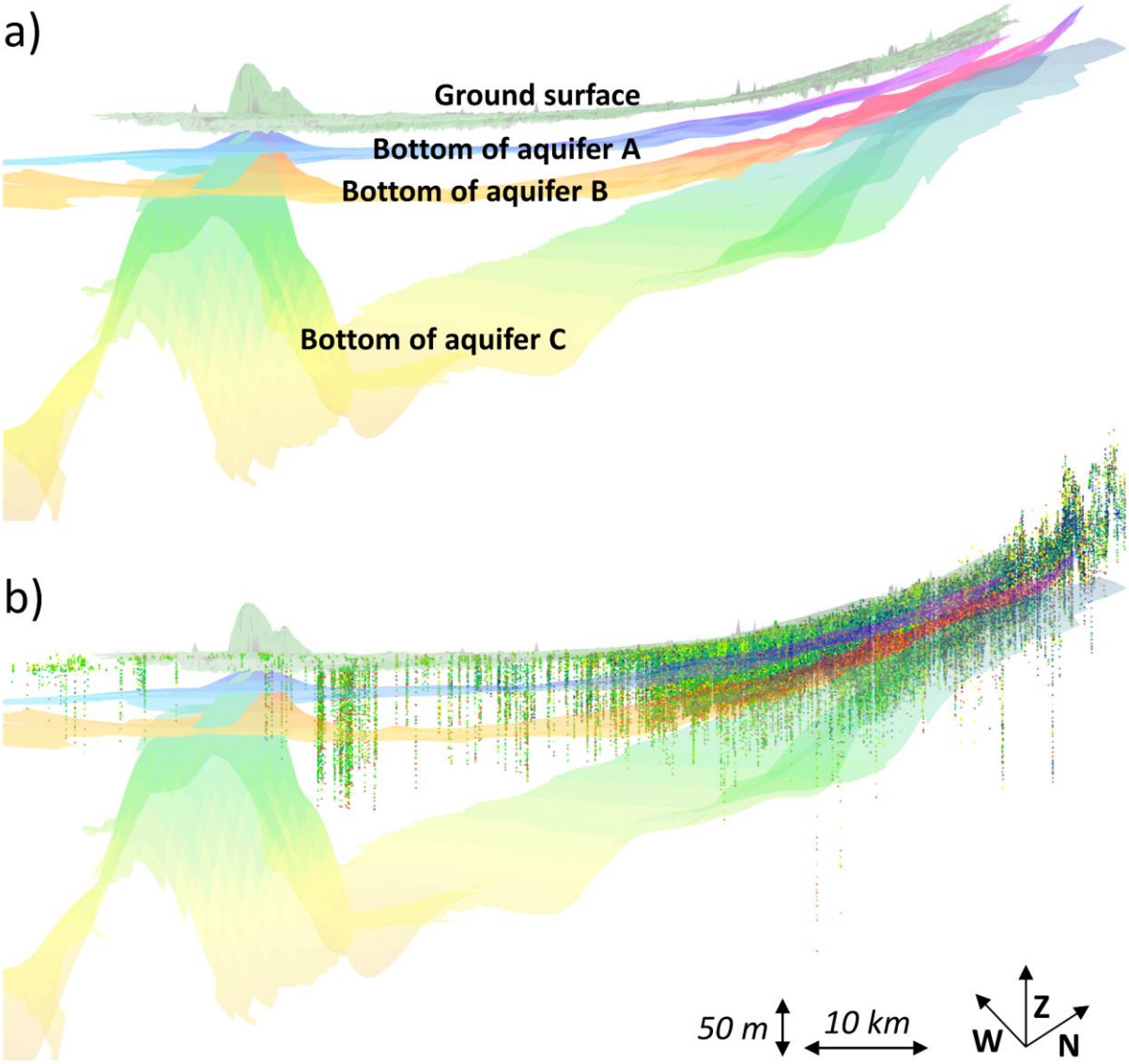


***Figure 5.10*** *– (a) 3D view of the boundary surfaces between the phreatic (A), semi-confined (B) and confined (C) aquifers as from* (De Caro et al., 2020b) *and (b) the available borehole logs in the study area. Please note the 50x vertical scale exaggeration. See* ***Figure 5.8*** *for the location and orientation of the viewpoint.*

## 5.7. The Milan city area (MCA)

This thesis investigates the effect of human activities and urbanization on the thermal regime of the shallow aquifers. The Milan city area (MCA) is highly populated and urbanized, but a thermal characterization of the subsurface is still lacking. In this area human activities have jeopardized the natural settings of the surface and subsurface environment. To quantify the impact of these anthropogenic modification, surface and subsurface comprehensive datasets are necessary. To this aim, we collected and homogenized information on the land cover, the hydrographic network, the surface/underground transport network (i.e. railway and metro lines), the location of water supply wells, shallow geothermal wells and ground source heat pumps (GSHP), the sewage and the district-heating pipe distribution networks, the groundwater depth and hydraulic gradient, and on the mean annual air temperature. Surface structure and infrastructure datasets were collected from the regional geographic database (Regione Lombardia, 2020), where surface information (e.g. land cover) were derived from satellite image interpretation. Subsurface information (e.g. tunnels, district heating network) were collected and digitized from available thematic maps and technical drawings. **Figure 5.11** shows the spatial distribution of the main natural and anthropogenic settings in the MCA.

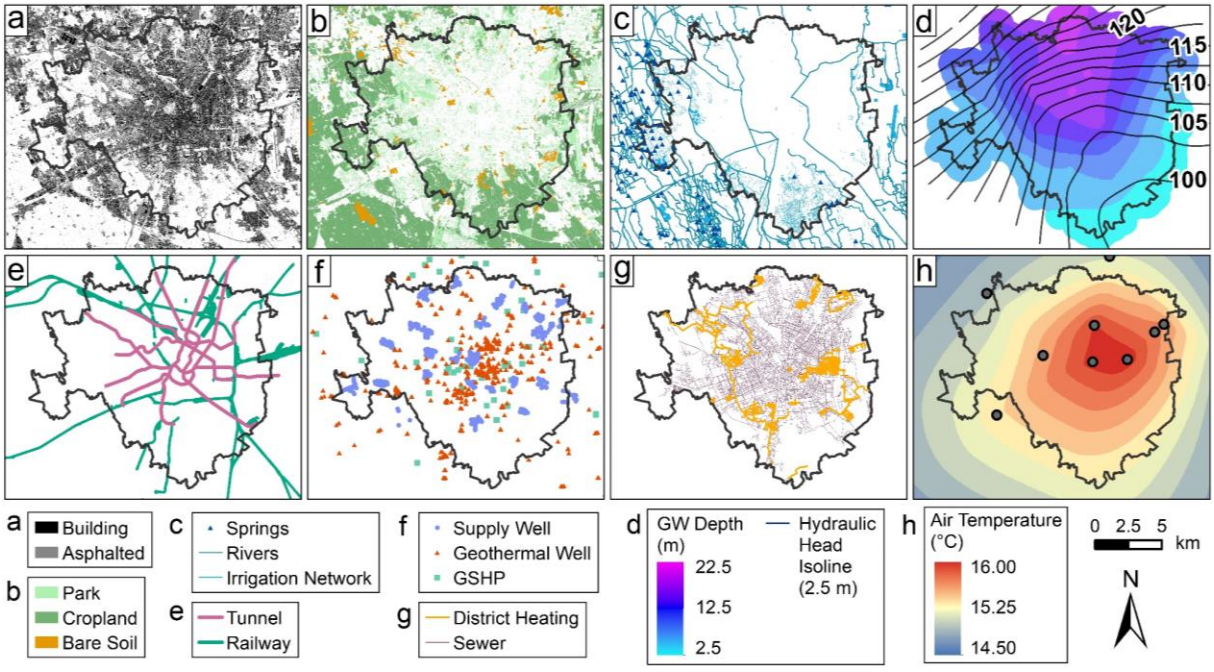


***Figure 5.11*** *– Maps of the Milan city area showing the spatial distribution of: (a) buildings and asphalted surfaces, (b) parks, croplands and bare soil, (c) surface waters and springs, (d) mean groundwater depth and hydraulic*

*head isolines, (e) underground tunnels and surface railways, (f) water supply wells, geothermal wells and Ground Source Heat Pumps (GSHP), (g) district heating and sewer networks, and (h) mean annual air temperature.*

### 5.7.1. Monitoring groundwater head and temperature

A monitoring network on the groundwater head and temperature of the shallow aquifer was developed in the Milan area by the applied Geology research group from University of Milano-Bicocca, dept. of Earth and Environmental Sciences. Since 2016, 22 open-pipe piezometers have been progressively equipped with automatic sensors and data loggers at fixed depth. Open-pipe piezometers were chosen according to their location and depth, the degree of structural protection, and the integrity of the borehole structure. At these locations, the transducers (Diver®, *VanEssen Instruments*) measure and record the pressure (±0.1 $cmH_20$) and temperature (±0.1 °C) every 15 minutes. In addition, vertical multi-parameter profiles and depth of the water table have been manually acquired since 2016 at 61 other locations inside and nearby the Milan city area. By moving a multi-parameters probe (AquaTROLL®, *InSitu Instruments*) into open-pipe piezometers from the bottom to the water table level, the water temperature, pH, electrical conductivity and dissolved oxygen were simultaneously recorded every 1 m steps. **Figure 5.12** summarizes the monitoring activities since 2016, for the location of the instrumented and manually measured piezometers see **Figure 5.3**.

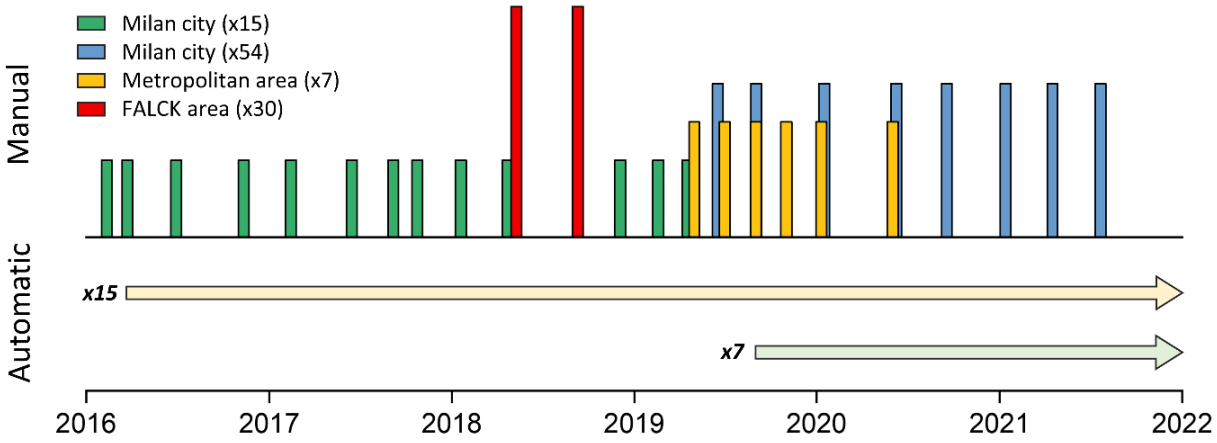


***Figure 5.12*** *– Summary of the groundwater monitoring activities since 2016. Columns indicate the vertical profiles acquisition campaigns; horizontal arrows indicate the time span covered by the high-resolution automatic pressure and temperature monitoring. See* ***Figure 5.3*** *for the location of manual and automatic monitoring locations.*

The temperature-depth profiles from 91 open-pipe piezometers (from 2016 to 2021 as described in **Figure 5.12**) are plotted in **Figure 5.13a**: 54 in the Milan municipality, 7 in the MCA and 30 in the FALCK area (**Figure 5.3**). The geothermal gradient evaluated across the Po plain by the GeoMol project (ISPRA, 2015) at non-urbanized locations is also shown. A schematic interpretation of the shape of the observed temperature-depth profiles is given in **Figure 5.13b** showing the progressive reduction of temperature fluctuations with depth and the portion of subsurface where heat accumulation from external (non-natural) sources is observed.

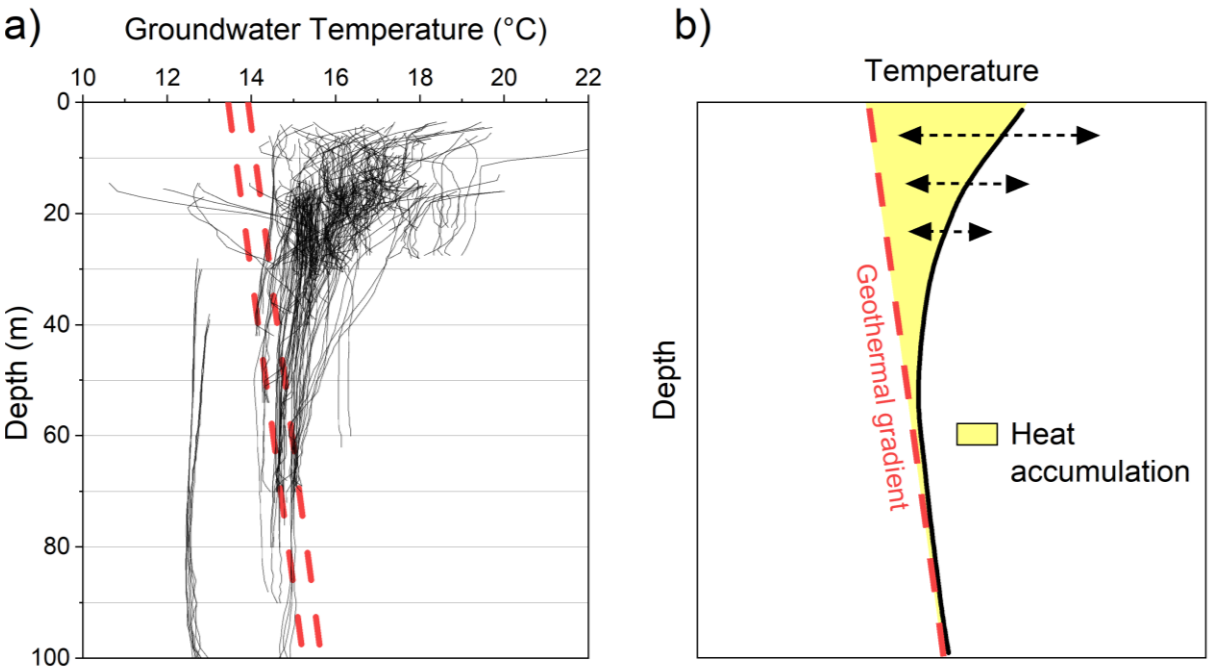


***Figure 5.13*** *– (a) Groundwater temperature-depth profiles (black) collected in the study area since 2016. Dashed red lines show the geothermal gradient measured at two locations in the study area by* ISPRA (2015)*. (b) Schematic interpretation.*

# 6. Deriving the geothermal potential of shallow aquifers at regional scale

This chapter is largely based on the following paper:

➔ Previati, A., & Crosta, G. B. (2021). Regional-scale assessment of the thermal potential in a shallow alluvial aquifer system in the Po plain (northern Italy). *Geothermics*, *90*, 101999. https://doi.org/10.1016/j.geothermics.2020.101999

## 6.1. Introduction

The European commitment on climate change mitigation and decarbonization focuses on ambitious and promising goals such as (i) reaching a share of at least 32% of renewable energy by 2030 (EU DIRECTIVE 2018/2001, 2018) and (ii) reducing greenhouse gas emissions to 80-95% below 1990 levels by 2050 (European Climate Foundation, 2010). Low enthalpy shallow geothermal energy is considered a valid alternative to common carbon-based heating/cooling techniques (e.g. fossil fuel burners, air-coupled heat pumps) (Lund and Boyd, 2016). Even though shallow geothermal systems require electricity to extract heat from the ground, a significantly lower amount of electrical power is required and lower volumes of greenhouse gases (GHGs) are emitted if compared to conventional heating/cooling systems (Bayer et al., 2012; Blum et al., 2010). It has been demonstrated that the use of geothermal energy in common residential and commercial buildings in Europe can reduce the emission of GHGs, such as $CO_2$, between 31% and 88% (depending on the source of the supplied electricity and the efficiency of the installation) compared to conventional heating systems such as oil and gas fired boilers and air-coupled heat pumps (Saner et al., 2010). Moreover, it was demonstrated low enthalpy geothermal systems to be the best cost-effective conditioning solution for a wide range of buildings, despite the high initial investment (Self et al., 2013).

In Italy, the low-enthalpy geothermal energy annual production (2,756 GWh in 2017) still accounts for only 0.4% of the total thermal energy production and represents about 2% of the renewable thermal energy production (GSE, 2018). However, a continuously increasing trend

has been observed since 2012 (+8% in 5 years) (GSE, 2018), and a strong rise of about 300% is expected within 2030 (Unione Geotermica Italiana, 2017). The most severe obstacles to the use of geothermal heat pumps are the high initial costs due to drilling and installation operations, and the high cost of domestic electricity (0.21 €/kWh) compared to methane (0.08 €/kWh) (EUROSTAT, 2019). To relieve these economic limitations, it was introduced a tax relief up to 65% of the total investment for energy-renovation of existing buildings (ENEA, 2018). Moreover, according to the recent Italian energy regulation on new buildings *(D.Lgs. 28/2011),* at least 50% of the thermal energy used for space heating and cooling (and for hot water supply) must come from renewable sources.

Another common obstacle is the lack of knowledge on the potential of this heating/cooling technique and about the sites where they can be more efficiently and easily installed. One of the best indicators of geothermal efficiency and suitability is the geothermal potential. Even though it is not uniquely defined (Bayer et al., 2019), the geothermal potential describes the capability to exchange heat with the ground or the groundwater.

Bayer *et al.* (2019) reviewed the most relevant works on geothermal potential assessment introducing the distinction (**Figure 2.9**) between the theoretical potential (i.e. the total energy stored in a reservoir or the amount of exchangeable heat based only on the hydrogeological and thermal properties of the exploitable aquifers) and the technical potential (i.e. the fraction of the theoretical potential that can be used by a certain technology). In practice only a fraction of the theoretical potential can be exploited depending on the technical restrictions and local regulations about the conservation of the groundwater resources and the protection of the thermal status of the aquifers. In this context, a comprehensive assessment of the thermal potential taking into account the hydrogeological and thermal settings (i.e. the hydraulic and thermal properties and the thermal regime of the subsurface), and the restrictions by local regulations, is needed to define the effective technical potential.

Many authors mapped the technical geothermal potential of GCHPs and GWHPs by combining climatic and thermo-geological information through theoretical physical equations (García-Gil et al., 2015; Zhu et al., 2011) or empirical equations (Böttcher et al., 2019; Casasso and Sethi, 2016b; Galgaro et al., 2015; Viesi et al., 2018) and derived techno-economic indicators such as the investment cost and payback times (Perego et al., 2019). At the city scale Epting *et al.*

(2018) and Mueller et al. (2018) evaluated the amount of extractable heat through numerical modeling techniques. These methods are very precise tools for city-scale geothermal potential assessment and thermal management of local aquifers but are computationally too expensive for regional-scale geothermal mapping.

The objective of this study is to characterize the low enthalpy geothermal potential for closed- and open-loop systems for an intensively urbanized and industrialized portion of the Po plain (Northern Italy) by linking geological and hydrogeological information to climatic data, and to discuss the potential of this fast-growing area to fulfill the extensive heating/cooling demand as well as to define which is the best technology according to the hydrogeological framework and heat demand scenarios. In this context, a GIS-based procedure was developed according to the following steps: (i) collection and homogenization of stratigraphic information as from borehole logs, (ii) assignment of hydraulic and thermal properties to the lithological units, (iii) estimate of the equivalent properties for different depth intervals, (iv) mapping of hydrogeological parameters and aquifer temperature, (v) application of analytical equations to derive the technical thermal potential, and (vi) discussion of the results by comparing the actual thermal energy demand of the municipalities in the study area.

## 6.2. Study area

The study area is located in the northern portion of the Po plain (northern Italy) and is bounded by the Adda, Ticino and Po rivers eastward, southward and westward, respectively, and by the alpine foothills to the north (**Figure 5.1**). This area has a great potential for shallow geothermal exploitation due to its advantageous hydrogeological settings (e.g. the equivalent horizontal hydraulic conductivity of the phreatic aquifer ranges between $5*10^{-5}$ and $1*10^{-2}$ m/s and the average saturated thickness is about 40 m) and due to the high heating/cooling demand (see section 5.4 for the current shallow geothermal applications in the study area).

## 6.3. Materials and methods

The spatial distribution of thermal and hydrogeological parameters is essential to assess the potential of shallow geothermal systems. Depending on the adopted technology, i.e. GCHP or GWHP, the geothermal potential was obtained by means of different analytical methods.

For GCHP systems we implemented the ASHRAE (Kavanaugh and Rafferty, 2014) analytical equation for ground heat exchanger borehole length sizing. The method is based on the assumption that the heat transfer rate to/from the ground (G) is directly proportional to the borehole length (L) and the temperature difference (ΔT), and it is inversely proportional to the overall resistance of ground and borehole materials ($R_{ov}$):

$$G = \frac{L * \Delta T}{R_{ov}} \qquad \textit{(Eq. 6.1)}$$

The heat transfer rates to/from the ground in heating ($G_H$) and cooling ($G_C$) mode are derived as follows:

$$G_H = H * (1 - \frac{1}{COP_H}) \; ; G_C = C * (1 + \frac{1}{COP_C}) \qquad \textit{(Eq. 6.2)}$$

where H and C are the heating and cooling loads and $COP_H$ and $COP_C$ the coefficient of performance for heating and cooling mode, respectively. (Eq. 6.1) is a steady-state equation and can be transformed to represent the time-varying heat rate of a ground heat exchanger (Ingersoll et al., 1954). By using a series of constant heat rate pulses, the thermal resistance per unit length of the ground is calculated as a function of time. Considering three heat pulses which correspond to the typical time-frequency over which we can observe a thermal perturbation (i.e. a short-term heat pulse with a daily period, a seasonal heat pulse with a monthly period and a life-time heat pulse with a multi-annual period) the required length is given by (Kavanaugh and Rafferty, 2014):

$$L = \frac{q_a R_{ga} + \; G \; (R_b + PLF * R_{gm} + F_{sc} * R_{gst})}{(t_g - t_f) + t_p} \qquad \textit{(Eq. 6.3)}$$

where

$q_a$ the net annual heat transfer rate from/to the ground obtained by considering the equivalent full-load hours (EFLH) for heating and cooling operating mode

$$q_a = \frac{G_H * EFLH_H - G_C * EFLH_C}{8760} \qquad \textit{(Eq. 6.4)}$$

$R_b$ thermal resistance of the borehole lining and grout [mK/W]

$PLF$ part-load factor that accounts for day and night thermal loads (0.3 for common working time)

$F_{sc}$ short-circuit heat loss factor between extraction and reinjection wells (1.05 for single-U "in series" boreholes, $Q_{carrier\text{-}fluid}$ = 0.05 l/s*kw)

$t_g$ undisturbed ground temperature [°C]

$t_f$ average temperature between the carrier fluid entering and leaving the heat pump [°C] (-2°C for heating and 32.5°C for cooling)

$t_p$ long-term ground temperature penalty [°C] reduced from $t_g$ to account for the imbalance between the heat removed and injected during the heating and the cooling season, respectively (-0.5°C after 20 years with $EFLH_C/EFLH_H \leq 0.5$)

$R_{ga}\ R_{gm}\ R_{gst}$ equivalent thermal resistances of the ground to long-term, monthly and short-term heat pulses, respectively; obtained by adapting the Carslaw and Jaeger (1959) cylindrical heat source solution to account for time-varying heat pulses (Kavanaugh and Rafferty, 2014):

$$R_{ga} = \frac{G_f - G_1}{\lambda_g},\ R_{gm} = \frac{G_1 - G_2}{\lambda_g}\ \ and\ \ \ R_{st} = \frac{G_2}{\lambda_g} \qquad \textit{(Eq. 6.5)}$$

where $\lambda_g$ is the thermal conductivity of the ground, $G_f$, $G_1$ and $G_2$ are obtained through the correlation nomogram between the G-factor and the dimensionless Fourier number ($F_0$) proposed by Ingersoll, Zobel and Ingersoll (1954):

$$F_O = \frac{4\ \alpha_g\ \Delta t}{d_B^2} \qquad \textit{(Eq. 6.6)}$$

where $\alpha_g = \frac{\lambda_g}{c_g \rho_g}$ is the bulk thermal diffusivity of the ground, dB is the borehole diameter and $\Delta t$ is the heat pulse duration.

The borehole thermal resistance ($R_b$) was evaluated with different methods by many authors (Lamarche et al., 2010). Since the carrier fluid, the piping and the backfill materials have a very little thermal mass compared to the surrounding ground, $R_b$ can be considered as steady-state (Kavanaugh and Rafferty, 2014). Shonder and Beck (1999) proposed an approximate model to assess the thermal resistance of single- and double-U boreholes considering the pipes as a single diameter-equivalent pipe. The effective pipe-to-borehole thermal resistance is given by:

$$R_b = \frac{1}{2\pi\lambda_{bf}} \ln\left(\frac{d_B}{d_p\sqrt{n}}\right) \quad \textit{(Eq. 6.7)}$$

where $n$ is the number of pipes in the borehole (e.g. for a double-U pipe, $n$ = 4), $d_B$ is the borehole diameter, $d_p$ is the pipe diameter and $\lambda_{bf}$ is the grout thermal conductivity.

Assuming no imbalance between heating and cooling operating hours (i.e. the amount of heat extracted from the ground during the heating season is about to heat injected into the ground during the cooling season) (Eq. 6.3) can be rewritten in the simplified (non-dominant) form:

$$L = \frac{G\ (R_b + PLF * R_{gm} + F_{sc} * R_{gst})}{(t_g - t_f)} \quad \textit{(Eq. 6.8)}$$

Then, assuming the heating load (H) equal to the cooling load (C), (Eq. 6.3) can be rewritten by expressing the ratio between the thermal load (Q=H=C) and the borehole length, obtaining the general correlation for closed-loop systems thermal potential assessment:

$$P_{GSHP} = \frac{(t_g - t_f) + t_p}{\frac{\left(1 - \frac{1}{COP_H}\right) * EFLH_H - \left(1 + \frac{1}{COP_C}\right) * EFLH_C}{8760} * R_{ga} + \frac{G}{Q} * (R_b + PLF * R_{gm} + F_{sc} * R_{gst})} \quad \textit{(Eq. 6.9)}$$

and its non-dominant form if no imbalance between heating and cooling hours is observed:

$$P_{GSHP} = \frac{(t_g - t_f)}{\frac{G}{Q}(R_b + PLF * R_{gm} + F_{sc} * R_{gst})} \quad \textit{(Eq. 6.10)}$$

The term $\frac{G}{Q}$ is equal to $1 - \frac{1}{COP_H}$ and $1 - \frac{1}{COP_C}$ in the heating and cooling mode, respectively.

Thus, by fixing the system fluid temperature ($t_f$), the duration of the heat pulses, and the correction factors ($F_{sc}$, $PLF$), $P_{GCHP}$ depends essentially on the ground/groundwater temperature and the thermal diffusivity of the ground.

While closed-loop dimensioning is generally performed with standardized techniques, the open-loop thermal potential mostly depends on the hydrodynamic parameters of the aquifer and the thermal diffusivity is less relevant. In fact, the heat exchange potential of a GWHP system is strictly elated to the amount of water that can be extracted from the aquifer, according to hydrogeological and regulatory constraints.

The equation to estimate the open-loop thermal potential was obtained from (Eq. 2.12) and depends on the amount of water and the temperature drop:

$$P_{GWHP} = c_w \rho_w \, Q \, \Delta T \qquad \textit{(Eq. 6.11)}$$

where

$c_w \rho_w$ Specific volumetric heat capacity of water (= 4.18 MJ/m$^3$K)

$Q$ Flow rate (m3/s)

$\Delta T$ Temperature difference between abstraction and injection wells (K).

Thus, $P_{GWHP}$ depends essentially on the aquifer exploitability, i.e. on the transmissivity, the existing regulatory thresholds about the abstraction and reinjection of water, and the allowable thermal perturbation.

### 6.3.1. Data collection

#### *6.3.1.1. Thermal and hydraulic parameters*

According to (Eq. 6.9) and (Eq. 6.11), the thermal potential of GCHPs and GWHPs depends on continuous variables that can be easily mapped for the entire study area through the interpolation of point information. By adopting the hierarchical classification of lithofacies and hydrofacies from (De Caro et al., 2020b), hydraulic and thermal parameters (**Table 5.1**) were assigned to each lithofacies.

- **Hydraulic conductivity and porosity**: for the unconfined aquifer were assigned to each lithofacies unit by analyzing the grain size distribution and by adopting various empirical correlations between specific grain size curve coefficients and the equivalent hydraulic parameters (De Caro et al., 2020b). Hydraulic parameters of the semi-confined aquifer units were assigned from the analysis of pumping test data provided by the local water supply agency (De Caro et al., 2020b).
- **Thermal conductivity and specific volumetric heat capacity**: were assigned from the literature (Di Sipio et al., 2014; VDI 4640/2, 2001) to each single grain-size unit (i.e. gravel, sand, silt and clay). The equivalent thermal parameters of composed units were obtained by the weighted average of each grain-size unit component according to its

relative weight proportion. The relative proportions were assigned according to the Italian soil classification standard commonly used in borehole stratigraphic logging descriptions (A.G.I., 1963). In particular, in a multiple term unit, the first term represents the most abundant grain size class, then specific forms are used to distinguish if the abundance of additional terms ranges between 50% and 25%, 25% and 10% or 10% and 5% of the total weight.

The adopted hydrostratigraphic conceptual model was introduced in section 5.2 (**Figure 5.2**) and will no longer be discussed. The boundary surfaces between the phreatic and the semi-confined aquifer and the bottom boundary surface of the semi-confined aquifer were obtained from (De Caro et al., 2020b). Piezometric head levels of the entire study area, as well as the digital elevation model (DEM cell size 5x5 m), were obtained from the regional geological database (Regione Lombardia - CASPITA, 2019; Regione Lombardia, 2020).

Equivalent thermal parameters were obtained for four reference borehole length scenarios (i.e. the average by length of 50, 100, 150 and 200 meters below the ground surface) by computing the weighted average of each unit along the borehole and by taking into account the presence of water (**Figure 6.1**). For each depth scenario only the stratigraphic logs reaching the reference length (with a 20% tolerance) were selected. The number of boreholes reaching the depth of each scenario was: 4693, 2988, 1302 and 627 respectively for the 50, 100, 150 and 200 m reference depth.

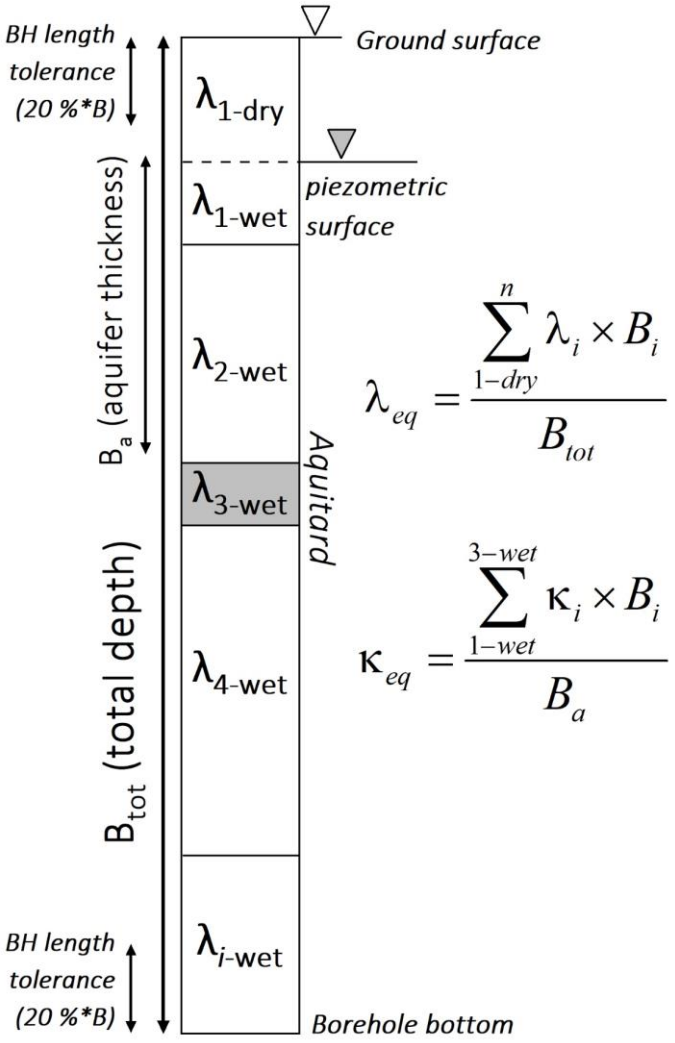


***Figure 6.1*** *– Schematic representation of the procedure to obtain equivalent thermal and hydraulic parameters.*

Then, the equivalent thermal parameters of each borehole were interpolated via Ordinary Kriging obtaining the thermal conductivity and volumetric heat capacity maps for each depth scenario (e.g. **Figure 6.2a** and **b** show the maps for the 100 m reference borehole length).

The equivalent horizontal hydraulic conductivity (**Figure 6.2c**) was calculated at each borehole location only for the unconfined aquifer (**Figure 6.1**) and multiplied by the saturated thickness (which is generally lower than 100 m) to obtain the transmissivity of the phreatic aquifer (**Figure 6.2d**). The areas considered for the thermal (**Figure 6.2a** and **b**) and hydraulic parameters (**Figure 6.2c** and **d**) differ in extent because to the north of the dashed line ("aquitard boundary") the shallow phreatic aquifer is not fully separated from deeper aquifers (as evidenced also by the cross-section in **Figure 5.2**). Thus, the regionalization of the aquifer transmissivity values is not applied in this area because the thickness and the extension (but

also the hydraulic properties) of the shallow aquifer vary significantly at local-scale, and the aquifer parameters cannot be spatially correlated to those south the "aquitard boundary" line.

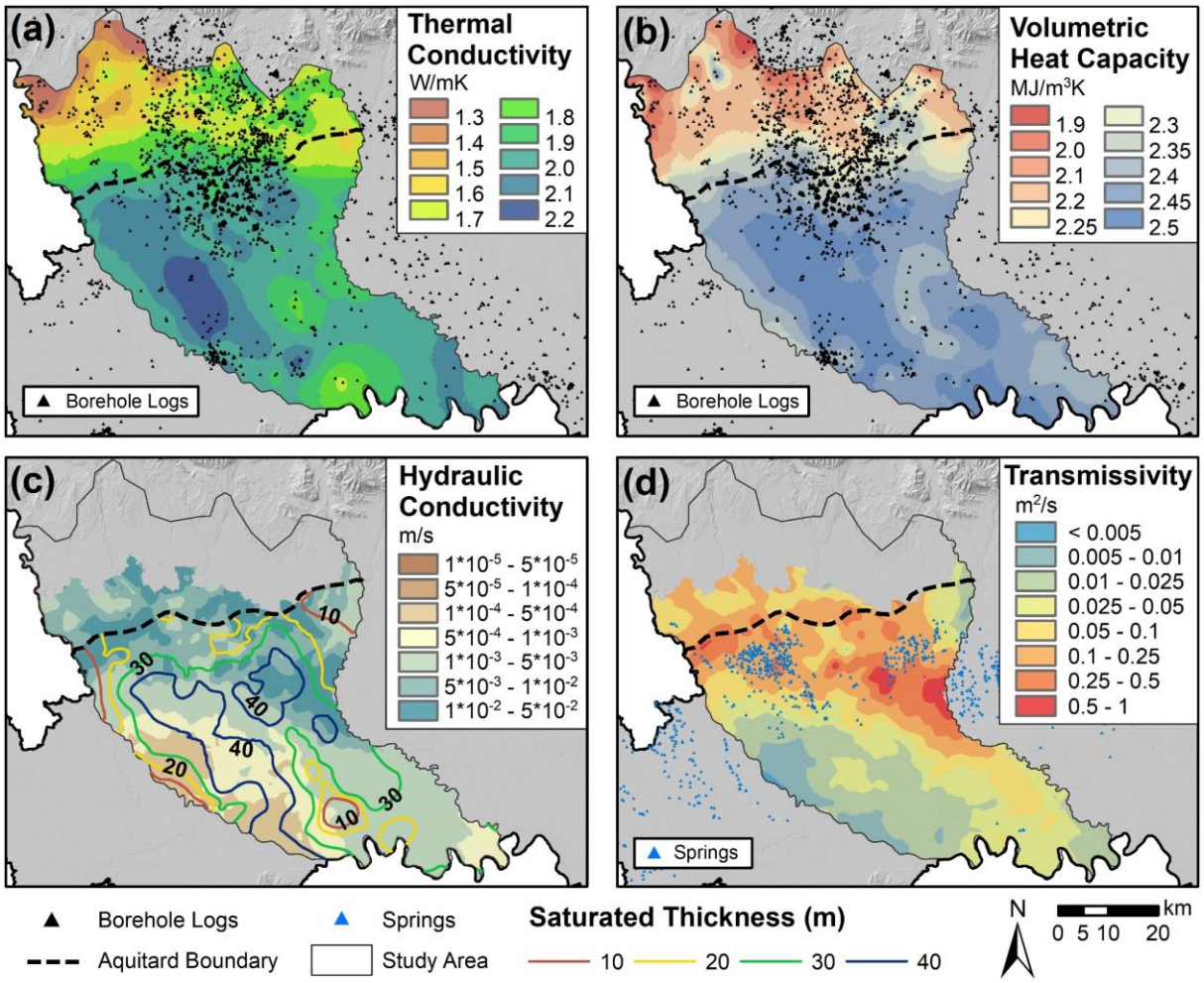


***Figure 6.2*** *– Maps of the study area showing: (a) the equivalent thermal conductivity and (b) the equivalent volumetric heat capacity for the 100 m reference length scenario, (c) the equivalent horizontal hydraulic conductivity, the saturated thickness and (d) the transmissivity of the phreatic aquifer.*

### *6.3.1.2. Groundwater temperature*

The underground temperature is one of the most difficult parameters to assess in regional-scale geothermal potential studies since it is controlled by various local-scale phenomena, such as (I) the thickness of the unsaturated zone that dampens the temperature fluctuations coming from the surface, (II) the groundwater flow velocity that drives the heat transport in advective-dominated aquifers, (III) the presence of surface water bodies and the degree of interaction with the groundwater, (IV) the percentage of sealed/cemented ground, (V) the presence of underground structures/infrastructures (e.g. tunnels) or deep foundations and

(VI) the use of low-enthalpy geothermal wells (Epting and Huggenberger, 2013; Kurylyk et al., 2015). In regional scale geothermal potential studies some authors considered the mean annual underground temperature equal to the mean annual air temperature (Viesi et al., 2018), while others related the underground temperature to other variables such as the altitude or the latitude (Galgaro et al., 2015; Perego et al., 2019; Signorelli and Kohl, 2004).

Since in the study area only 32 air temperature monitoring stations are available (**Figure 6.3a**), we collected water temperature data from physic-chemical datasets provided by local and regional water supply agencies, from Thermal Response Tests values reported in the regional closed-loop system database (Regione Lombardia, 2021) and from multi-temporal vertical temperature profiles collected for the shallow aquifer with a multi-meter probe. After homogenization and quality check (only those points with at least four measurements at different times of the year were considered) the datasets were merged into a single spatial database to obtain the mean annual groundwater temperature. 750 temperature data representatives of the phreatic and the semi-confined shallow aquifers were used and interpolated in the study area through ordinary kriging (**Figure 6.3b**). The mean annual air temperature and the mean annual temperature of the shallow groundwater are well correlated in the study area (**Figure 6.3c** and **d**). The most relevant deviation is observed in the northern portion of the study area and downwards the Milan city area. In the first case, the groundwater temperature is lower than the air temperature due to the greater depth of the water table whereas, in the second case, the groundwater temperature is higher due to the propagation of the heat island effect towards the main flow direction (i.e. parallel to the section line A-A' in **Figure 6.3b**).

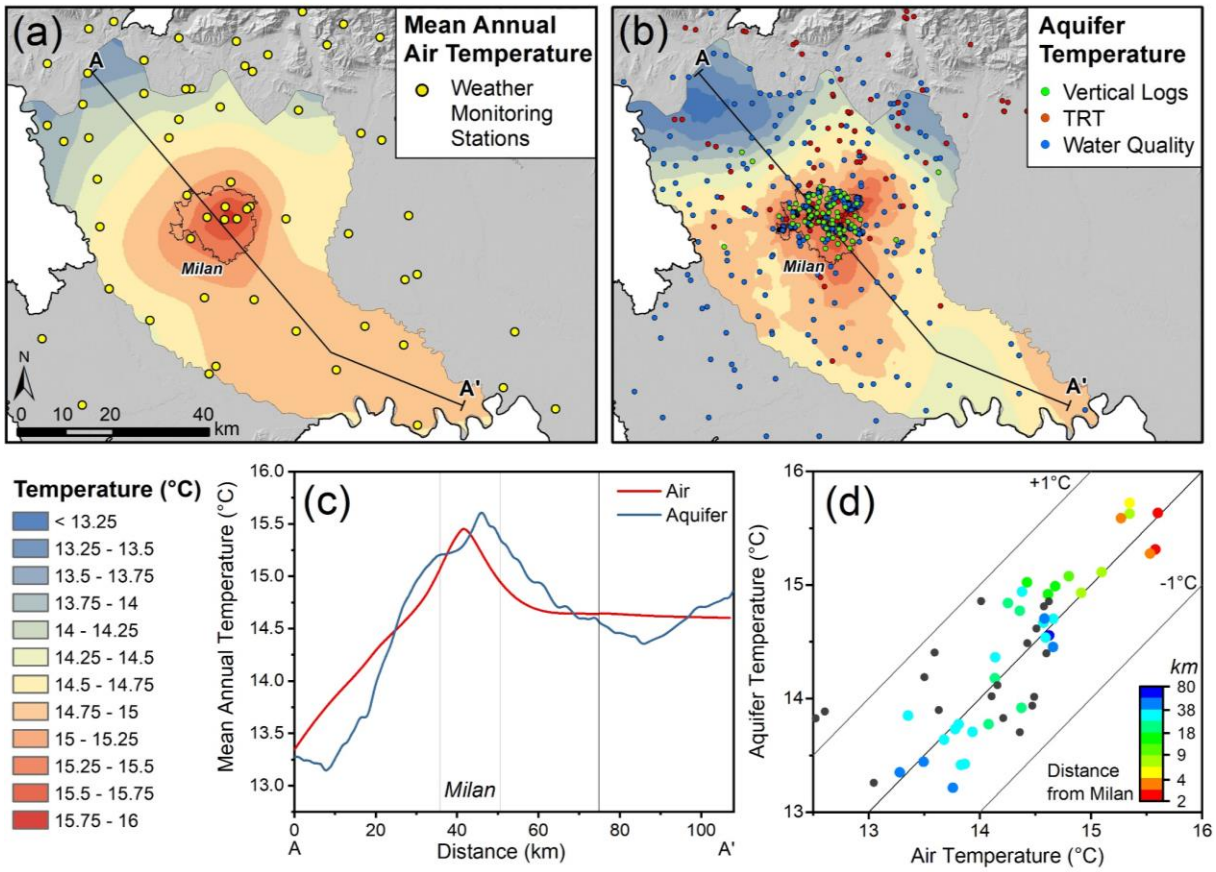


***Figure 6.3*** *– (a, b) Maps showing the spatial distribution of the mean annual air and aquifer temperature, respectively. (c) Mean annual air and aquifer temperature along the AA' profile and (d) scatter plot showing the correlation between the mean annual aquifer temperature and the mean annual air temperature. Dots are colored by the distance from the Milan city area, where the highest temperature is observed.*

### *6.3.1.3. Climatic data*

The amount of thermal energy required to heat/cool indoor spaces depends on the external air temperature and the thermal insulation of buildings. In this study we collected mean hourly air temperature data from 69 rain gauge stations (32 inside the study area) available for the last three years (2017-2019). One of the most adopted methods to estimate building energy consumption is to derive the equivalent full-load operating hours (EFLH) from climatic data. The EFLHs describe the number of hours a cooling or heating system needs to operate at full load to consume the total annual required amount of energy as expressed by the equation:

$$EFLH = \frac{\sum hDDs}{|T_{peak} - T_{ref}|} \qquad \textit{(Eq. 6.12)}$$

where

$hDDs$ are the hourly degree days obtained as the difference between the mean hourly air temperature and the reference indoor temperature ($T_{ref}$) for cooling mode and, vice versa, for heating mode. According to Banks (2009a) $T_{ref}$ was set to 18.3°C for heating and 23.8° for cooling, respectively;

$T_{peak}$ is the project peak temperature and was assumed as the 1st and the 99th percentiles of the mean hourly air temperature frequency cumulative distribution for heating and cooling mode, respectively (Kavanaugh and Rafferty, 2014).

To obtain the annual EFLH, the sum (considering only positive values) of the hourly degree days over an entire year (8760 hours in total) was divided by $T_{peak} - T_{ref}$. **Figure 6.4** shows the spatial distribution of the EFLHs for heating and cooling in the study area. We can observe that, due to the heat island effect, in the Milan city area the number of EFLHs for cooling is higher than anywhere else in the study area and the number of EFLHs for heating is the lowest.

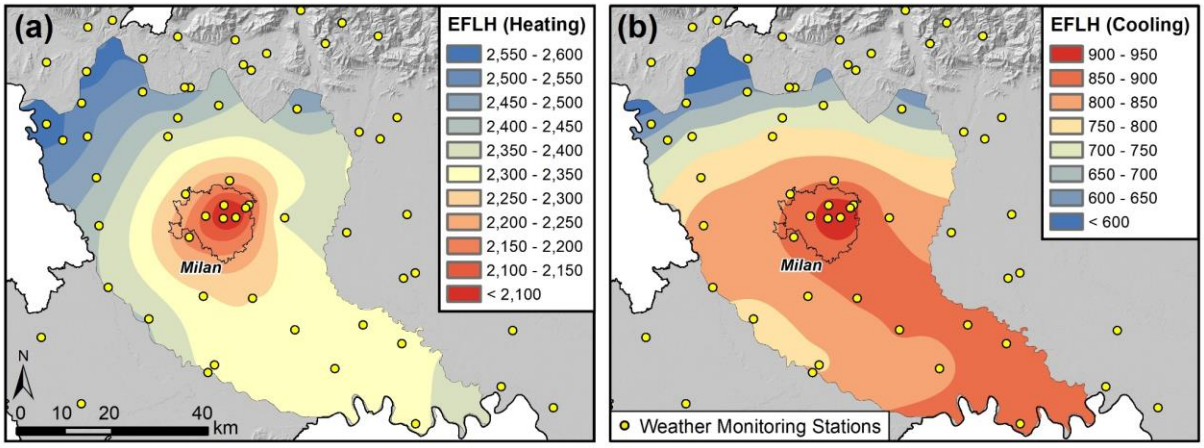


***Figure 6.4*** *– Maps of the study area showing the spatial distribution of the annual equivalent full-load hours (EFLH), (Eq. 6.11), for heating (a) and cooling (b).*

## 6.4. Closed-loop geothermal potential

Since GCHPs do not require the abstraction of groundwater and the main limiting factor is the techno-economic feasibility, the spatial distribution of the technical thermal potential is pivotal to their development. Some restrictions to the installation of GCHPs exist if there is the possibility to connect the aquifers exploited for drinking water withdrawal with more contaminated shallow aquifers (Busby et al., 2009). This can be prevented by a properly grouted section along the aquitard that also provides a good thermal contact if a high thermal

conductivity grout is used. According to the regional geothermal regulation (Regione Lombardia, 2010), the installation of a GCHP system in the study area is allowed without restrictions up to 150 m in depth while deeper installations are subjected to an authorization procedure and the assessment of the thermal impact of the system is required. Furthermore, for the installation of GCHPs with a thermal power greater than 50 kW the TRT is also required. According to the regional closed-loop system database (**Figure 5.6**), a length of 100 m was considered as the most likely exploitation scenario. The thermal potential was calculated in non-dominant mode (Eq. 6.10), i.e. by assuming no imbalance between cooling and heating loads and no significant differences between the amount of heat extracted from the ground during the heating season and the heat injected into the ground during the cooling season. Then, the result was compared with the thermally unbalanced potential obtained by means of equation (Eq. 6.9) considering 50 years as a lifetime and the operative equivalent full-load hours for heating and cooling described in section 6.3.1.3. The parameters adopted in (Eq. 6.9) are listed in **Table 6.1**.

***Table 6.1*** *– Overview of the parameters to obtain the GCHP thermal potential*

| *Parameter* | | *Description* | *Unit* | *Value* |
|---|---|---|---|---|
| $t_g$ | | *Undisturbed ground temperature* | *°C* | ***Raster map (Figure 6.3b)*** |
| $t_f$ | | *Temperature threshold of the carrier fluid* | *°C* | *-2 (heating), 32.5 (cooling)* |
| $t_p$ | | *Temperature penalty resulting from imbalances between the heat removed and injected in heating and cooling mode ($EFLH_H/EFLH_C>2$)* | *°C* | *-0.5* |
| $EFLH_H$ $EFLH_C$ | | *Equivalent full-load hours* | *h* | ***Raster map (Figure 6.4)*** |
| $R_b$ | | *Borehole thermal resistance* | *mK/W* | ↓ |
| | $\lambda_{bf}$ | *Thermal conductivity of the grout* | *W/mK* | *2* |
| | $d_B$ | *Borehole external diameter* | *m* | *0.075* |
| | $d_p$ | *Pipes diameter* | *m* | *0.016* |
| | $n$ | *Number of pipes* | *-* | *4* |
| $PLF$ | | *Part-load factor according to* (Kavanaugh and Rafferty, 2014) | *-* | *0.3* |
| $F_{sc}$ | | *Short circuit heat loss factor (one U-tube in series, $q_{carrier-fluid} = 0{,}05\ l\ /\ s * kw$)* | *-* | *1.05* |
| $R_{ga}$ $R_{gm}$ $R_{gst}$ | | *Thermal resistance of the ground calculated for the long-term (a), monthly (m) and short-term (st) heat pulses* | *mK/W* | ↓ |
| | $\lambda_g$ | *Equivalent thermal conductivity of the ground* | *W/mK* | ***Raster map (Figure 6.2a)*** |
| | $c_g\rho_g$ | *Equivalent volumetric heat capacity* | *J/m³K* | ***Raster map (Figure 6.2b)*** |

**Figure 6.5** shows the closed-loop geothermal potential for a 100-meters-length GCHP. Non-dominant thermal potential ranges between 35 and 67 W per m of installed borehole but, considering the operative EFLHs (**Figure 6.4**), it can decrease up to 12% and increase up to 16% for heating and cooling mode, respectively. We can observe that GCHPs are more efficient in the southern portion of the study area where the water table is closer to the surface. To the north we can observe greater potential values in the eastern sector due to the presence of cemented conglomeratic units (e.g. the "Ceppo" formation), that are generally more conductive than loose deposits. The thermal potential in the MCA decreases significantly switching from heating to cooling modality as a result of the UHI effect.

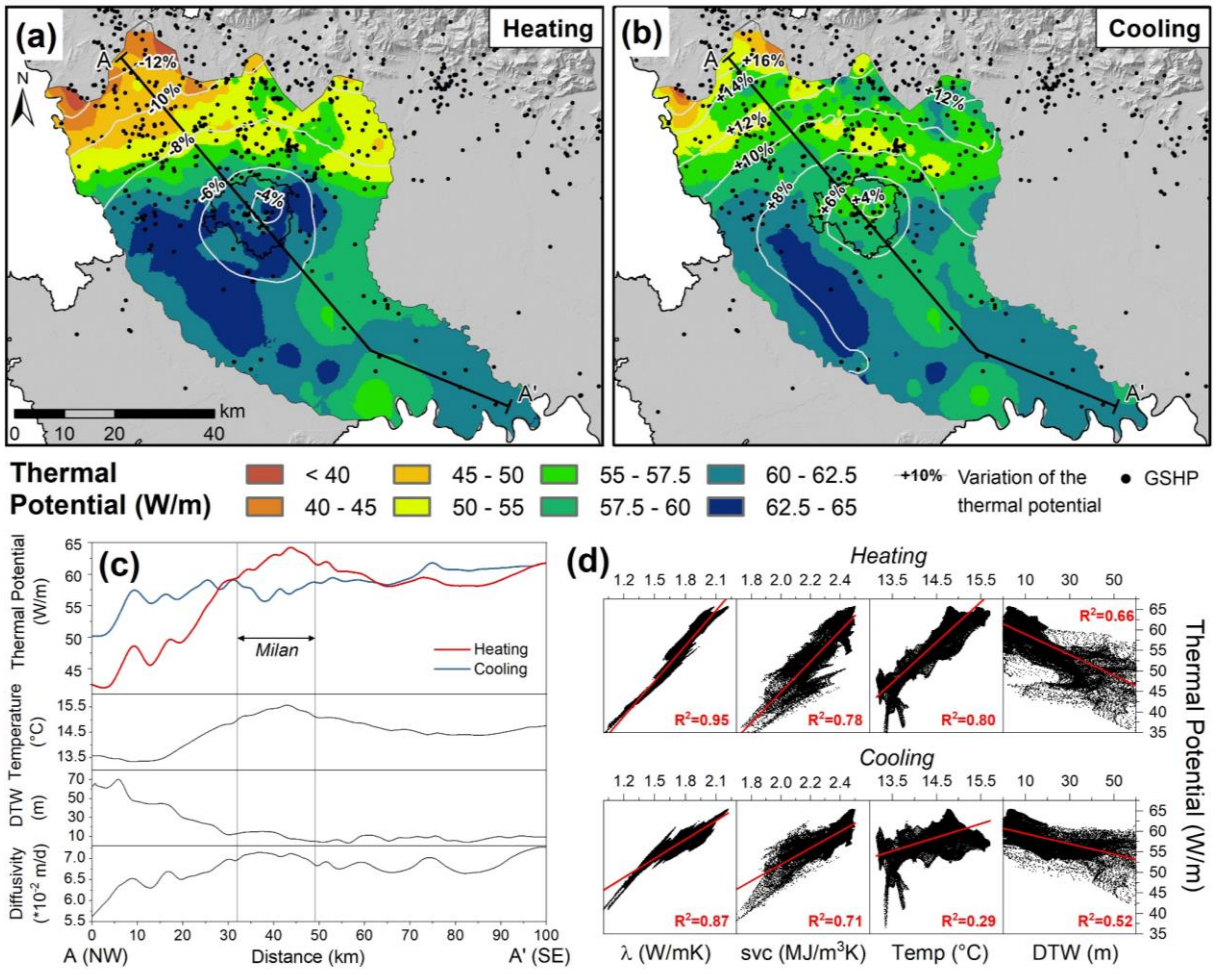


***Figure 6.5*** *– (a, b) Maps showing the spatial distribution of the GCHPs (non-dominant) thermal potential for heating and cooling mode, respectively. Grey isolines represent the increase/reduction of the thermal potential if the general equation is considered (Eq. 6.9). (c) Cross-section profiles and (d) correlation between the thermal potential and the thermal parameters (λ and svc), the groundwater temperature and the depth of the water table (DTW).*

## 6.5. Open-loop geothermal potential

The open-loop geothermal potential depends essentially on the amount of water that can be extracted and re-injected from/into the aquifer or disposed in a surface water body. This amount depends firstly on the aquifer characteristics, such as the transmissivity, but also on regulations about the use and the conservation of the quantity and quality of the groundwater resources. Following the steps proposed by Böttcher et al. (2019), we adopted thresholds on local regulatory restrictions and common groundwater conservation principles such as:

1. **Maximum recommended drawdown** $(Q_d)$: was imposed to avoid excessive consumption of the groundwater resources. According to Bezelgues-courtade *et al.* (2010) well dynamic piezometric level should not be lower than one-third of the saturated thickness of the phreatic aquifer and the drawdown must not exceed a threshold value. Drawdown thresholds are also important to prevent soil settlements in urban areas. For this reason, in addition to the one-third rule we set a maximum well lowering threshold of 10 meters. This value represents the mean historical groundwater level recorded in the Milan city during the '70s due to the head depression cone caused by intensive groundwater withdrawals (see section 5.4). If the shallow deposits in the Milan city area have undergone consolidation due to the pore pressure lowering in the past decades, the surrounding less urbanized areas have not experienced such a phenomenon. For this reason, site-specific assessments in the areas where the difference between the present and the historical groundwater levels is significantly lower than 10 meters are recommended.
2. **Maximum allowable rising** $(Q_r)$: was imposed to avoid an excessive rise of the groundwater level that might result in basements or surface flooding. According to typical underground basement depths, the groundwater level should not overcome at least three meters below the ground surface. In some portions of the study area, the water table is so close to the surface (less than 2 meters) that the re-injection of water must be carefully planned. If the disposal in surface water bodies is not achievable some "low-impact" re-injection techniques can be adopted such as a group of reinjection wells instead of a single well or drainage trenches.

The maximum flow rate to avoid excessive rising and drawdown was derived through the Cooper & Jacob equation:

$$Q = \frac{4\,\pi\,T\,\Delta H}{\log(2{,}25\frac{T\,t_{pump}}{S\,r_w^2})} \qquad \textit{(Eq. 6.13)}$$

3. **Thermal breakthrough constraint** $(Q_b)$: the reinjection of water downstream or upstream the abstraction well causes a thermal alteration plume. Not properly sized geothermal well fields can undergo thermal recycling processes if the thermal alteration plume propagates back towards the abstraction well, reducing the efficiency of the system (Banks, 2009b). Depending on the discharge of the system, the minimum injection/extraction well distance can be estimated according to (Eq. 6.14) (Banks, 2009b; Lippmann, 1980). By setting the reference space length to a typical value (according to (Regione Lombardia, 2021) L=100 m) we can obtain the maximum allowable flow rate to prevent the thermal breakthrough between a 100-meters-spaced well doublet:

$$Q = \frac{\pi * L * T * i}{1{,}96} \qquad \textit{(Eq. 6.14)}$$

4. **Temperature difference constraint:** according to the local regulation on the use of shallow groundwater resources (see section 5.5.1) (Regione Lombardia, 2017), the maximum temperature change between the abstraction and injection wells was set to 5 °C. Moreover, the maximum reinjection temperature is restricted to 21 °C.

**Figure 6.6** shows the maximum recommended flow rate according to the drawdown and rising constraints and the relative minimum distance between the extraction and injection well obtained by substituting the maximum flow rate in (Eq. 6.14). The area considered for the installation of GWHPs (**Figure 6.6** and **Figure 6.8**) differs in extent from that of GCHPs (**Figure 6.5**) as explained in section 6.3.1.1. The installation of GWHPs north of the dashed line is still possible but to assess the thermal potential local investigations are necessary.

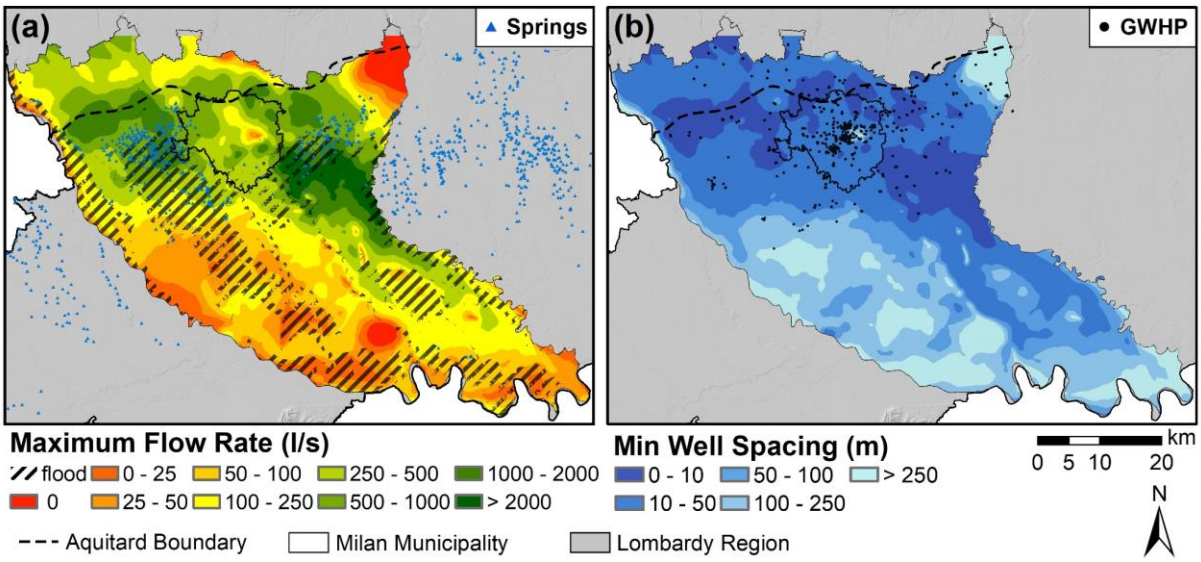


***Figure 6.6*** *– (a) Maximum recommended flow rate obtained by combining the drawdown and rising constraints and (b) minimum allowable distance to prevent thermal breakthrough between the extraction and the injection well. Banded field ("flood") represents the area where re-injection of wastewater is not allowed to avoid basement flooding.*

The Milan metropolitan area is the most urbanized portion of the study area. In this region many industrial activities have flourished since the early 60s leading to intense groundwater exploitation up to the early 90s (see section 5.4). If during the industrial period the water table was lowered by up to more than 15 meters, nowadays most of the activities have been relocated and the groundwater rebound phenomenon has been observed in many piezometric time series (Crosta and De Caro, 2018). Comparing the historical piezometric data available for the study area, the maximum groundwater fluctuation was estimated as the difference between the present level and the lowest available historical level (**Figure 6.7**). Where the historical groundwater fluctuations were lower than 10 meters we suggest considering if soil settlements caused by pore pressure lowering could damage surface infrastructures.

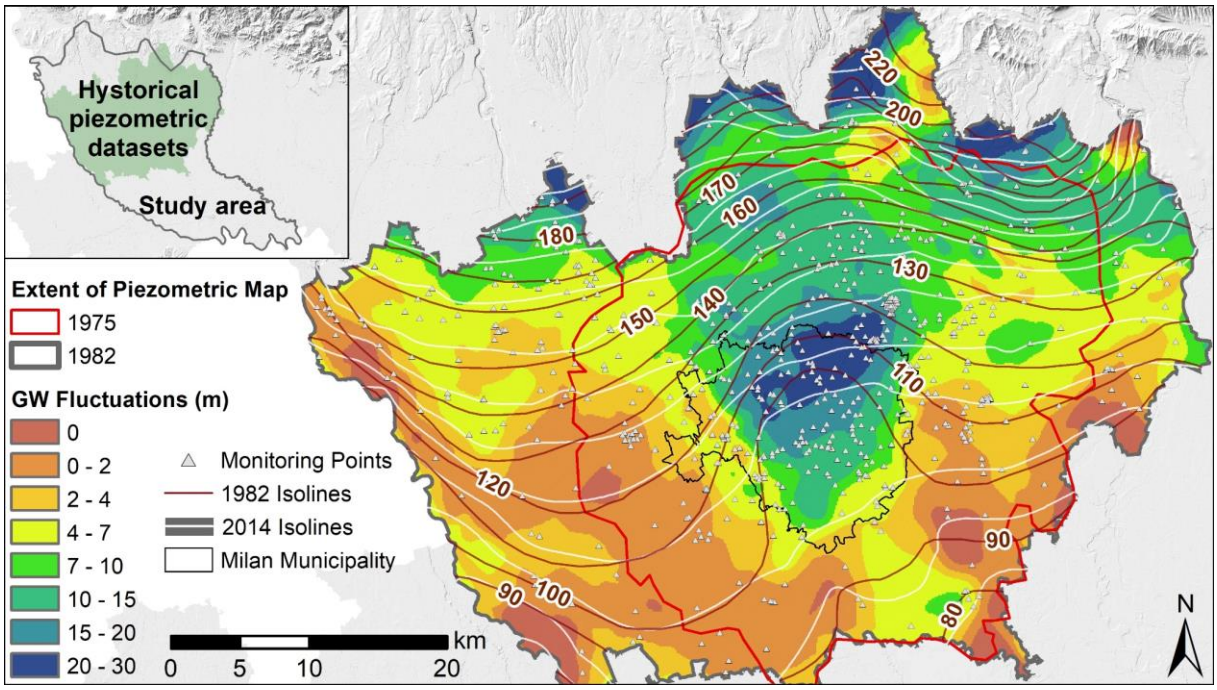


***Figure 6.7*** *– Map of the MCA showing the spatial distribution of the difference between the minimum historical piezometric level and the piezometric level as on 2016. Piezometric levels within the red area were obtained from the piezometric map available for 1975, whereas outside this area a piezometric map of 1982 and historical piezometric point data were compared.*

The effective open-loop geothermal potential, $P_{GWHP}$ [W], was derived combining the flow rate obtained from (Eq. 6.13) and (Eq. 6.14), considering two operative configurations:

- Re-injection of wastewater:

$$P_{GWHP} = c_w \rho_w \, \Delta T \, min(Q_d, Q_r, Q_b) \qquad \textit{(Eq. 6.15)}$$

- Surface disposal:

$$P_{GWHP} = c_w \rho_w \, \Delta T \, Q_d \qquad \textit{(Eq. 6.16)}$$

The parameters adopted to derive $P_{GWHP}$ are summarized in **Table 6.2**.

***Table 6.2*** *– Overview of the parameters to obtain the GWHP thermal potential*

| *Parameter* | | *Description* | *Unit* | *Value* |
|---|---|---|---|---|
| $T$ | | *Transmissivity of the shallow aquifer* | *$m^2/s$* | ***Raster map (Figure 6.2d)*** |
| $\boldsymbol{B}$ | | *Saturated thickness of the shallow aquifer* | *m* | ***Raster map (Figure 6.2d)*** |
| $\Delta H$ | *Abstraction* | *Max. allowable drawdown* | *m* | $min\left(\frac{1}{3}\boldsymbol{B}\,;10\ m\right)$ |
| | *Injection* | *Max. allowable rising* | *m* | $z - h < 3\ m$ |
| $L$ | | *Distance between abstraction and injection wells* | *m* | *100* |
| $t_{pump}$ | | *Pumping time (180 days/year for 50 years)* | *s* | *$7.9*10^8$* |
| $r_w$ | | *Well radius* | *m* | *0.25* |
| $S$ | | *Storage coefficient* | *[]* | *0.2* |
| $c_w\rho_w$ | | *Volumetric heat capacity of water* | *$J/m^3K$* | *$4.18*10^6$* |
| $\Delta T$ | | *Regulatory threshold on temperature perturbation* | *°C* | *5* |

The open-loop geothermal potential (with and without reinjection) is presented in **Figure 6.8**. We can observe that to the south of the lowland spring belt, due to the proximity of the water table to the surface, the thermal potential is strongly limited by the groundwater rising constraint and, generally, the thermal potential is higher if only the abstraction of groundwater is considered. The disposal of wastewaters in surface water bodies (e.g. canals, rivers, lakes) is possible if they border (or flow very close to) the extent of the installation site property, which is unlikely in urban areas and frequently restricted. Nevertheless, the Milan area is characterized by the presence of a dense network of channels (Navigli) and others of minor order (**Figure 5.3**) that could constitute in specific cases a way of disposing the thermally altered wastewaters.

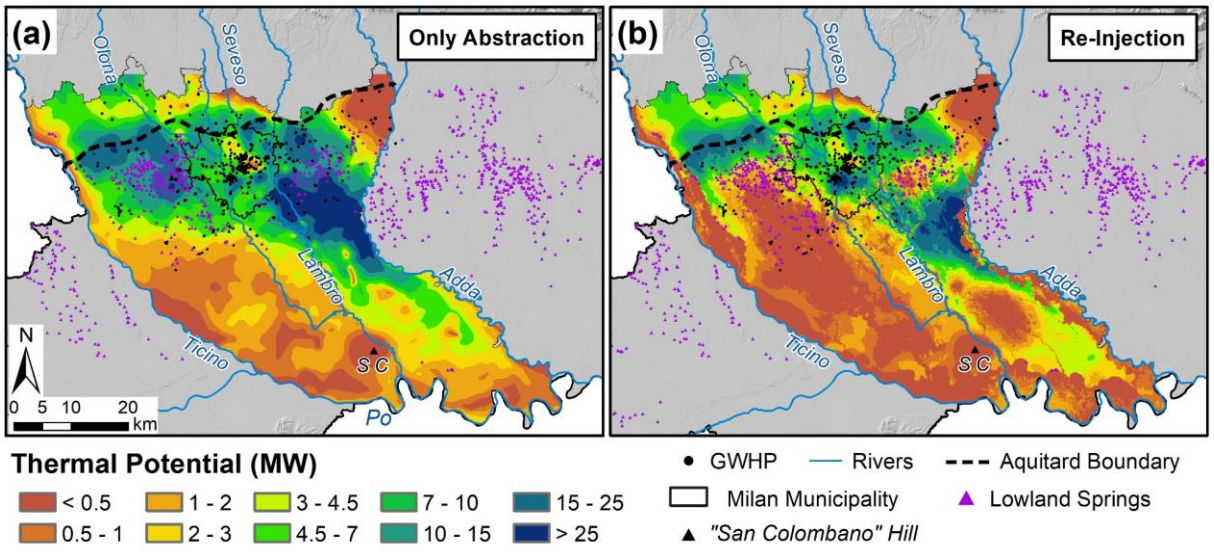


***Figure 6.8*** *– Maps showing the spatial distribution of the GWHP thermal potential for the only-abstraction (a) and the re-injection operative mode (b).*

## 6.6. Discussion

Regional geothermal potential mapping aims to promote sustainable planning and design of shallow geothermal systems such as GCHP and GWHP. In this work we assessed the capability of the study area to host different low enthalpy geothermal systems. Therefore, under different assumptions, specific heat exchange rates were derived by combining the spatial distribution of hydraulic and thermal parameters of the underground and the aquifer characteristics with the groundwater temperature and some regulatory restrictions.

During the last years in Europe many efforts were made to derive the geothermal potential in densely populated areas such as the metropolitan area of Barcelona (García-Gil et al., 2015), the city of Basel (Epting et al., 2018) and Munich (Böttcher et al., 2019), in Alpine regions (Casasso et al., 2017; Casasso and Sethi, 2016b; Viesi et al., 2018) but also at the scale of entire Europe (Bertermann et al., 2015). Generally, the main challenge is to obtain the effective potential based on underground data and real operative conditions (i.e. the “technical potential” of Bayer et al., 2019). This issue is well addressed in the work by analyzing and merging different datasets (e.g. stratigraphic information, groundwater temperature data and climatic conditions). The results obtained in this study are consistent with those obtained from various studies in other European cities and demonstrate the high potential of a highly conductive alluvial aquifer, especially if the thermal energy demand is very high.

Nevertheless, the outcome of this work should not be considered as a specific design rule for the installation of geothermal systems but could be significant for regional energy planning and stakeholders. The thermal potential maps are therefore the preliminary step for further local assessments and in-situ efficiency tests (e.g. TRT) that better characterize the effective heat exchange rate under real design conditions.

### 6.6.1. Comparison with other methods

A general assessment of the low enthalpy geothermal potential in this area was provided by the local environmental authority (Regione Lombardia, 2019a) for the only closed-loop configuration. This evaluation is based on the juxtaposition of specific extraction rates provided by the German guidelines (VDI 4640/2, 2001) on the spatial distribution of shallow loose deposits and outcrops derived from the regional scale geological map. The German guidelines are based on empirical correlations between real extraction rates and lithologies at the development sites and are commonly adopted by GCHP installers as a “rule of thumb” but have some limitations. First, the ground and groundwater temperature that affects the efficiency of the system are not considered. Moreover, there is no distinction between heating and cooling mode and the real operating hours per year are not considered. Lastly, the existing potential map is based only on the shallow deposits and outcrops whereas also the vertical variability should be considered to predict the overall thermal response of deep borehole heat exchangers. In this study we overcome these limitations by integrating hydraulic and thermal parameters and temperature data into the analytical equation proposed by Kavanaugh and Rafferty (2014). As regards the open-loop configuration there are no thermal potential studies in this area due to the highly fragmented regulation on the use of groundwater for thermal purposes. The authors think that this lack has strongly hindered the development of this technology in the study area.

### 6.6.2. Considerations on the use of GCHP or GWHP

The best choice between GCHP and GWHP, from an energy-efficiency and economical point of view, may depend on several aspects, among these: [1] the possibility to withdraw/reinject water from/into the aquifers; [2] the space availability to place extraction and injection wells

far enough to prevent thermal short-circuit; [3] the prevention of local excessive groundwater fluctuations and soil subsidence that could damage surface structures and infrastructures (Stauffer et al., 2013). Apart from these technical limitations, one of the most important deciding factors is the required thermal load. Generally, for large plants it is preferable to decide for an open-loop system, whereas for smaller ones both solutions are suitable. This is due to the high transmissivity of the aquifers in the study area that can provide a wide range of flow rates for a single well (this rule could not be valid in different hydrogeological settings). On the contrary, the ratio between the thermal load and the required GCHP length is generally constant, leading to unprofitable drilling costs for great energy demand projects. In **Figure 6.9** the required GCHP length and the number of geothermal wells for two thermal load scenarios are compared. **Figure 6.9a** shows the minimum length required by a GCHP system to satisfy a 45 kW thermal load, whereas **Figure 6.9b** shows the number of geothermal wells required to satisfy a 10 MW thermal load assuming that each well is working at its highest flow rate potential. The contour lines in each representation display a comparison with the other methodology. We can observe that for a 45 kW thermal load the total GCHP length ranges between 750 and 1,000 m (between 7 and 10 100-meters-length GCHPs) whereas the same load could be satisfied by a GWHP system using at most 1% of its maximum discharge. On the contrary to fulfill a 10 MW heat demand up to 10 abstraction wells might be necessary in the study area. This great amount of energy could be satisfied with an estimated average number of about 2,000 100-meters-length GCHPs. This solution is unrealistic or hardly feasible both for the required space and the total drilling costs. In fact, from a local cost analysis, considering about 50-60 €/m for drilling and setting up a GCHP system, and 200-300 €/m for a GWHP system, in the first scenario both technologies are profitable whereas in the second scenario the GCHP configuration is unprofitable.

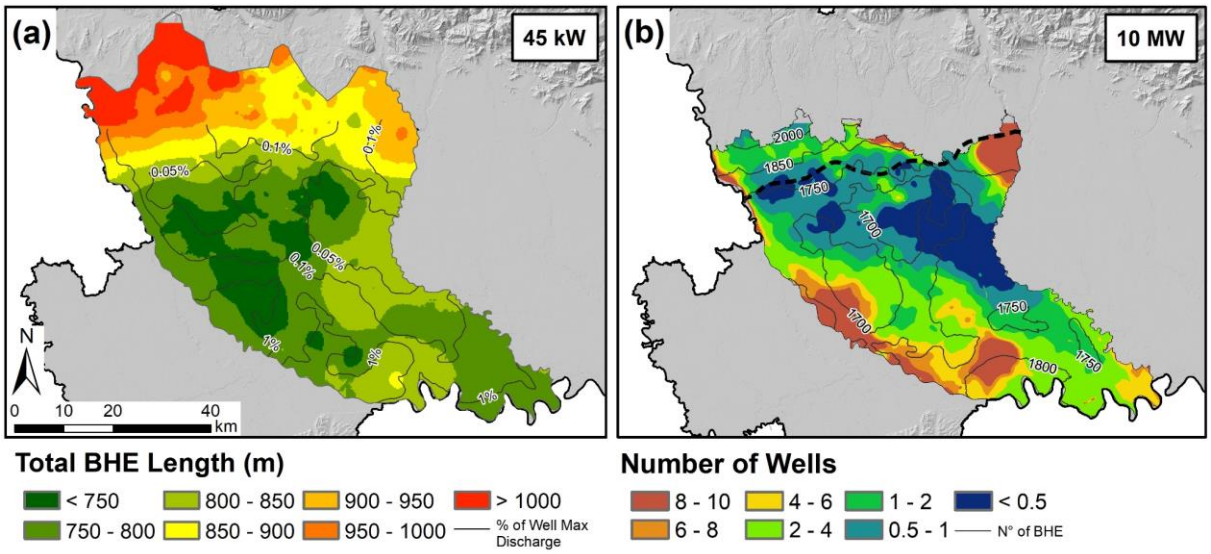


***Figure 6.9*** *–Maps showing the spatial distribution of (a) the length required by a GCHP system to fulfill a 45 kW thermal load and (b) the number of wells required to meet a 10 MW thermal load. The two areas in the figure differ in extent as explained in section 6.3.1.1.*

### 6.6.3. Thermal potential and city-scale heat demand

The study area covers one of the most densely populated regions in Italy and Europe and this is reflected by an intense thermal energy demand for heating and cooling purposes. A countercheck on the potential of the study area to host shallow low-enthalpy geothermal systems was made by comparing the calculated thermal potential with the actual thermal energy demand based on the thermal energy used in 2019 by conventional systems (e.g. gas/oil/coal burning systems, air-coupled heat pumps) in each municipality (Regione Lombardia, 2019b). The average actual thermal demand of each municipality was compared with the thermal potential of a 100-meters-length GCHP (**Figure 6.10a** and **b**) whereas the maximum actual thermal demand was compared with the thermal potential of GWHPs systems (**Figure 6.10c** and **d**).

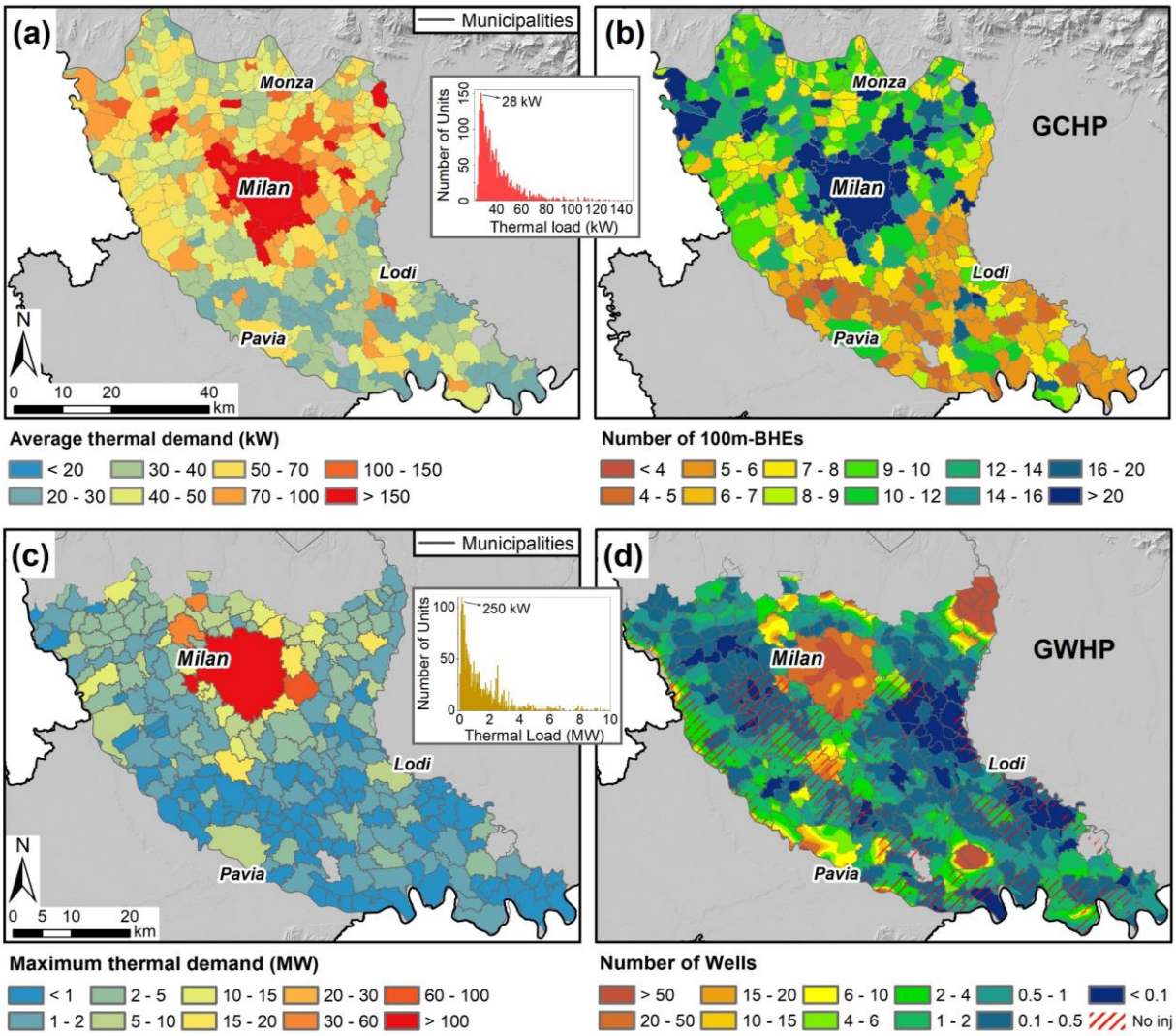


***Figure 6.10*** *– Maps showing the spatial distribution of (a) the average thermal demand based on the energy used in 2019 by conventional systems in each municipality, (b) the number of 100-meters-length GCHPs required to satisfy the average thermal demand, (c) the maximum thermal demand of each municipality and (d) the number of geothermal wells required to satisfy the maximum thermal demand.*

We can observe that the average thermal demand in the study area can almost everywhere be satisfied by a number of GCHPs between 4 and 20 (**Figure 6.10b**). This solution is attractive from an initial investment cost point of view and can be adopted in the whole study area without restrictions. The energy demand of big buildings or entire city districts (e.g. supplied by district-heating) is represented by the maximum thermal load and can be fulfilled by at most a group of 20 geothermal wells (**Figure 6.10d**). However, for a large number of municipalities in the study area (except for the Milan city) the maximum thermal demand could be fulfilled by one or two wells.

# 7. Characterization of the subsurface urban heat island and its sources in the Milan city area

This chapter is largely based on the following paper:

➔ Previati, A., & Crosta, G. B. (2021). Characterization of the subsurface urban heat island and its sources in the Milan city area, Italy. *Hydrogeology Journal*, 1-14. https://doi.org/10.1007/s10040-021-02387-z

## 7.1. Introduction

Urban areas are major contributors to local atmospheric and groundwater environment modifications (Oke, 1973) since human activities can affect the air and groundwater natural physical-chemical conditions. Among these, the groundwater thermal regime is one of the most emergent issues in urban areas due to the increasing awareness about the quality and the conservation of groundwater resources. Many recent studies showed the extent and the intensity of the SUHI effect in several cities worldwide (for a review, Bayer et al., 2019 and Zhu et al., 2011; Berlin, Cologne and Karlsruhe, Benz et al., 2016 and Menberg et al., 2013a; Basel, Epting and Huggenberger, 2013; Cardiff, Farr et al., 2017; Paris, Hemmerle et al., 2019; Munich, Frankfurt and Darmstadt, Menberg et al., 2013a; Tokyo, Seoul, Osaka and Bangkok, Taniguchi et al., 2007; Amsterdam, Visser et al., 2020). The UHI was documented in densely populated and highly developed cities as its formation is related to the modifications of the environment due to urbanization, such as land artificial covering/sealing with buildings, asphalt and surface infrastructures, and heat losses from anthropogenic sources. Such factors modify the solar radiation balance and the energy balance at the earth's surface, leading to the local warming of the air and the ground temperature. Moreover, the shallow subsurface hosts several kinds of geothermal systems for heating and cooling purposes which cause thermal disturbances. For the above mentioned city sites, the shallow mean annual groundwater temperature is 2 to 8 °C warmer than in suburban areas and, for some of them,

a warming trend was recognized due to global warming and urbanization effects. Benz et al. (2015) evaluated the thermal contribution of various anthropogenic heat sources for Cologne and Karlsruhe revealing the building basements and the elevated ground surface temperatures as the dominant heat sources on a citywide scale.

SUHIs were documented as an environmental issue since elevated temperatures can affect the groundwater quality in terms of chemical, physical and biological conditions (Blum et al., 2021) and living ecosystems (Brielmann et al., 2009). However, elevated groundwater temperatures may also represent an opportunity in areas with high energy demand since the thermal energy stored in the aquifers can be exploited by shallow geothermal systems (Arola and Korkka-Niemi, 2014; Bayer et al., 2019). This, besides recovering part of the energy released by human activities and stored in the subsurface, might control the size and the intensity of the SUHI in large cities (and the above-mentioned side effects). Thus, the analysis of the thermal regime is essential to a sustainable management of the subsurface thermal resource and to reach, by a cautious usage, a balance between the heat released by anthropogenic pollution and the heat extracted by geothermal installations. As an example, Zhu et al. (2011) estimated the thermal potential of SUHIs in several big cities due to elevated groundwater temperatures to be always higher than the total city heating demand.

The relevant studies about anthropogenic thermal pollution in the study area are focused only on the atmosphere and pointed out the correlation between the size and the intensity of the UHI and the degree of urbanization during the evolution of the Milan City (Bacci and Maugeri, 1992; Pichierri et al., 2012). In this context, a comprehensive analysis of the thermal status of the aquifers beneath the MCA is still lacking but is pivotal to a sustainable and efficient geothermal energy planning, considering the high density of subsurface infrastructures and the thermal demand of the city. In this study we present a detailed characterization of the subsurface thermal regime of Milan and evaluate the natural and anthropogenic controls on groundwater temperatures within the urban area, which are also fundamental to assess the aquifer thermal potential and for the purpose of de-risking the development of shallow geothermal energy (Farr et al., 2017). The extent of the SUHI in the groundwater is outlined by analyzing high-resolution groundwater temperature data, collected by the authors since 2016, through spatio-temporal statistical techniques. The correlation between the

groundwater thermal regime and various natural (e.g., depth to the water table, air temperature) and anthropogenic (e.g., percentage of area covered by buildings, sealed surfaces) indicators reveals a complex thermal framework, in which local anthropogenic thermal contribution significantly affects the overall thermal regime by shaping the extent and the intensity of the SUHI.

## 7.2. Study area

The study area (MCA in **Figure 5.1**) is located in the northern portion of the Po plain (Northern Italy) and covers an area of 181.7 $km^2$. In the MCA, the development of human infrastructures is extremely intensive both at the ground surface and in the subsurface reaching 35% and 50% of land covered by buildings and asphalt, respectively, in a 3km-radius circle centered on the city center (17% and 37% in the municipality). This area hosts six underground metro lines (for a total length of 106 km), 414 deep water supply wells, 544 shallow geothermal wells, 311 ground-source heat pumps, and many deep foundations. In this context, the shallow aquifers are exploited for drinking, thermal energy production, and industrial purposes leading to a complex framework of positive and negative thermal sources.

## 7.3. Materials and Methods

### 7.3.1. Air temperature

Air temperature time series for the period 2016-2020 were obtained from the meteorological stations database managed by the regional environmental monitoring agency (ARPA Lombardia, 2021). Seven monitoring stations located in the study area were used to obtain mean annual temperature maps. Data from two locations, in the suburban area to the north (A1) and in the city center (A2), respectively, are presented in **Figure 7.1** (see **Figure 7.2** for their location). The mean annual air temperature recorded in the city center is 16.0 °C whereas outside the city is 14.7 °C. Direct air temperature measurements of the last 4 years well agree with the UHI intensity observed through remote sensing techniques by Pichierri et al. (2012) and show an average annual heat island of 1.8 °C with positive peaks during the cold season of about 5°C (**Figure 7.1b**).

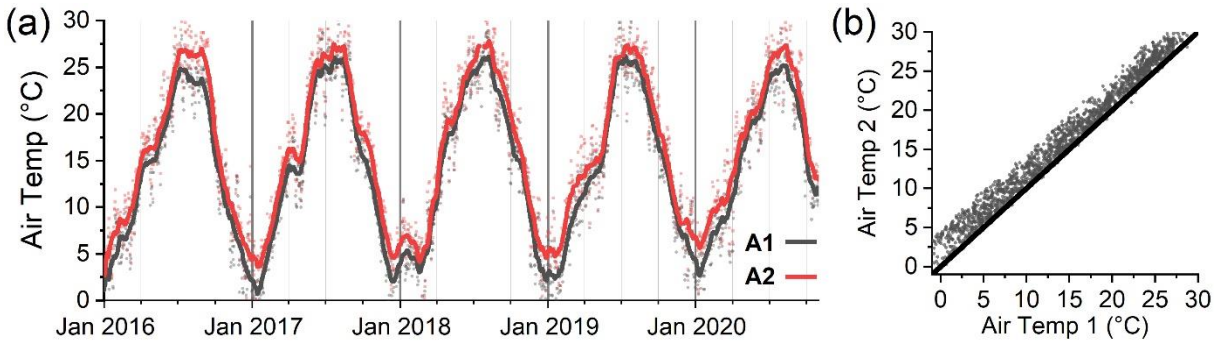


***Figure 7.1*** *– (a) Mean daily air temperature recorded by two meteorological stations in the Milan City area (A1 – Outside the City, A2 – City center, see* ***Figure 7.2*** *for their location); (b) correlation between the temperature in the City center and outside the City.*

### 7.3.2. Groundwater temperature

The shallow groundwater temperature has been monitored by the authors since 2016 with submersed automatic sensors at specific depth and with periodic temperature-depth manual logging. Open pipe piezometers were selected according to their location and depth, the degree of structural protection (i.e., within public parks and schools), and the integrity of the borehole structure. In total 61 open pipe piezometers (**Figure 7.2**) have been monitored and, within 15 of them ("H-R Wells" in **Figure 7.2a**), submersible sensors were installed at specific depth to continuously monitor the pressure and the groundwater temperature. Groundwater vertical temperature profiles were acquired regularly in the 15 instrumented piezometers since 2016 and, from 2019, in other 46 piezometers located within and nearby the Milan municipality (**Figure 7.2b**). **Figure 7.2** shows the spatial distribution of the groundwater monitoring points colored by the mean annual shallow groundwater temperature and sized by the annual groundwater temperature standard deviation.

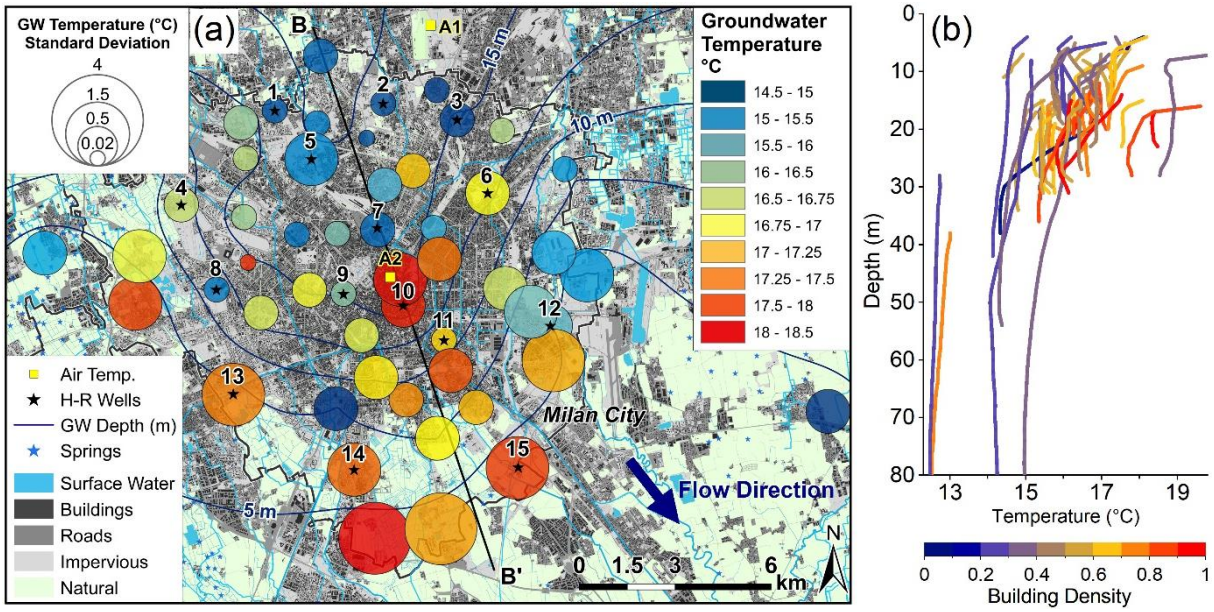


***Figure 7.2*** *– (a) Map of the study area showing the location of the monitored piezometers (colored by the mean annual groundwater temperature and sized by the groundwater temperature standard deviation), the meteorological stations (A1, A2), the land use, the depth of the groundwater and the main groundwater flow direction. The 15 instrumented piezometers (H-R wells) are highlighted with a black star icon and numbered. (b) Mean annual temperature-depth profiles obtained by monthly manual measurements (lines are colored by the percentage of area covered by buildings inside a 500m-radius-circle centered on each monitoring point).*

### *7.3.2.1. Temperature-depth profiles*

Groundwater temperature vs depth profiles are a comprehensive tool to examine the thermal regime in space (both horizontally and vertically) and in time. They are often used to estimate subsurface water flow patterns and heat fluxes caused not only by conduction but also by advection processes (Kurylyk et al., 2019; Taniguchi et al., 1999; Zhu et al., 2015). The temperature-depth profiles presented in this study were recorded approximately every 3 months from June 2019 to September 2020 at 61 locations (5 acquisitions each). Moreover, at the 15 instrumented piezometers temperature-depth profiles have been collected since 2016, and 18 temperature-depth profiles are available for each location. The mean borehole depth from the ground surface is about 25 m (with a max of 100 m) covering mainly the shallow part of the phreatic aquifer (P) (average water column of about 15 m with a max of 90 m). The temperature was recorded (accuracy of ±0.1 °C) by moving a submersible multi-meter probe (In-Situ® Aqua TROLL 600) from the bottom of the piezometer to the water table with a 1 m vertical spacing. The temperature-depth profiles are presented in **Figure 7.2b**

colored by the degree of urbanization (the percentage of area covered by buildings inside a 500m-radius-circle centered on each monitoring point). Map in **Figure 7.2a** shows the mean annual groundwater temperature of the shallowest portion of the temperature-depth profiles (i.e., first 2 m) together with the temperature standard deviation during the period 2019-2020.

#### *7.3.2.2. Groundwater head and temperature time series*

Temperature-depth profiles cover a significant portion of the study area, but their temporal resolution is very low due to the time required (about one week) to complete each measurement campaign. Groundwater levels have been recorded by the local water supply agency (MM spa) since early '70 at many locations in the study area but, unfortunately, direct measurements of the groundwater temperature before 2016 were not available and, for this reason, the hydraulic head and groundwater temperature fluctuations were analyzed only for the period covered by continuous measurements. The selected piezometers ("H-R Wells" in **Figure 7.2**) are equipped with submersible transducers (*Van-Essen Instruments*, Micro-Diver®) placed at constant depth by means of a stainless-steel cable of known length ($L_{cable}$) and autonomously record the pressure (±0.1 cmH2O) of the above water column (plus the atmospheric pressure) and the temperature (±0.01 °C) every 15 minutes. To compare temperature data from different piezometers, the monitoring devices were placed approximately at the same depth below the water table (between 3 and 5 m). Pressure data recorded by each sensor were corrected by the atmospheric pressure and converted into piezometric head (masl), knowing the ground surface elevation at each measuring location. The piezometric head is obtained through the following equation:

$$H(t) = Z_{sens} + P_{tot}(t) - P_{air}(t) \qquad \textit{(Eq. 7.1)}$$

where $H(t)$ is the piezometric head (masl) at time $t$, $Z_{sens}$ the elevation (masl) of the sensor obtained by subtracting $L_{cable}$ to the ground surface elevation, $P_{tot}(t)$ the pressure measured by the sensor at time $t$ and $P_{air}(t)$ the atmospheric pressure at time $t$.

**Figure 7.3** shows the hydraulic head and temperature time series recorded at three piezometers located north of the city (#1), in the city center (#10), and south of the city (#15), respectively (see **Figure 7.2a** for the location). The configuration of each piezometer is

summarized in **Figure 7.3a**. Note that the depth of the groundwater changes substantially from north to south as outlined by contour lines in **Figure 7.2a**.

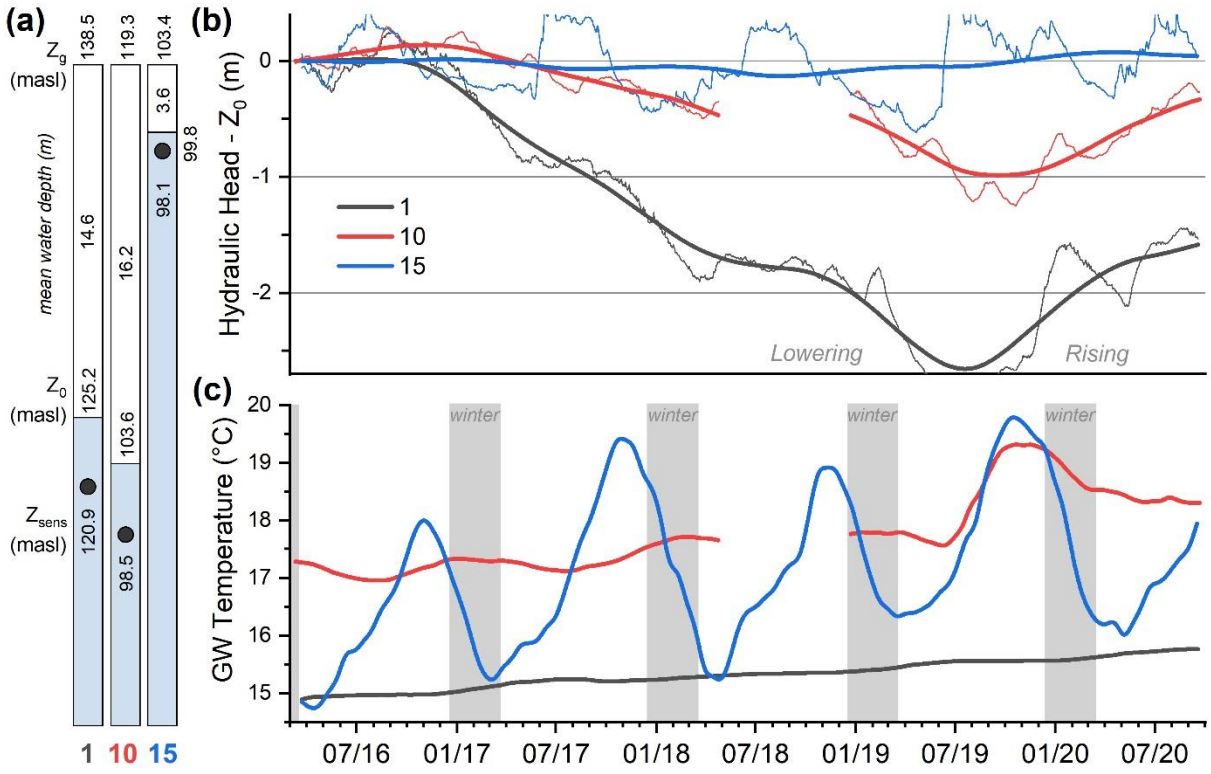


***Figure 7.3*** *– Time series at three selected locations (#1, 10 and 15 in* ***Figure 7.2a****) for the period 2016-2020: (a) ground elevation ($Z_g$), water table depth, hydraulic head as on march 2016 ($Z_0$) and sensor (black dots) elevation ($Z_{sens}$), (b) hydraulic head time series and one-year moving average, referred to $Z_0$ (m asl) reported in (a), and (c) groundwater temperature time series. Grey bars indicate the winter season.*

The unsaturated layer between the ground surface and the water table can be considered a thermal resistant material able to dampen the temperature signal coming from the surface and to shift it in time. Thus, the downward heat propagation depends essentially on the thickness of the unsaturated soil and the thermal properties of the soil but, in a densely urbanized environment, the input signal from the surface can be altered by site-specific anthropogenic heat sources located at the surface (e.g., heat losses from building foundations, land use and land cover materials) or in the subsurface (e.g., heat losses from underground structures, infrastructures or geothermal installations and water leakage from sewage and district heating systems) (Attard et al., 2016; Benz et al., 2015; Epting et al., 2017b).

Cross-correlation is used to quantify the similarity of two time series as a function of the displacement of one relative to the other. The cross-correlation (Cryer and Chan, 2008) is a function of time shift ($t$) that expresses the covariance between the output signal (f) (i.e., the

groundwater temperature) and the input signal (g) (i.e., surface air temperature) shifted by a time ($t$), divided by the square root of the product of the variance of the signals:

$$CCF(t) = \frac{Cov\,(f(0), g(0+t))}{\sqrt{(Var(f) * Var(g)}} \qquad \textit{(Eq. 7.2)}$$

To assess the connection between the surface thermal regime and the groundwater thermal regime a cross-correlation analysis between the air temperature and the groundwater temperature time series recorded at the 15 instrumented piezometers was carried out.

### 7.3.3. Human-made structures and infrastructures

Urban areas are characterized by a dense texture of structures and infrastructures that modify the water infiltration and groundwater flow processes, the heat transfer between the surface and the subsurface, and eventually the heat transport in the aquifer. In this context, the groundwater thermal regime is affected by several natural and human-activities-related factors already identified by many authors (Benz et al., 2015; Epting and Huggenberger, 2013; Ferguson and Woodbury, 2004; Menberg et al., 2013b; Taylor and Stefan, 2009), such as:

i) the thickness of the unsaturated zone that dampens the temperature fluctuations coming from the surface,
ii) the groundwater flow velocity that drives the heat transport in advective-dominated aquifers,
iii) the presence of surface water bodies and the degree of interaction with the groundwater,
iv) the percentage of buildings, surface infrastructures and sealed/cemented ground,
v) the presence of underground structures/infrastructures (e.g., tunnels) or deep foundations,
vi) the use of low-enthalpy geothermal wells.

In densely populated urban areas the anthropogenic component of the subsurface thermal budget is non-negligible or even prevailing (Epting and Huggenberger, 2013). Thus, to characterize the influence of non-natural thermal contributors on the groundwater thermal regime information on surface and subsurface natural and anthropogenic settings were collected and homogenized as described in section 5.7 (**Figure 5.11**).

## 7.4. Results and discussion

In many big cities worldwide, the shallow mean annual groundwater temperature at urbanized locations was found from 2 to 8 °C warmer than less urbanized suburban areas (Arola and Korkka-Niemi, 2014; Epting and Huggenberger, 2013; Farr et al., 2017; Menberg et al., 2013a; Taniguchi et al., 2007; Visser et al., 2020; Zhu et al., 2011). According to the authors, this is due to anthropogenic heat losses in the subsurface (e.g. from tunnels, foundations, GSHP) and to indirect heat accumulation of urban surface structures and infrastructures (e.g. due to solar radiation on concrete structures). It has been demonstrated that the development of the SUHI is related to anthropogenic modifications of the land use and the percentage of area covered by buildings (Benz et al., 2018, 2015). On the other hand, in order to quantify the amount of heat released in the aquifer, a robust knowledge on the hydrogeological setting of the area and adjacent regions is essential (Bidarmaghz et al., 2019). In this work, the groundwater level and the shallow groundwater temperature fluctuations observed in the MCA were analyzed by means of spatio-temporal statistical and correlation techniques, revealing a SUHI effect up to 3°C intense. This value falls within the above cited range for the observed shallow groundwater SUHI in large cities.

North-south section B-B' across the Milan City (**Figure 7.4**) summarizes the shallow groundwater thermal regime along the main groundwater flow direction highlighting the extent and the intensity of the SUHI effect in the groundwater and the location and intensity of the most relevant heat sources.

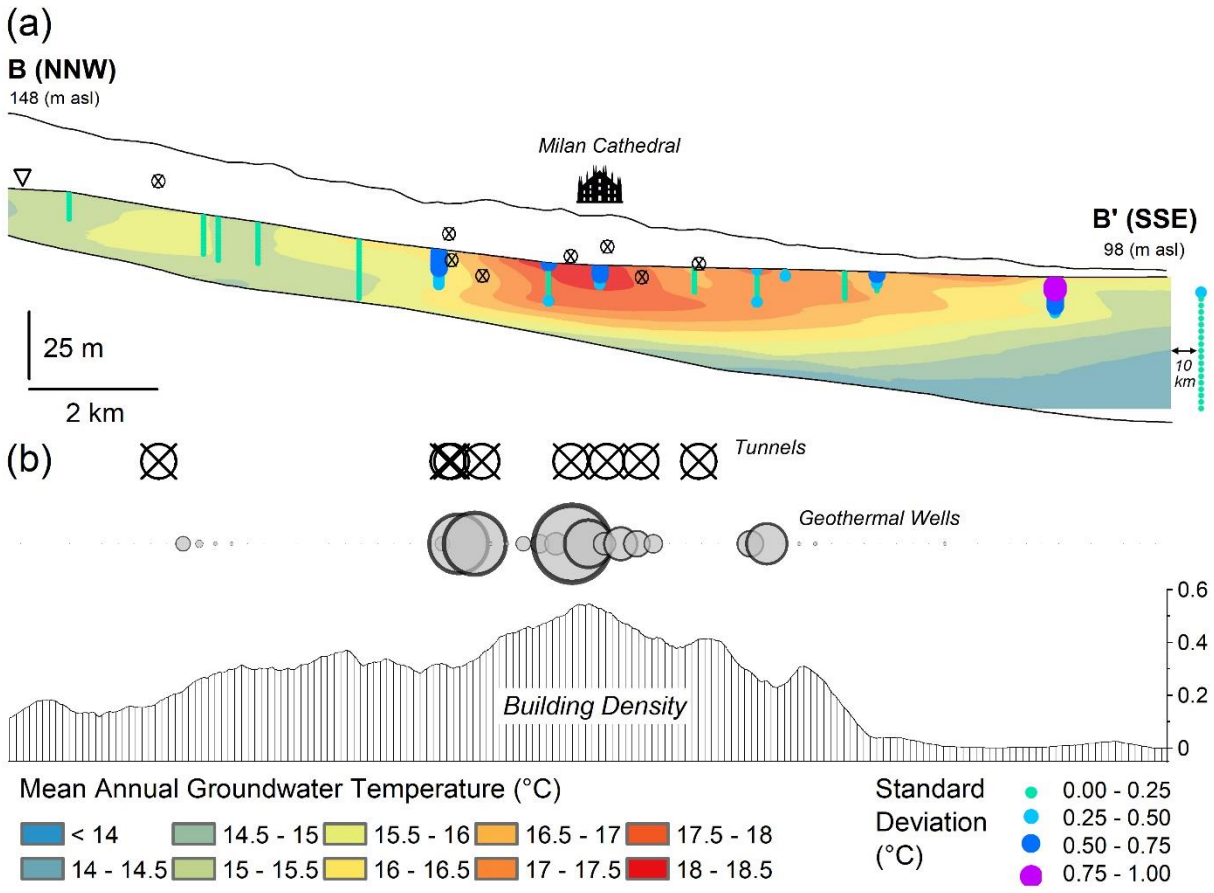


***Figure 7.4*** *– North-south cross-section (see* ***Figure 7.2a*** *for its location) showing (a) the groundwater depth and the distribution of the mean annual groundwater temperature interpolated using data from temperature-depth profiles of 2020 within 500 m from both sides of the section line, and the temperature annual standard deviation; (b) the tunnels crossed by the section, the number of geothermal wells within 250 m from both sides of the section (biggest circle = 20 wells) and the building density.*

### 7.4.1. Spatial analysis

Groundwater temperature-depth profiles in the study area show a significant variation of the thermal regime. To untangle this variability, the groundwater temperature-depth profiles were interpolated over time. This allowed to identify 4 main groups according to the shape of the profiles and the temperature fluctuations **Figure 7.5**: (i) undisturbed (i.e., the mean annual GW temperature is equal to the mean annual air temperature) profiles with shallow groundwater (< 10 m), (ii) undisturbed profiles with deep groundwater (> 10 m), (iii) disturbed (i.e., the mean annual GW temperature is more than 1°C higher than the mean annual air temperature) profiles in highly urbanized areas and (iv) profiles close to shallow water bodies.

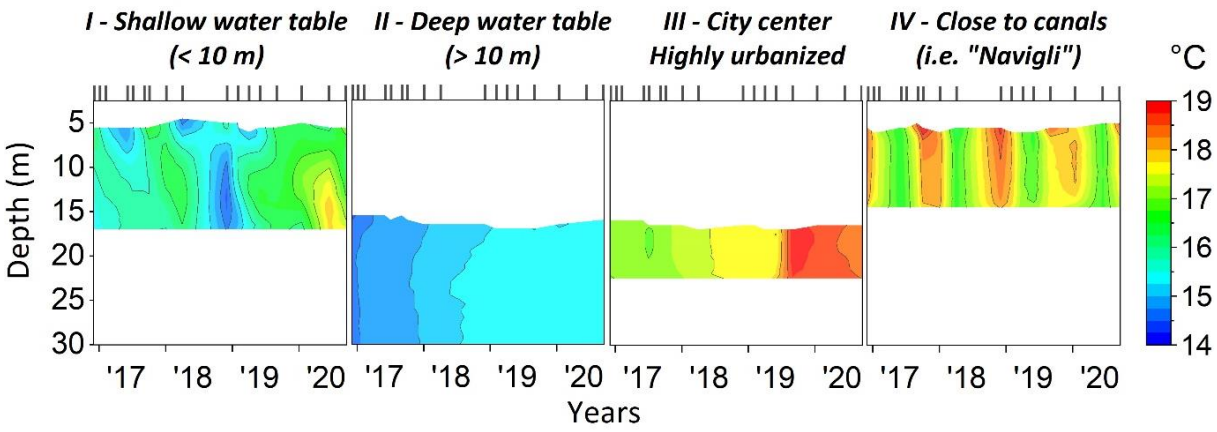


***Figure 7.5*** *– Groundwater temperature-depth profiles interpolated over time (2016 - 2020). Dates of sampling are highlighted with ticks at the top of each box. The location of the selected profiles is shown in* ***Figure 7.2a*** *with the following codes (from left to right): 12, 1, 10 and 13.*

#### *7.4.1.1. Spatial correlation*

To assess the impact of natural and anthropogenic variables on the groundwater thermal regime the mean annual groundwater temperature (GW Temp) and the temperature standard deviation (St Dev) from shallow temperature data (between 0 and -2 m below the water table), were compared to 12 site-specific parameters. These twelve parameters include, namely:

(i) the mean annual groundwater depth (GW Depth) obtained from manual measurements,
(ii) the mean annual air temperature (Air Temp) obtained from meteorological stations,
(iii) the percentage of area covered by buildings,
(iv) the percentage of area covered by asphalt,
(v) the percentage of area covered by railway ballast,
(vi) the percentage of area covered by green areas,
(vii) the upstream distance to underground tunnels along the main flow direction,
(viii) the distance to the nearest river or canal,
(ix) the number of GSHPs,
(x) the total length of district heating pipelines,
(xi) the equivalent horizontal hydraulic conductivity of the phreatic aquifer (K),
(xii) the local hydraulic gradient.

The values for (iii), (iv), (v), (vi), (ix) and (x) were computed over a 500m-radius-circle centered on each monitoring point. The values for (xi) and (xii) were obtained from (De Caro et al., 2020b). The correlation between each combination of GW Temp and St Dev with the 12 selected variables was evaluated by means of the Pearson's correlation coefficient (R). **Figure 7.6** shows the correlation of each pair, where the Pearson's R is specified below each plot and the significance (i.e. *p*-value) is given in brackets (emphasized in bold if the *p*-value is lower

than 0.05). The Pearson's R is also represented by the color and the elongation of the ellipses, and a thick red shows the linear best fit. Note that the slope of the linear fit does not necessarily represent the correlation, and the scale of the variables varies significantly.

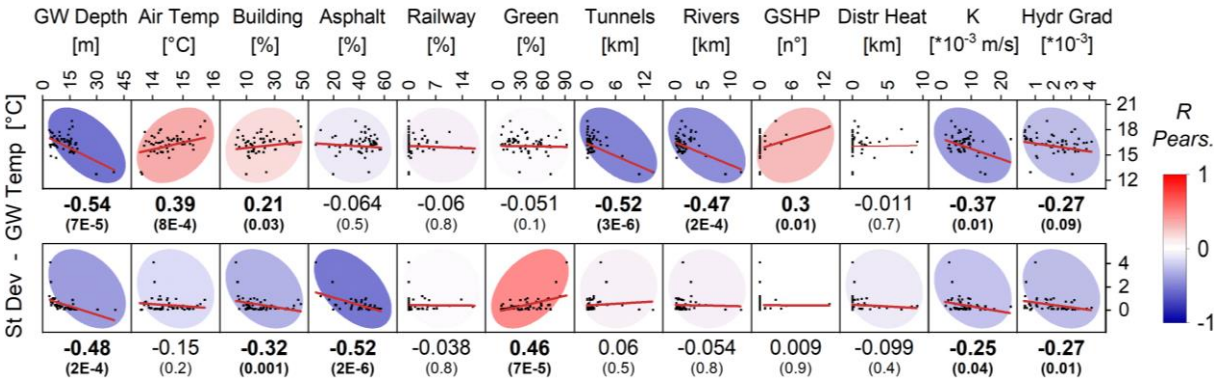


***Figure 7.6*** *– Correlation between the mean annual groundwater temperature (GW Temp), the temperature standard deviation (St Dev) and the 12 selected variables. The red line shows the linear best fit, the ellipsis color intensity and their elongation represent the Pearson's R, which is also reported below each plot and emphasized in bold if the p-value (between brackets) is lower than 0.05.*

We observe that the mean annual groundwater temperature is positively correlated to the air temperature and the percentage of buildings, and negatively to the groundwater depth, the distance from tunnels, and canals or rivers. These last ones are inversely correlated to the degree of urbanization as the canals crossing the city are typically culverted and sealed. A lower, but still significant ($p < 0.05$), inverse correlation is observed between the mean annual groundwater temperature, the hydraulic conductivity and the hydraulic gradient. The groundwater temperature standard deviation is inversely correlated to the groundwater depth and the percentage of area covered by asphalt and, directly, to the percentage of green unsealed areas. This suggests that, among natural variables, the thickness of the unsaturated zone dampens the amplitude of seasonal temperature fluctuations (Kurylyk et al., 2015) and the groundwater flow velocity controls the heat accumulation in the groundwater (Ferguson and Woodbury, 2004; Zhu et al., 2015). In addition, human-related activities appear to strongly affect the shallow groundwater thermal regime. Among these, the percentage of built area and the distance from tunnels are the most correlated with the mean annual groundwater temperature. This is highlighted in **Figure 7.7** where the mean annual groundwater temperature and the standard deviation are summarized by means of a

correlation plot against the groundwater depth, the building density and the upstream distance to tunnels along the main groundwater flow direction. We observe (**Figure 7.7a**) that with shallow water table and low building density the standard deviation is significantly higher while the mean GW temperature is variable (but in general higher with respect to deeper locations) as the groundwater is more sensitive to thermal inputs from the surface. At deeper groundwater locations, the standard deviation is lower and the mean GW temperature is related to the building density and, thus, depends on the degree of urbanization. Due to the complexity of superimposed thermal contributors some outliers in **Figure 7.7a** can be related to site-specific conditions, e.g. the proximity to specific heat/cool sources such as canals, geothermal reinjection wells and tunnels. As demonstrated by Attard et al. (2016), underground structures such as tunnels can generate a very strong heat flow, but their thermal perturbation is appreciable only at local scale (approximately within 200 m from the heat source, depending on the volume of the structure, the thermal properties and the groundwater flow velocity). **Figure 7.7b** shows the mean annual groundwater temperature and the standard deviation at locations within 800 m downstream underground tunnels. We can observe that many points located at a distance smaller than 200 m from tunnels show mean annual temperatures higher than 18 °C. For those locations we can assume a strong thermal perturbation but, in this area, it is difficult to disentangle the perturbation caused only by tunnels as they are located within the city center where the mean annual groundwater temperature is mostly around 18 °C and multiple heat sources act together to obtain a complex thermal regime.

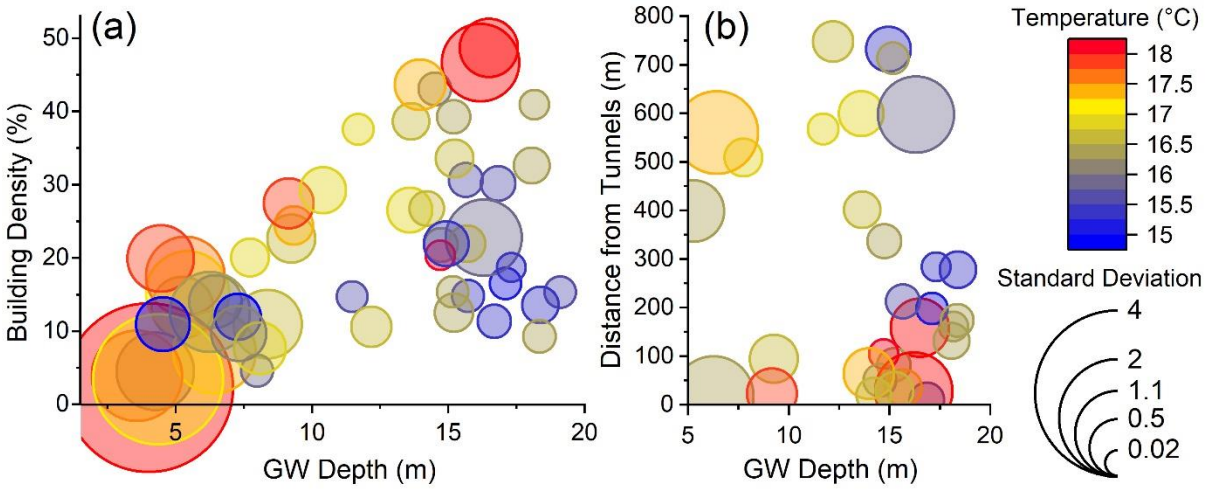


***Figure 7.7*** *– Correlation plots showing the relation between the mean annual groundwater temperature (color scale), the temperature standard deviation (bubble size), the groundwater depth (x-axes) and, (a) the building density and (b) the distance from tunnels upstream the main groundwater flow direction.*

#### *7.4.1.2. Principal component analysis (PCA)*

The PCA is a multi-variate data exploration technique often used to explain the variance of a dataset (i.e. how do variables influence the data structure?) and reduce the dimensionality (i.e. are there groups of correlated variables?) (Jolliffe, 1986; Krzanowski, 2000). The PCA is based on the transformation of the original data matrix, $X$ ($m$ x $n$) (where rows represent the observations and columns the variables affecting the system), into a new matrix $Y$, having the same size and rotated coordinates so to reach the maximum data dispersion along the "new" axis, known as principal components (PC). In other words, the PCA transforms the variables into "new" variables, which are linear combinations of the original variable. The transformation matrix, $W$, is obtained by the diagonalization of the correlation (or covariance) matrix ($n$ x $n$) and is composed in two matrices: the eigenvalues and the eigenvectors (or loadings) matrices ($n$ x $n$). The eigenvalues matrix is a diagonal matrix where each value represents the variance of the corresponding principal component and is used to calculate the part of information explained by each component. The eigenvectors matrix stores the coefficients of the linear combination of variables that define the principal components. Finally, the scores matrix contains the coordinates of the samples (observations) in the PC space. A biplot representation of the observations in the PC space (score plot) superimposed to the eigenvectors of the input variables (loading plot), is useful to summarize the variables

(i.e. eigenvectors with similar orientations) and find patterns and clusters in the observations (i.e. by analyzing the distribution in the score plot).

In this analysis, variables related to the subsurface thermal regime were arranged in a 46 (monitoring locations with at least 4 profiles in one year) x 13 (variables identified in section 7.4.1.1, plus the annual standard deviation of the groundwater level) matrix and a PCA was performed through the correlation matrix by means of the OriginPro® toolbox. The explained variance by the first three PCs is 59.8% (31.8, 15.6, 12.4% each). Higher order PCs were not considered as their contribution to the variance of the dataset is not relevant compared to the first three. Groundwater mean annual temperature and annual standard deviation at each observation point were implemented in the biplots by dot color and size to interpret the response of the system in the "new" PC space (**Figure 7.8a** and **b**). A clear gradation in the mean annual groundwater temperature (dot color) is observed along the PC1 and PC2 axes, and a visible pattern of the temperature standard deviation (dot size) along both PC1 and PC3 axes. **Figure 7.8c** shows the loading coefficient for each variable in each PC space: PC1 represents the variance of the dataset due to urbanization-related variables (e.g. buildings, asphalt, air temperature, GSHP, tunnels); PC2 represents the variance related to hydrogeological settings such as the hydraulic gradient and depth of the water table; PC3 represents mostly the effect of rivers (e.g. distance to rivers, standard deviation of the water table depth which is higher close to rivers) but is mixed with the effects of point sources such as GSHP. As described in section 7.4.1.1, the mean annual groundwater temperature and the standard deviation are affected by a combination of human-related factors and hydrological conditions (e.g. depth of the water table) which is impossible to disentangle. A clearer perspective is given by plots (a) and (b) in **Figure 7.8**, where the mean temperature and the standard deviation are arranged in specific patterns, governed by groups of eigenvectors.

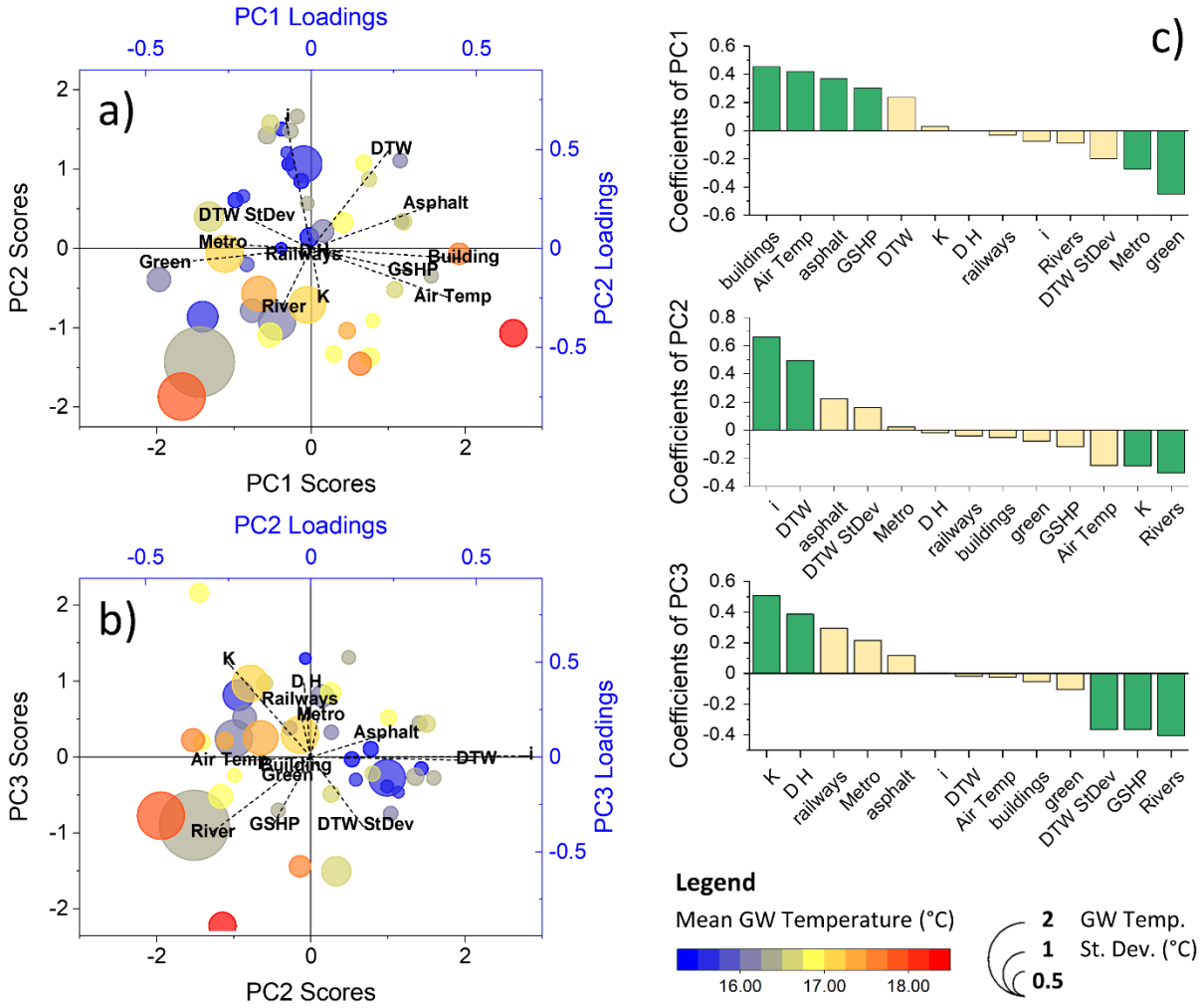


***Figure 7.8*** *– (a), (b) biplots showing scores and loadings of PC1 vs PC2 and PC2 vs PC3, respectively. (c) Loadings of specific variables in the PC1, PC2 and PC3 spaces (variables in green contribute most to variance on each PC).*

### *7.4.1.3. Vertical heat flow*

Temperature-depth profiles were used to estimate the vertical heat flow in the shallow part of the aquifer by computing the thermal gradient between the groundwater temperature at the water table and 2 m below. With this assumption (which neglects the effects of horizontal advective flow) the vertical thermal gradient was considered an indicator of the thermal perturbation from above. The shallow thermal gradient was computed at 61 different locations for each of the five measurement campaigns. **Figure 7.9** shows the statistical distribution of the thermal gradient for 5 groundwater depth intervals and 3 building density classes. Positive values indicate heat flow directed from the ground surface to the aquifer and, vice versa, negative values indicate heat flow towards the surface. Shallow groundwater

classes (from 0 to 10 m) show both positive and negative thermal gradient according to the season, while the thermal gradient of deep groundwater classes (more than 10 m) is slightly positive for all the seasons (i.e. there is a constant heat flow directed to the aquifer). Similarly, the thermal gradient is more sensitive to seasonality where the building density is lower and it is almost constant, with positive values, for high building-density classes. From the analysis of vertical profiles, we can infer that groundwater is warming in almost the entire study area. Seasonal fluctuations are more pronounced where the groundwater is shallow and where the urban density is low. At high urban density locations, we observe positive heat flow directed towards the aquifer due to heat losses from building basements/foundations and the heat accumulation in the shallow subsurface is reflected by a significant groundwater warming during all the seasons.

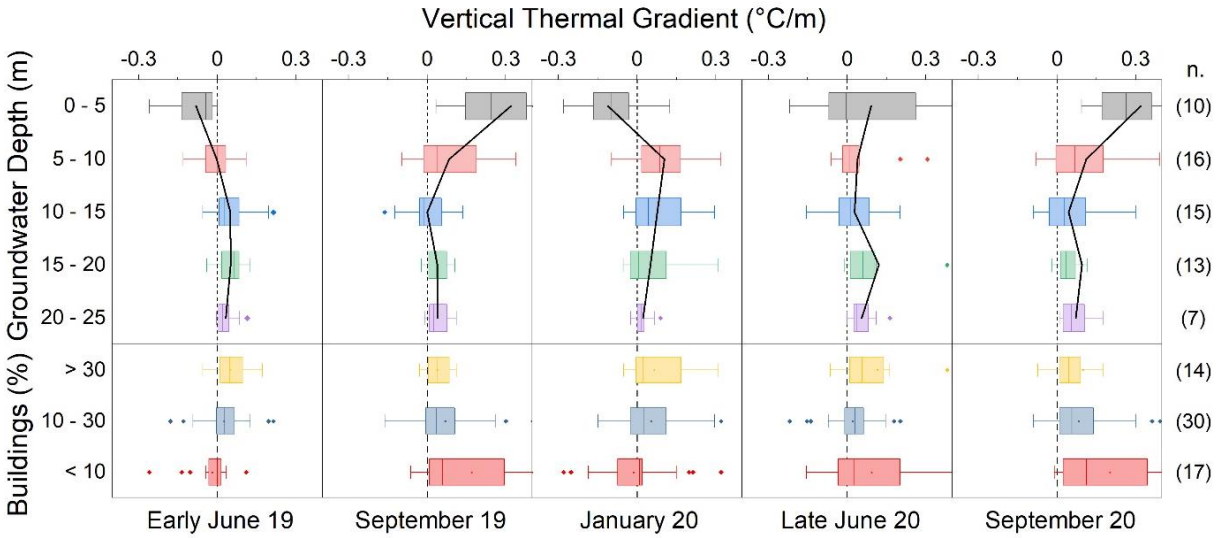


***Figure 7.9*** *– Vertical thermal gradient computed as the difference between the groundwater temperature at the water table and 2 m below, classified by the groundwater depth and building density (on the right the number of samples in each class). Positive values indicate heat flow directed from the ground surface to the aquifer and, vice versa, negative values indicate flow towards the surface.*

## 7.4.2. Temporal Analysis

### *7.4.2.1. Cross-correlation*

High-resolution groundwater head and temperature time series available from 2016 at specific depth were used to estimate the surface/groundwater interactions by means of a cross-correlation analysis between the air and groundwater temperature time series (**Figure**

**7.10**). As an example, **Figure 7.10a** shows the air and the groundwater temperature time-series at location #8 (**Figure 7.11**). The cross-correlation function obtained for each of the 15 instrumented OW is shown in **Figure 7.10b**. At each location, we derived the time shift, also referred to as Lag (days), to which corresponds the best correlation between the signals (positive peak) and the value of the cross-correlation function for that specific time shift *t* (referred to as the Cross-Correlation Coefficient: CCC).

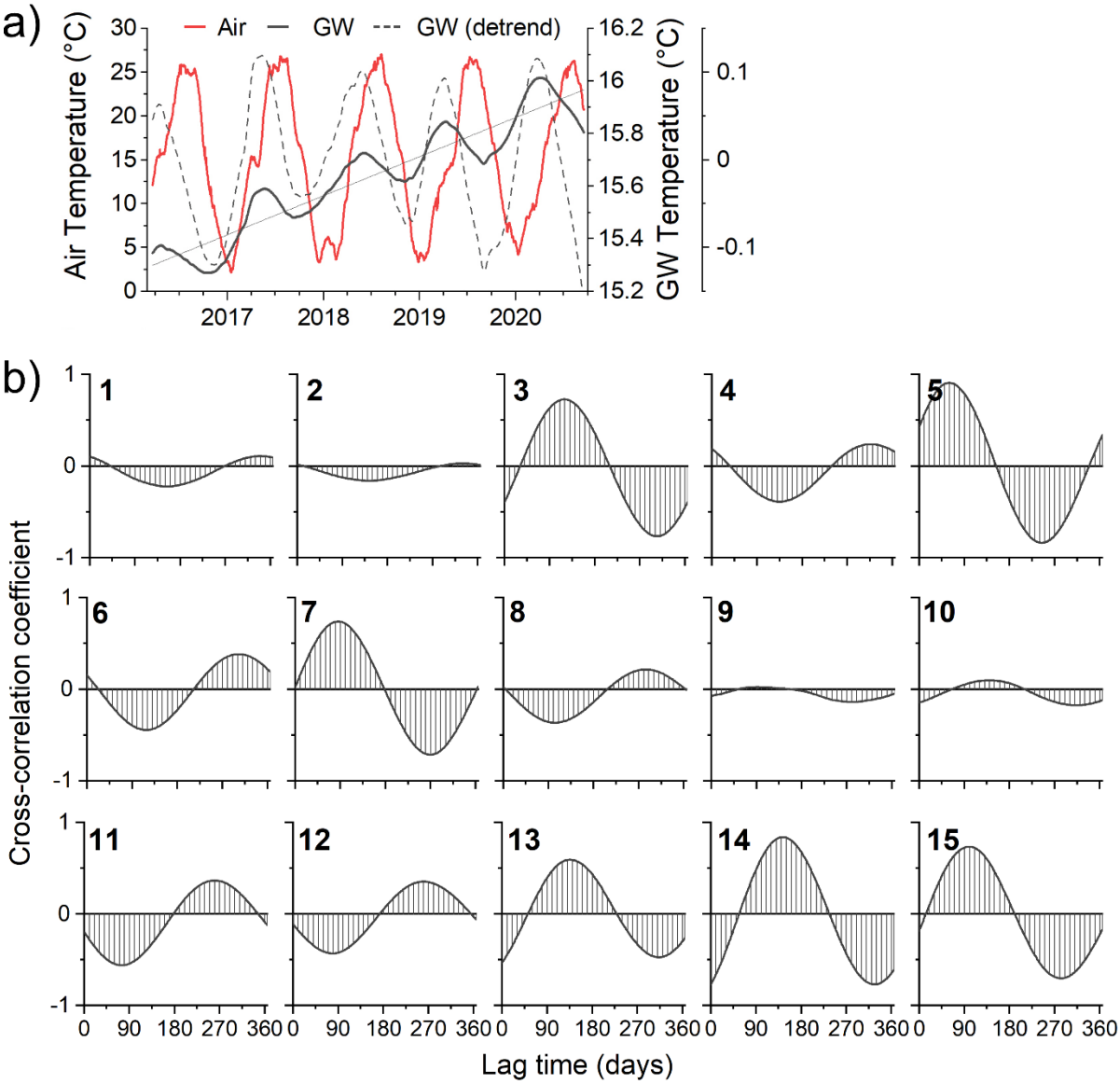


***Figure 7.10*** *– Cross-correlation analysis: (a) air (red) and groundwater (black) temperature time series recorded at well #8, dashed line represents the difference between the groundwater temperature and the linear trend (thin line). (b) Cross-correlation functions derived from the 15 instrumented OW. At well #8, best correlation is observed with a lag of 285 days.*

**Figure 7.11a** shows the spatial distribution of the calculated Lag and CCC, where the first indicates the delay between the signals and the second the similarity between the signals.

Then, similarly as described in section 7.4.1.1, Lag and CCC were compared to the groundwater depth, the groundwater flow velocity, and variables related to urban density by means of a correlation analysis (**Figure 7.11b**). In such a complex environment many factors contribute to affect the groundwater temperature time series by shifting and dampening the surface source signal. For this reason, the significance of the correlations between Lag and CCC with each parameter is weak (not shown, *p*-value > 0.05), but the correlation coefficient for some factor is higher that is worth discussing.

According to the theoretical hypothesis (Ferguson and Woodbury, 2004; Kurylyk et al., 2015; Zhu et al., 2015), the depth of the groundwater table and the groundwater flow velocity play a role in lowering the CCC (i.e. by dampening the temperature fluctuations) and shifting the groundwater temperature signal in time. Urbanization also plays a significant role, leading to a decrease in correlation with the increase of the building density (small dots in **Figure 7.11a**). Moreover, the percentage of green areas is inversely correlated to the lag times as progressive surface land covering with asphalt/concrete dampens the amplitude of groundwater temperature fluctuations. Some anomalies with respect to the generally observed trend (governed by groundwater depth and urban density) were observed at specific locations (#3, 5 and 7), where a very high correlation coefficient (> 0.6) and small lag times (< 90 days) were observed despite deep groundwater (> 15 m) and relatively dense urbanized conditions (building density > 30 %). To untangle this unexpected regime, the variables reported in **Figure 7.11b** were analyzed revealing a strong effect of the percentage of area covered by railway ballast (at locations #3, 5 and 7 the highest percentage of railway was observed). A further analysis is needed as the railway ballast seems to improve the thermal link between atmosphere and groundwater, possibly by favoring both rainfall infiltration and air circulation. Moreover, at well #5 some very close (<10 m) excavation works (open pit 20 x 20 m wide and 3-5 m deep) may have further influenced the natural water infiltration and heat transport processes.

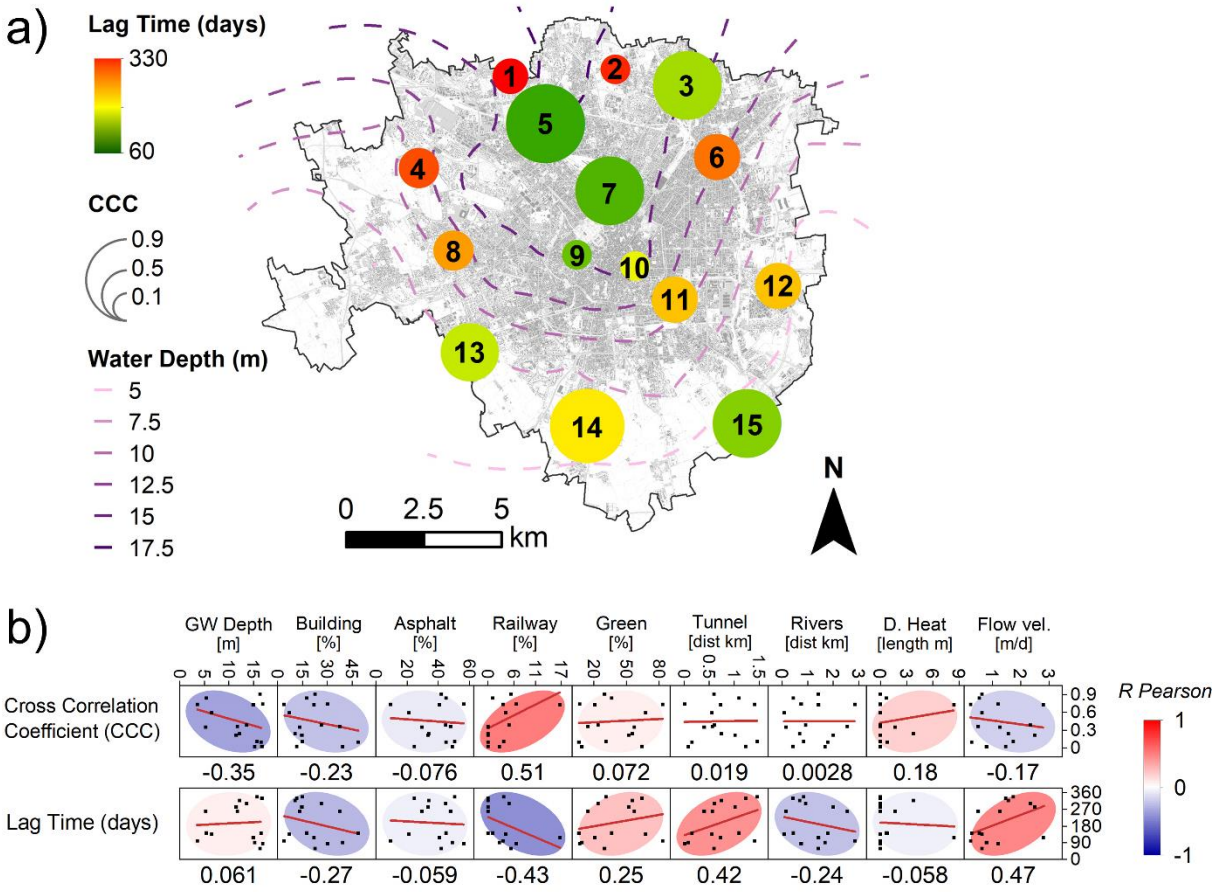


***Figure 7.11*** *– (a) Map showing the spatial distribution of the lag times and the cross-correlation coefficients (CCC) for the 15 high-resolution OW in the study area. (b) Correlation between lag times, CCC, hydrogeological settings (GW depth, Rivers, Flow velocity) and variables related to urbanization (% of Buildings, Asphalt, Railway and Green areas, Tunnels and District heating). The Pearson's R is reported below each plot.*

### *7.4.2.2. Trend analysis*

**Figure 7.12a** and **b** show the hydraulic head and temperature fluctuations with respect to the hydraulic head of March 2016 and to the mean annual temperature of 2016. During the monitored years, a general groundwater lowering was observed from 2016 to 2019 followed by a rising after 2019 (**Figure 7.12a**). The analysis of groundwater temperatures time series revealed a comprehensive warming trend at almost all the monitored locations (**Figure 7.12b**). To assess the temperature trend for the period 2016-2020 the groundwater temperature time series were averaged by means of a one-year moving window. Then, to compare the multi-annual temperature variation, each yearly-averaged time series was fitted with a linear regression model to obtain the temperature change rate ranging from ~0 to ~0.5 °C/year in

the city center (**Figure 7.12c**). The yearly trend of the air temperature was calculated accordingly showing no significant variation for the period analyzed.

Similarly, the groundwater fluctuation rate was calculated at each location separately for the period 2016-2019 and 2019-2020 (**Figure 7.12d**), showing rates up to 1 m/y to the north of the city where most of the industrial activities were located and the aquifer transmissivity is higher. **Figure 7.12e** shows the spatial distribution of the groundwater level change for the period 2016-2019 (red, decreasing) and 2019-2020 (green, rising).

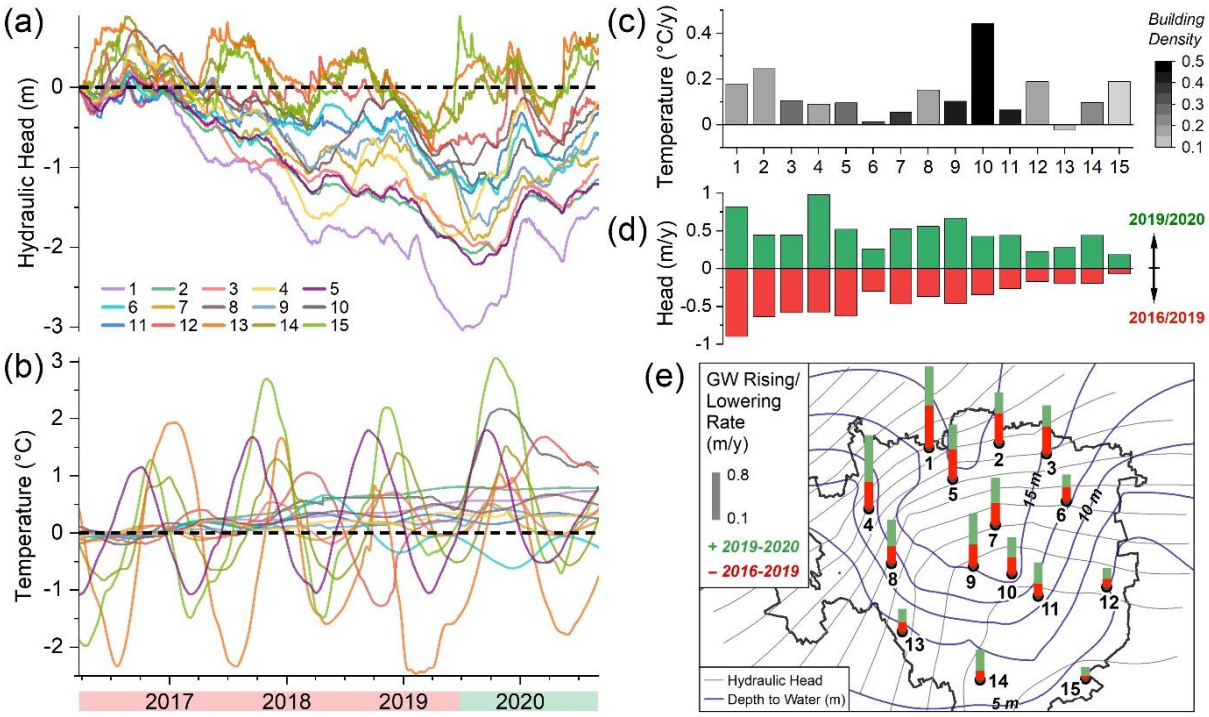


***Figure 7.12*** *– Hydraulic head (a) and temperature (b) fluctuations with respect to the hydraulic head of March 2016 and to the mean annual temperature of 2016. (c) Bar plot showing the linear fit trend of the groundwater temperature time series from 2016 to 2020; the gray scale represents the building density at each location. (d) Bar plot showing the hydraulic head lowering and rising rate observed from 2016 to 2019 (red) and from 2019 to 2020 (green), respectively, and (e) map showing the spatial distribution of the hydraulic head fluctuation rates.*

The temperature trend obtained from linear regression (**Figure 7.12c**) was interpolated over the study area by means of Ordinary Kriging as shown in **Figure 7.13a**. The difference between the mean daily groundwater temperature and the one-year moving window average was computed for each day of the monitored period (from July 2016 to July 2020 to represent 4 full years) and summarized by the standard deviation of the computed differences at each location (size of the circles in **Figure 7.13a**). Higher values indicate strong seasonal fluctuations

around the one-year moving window average value. We can observe an overall warming trend of about +0.15 °C/y in the entire study area with positive exception in the city center (+0.44 °C/y) and in the northern and southern sectors (+0.24 °C/y). A slightly negative trend was observed at well #13 located close to one of the main canals of the city. Hence, this well is probably affected by the periodic opening and closing of the canals which can affect the temperature signal.

This positive warming trend leads to heat accumulation in the shallow aquifer. By considering a constant temperature variation along the entire shallow phreatic aquifer (i.e., considering only the shifting of temperature-depth profiles towards higher temperature as shown in **Figure 7.5**) the energy gained per year by the shallow aquifer was estimated accordingly:

$$E_{gain} = C_{bulk} * B * \Delta T \qquad \textit{(Eq. 7.3)}$$

where $C_{bulk}$ is the equivalent thermal capacity of the bulk aquifer which, according to (VDI 4640/2, 2001), was set 2.4 MJ/m$^3$/K for the saturated portion of the phreatic aquifer; $B$ is the saturated thickness of the phreatic aquifer, and $\Delta T$ is the mean annual temperature variation shown in **Figure 7.13a**. The size of circles in **Figure 7.13b** represents the energy already stored in the shallow aquifer with respect to a constant reference temperature of 14.7 °C (mean annual air temperature of the investigated years, **Figure 7.13c**) and was obtained for each location by replacing $\Delta T$ in (Eq. 7.3) with the difference between the mean annual groundwater temperature of 2016 and the reference temperature. The statistics of the groundwater temperature for the period 2016-2020 are summarized through boxplots in **Figure 7.13c** where the mean annual air temperature is also shown.

Since the analysis of the air temperature time series in the study area did not reveal a significant warming trend for the last 30 years, we can infer that the warming rate observed from temperature-depth profiles and temperature time series (that is reflected by up to +25 MJ/y/m$^2$ of thermal energy gained by the shallow aquifer beneath the City center) must be mainly due to human-related heat sources. This value agrees with the estimates of +70 MJ/y/m$^2$ for the only urban area of Cologne (Zhu et al., 2011), +2.1 and +1.0 *10$^9$ MJ/y for the municipalities of Karlsruhe (61.9 km$^2$, +33.9 MJ/y/m$^2$) and Cologne (81.3 km$^2$, +12.3 MJ/y/m$^2$) (Benz et al., 2015).

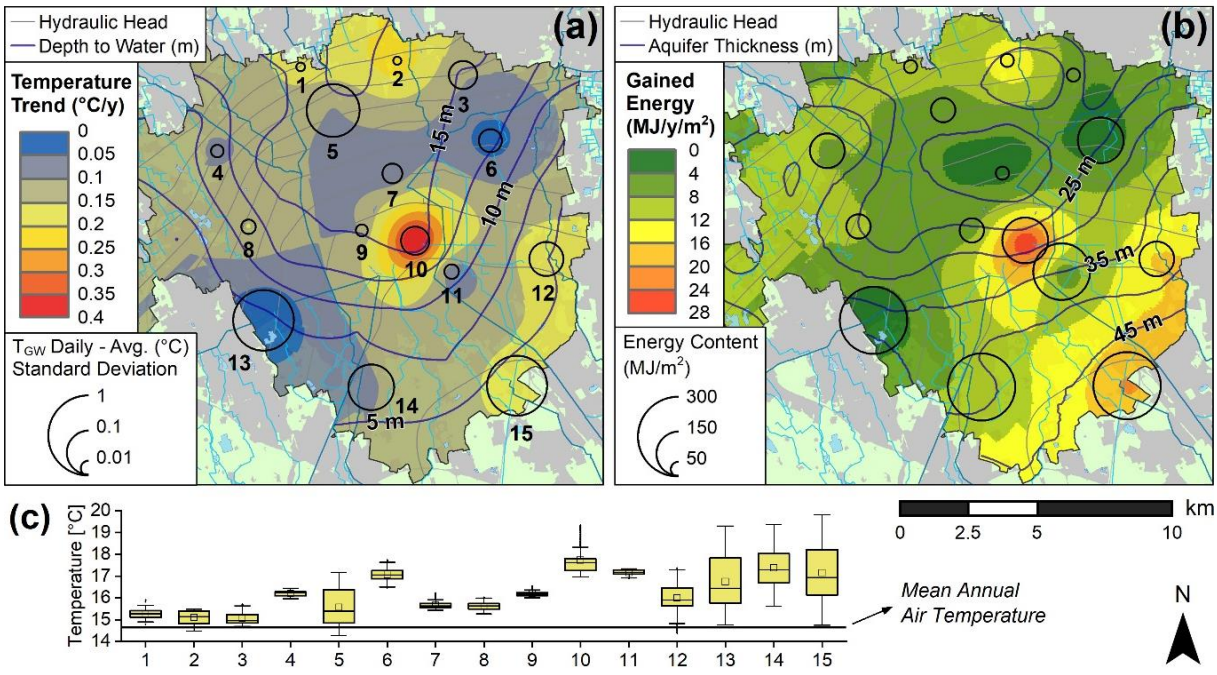


***Figure 7.13*** *– Maps showing: (a) the groundwater temperature trend observed from 2016 to 2020 and the amplitude of the seasonal fluctuations expressed by the standard deviation of the differences between the daily groundwater temperature and the one-year moving window average; (b) the energy gained yearly by the shallow aquifer and the energy content with respect to a reference temperature of 14.7 °C (mean annual air temperature). (c) Box and whiskers plots showing the distribution of the groundwater temperature during the continuous monitoring (2016-2020) at the wells labelled in (a). The reader must be aware that interpolation in these maps is only representative, and the heterogeneity of these variables is very high in such a complex environment.*

# 8. Chemical, physical, and bacteriological investigations

## 8.1. Introduction

Groundwater quality depends on natural and anthropogenic influences. Minerals and dissolved ions are necessary components of good quality water as they help maintain the health and vitality of organisms that rely on this ecosystem service such as the groundwater fauna (Khatri and Tyagi, 2015). Moreover, groundwater constitutes the largest reservoir of freshwater in the world, accounting for over 97% of all freshwaters available on earth (EU DIRECTIVE 2006/118, 2006) and human development relies on its availability in good quality and sufficient quantity. Thus, groundwater management strategies cannot disregard the comprehension of chemical/physical processes able to alter the quality of groundwater and its ecosystems. Without human influences, the water chemistry would be influenced only by natural processes such as weathering of bedrock minerals and aquifer deposits, concentration due to evaporation, dilution due to precipitation and surface waters, natural leaching of organic matter and nutrients from soil, and biological processes that may change the physical and chemical composition of water. During groundwater flow from recharge to discharge areas, a variety of chemical reactions occurs, depending on the chemical composition of the initial water, the mineralogy of rocks and deposits where it flows, the residence time and chemical-physical conditions of groundwater bodies such as temperature, pH, etc. The resulting concentrations of major ions in groundwater can be used to identify the intensity of rock-water interaction and chemical reactions. This chemical composition can be altered by point and/or diffused anthropogenic sources which contribute most in urban areas due to intense modifications of the shallow soil (e.g. land cover/sealing), subsurface (e.g. sewage pipes, tunnels) and groundwater uses and budget (e.g. due to industrial, drinking and thermal uses), but also in rural areas due to agriculture (e.g. use of fertilizers/pesticides and soil disintegration) (Khatri and Tyagi, 2015). Since groundwater moves slowly through the subsurface, the impact of anthropogenic activities may last for a long time and, thus, the study

of actual pollution mechanisms is essential to prevent future water quality issues. Furthermore, as healthy groundwater ecosystems help to provide clean drinking water (Danielopol et al., 2003), it is necessary to assess their ecological conditions and possible relation with urbanization and the SUHI in groundwater. It was demonstrated that a key parameter for water chemical composition in sedimentary systems is temperature, which is directly related to the density and viscosity of water, the solubility of gases, geochemical processes such as dissolution or precipitation of minerals, and biological processes (Brielmann et al., 2009; Griebler et al., 2016). Many studies worldwide (e.g. Khatri and Tyagi, 2015; Trauth and Xanthopoulos, 1997) and in the MCA (e.g. Alberti et al., 2018; De Caro et al., 2017) showed groundwater quality issues related to the release in the subsurface of undesired compounds (e.g. PCE, Cr-VI, etc.) and the relation between the degree of urbanization and contamination (De Caro et al., 2017). However, the water quality can be indirectly influenced by temperature-dependent physical, chemical, and biological processes. In fact, most physical properties and chemical reactions are temperature dependent and an increase in temperature can lead to increased solubility of minerals or to increased growth of undesired bacteria modifying the redox potential, pH and the metabolism (Bonte et al., 2013; Brielmann et al., 2009; Griebler et al., 2016; Retter et al., 2020). However, the effects of anthropogenic thermal pollution on the status of groundwater and its ecosystems are still poorly investigated (Koch et al., 2020). In this chapter, the spatial distribution, and the relation with urbanization (and the SUHI intensity) of major chemical-physical parameters, dissolved ions and the abundance of groundwater microfauna is presented and discussed for the MCA.

## 8.2. Materials and methods

### 8.2.1. Chemical-physical analysis

Chemical-physical parameters were measured in-situ since 2016 by a portable multi-meter probe. Both Hanna HI-9829® and In-Situ Aqua Troll® 500 were used to measure simultaneously the temperature (± 0.1 °C), pH [± 0.1 pH unit], specific electrical conductivity (EC) [± 1 µS/cm], dissolved oxygen (DO) [± 0.1 mg/l] and oxidation-reduction potential (ORP) [±5 mV]. The amount of total dissolved solids (TDS) [ppt] was estimated multiplying the EC by

the typical value of $6.5*10^{-3}$ (Rusydi, 2018). The DO [%] is expressed as the percentage ratio between the dissolved oxygen and the maximum oxygen concentration at the given temperature. Vertical multi-parameter profiles (inside open-pipe piezometers) are available at locations shown in **Figure 5.3** according to measuring campaigns summarized in **Figure 5.12**. Major dissolved cations and anions were measured by De Caro (2018) and, in the scope of this thesis, at 21 locations in the MCA during July 2021 ("Automatic" monitoring points in **Figure 5.3**). The sampling of 250 ml of groundwater was performed at each well by means of the Proactive Tornado® submersible pump (12V powered, max flow rate 15 l/min) after stabilization of the EC parameter. Samples were kept cool and analyzed successively in the laboratory by ion chromatographer Metrohm® 883 Basic IC Plus. The ion chromatography technique uses ion-exchange resins to separate atomic or molecular ions based on their interaction with the resin. The greater the charge on the ion the more strongly it is attracted to the surface of the resin. Also, larger anions generally move more slowly through the column than smaller anions. The result is that the sample is separated into bands of different kinds of ions as it travels through the column. The EC of the fluid coming out from the resin column is measured continuously obtaining a chromatogram. By determining the peak area or peak height, the concentration of single ions can be deduced by comparison with known standards. Moreover, the groundwater alkalinity was estimated by titration with a strong acid (HCl) according to the Gran's method. Below the specific threshold of 4.5, the pH changes linearly with the volume of added acid according to the total alkalinity of the sample. Considering the Bjerrum diagram describing the carbonate system and the pH range in the analyzed samples, the total alkalinity was assumed equal to the concentration of the bicarbonate ion $HCO_3^-$.

### 8.2.2. Flow cytometry (FCM)

The microbial abundance in the 21 groundwater samples collected in the MCA in July 2021 ("Automatic" monitoring points in **Figure 5.3**) was measured at the Dept. of Environmental Sciences at the University of Basel (CH) using the Sigrist/bNovate Bactosense® for automated FCM. The groundwater was collected as described in section 8.2.1 with 50 ml sterile vials after piezometer purging and samples maintained cool during the sampling day. For each site, two samples were collected: one kept cool and the other fixed with glutaraldehyde at 1%

concentration (Günther et al., 2008), flash frozen with liquid nitrogen, kept frozen at -20°C and measured within seven days.

FCM is a technique for sensing cells or particles as they move in a liquid stream through a laser. The scattered light and color-discriminated fluorescence by microscopic particles are measured and used to differentiate the cells on their characteristics such as size, granularity, and whether the cell is carrying fluorescent molecules in the form of antibodies or dyes (Macey, 2007). Traditional FCM requires manual sample preparation such as dye addition, mixing and incubation. Recently, researchers at the Swiss Water Research Institute (EAWAG) developed a fast (<15 min.) microbial total cell-counting (TCC) method based on FCM which is totally integrated and automated by the Sigrist/bNovate Bactosense® (size detection limit 0.1 µm, total detection limit 100 cells/ml - 5000000 cells/ml, accuracy <5% relative) as illustrated in **Figure 8.1**. A dye (SYBR Green 1) is added to 90 µl of sample binding to the DNA of microbial cells causing fluorescence. The resulting DNA-dye-complex absorbs blue light ($\lambda_{max}$ = 497nm) and emits green light ($\lambda_{max}$ = 520nm). Then, the sample is automatically mixed and incubated at 37 °C for 10 min and, finally, passed into the flow cell where it is irradiated by a 488nm laser light. Three optical detectors are placed besides to simultaneously record the intensity of side scattered light SSC at 488nm, and emitted fluorescence FL1 and FL2 at 525 and 715nm, respectively.

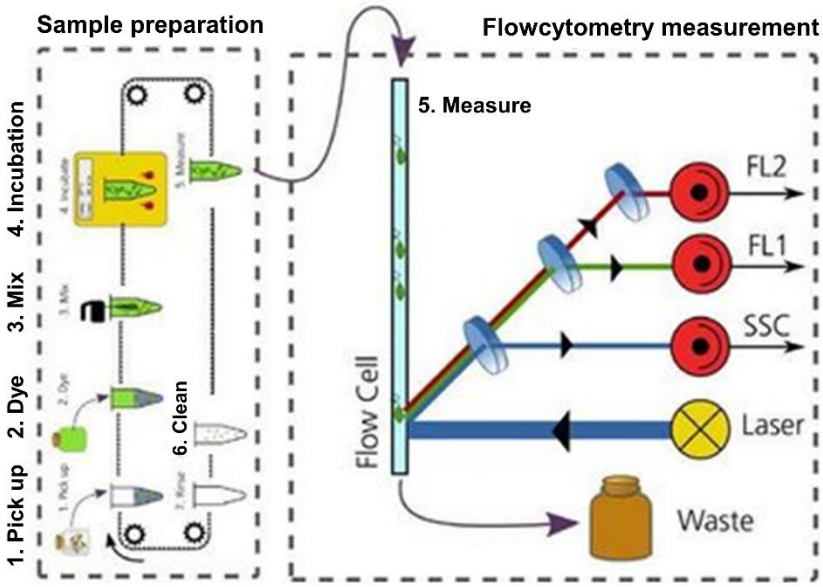


***Figure 8.1*** *– Automatic flow cytometry scheme performed by the Bactosense analyzer (adapted from Sigrist®)*

Cells suspended in the sample flows through the detector generating signal peaks on the 3 channels: SSC, FL1 and FL2. The logarithm of their intensity is plotted to obtain the cytograms SSC vs FL1 and FL2 vs FL1 (**Figure 8.2**). A gating procedure on the FL2 vs FL1 cytogram was used to discretize between low-nucleic acid (LNA) and high-nucleic acid (HNA) cells, and noise/debris due to suspended particles and broken cells (**Figure 8.2**). The total cell-count (TCC) was obtained as the sum between LNA and HNA cell counts. In addition, the high-nucleic acid percentage (HANP) index was obtained as the percentage of HNA with respect to the TCC.

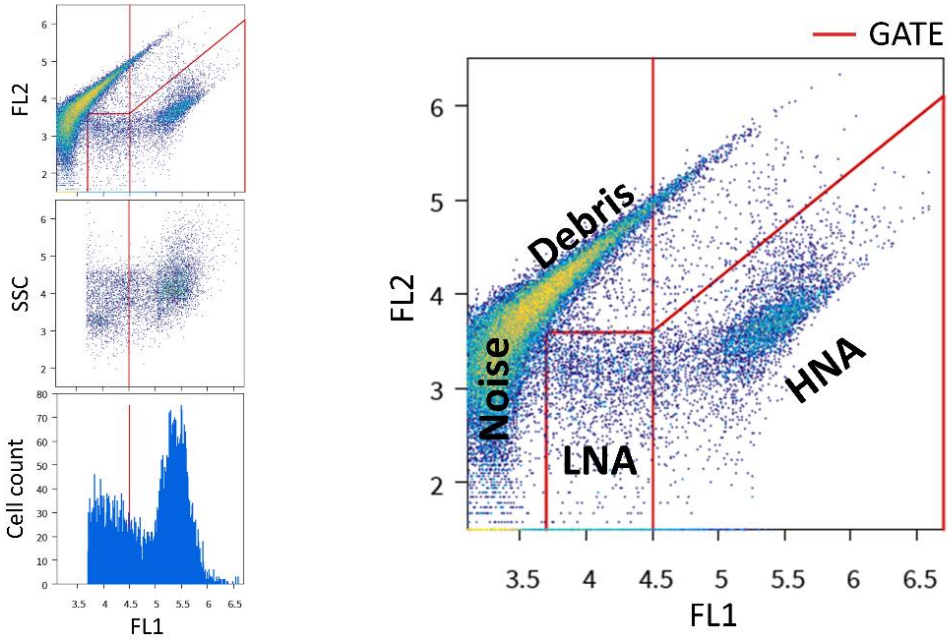


***Figure 8.2*** *– Typical cytograms obtained by FCM analysis showing the gating procedure to identify the HNA, LNA, noise and debris clouds.*

## 8.3. Results and discussion

Major cations and anions detected by ion-exchange chromatography and alkalinity are $Ca^{2+}$, $Mg^{2+}$, $Na^{+}$, $K^{+}$, $HCO_3^{-}$, $SO_4^{2-}$, $Cl^{-}$ and $NO_3^{-}$. Piper and Schoeller diagrams were used for groundwater chemical facies classification (**Figure 8.3**). **Figure 8.3a** shows the Piper diagram together with the total dissolved solids (TDS) and the building density indicator described in section 7. All the analyzed samples fall in the calcium-carbonate facies showing no significant variation except for the chloride concentration, which is positively correlated with the degree of urbanization at the sampling location (**Figure 8.3b**). Thus, the prevailing carbonate footprint can be explained by the mineralogical composition of the catchment areas of the alluvial fan

systems. As described in section 5.2, in the Milan area four main alluvial megafans coalesce into a continuous "bajada" of deposits (Fontana et al., 2014; Guzzetti et al., 1997). These are, namely from east to west, the Molgora, Lambro, Seveso and Olona megafans fed by south-alpine catchments mainly composed of carbonate rocks.

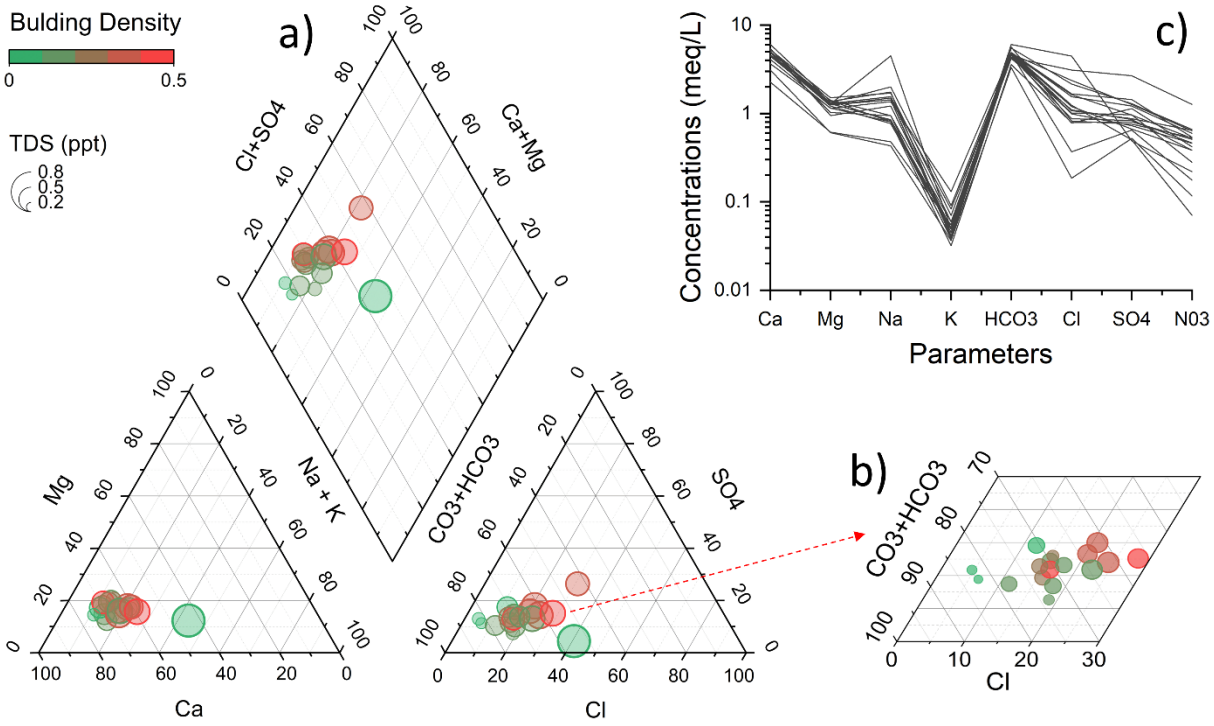


***Figure 8.3*** *– Characterization of the major ions dissolved in groundwater in the MCA: (a) Piper diagram showing the calcium-carbonate facies and (b) the correlation between percentage of Cl and urbanization (building density). (c) Schoeller diagram.*

Multi-parameter vertical profiles were analyzed to investigate the vertical and temporal variability of temperature, pH, EC, DO and ORP (vertical profiles for "Automatic" monitoring points in **Figure 5.3** are provided in the Supporting material). Due to malfunctioning of the pH sensor, the data acquired in September 2019 were considered as the most representative for the MCA due to the completeness of the dataset and integrity of all the sensors. According to vertical profiles shown in the Appendix, the variation of EC and DO between 2019 and 2021 is little, the temperature variation depends on the depth of the water table and hydrological settings while pH was not comparable due to malfunctioning. **Figure 8.4a**, **b**, **c**, and **d** show the spatial distribution of DO, pH, TDS and ORP in 2019 averaged along the entire length of the profile and interpolated by inverse distance weighting.

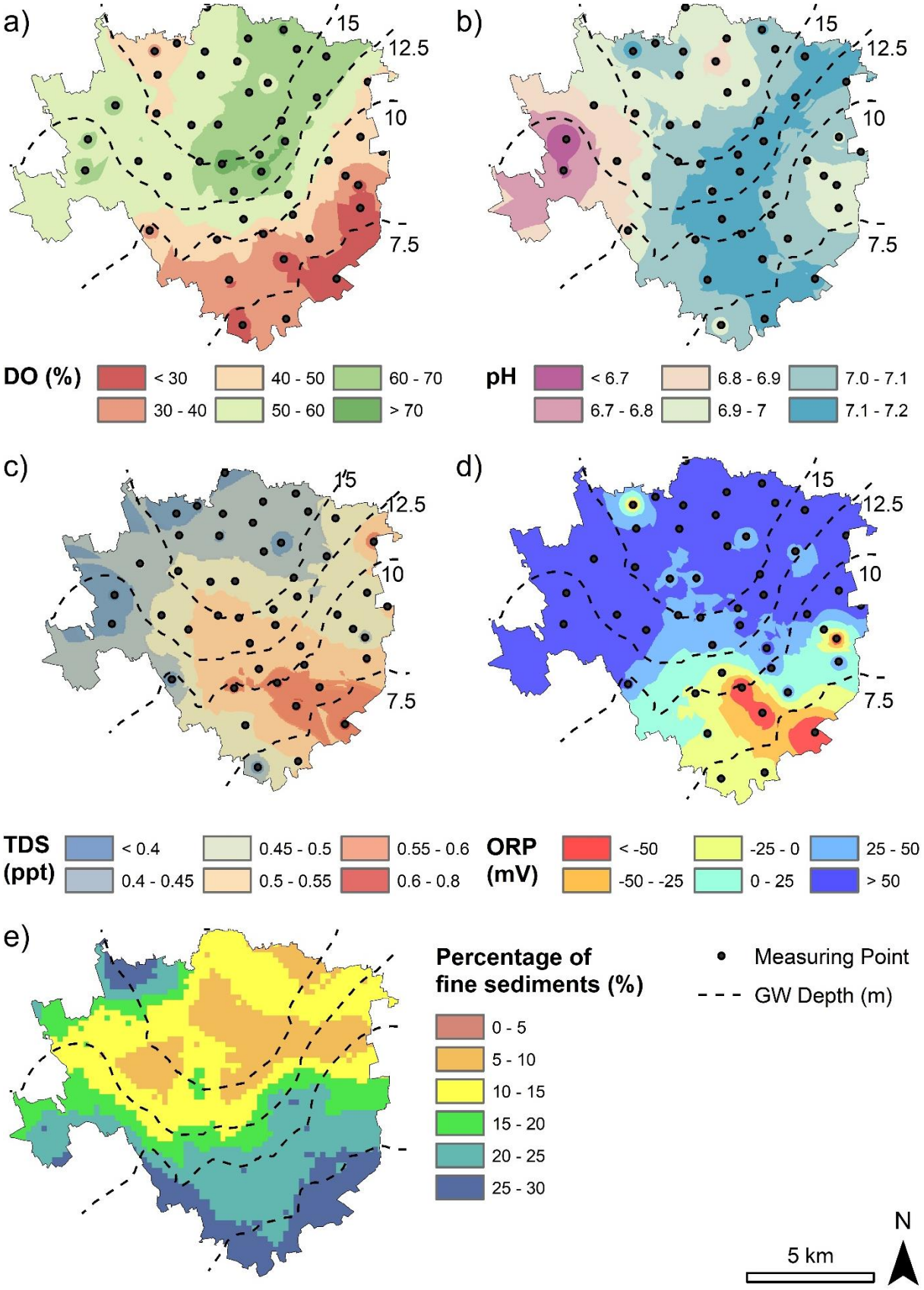


***Figure 8.4*** *– Maps showing the spatial distribution of the (a) dissolved oxygen (DO), (b) pH, (c) total dissolved solids (TDS), (d) oxidation-reduction potential (ORP), and (e) percentage of fine sediments in the MCA (physical-chemical parameters were measured in September 2019).*

Contrary to early expectations, DO, TDS and ORP are inversely correlated with the thickness of the unsaturated zone. The atmosphere is the main source of oxygen dissolved in groundwater, but It has often been assumed that oxygen derived from the atmosphere is rapidly consumed in the soil and the unsaturated zone by microbial respiration and the decomposition of organic matter (Rose and Long, 1988). Thus, the degree of groundwater-surface interactions and the thickness of the vadose zone control the DO in the shallow portion of groundwater bodies. On the contrary, significant concentrations of DO (> 1 mg/l) have been measured in deep groundwater samples in alluvial aquifers indicating that the microbial reduction of $O_2$ can be limited and/or oxygen can be effectively transported through the vadose zone to aquifer bodies (Rose and Long, 1988). Thus, the observed behavior was explained looking at the percentage of fine/cohesive sediments (i.e. grain size < 0.075 mm) in the phreatic unit calculated similarly as described in section 6.3.1.1. **Figure 8.4e** shows the spatial distribution of fine sediments which can be correlated to DO and ORP. Considering the small range of variation and the proximity to rivers of two outliers to the west, no significant spatial trend was observed for the pH.

The results of the flow cytometry analysis (TCC and HNAP index), considering the gating shown in **Figure 8.2**, are given in **Table 8.1**.

***Table 8.1*** *– Flow cytometry results (total cell count – TCC/ml – and high-nucleic acid percentage index – HNAP) compared to physical-chemical parameters of water (temperature, EC, pH, DO, ORP, TDS), aquifer characteristics (% fine sediments, rivers) and urbanization (% green).*

| | TCC (/ml) | HNAP (%) | Temperature (°C) | EC (µS/cm) | pH (pH) | DO (mg/l) | DO (%Sat) | ORP (mV) | TDS (ppt) | Green (%) | Rivers |
|---|---|---|---|---|---|---|---|---|---|---|---|
| 1 | 217455 | 79 | 15.7 | 637 | 8.20 | 1.3 | 13 | 73 | 0.41 | 0.31 | |
| 2 | 76322 | 69 | 15.5 | 666 | 7.39 | 7.6 | 77 | 79 | 0.43 | 0.64 | |
| 3 | 55900 | 70 | 15.2 | 644 | 7.55 | 7.5 | 76 | 23 | 0.42 | 0.21 | |
| 4 | 188411 | 49 | 16.7 | 661 | 7.56 | 6.9 | 72 | 39 | 0.43 | 0.55 | |
| 5 | 38144 | 76 | 15.8 | 492 | 7.36 | 6.7 | 69 | 75 | 0.32 | 0.30 | |
| 6 | 159900 | 67 | 17.3 | 618 | 7.77 | 6.9 | 73 | 107 | 0.40 | 0.24 | |
| 8 | 86222 | 60 | 16 | 815 | 7.74 | 6.2 | 63 | 100 | 0.53 | 0.52 | |
| 10 | 33566 | 55 | 18.9 | 820 | 7.78 | 8.1 | 88 | 79 | 0.53 | 0.06 | |
| 11 | 63533 | 73 | 17.1 | 769 | 7.64 | 5.8 | 61 | 72 | 0.50 | 0.15 | |
| 12 | 1207333 | 51 | 16.2 | 437 | 7.58 | 0.043 | 0 | -200 | 0.28 | 0.57 | Y |
| 13 | 394283 | 44 | 15.7 | 361 | 7.95 | 2.1 | 22 | 113 | 0.23 | 0.67 | Y |
| 14 | 72628 | 57 | 16.7 | 654 | 8.10 | 2.0 | 21 | 76 | 0.43 | 0.36 | |
| 16 | 102011 | 73 | 16.1 | 1045 | 7.88 | 3.8 | 39 | 92 | 0.68 | 0.71 | |
| 17 | 157422 | 71 | 15.8 | 785 | 7.81 | 4.0 | 41 | 75 | 0.51 | 0.12 | |
| 18 | 234977 | 52 | 18.7 | 398 | 7.62 | 4.8 | 52 | 35 | 0.26 | 0.58 | |
| 19 | 71622 | 72 | 16.3 | 733 | 7.76 | 5.1 | 53 | 63 | 0.48 | 0.27 | |
| 20 | 74477 | 60 | 16.9 | 832 | 7.71 | 4.7 | 49 | 78 | 0.54 | 0.13 | |
| 23 | 73777 | 66 | 17.8 | 650 | 7.43 | 3.7 | 39 | 74 | 0.42 | 0.16 | |
| 24 | 24529 | 62 | 16.4 | 725 | 7.91 | 7.4 | 77 | 77 | 0.47 | 0.04 | |
| 25 | 43911 | 74 | 16.6 | 859 | 7.74 | 6.9 | 72 | 65 | 0.56 | 0.15 | |

The TCC has a log-normal frequency distribution with a median value of $7.5*10^4$ and $10^{th}$ and $90^{th}$ percentiles of $5.9*10^4$ and $1.7*10^5$. These values fall within the range of good quality drinking waters (e.g. Evian = $7.7*10^4$, Zilia = $1.3*10^5$ TCC). Two outliers were found at wells #12 and 13, respectively located within 500 m to the Lambro River and the Naviglio Grande canals. Moreover, the high TCC together with a negative ORP at well #12 suggest that a strong local bacterial activity is consuming oxygen and degrading organic matter, leading to poor quality groundwater. The spatial distribution of TCC and HNAP is given by maps in **Figure 8.5**.

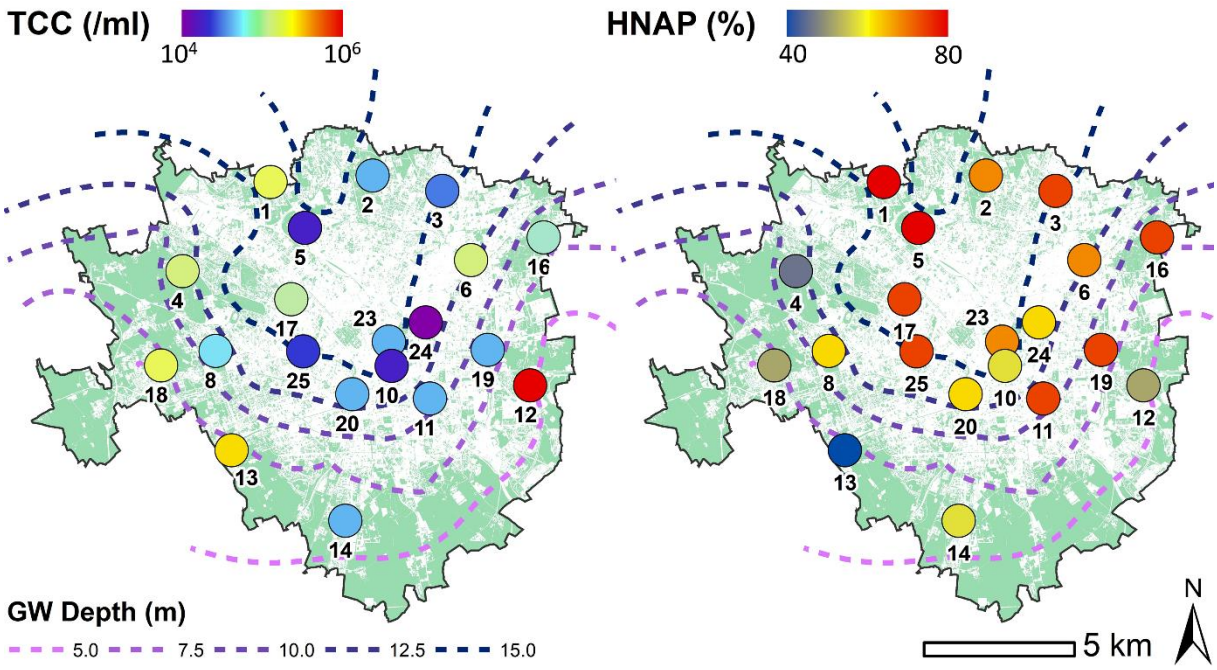


***Figure 8.5*** *– Maps showing the spatial distribution of the total cell count (TCC) and the high nucleic acid percentage (HNAP) in the MCA.*

Due to the complexity of the investigated phenomena and the importance of local equilibrium conditions, no significant spatial trends were observed, but the relation with the degree of urbanization, the depth of the water table and the percentage of fine deposits can be roughly assessed. To untangle the most important factors that govern the growth of groundwater microfauna, a correlation matrix between TCC, HNAP and physical-chemical parameters (temperature, pH, DO, TDS), aquifer characteristics (% of fine sediments), and degree of urbanization (% of green) was evaluated (**Figure 8.6**).

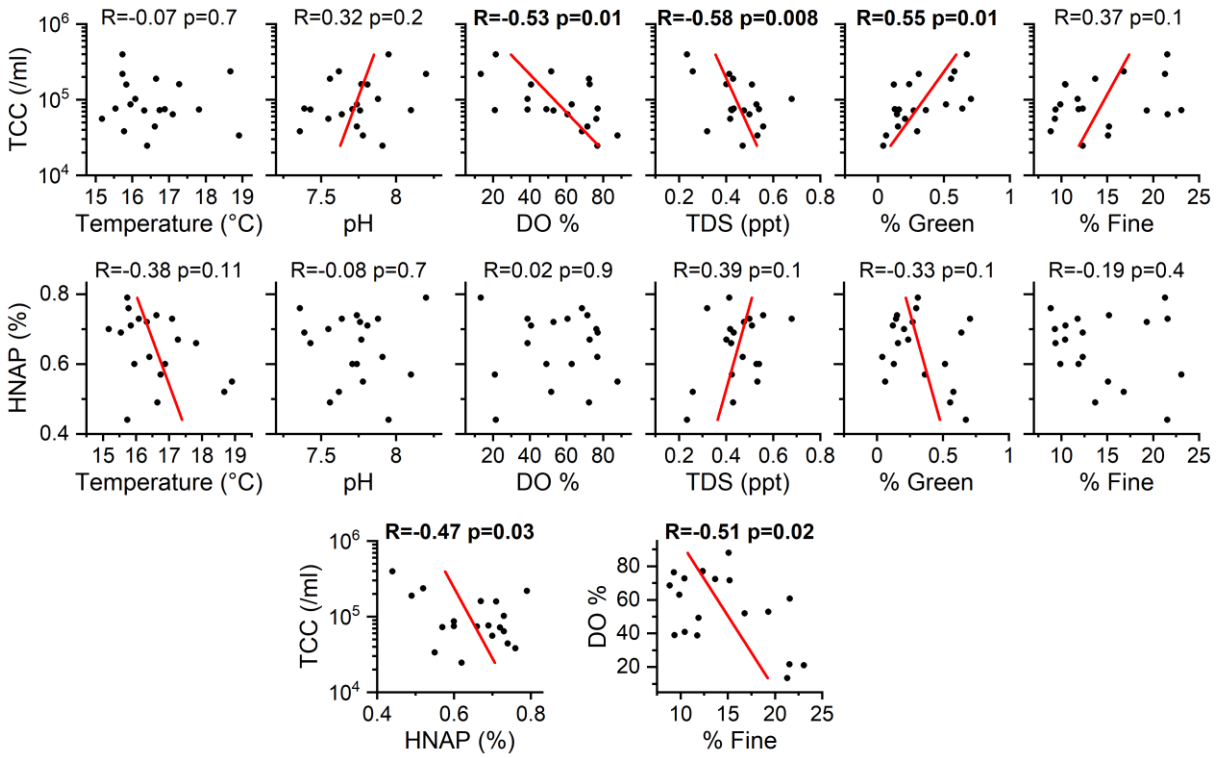


***Figure 8.6*** *– Correlation matrix between total cell count (TCC), high-nucleic acid percentage (HNAP) and the physical-chemical parameters (temperature, pH, DO, TDS), aquifer characteristics (% of fine sediments) and urbanization (% of green). The correlation between HNAP and TCC, DO and % of fine sediments are also shown. The Pearson's R and p-values are reported above each plot and, for R higher than 0.3, the linear fit is shown.*

The total number of microbial cells is inversely correlated with the available oxygen and the total dissolved solids, and positively with the percentage of green unsealed areas and the percentage of fine sediments. Assuming oligotrophic conditions in groundwater, the oxygen consumption is limited mainly by the availability of organic matter which is the primary source of nutrients for the heterotrophs living in the groundwater ecosystem.

Thus, the total number of microbials depends on the interactions between atmosphere and groundwater that assure the replenishment of organic matter in the subsurface (i.e. first, on the % of green areas and, secondly, the groundwater depth). Moreover, an inverse correlation between DO and the percentage of fine sediments exists, suggesting that finer deposits can hamper the replenishment of oxygen consumed by the living ecosystems, leading to low values of DO. Thus, the equilibrium between the available organic matter (correlated to the percentage of green natural areas) and the replenishment of oxygen consumed by the living ecosystems (correlated to the percentage of fine sediments) controls both the oxidation-reduction status and the health of groundwater ecosystems, in terms of total number of living

units (TCC) and morphological characteristics (e.g. the HNAP index reflects differences in the cell morphometry). **Figure 8.7** summarizes the conceptual model proposed to explain the distribution of TCC in the study area and illustrates the equilibrium between supply of nutrients, microbial growth, and oxygen replenishment. Direct measurements of DOC will be essential to verify and improve the proposed model.

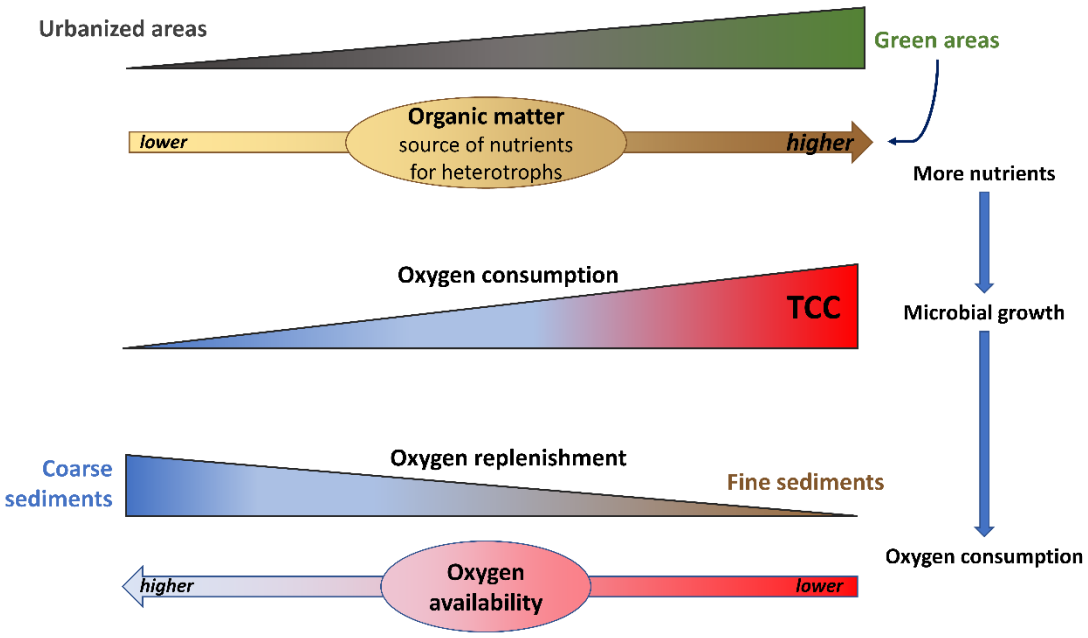


***Figure 8.7*** *– Schematic representation of the observed correlations between the TCC, DO, the percentage of green areas and fine sediments illustrating the conceptual model for the microbial growth in the study area.*

Despite an increase in the temperature generally leads to changes in concentration of some nutrients and major ions and enhances the metabolic activities (Griebler et al., 2016), no significant correlations were observed between the TCC and groundwater temperature. Bonte et al. (2013) demonstrated by laboratory tests that significant effects by a temperature increase from 11°C (in situ) to 25°C are observed on the redox processes (i.e. changing from iron-reducing to sulfate-reducing conditions) and associated microbial communities in anoxic unconsolidated subsurface sediments. However, it is important to consider that every species has its individual temperature range with an optimum and a lower and upper limit for individual activities (e.g. stress and growth). Due to the little variability in the groundwater temperature in the study area (e.g. SUHI of approx. 3°C), the effects of temperature on the microbial growth assessed by the FCM analysis are secondary with respect to the interactions with the surface that define the oxidation-reduction status and the supply of nutrients.

# 9. A modeling approach covering present and future thermal effects on groundwater regimes

This chapter is largely based on the following paper:

➔ Previati, A., Epting, J., & Crosta, G. B. (2021). The subsurface urban heat island in Milan (Italy)-A modeling approach covering present and future thermal effects on groundwater regimes. *Science of The Total Environment*, 152119.

https://doi.org/10.1016/j.scitotenv.2021.152119

## 9.1. Introduction

In the last decades, it has been observed that many anthropogenic and urbanization-related activities, the use of shallow geothermal energy and climate change can affect the subsurface thermal regime in the vadose zone and the groundwater. Section 7 described the SUHI phenomenon and showed the most relevant heat contributors in the study area, but the impact SUHIs may have on groundwater quality (e.g., biological, chemical and physical effects) and on the potential and sustainability of shallow geothermal systems is mostly unexplored and of increasing interest among drinking water suppliers and energy planners (Blum et al., 2021). Although many studies recognized and mapped the SUHI beneath metropolitan areas (e.g. for a review: Bayer et al., 2019 and Zhu et al., 2011; Basel, Epting and Huggenberger, 2013; Cardiff, Farr et al., 2017; Paris, Hemmerle et al., 2019; six German cities, Menberg et al., 2013a; Milan, Previati and Crosta, 2021a; Amsterdam, Visser et al., 2020), few addressed the processes that lead to SUHI, including the quantification and city-scale comparison of natural and anthropogenic heat sources. Visser et al. (2020) linked the development of the SUHI in the city of Amsterdam with the progressive city expansion and climate change of the last century. Benz et al. (2015) and Menberg et al. (2013b) evaluated analytically the thermal contribution of specific natural and anthropogenic heat sources, their temporal evolution in

the last decades and the total heat content in the aquifer of Cologne and Karlsruhe. Epting et al. (2017b, 2013) and Bidarmaghz et al. (2020) proposed large-scale FEM modeling approaches to capture the subsurface temperature elevation resulting from anthropogenic heat sources in the city of Basel and a London district, respectively. Even though the above-mentioned case studies are medium to small size cities with different settings and urban density, the heat released from buildings and elevated ground surface temperature was revealed a dominant contributor of the anthropogenic heat flow into the urban aquifers.

In the Milan metropolitan area many activities related to urbanization contribute to modify the atmospheric and groundwater environments such as the land occupation by buildings and concrete structures, and the subsurface occupation by foundations, tunnels, and geothermal systems. The superimposition of several thermal sources related to human activities and environment modifications led to an increase of the mean annual groundwater temperature near the city center, of up to more than 3 °C with respect to the immediate suburban areas (Previati and Crosta, 2021a), where the highest density of heat sources is encountered (e.g. 10.6 geothermal wells/km$^2$, 1.6 km of tunnels/km$^2$, 35.6 and 22.3 % of land occupied by buildings and asphalted surfaces, respectively).

Moreover, the thermal energy demand in the Milan area is the highest of the region (200 kW is the average peak thermal power demand in the municipality) and, in this area, there is a growing interest in replacing the existing traditional heating/cooling systems into more sustainable solutions (Previati and Crosta, 2021b). Among these, the potential to host low enthalpy geothermal installations was already discussed at a regional scale through analytical solutions is section 6 but a quantification at the city scale is still lacking.

In this context, the monitoring of groundwater temperatures was essential to evaluate the thermal state of urban groundwater bodies (e.g. Farr et al., 2017; Mueller et al., 2018; Previati and Crosta, 2021a) but in order to assess thermal boundary conditions over time, as well as to quantify the amount of heat stored/storable in the aquifers, appropriate modeling tools are necessary. Physically-based numerical modeling of fluid flow and heat transport has been demonstrated to be an effective (and relatively cheap) technique to support the thermal management of groundwater at the city scale (Bidarmaghz et al., 2020; Epting et al., 2017a; Epting and Huggenberger, 2013). Several aspects must be considered to develop a robust city-

scale groundwater flow and heat transport model such as, among others, the availability of detailed geological and hydrogeological information, long-term groundwater level and temperature data, the location, geometry and thermal regime of surface/subsurface structures and infrastructures, and information about the characteristics and location of shallow geothermal systems and their annual thermal load. Lastly, the computational costs of a large city-scale groundwater flow and heat transport model must be considered since an excessive spatio-temporal resolution could hinder the development of transient simulations.

The 3D FEM numerical model developed for the MCA aims to introduce possible city-scale applications such as: (1) understanding the hydro-thermal regime of the urban aquifer and the thermal contribution of natural and anthropogenic heat sources, (2) quantifying the geothermal potential and (3) investigating the effects of urbanization and climate change scenarios.

Focusing on the most relevant heat sources (boundaries) and transport mechanisms (parameters), new approaches were developed and combined with already existing modeling techniques to improve a large city-scale FEM model focusing on the most relevant boundaries and parameters for the heat in/outflow and transport. Among these, (I) aquifer heterogeneities were modeled to consider the advective heat-transport by the 3D interpolation of borehole logs hydrogeological information, and a thermofacies classification was derived from grain-size based hydrofacies to account for the assessment and calibration of thermal parameters. (II) The multilayer analytical solution by Händel et al. (2013) was coupled to the numerical solution by means of the SoilTemp tool (Kupfersberger et al., 2017; Rock and Kupfersberger, 2018) and applied at the city-scale to estimate the heat in/outflows from the upper boundary. To this aim, a high-resolution land use map was used to classify the upper elements on the percentage of land cover type. (III) A holistic approach is proposed for the Milan city area considering natural and human-related fluid and heat sources and implementing in the model as transient boundary conditions. (IV) By means of a fluid and heat budget analysis the most relevant heat sources at the city-scale were quantified and, by a space and time validation of the simulated temperature, possible under/overestimated heat sources were highlighted for further investigations. Finally, the city-scale model, calibrated on the current thermal regime, was used to assess (V) the low enthalpy geothermal potential and

to quantify (VI) the change in thermal energy stored in the shallow groundwater bodies due to changes in natural and anthropogenic factors such as climate, city size and shallow geothermal installations.

## 9.2. Study area

The MCA (**Figure 9.1**) is characterized by a dense texture of structures and infrastructures that modify the water infiltration and groundwater flow processes, the heat transfer between the surface and the subsurface, and eventually the heat transport in the aquifer. Due to the high urban density and related construction works, there is an exceptional amount of qualitative and quantitative information on the subsurface (e.g. about 10 borehole logs every km$^2$) that makes this area eligible for the development of a city-scale 3D geological and fluid-flow/heat-transport FEM model. **Figure 9.1** shows the location and the extent of the model boundary together with the available subsurface information (borehole logs).

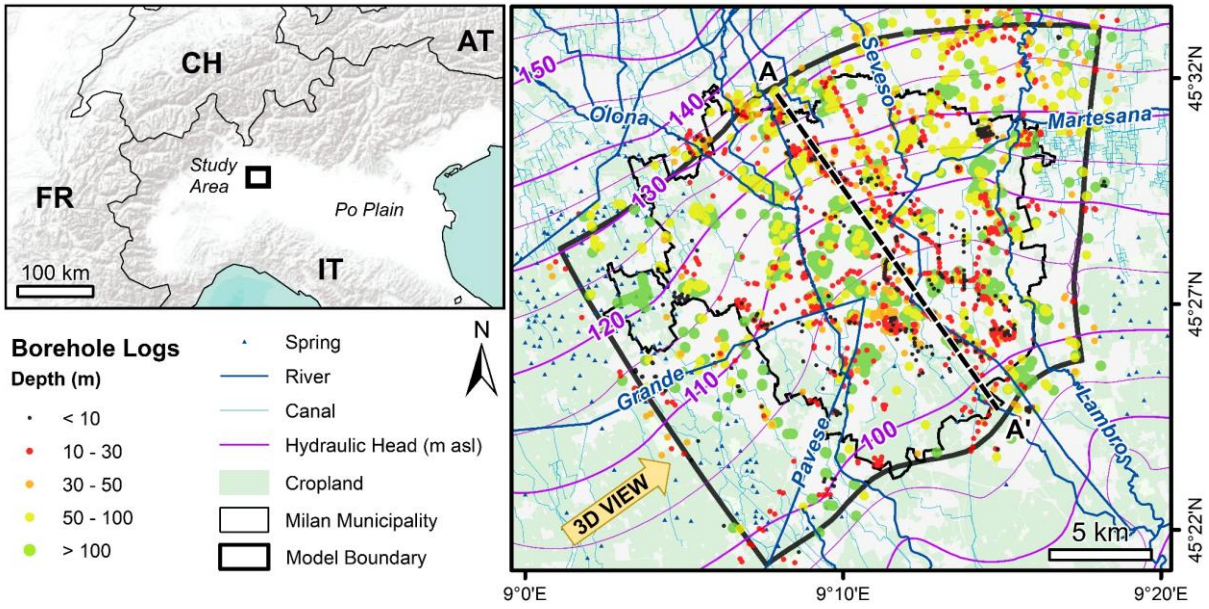


***Figure 9.1*** *– Map of the study area showing the modeling domain, the hydrological network, the regional-scale hydraulic head distribution and the available borehole logs colored by their total length. Dashed line represents the cross-section A-A' shown in* ***Figure 9.6****.*

## 9.3. Conceptual model

Based on the theoretical background (sections 2,3 and 4) and characterization of the current thermal regime from groundwater monitoring (section 7), a holistic conceptual model is

proposed to support the thermal modeling of shallow aquifers in the Milan city area. Regional fluid and heat boundaries were identified in the regional groundwater flow and head distributions, directed southeastward from the alpine foothills to the Po River) and in the atmosphere-groundwater interactions regulated by the thickness of the unsaturated zone that act as a thermal resistance to the perturbations coming from the surface (see section 2.3 for details). In addition, local disturbances to the regional groundwater flow and heat transport were identified among relevant natural and anthropogenic processes such as (1) the groundwater recharge and heat sources from precipitation and the interaction with surface water bodies, (2) water abstraction from drinking water supply wells, (3) disturbances to the fluid-flow caused by impervious subsurface infrastructures (e.g., tunnels), (4) the heat flow into/from the subsurface according to the land cover material and the air temperature, (5) the heat flow from/to tunnels to/from the ground/groundwater, and (6) the fluid and heat abstraction and injection from shallow groundwater heat pumps (GWHP). Finally, fluid flow and heat transport mechanisms in porous media are well described in section 2.2 and by equations in section 4.2.3 where the importance of aquifer heterogeneities was discussed. Considering some typical values of Darcy flow velocities and the median grain-size for the aquifers P ($q$ from $5*10^{-6}$ to $5*10^{-4}$ m/s and $d_{50}$ from 1 to 10 mm) and SC ($q$ from $1*10^{-9}$ to $5*10^{-5}$ m/s and $d_{50}$ from 0.2 to 2 mm), the Péclet number (Eq. 2.8) indicates advection as the main heat transport mechanism in the aquifer P and a combination (with strong local variability due to the logarithmic nature of hydraulic conductivity) of advection and conduction in the SC. In the unsaturated zone, due to the very low heat capacity of air filling the pores, the Péclet number is significantly lower than 1 (from 0.001 to 0.1) assuming the heat conduction as the only relevant heat transport mechanism. Thus, the heat flux from/to the surface to/from the groundwater (i.e. throughout the vadose zone) is mainly governed by conduction while in the saturated zone by advection.

**Figure 9.2** shows a schematic conceptual model to support the development of a coupled fluid flow and heat transport city-scale model in the MCA. The spatial distribution of regional scale (mostly natural) settings is generally parallel to the slope gradient distribution (i.e. to the southern alps and Po plain geomorphology), whereas anthropogenic factors are typically concentric, centered in the city center.

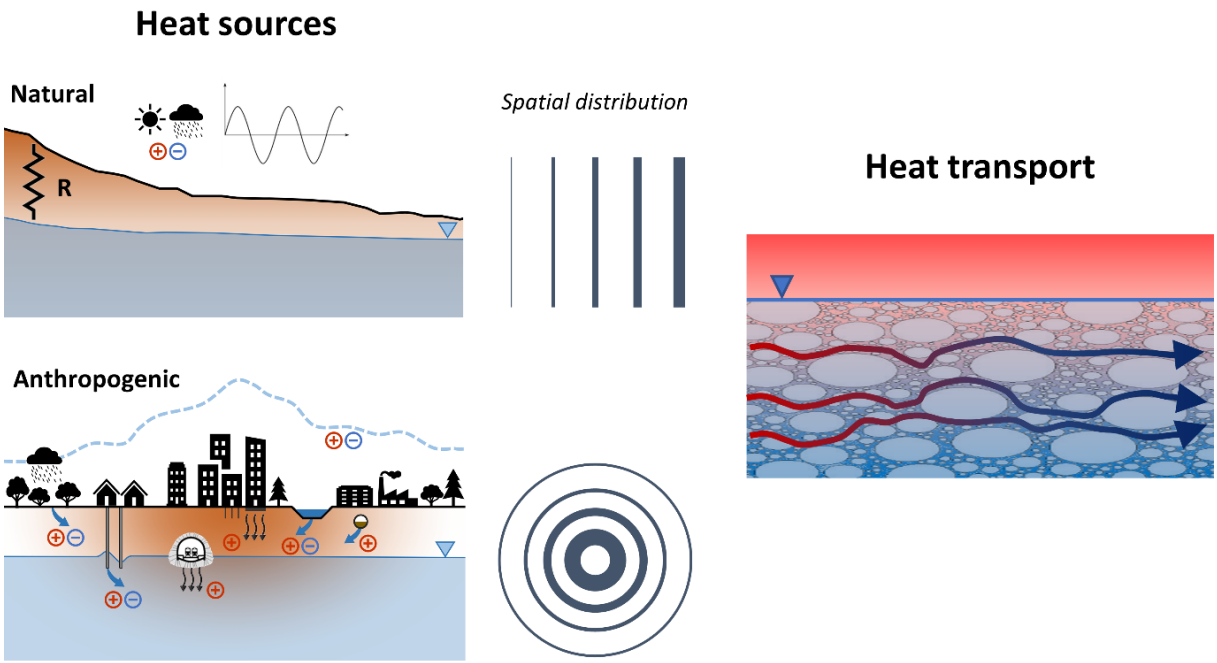


***Figure 9.2*** *– Schematic conceptual model for the natural and anthropogenic heat sources and transport mechanisms in the subsurface of the Milan city area.*

## 9.4. Materials and methods

### 9.4.1. Monitoring network and land cover

Groundwater level and temperature data were directly collected by the authors at 61 observation wells (OW) (**Figure 9.3a**; 6 locations out of 61 are outside the map extent) and were combined to set up and calibrate the model. Among these, at 15 open-pipe piezometers the pressure and temperature were recorded since 2016, and at 46 more locations inside and nearby the study area temperature-depth profiles were acquired (see also section 5.7.1). Information on the land cover, the surface/underground transport network (i.e., railway and metro lines), the location of water supply wells, shallow geothermal wells were collected and homogenized from the regional geographic database (Regione Lombardia, 2020) (land cover derived from satellite image interpretation) and from technical drawings and databases provided by two public companies (MM Spa for the wells and tunnels of the Milan municipality and CAP Holding for the wells outside the city). **Figure 9.3a** shows the land cover classification adopted to derive infiltration coefficients and evaluate the upper thermal boundary.

Mean daily air temperature time series and rainfall data were collected from the regional environmental agency database (ARPA Lombardia, 2021) for the years 2014 to 2021 at 12 locations (**Figure 9.3a**; 3 locations out of 12 are outside the map extent). The mean annual air temperature for the selected period was interpolated over the study area and the city was divided into four concentric zones (Z1 to Z4 from the center outwards) according to the mean annual air temperature isolines (**Figure 9.3a**). **Figure 9.3b** shows two selected air temperature time series (A2 city center, A1 suburban areas; see location in **Figure 9.3a**) and **Figure 9.3c** shows the daily difference between the two time series where a UHI effect up to more than 2°C is clearly evident. **Figure 9.3d** shows the percentage of land cover type inside the four concentric zones identified by the 0.25 °C mean annual air temperature isolines. This classification was used to assign the external reference temperature for the upper thermal boundary condition definition.

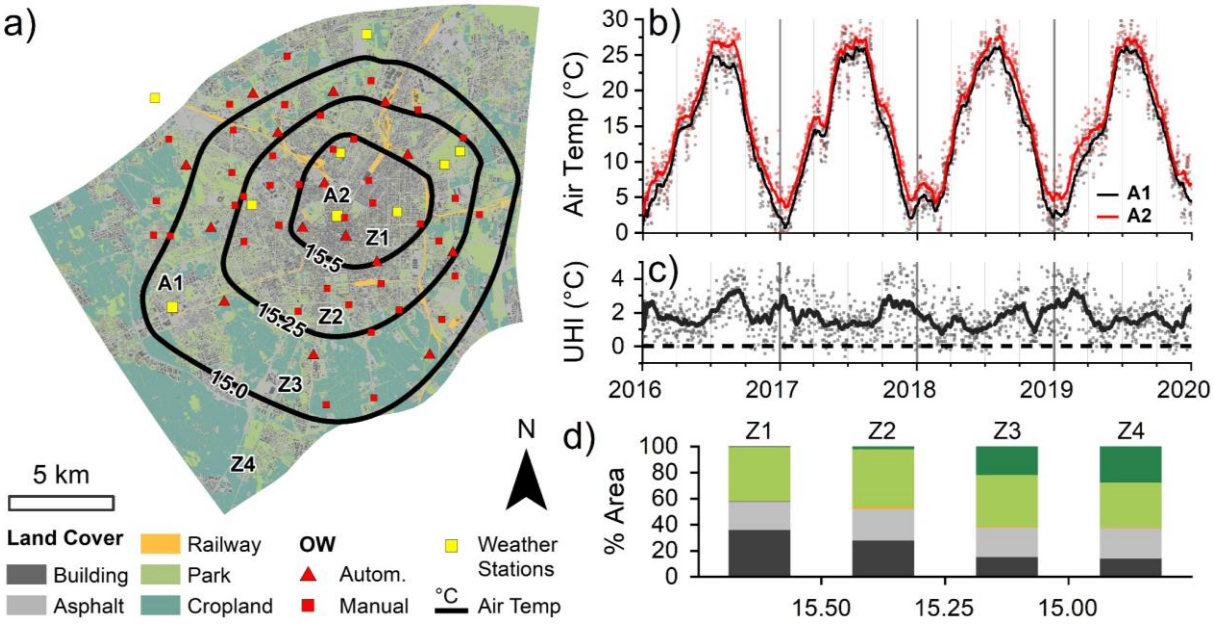


***Figure 9.3*** *- (a) Map showing the spatial distribution of the land cover type, the groundwater instrumented (autom.) and manually measured observation wells (OW) and the weather monitoring locations. Isolines show the mean annual air temperature for the period 2014 to 2021 and divide the study area into four concentric zones (Z1 to Z4 from the center outwards). (b) Air temperature time series recorded at locations A1 and A2. (c) Daily difference between the air temperature recorded at A2 and A1 showing the UHI effect. (d) Percentage of land cover type inside the four zones of the city.*

### 9.4.2. FEM numerical model

The global problem of the subsurface for the transient fluid mass and thermal energy balance is described by (Eq. 4.1) and (Eq. 4.2). The cumulative impact of fluid and heat sources on the groundwater thermal regime in the study area was investigated developing a city-scale 3D FEM numerical model with the commercial code FEFLOW® (Diersch, 2014). The fluid flow and heat transport in the shallow aquifers was simulated adopting the continuum assumption (section 4.2), the domain was discretized into elements, and time into intervals (time steps). Combining the size of the model and the spatial resolution (element size) a great number of elements was necessary resulting in high computational requirements. The ratio between simulated and real time during a transient coupled simulation was about 0.0025 (meaning that 22 hours are needed to simulate 1 year) with a quad-core 3.7 GHz processor. To save time during the calibration procedure parallel simulations were performed on up to 4 machines.

### 9.4.3. Mesh geometry

The computational domain is a fully 3D mesh generated through the layered mesh approach by FEFLOW® (i.e. triangular prisms generated by vertical translation of a 2D plain triangular mesh). The domain (**Figure 9.1**) covers an area of 307 $km^2$ (approx. 16 x 20 km) and the total vertical thickness ranges between 70 and 125 m. The northern (upgradient – inflow) and southern (downgradient – outflow) boundaries follow two regional hydraulic head isolines, as from mean piezometric elevation; to the east and west the model is bounded by two flow lines (i.e. perpendicular to the head isolines, assuming no transversal flow). Vertically, the model is bounded to the top and bottom by the ground surface and the base of SC aquifer, respectively. The total volume is $3.23*10^{10}$ $m^3$ divided in 6,260,142, arranged in 49 layers of 127,758 elements each. The maximum horizontal dimension of the elements is 250 m with local refinement around wells, canals and tunnels up to a minimum dimension of 3 m. The vertical size (i.e. the distance between layers) ranges between 1.3 and 3.4 m and averages to 2.1 m.

### 9.4.4. Material properties

The heat transport in highly conductive aquifers is mainly dominated by advection (Bear, 1972; Deming, 1994) and the characterization of aquifer heterogeneities is essential to reproduce the groundwater flow velocity field that governs the heat transport in groundwater (see also section 4). As said above, only the first two shallow depositional sequences (aquifer P and SC) were considered. The variability of hydraulic and thermal parameters due to depositional processes was spatialized in the domain by means of 3D geostatistical techniques from borehole logs and lithological descriptions parametrized in previous studies (**Table 5.1**). A total of 2,876 borehole logs were available with average depth of 52 m and maximum depth of 580 m (**Figure 9.4a**). The average spacing between borehole was about 250 m with a strong difference between the city center and outer areas due to the occurrence of construction works and deep well fields that need subsurface characterization by bore logging (**Figure 9.4a**). Each log was subdivided into stratigraphic units and classified according to (De Caro et al., 2020b) as described in section 5.6. Accordingly, hydraulic conductivity and porosity values estimated from grain-size distribution data (De Caro et al., 2020b) were associated to each borehole layer (**Figure 9.4c**) according to the hydrofacies classification shown in **Table 5.1**.

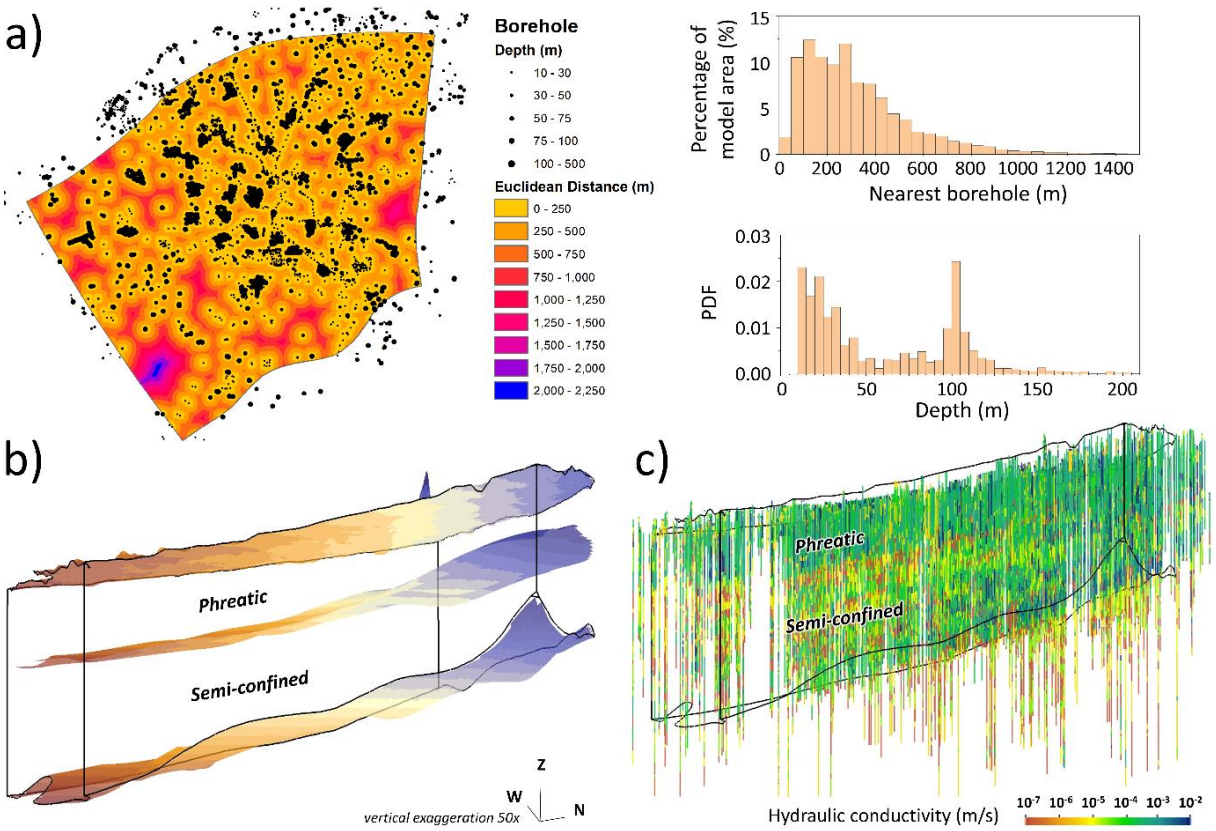


***Figure 9.4*** *– (a) Map of the model domain showing the spatial distribution of the available borehole logs and the proximity analysis (Euclidean distance). The frequency distributions of the proximity of a borehole and the borehole depth are shown by histograms. 3D views of (b) the boundary surfaces between the phreatic and semi-confined aquifer and (c) the available borehole logs with the estimated hydraulic conductivity (m/s) of each layer as from (De Caro et al., 2020b).*

Since the frequency distribution of the hydraulic conductivity is typically log-normal, the data were transformed into the argument of the base-ten-logarithm to obtain a Gaussian distribution (**Figure 9.5a**). The transformed values were interpolated through 3D Ordinary Kriging over the mesh nodes with the following exponential model parameters: nugget = 0.1 Log m/s, partial sill = 1.73 Log m/s, horizontal range = 1000 m, vertical range = 6 m. The spatial distribution of the variance of the estimation (i.e. Kriging error/uncertainty) is shown in **Figure 9.5b** where the dependency on the surrounding data is clear. The frequency distribution of the interpolated hydraulic conductivity in the phreatic (P) and semiconfined (SC) aquifers was grouped based on the hydraulic conductivity range of the previously identified lithofacies obtaining the following classes (**Figure 9.5**): gravel ($9*10^{-2}$ m/s > K > $5*10^{-4}$ m/s), sand ($5*10^{-4}$ m/s ≥ K > $4*10^{-5}$ m/s), silt ($4*10^{-5}$ m/s ≥ K > $3*10^{-6}$ m/s) and clay ($3*10^{-6}$ m/s ≥ K > $1*10^{-8}$ m/s).

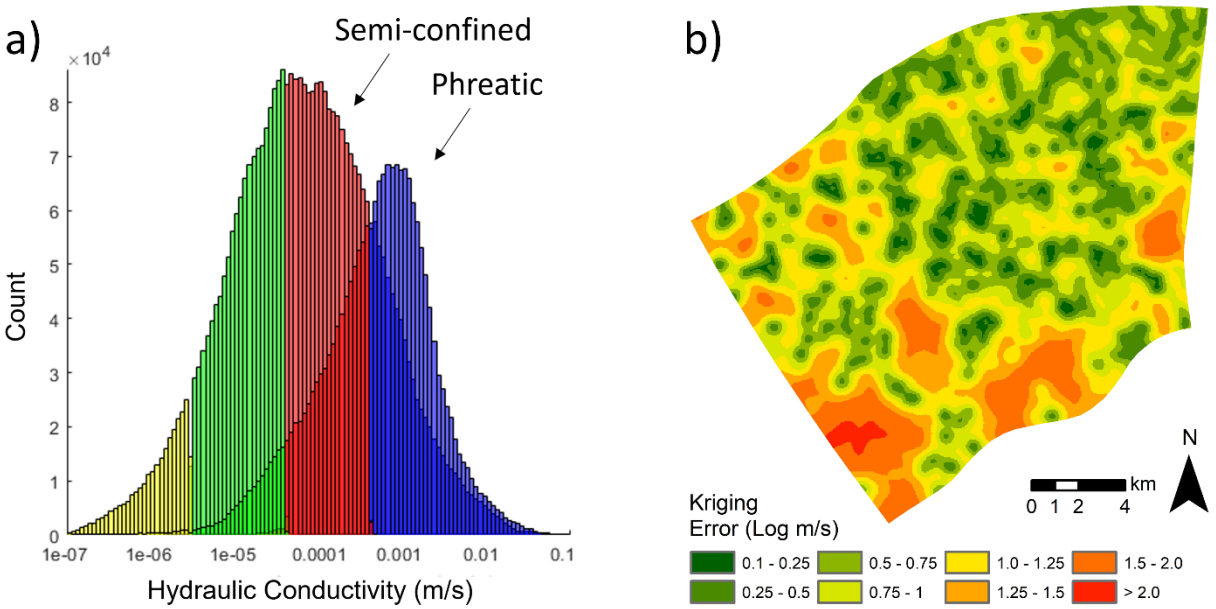


***Figure 9.5*** *– (a) Frequency distribution of the interpolated hydraulic conductivity of the phreatic and semi-confined aquifer units. Thresholds of conductivity used to discretize the gaussian distribution are emphasized by colors (blue=gravel, red=sand, green=silt, yellow=clay). (b) Map of the model domain (top view) showing the spatial distribution of the variance of the estimation (i.e. Kriging error).*

The spatial distribution of the hydraulic conductivity was then simplified considering the volume weighted average of the conductivity of the elements in each class as a unique equivalent-value. The equivalent-conductivity values of $1.25*10^{-3}$, $1.30*10^{-4}$, $1.44*10^{-5}$ and $1.20*10^{-6}$ m/s were assigned to the gravel, sand, silt and clay classes, respectively. This approach, known as structural regularization (DHI-Wasy, 2016; Doherty et al., 1994), significantly reduces the calibration computing time without losing information on large scale heterogeneities. Thus, grain-size based classes were used to assign other essential parameters into the model converting the hydrofacies classification proposed by (De Caro et al., 2020b) into thermofacies based on the grain-size distribution. The thermal conductivity (λ) and volumetric heat capacity (*svc*) values were assigned to each grain-size-based subdomain of the model from (VDI 4640/2, 2001). The proposed values for the hydro- and thermofacies are summarized in **Table 9.1**.

***Table 9.1*** *– Hydraulic and thermal properties assigned to the homogeneous-equivalent grain-size units.*

| Hydro-/ Thermofacies | **Mean $K_{XY}$ (m/s)** | **Total Porosity (-)** | **Thermal conductivity (W/mK)** | **Vol. heat capacity ($MJ/m^3K$)** |
|---|---|---|---|---|
| ***source*** | *Grain-size distribution* (De Caro et al., 2020b) | | *Parameters from VDI 4640 (2001)* | |
| *Gravel* | $1.25*10^{-3}$ | 0.29 | 2.12 | 2.45 |
| *Sand* | $1.30*10^{-4}$ | 0.33 | 2.17 | 2.48 |
| *Silt* | $1.44*10^{-5}$ | 0.38 | 2.02 | 2.5 |
| *Clay* | $1.20*10^{-6}$ | 0.45 | 1.72 | 2.5 |

To support the calibration of the hydraulic conductivity, the effects of different grain-size distributions between the aquifer P and SC were considered by further subdividing the classes according to the pertaining aquifer. The equivalent hydraulic conductivity of each subclass in the shallow aquifer was imposed to be greater than its corresponding subclass belonging to the semi-confined unit. The distinction between these two regional groundwater bodies is represented by the regional aquitard layer shown in **Figure 9.4b**.

**Figure 9.6** shows a 3D view of the available borehole logs colored by the grain-size distribution based hydraulic conductivity, the spatial distribution of the interpolated hydraulic conductivity and the classification in homogeneous grain-size based classes with their equivalent calibrated value along the NNW-SSE cross section.

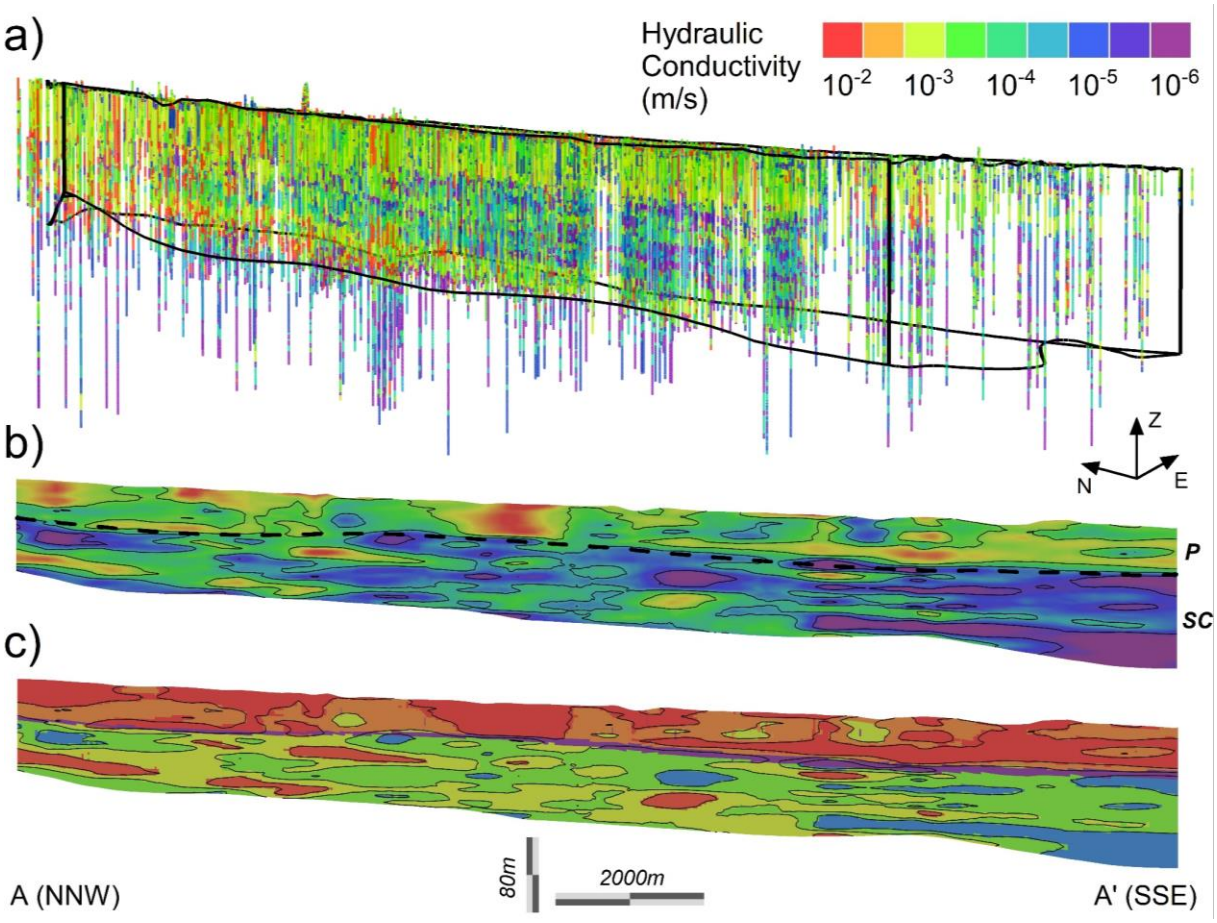


***Figure 9.6*** *– (a) 3D view of the available borehole logs colored by the hydraulic conductivity based on grain-size distributions* (De Caro et al., 2020b)*. Cross-sections showing: (b) the hydraulic conductivity field interpolated by means of Ordinary Kriging for the phreatic (P) and the semi-confined (SC) aquifers (the dashed line represents the aquitard dividing the two units), and (c) the classification of the domain in homogeneous grain-size based classes with their equivalent calibrated value. (See* ***Figure 9.1*** *for the location of the cross-section and viewpoint).*

### 9.4.5. Calibration and validation

The continuous groundwater head and temperature data at specific depth from 15 locations were used to calibrate the flow and heat-transport parameters based on the period 2016 to 2019, while temperature-depth profiles from 55 locations (15 from the calibration set and 40 at other locations, **Figure 9.3a**) from 2019 to 2021 were used to validate the model results. The calibration of hydraulic and thermal parameters was performed means of the PEST algorithm for automatic parameters estimation (Doherty et al., 1994), implemented in FEFLOW® with the FePEST utility (DHI-Wasy, 2016). The calibration of transient fluid-flow/heat-transport coupled numerical models requires significant efforts in terms of number of runs and computing time. Since the number of simulations required for the automated

calibration algorithm is proportional to the number of identified changeable parameters (Doherty et al., 1994), to reduce the total computing time, the parameter space was optimized by applying structural and subspace regularizations (DHI-Wasy, 2016).

The structural regularization was used to reduce the total number of hydraulic and thermal parameters by choosing a limited number of zones where a unique equivalent parameter is assigned and correspond to a subset of elements identified by intervals of interpolated hydraulic conductivity (i.e. grain-size classes). The number of parameters that PEST can change to minimize the objective function was reduced by quantifying how each parameter influences the hydraulic head and temperature observations in the model. The choice between changeable and non-changeable parameters, known as subspace regularization, was supported by a linear sensitivity analysis where the influence of parameters variation on the observations is expressed in a Jacobian matrix in terms of derivatives of the model-generated observations with respect to the parameter variations. The Jacobian matrix was computed for a steady-state scenario for the fluid-flow and for one year of transient simulation for the heat-transport. **Table 9.2** lists all the model parameters which were selected for calibration according to the composite sensitivities presented in the results section and to the effective range of variation. Moreover, a sensitivity analysis was conducted to study the effects of the thermal dispersivity on the groundwater temperature distribution. The phase shifting between the simulated and measured temperature was evaluated by comparing the Spearman's correlation index between the time derivatives (daily increment) of the simulated and measured temperature.

***Table 9.2*** *– Hydraulic and thermal parameters included in the model*

| *Parameter* | *Symbol* | *Unit* | *Subdivision* | *Calibrated* |
|---|---|---|---|---|
| ***Hydraulic properties*** | | | | |
| Hydraulic Conductivity (ratio $K_h/K_z$ = 5) | K | m/s | G-S class | Yes |
| Porosity | ϕ | - | G-S class | No |
| Specific Storage | $S_S$ | 1/m | Domain | No |
| Fluid Transfer rate ($3^{rd}$ kind river boundaries) | - | 1/s | River paths | Yes |
| ***Thermal properties*** | | | | |
| Thermal conductivity | λ | W/mK | G-S class | No |
| Volumetric heat capacity | svc | $J/m^3K$ | G-S class | No |
| Fluid Transfer rate: | | | | |
| • $3^{rd}$ kind river boundaries | - | $W/m^2K$ | River paths | Yes |
| • Underground tunnels | | | Tunnel tracks | No |
| Longitudinal and transversal dispersivity ($D_L$ / $D_T$ =10) | $D_L$ , $D_T$ | m | Domain | Yes |

### 9.4.6. Boundary conditions (BCs)

As mentioned above, the model domain is bounded by two hydraulic head isolines (up- and downgradient boundaries) and, laterally, by two flow lines. Due to the high conductivity contrast between the semi-confined (SC) and the deeper confined aquifer (C), not considered in this model, fluid and heat exchanges between these two units were neglected and the bottom of the model was assumed as a no fluid- and heat-flow boundary. All the natural and anthropogenic boundaries that contribute to the fluid and heat budget considered in this model (described in the following sections) are summarized in a 2D plain view in **Figure 9.7** and listed in **Table 9.3**. **Figure 9.8a** shows a 3D view of the modeling domain and the location and geometry of the main boundary conditions in the subsurface; **Figure 9.8b** shows a detail of the mesh refinement around the pumping and geothermal wells and along with the tunnel tracks, and **c** shows in detail the vertical division of the domain into 49 layers.

***Figure 9.7*** *– Plain view of the modeling domain showing the spatial distribution of the fluid and heat boundary conditions. For the 3D geometry of the boundary conditions in the subsurface see* ***Figure 9.8****.*

**Table 9.3** – *Summary of the boundary conditions applied to the model*

| | ***Fluid*** | ***Heat*** |
|---|---|---|
| ***Upgradient Boundary*** | 1st kind BC – Groundwater head values from regional hydraulic head maps and transient daily fluctuations from nearby OW. | 1st kind BC – Temperature of groundwater entering the model upgradient derived from vertical temperature profiles near the boundary. |
| ***Downgradient Boundary*** | | Heat leaving the model through the fluid outflow from the downgradient boundary. |
| ***Top Surface*** | *Recharge from infiltration:*<br>2nd kind BC – Precipitation data obtained from rain-gauge stations. Daily values corrected by the evapotranspiration rate calculated according to the FAO method based on the Penman-Monteith equation (Allen et al., 1998) and reduced by runoff according to the percentage of sealed surfaces around each node (considering the Voronoi tessellation of the mesh nodes).<br><br>*Outflow from phreatic springs:*<br>1st kind BC – Pressure ≤ 0 kPa | *Heat sink/source* calculated via the SoilTemp 1D multi-layer analytical solution by JR-AquaConSol (Kupfersberger et al., 2017; Rock and Kupfersberger, 2018).<br>The soil cover from a high-resolution land use map was divided into four classes: (1) building, (2) asphalt, railway (3) and (4) green. For each class, surface temperature time series and vertical profiles of the shallow underground thermal properties were assigned.<br>The heat flux between the surface and the SoilTemp/FEFLOW interface is obtained through a 1D analytical solution considering the difference between the surface temperature at time *t* and the calculated temperature at the reference depth at time *t-1*. The total heat flux in each element is obtained combining the fluxes of each class with the relative land cover proportion and is converted into a sink/source term at the interface depth. |
| ***Canals*** | 3rd kind BC – In/out-flow proportional to the difference between the river/canal water level and the river/canal bed or the groundwater level for losing and gaining conditions, respectively, and the river/canal bed conductance expressed with the fluid-transfer coefficient. Water levels were obtained from hydrometric stations and the canal bed elevation was derived from representative hydraulic sections (**Figure 5.4**). | 3rd kind BC – Water temperature time series were obtained from the hydrometric monitoring network.<br>The transfer coefficient was calibrated using groundwater temperature data from two OW located 300 and 750 m downgradient of the *"Grande"* and *"Martesana"* canals, respectively. |
| ***Water Supply Wells*** | Weekly abstraction rates ($Q$) distributed along the well screens (average screen bottom 100 m, average screen interval 50 m). 476 wells in total. | Heat removed from the aquifer (H) by removing the fluid mass (Q):<br>$H = Q * \Delta T * svc$ |
| ***Geothermal Wells*** | No fluid imbalance. Abstraction = injection rates were calculated according to the power demand and the temperature drop through the following equation:<br>$Q = P \,/\, svc\, \Delta T$ | Daily power extraction rates ($P$) calculated considering degree days and average peak loads for heating and cooling mode, respectively. 262 abstraction and 283 reinjection wells organized in 185 well fields. |
| ***Tunnels*** | Six underground lines: quasi-impervious elements. | 3rd kind BC – Daily temperature inside tunnels.<br>Transfer coefficient calculated considering the thickness and the thermal properties of the structural tunnel lining and the portion of ground filled with grout. |

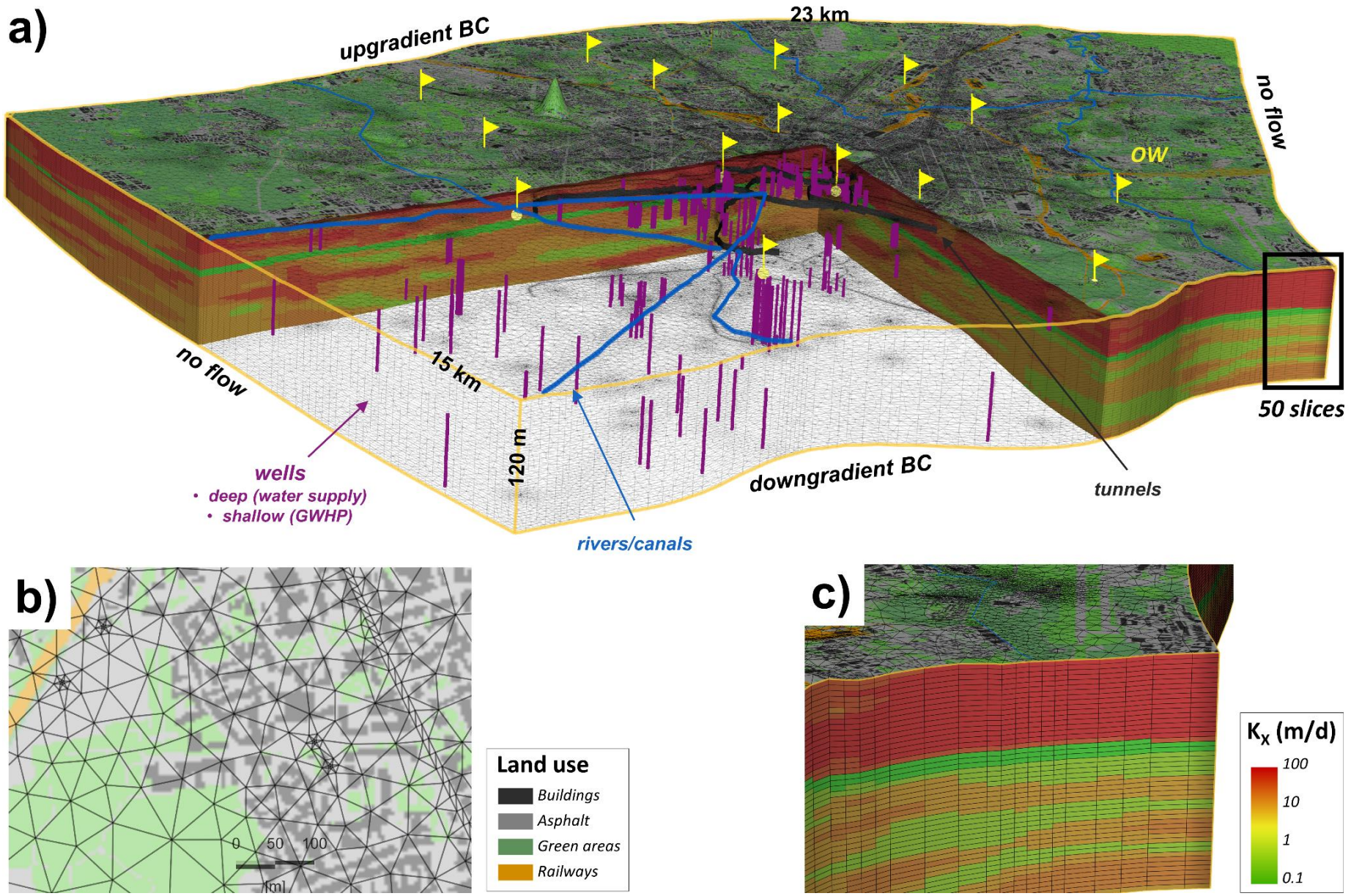
a)
upgradient BC
23 km
no flow
OW
no flow
15 km
120 m
50 slices
wells
• deep (water supply)
• shallow (GWHP)
rivers/canals
downgradient BC
tunnels
b)
0 50 100
[m]
Land use
Buildings
Asphalt
Green areas
Railways
c)
$K_X$ (m/d)
100
10
1
0.1

***Figure 9.8*** *– (a) 3D view of the modeling domain showing the spatial distribution of the hydraulic conductivity ($K_X$) and the main boundary conditions (for a plain view see Fig. 9.7). The elements are partly hidden to show the location and geometry of the boundary conditions in the subsurface. (b) 2D view of a slice plane showing the land use and the mesh refinement around the pumping and geothermal wells and along with the tunnel tracks. (c) Detail of the 3D view in (a) showing the vertical division of the domain into 49 layers.*

#### *9.4.6.1. Regional groundwater flow and heat-transport*

Up- and downgradient vertical boundaries were set as 1$^{st}$ kind fluid BC by considering the hydraulic head time series of the closest up- and downgradient head observation well (OW 1 and 15 in **Figure 5.3**), adjusted by the distance and the local hydraulic gradient along the groundwater flow direction between the point and the boundary. For the thermal transport, a 1$^{st}$ kind BC was assigned to the upgradient vertical boundary from the temperature-depth profiles located north of the study area considering the depth of each node. To simulate the natural heat outflow along the downgradient boundary due to the fluid outflow, no thermal boundary condition was assigned.

#### *9.4.6.2. Upper boundary condition*

***Groundwater recharge***

Groundwater recharge from precipitation was calculated by means of a 2$^{nd}$ kind BC applied to the nodes at the top surface. First, the total daily precipitation was scaled by the daily evapotranspiration rate calculated according to the FAO Penman-Monteith equation (Allen et al., 1998). Daily time series of precipitation, air temperature, humidity, wind speed, and solar radiation were obtained from the regional meteorological stations database (ARPA Lombardia, 2021). **Figure 9.9a** shows the total precipitation ($P_{tot}$), the potential evapotranspiration rate ($ET_0$), the effective evapotranspiration ($ET_R$) and the effective precipitation ($P_{eff}=P_{tot}- ET_R$) for the year 2019. Then, to obtain the groundwater recharge rate at each node, $P_{eff}$ was scaled by the infiltration coefficient according to the percentage of potential infiltration areas (e.g., parks, green spaces, bare soil) inside the Voronoi polygon enclosing each node (**Figure 9.9b**, **c**, **d, e**).

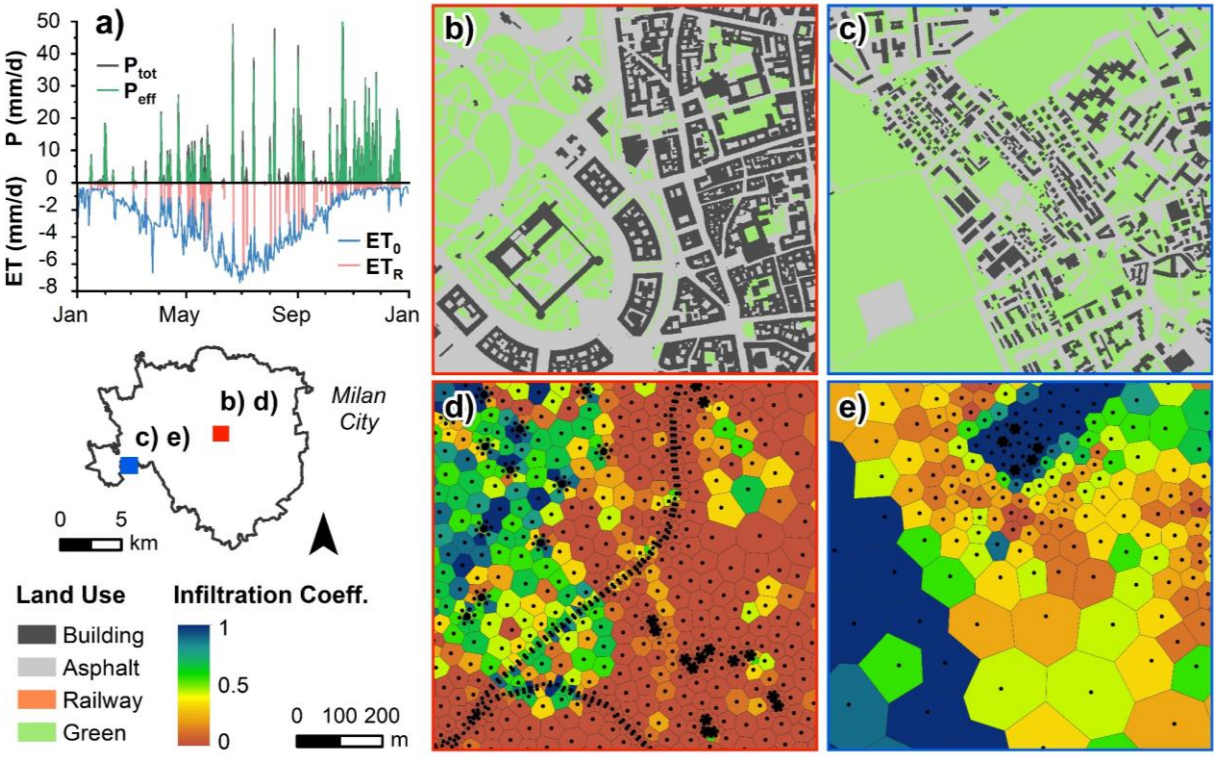


***Figure 9.9*** *– (a) Total daily precipitation ($P_{tot}$), potential ($ET_0$) and effective ($ET_R$) evapotranspiration and effective precipitation ($P_{eff}$), time series for 2019. Maps showing the land use discretization of the surface at two locations (b and c) and the calculated infiltration coefficient (d and e).*

***Thermal recharge***

The heat flux from the surface into the subsurface results from different sources such as the shallow soil thermal regime and heated buildings basements. Theoretically, these sources could be implemented as discrete boundary conditions in the 3D FEM model domain according to their geometry, but practically, not enough soil temperature data were available in the study area (generally their spatial density is too poor for a large scale analysis) and the spatial discretization of the domain according to the land cover (e.g. by forcing the mesh element edges to follow the outlines of buildings, roads, green areas) would lead to very complex mesh geometries and extensive computational times. To the aims of this city-scale analysis, a simplification and upscaling of the upper thermal boundary was adopted by coupling the multi-layer conductive analytical solution (valid only above the water table) by Händel et al. (2013) through the SoilTemp plug-in by JR-AquaConSol (Kupfersberger et al., 2017; Rock and Kupfersberger, 2018) to the numerical computation of heat transport by the FEFLOW® code.

By means of the SoilTemp plug-in, the conductive heat transfer between the surface and a subsurface interface depth is obtained analytically for each element by averaging the single contribution of each land use type according to their proportions and releasing this amount of heat into the FEFLOW® code as a sink/source term at the SoilTemp/FEFLOW® interface. The depth of the interface was assumed 6 m below the ground surface to be always above the water table and to fully enclose the bottom of building basements.

The analytical solution by Händel et al. (2013) accounts for the heat transport through multiple layers by conduction. First, a 1D vertical profile of the thermal properties has to be defined and, secondly, the heat transfer between the ground surface (at temperature $\mathbf{T_{surface}}$) and the subsurface (at temperature $\mathbf{T_{model}}$) is calculated across the vertical layers considering the heat conduction and energy conservation laws and, finally, converted into thermal energy as shown in **Figure 9.10**.

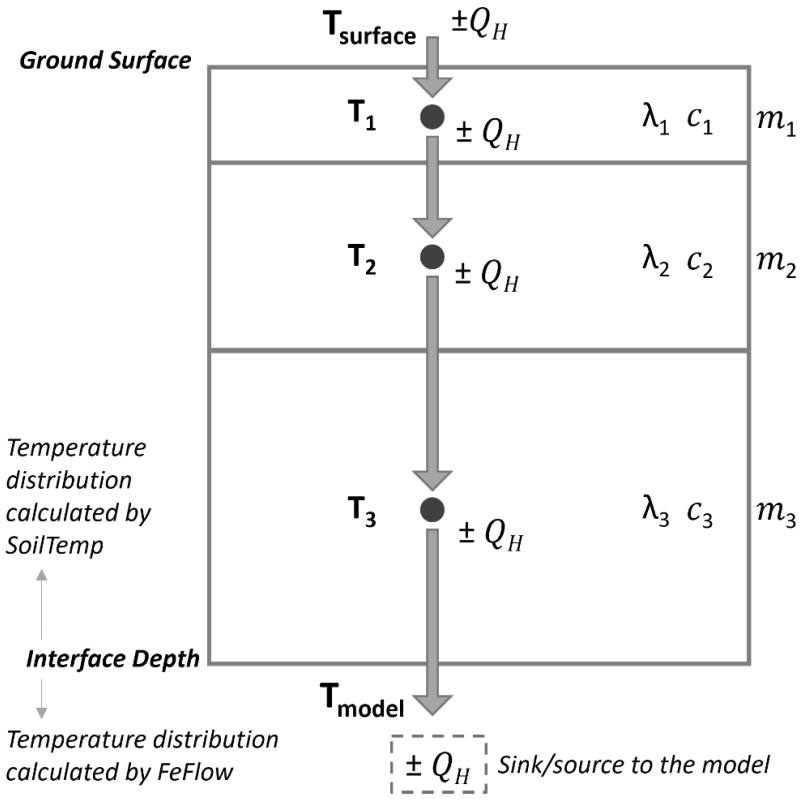


***Figure 9.10*** *– Schematic representation of the multi-layer analytical solution by Händel et al. (2013) to calculate the heat flow from the surface to the model.*

Thus, the heat transfer from the surface to the model is calculated by computing the temperature distribution in the layers through an iterative procedure starting from layer *1* to layer *n* (interface depth), and converting the temperature change in thermal energy as follows:

1. The heat flow from one layer from/to the next below ($\pm Q_H$) at each time step $t_i$ is obtained considering the temperature difference $\Delta T_i$ between the upper layer (at time $t_{i-1}$) and the lower layer (at time $t_i$), the time step duration ($t_i - t_{i-1}$), the weighted average thermal conductivity of the layers ($\lambda_{eq}$), and the distance between the layer centers ($e$):

$$Q_h = \lambda_{eq} * \frac{\Delta T_{ti}}{e} * (t_i - t_{i-1}) \qquad \textit{(Eq. 9.1)}$$

2. Successively, the heat flow is converted into temperature changes $\Delta T$ of the lower layer considering the thickness of the layer ($m$), the volumetric specific heat capacity ($c$), and the heat flows from the upper/lower layers into the current layer:

$$\Delta T = \frac{\pm Q_H}{m * c} \qquad \textit{(Eq. 9.2)}$$

3. Iteratively, the temperature change between all the layers is calculated and the total positive/negative heat flow from the surface to the model implemented into the numerical computation as a sink/source term.

This 1D analytical solution is implemented in the SoilTemp plug-in which considers different vertical profiles of thermal properties according to the land use class and averages their single contribution for each upper elements according to their relative proportions. Hence, the 1D vertical profiles of the subsurface thermal properties **(i)** and the associated surface temperature time-series **(ii)** have to be characterized for each land use type. Finally, the percentage of each land use class has to be calculated for each element **(iii)** and organized in a thermotop (i.e. elements with similar percentages of land use classes) classification table.

**(i)** The vertical profile of the subsurface thermal properties of the was defined. A typical basement depth of 3 m was uniquely assigned to the “building” class. This configuration represents buildings with shallow foundations, which from an analysis based on the age of the buildings can be assumed for most of the cases. More recent buildings with deeper

foundations and underground spaces are not well represented due to the lack of information on the subsurface occupation of the study area. The “asphalt” class was characterized by 0.1 and 0.4 m of asphalt and compacted gravel, and the “railway” class by 0.7 m of railway ballast, below which lies the natural soil. The thermal properties of the ground and the other materials were derived from (VDI 4640/2, 2001).

**(ii)** Then, a reference temperature time-series was assigned to the “asphalt”, “railway” and “green” classes according to the air temperature measured by the meteorological stations in the study area. In total, three different time series were created to account for the UHI effect in the atmosphere (Pichierri et al., 2012; Previati and Crosta, 2021a). **Figure 9.3a** shows the location of the available weather monitoring stations and the mean annual air temperature isolines where the atmosphere UHI is clearly visible. The temperature time-series (**Figure 9.3b**) recorded at station A2 was assigned to the elements enclosed by the 15.5 °C isoline, the temperature from station A1 to the elements outside the 15.25 °C isoline, and to the elements in between ($15.5 > T_{mean} > 15.25$ °C) the average of the two series. For the building basements, a sinusoidal temperature time series was assumed ($T_{mean}$=19 °C, amplitude=1 °C).

**(iii)** Finally, the percentage of area covered by buildings, roads, railway tracks, and green areas was computed for each element and rounded to 10% as shown in **Figure 9.11**.

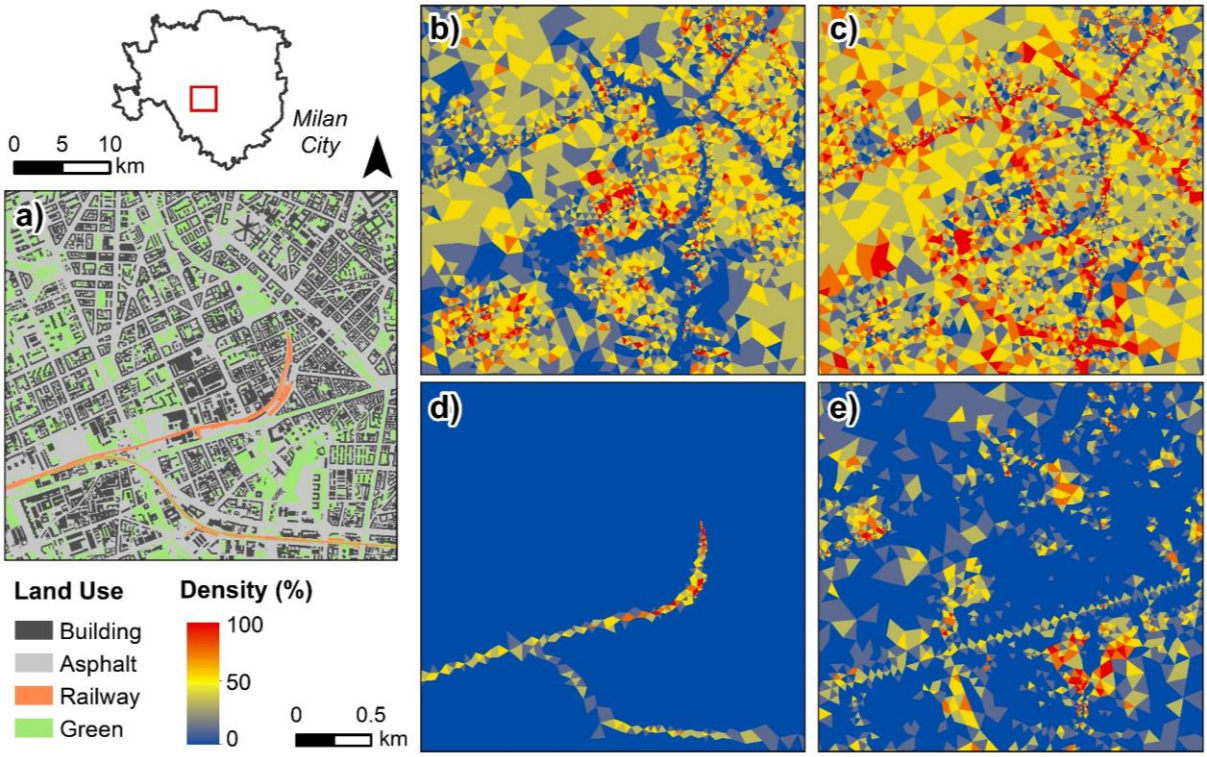


***Figure 9.11*** *– Maps showing a detail of the land cover classification for a specific area (a) and the surface spatial discretization (mesh elements) together with the percentage of area (density) covered by buildings (b), asphalt (c), railway (d) and green areas (e).*

The 10%-rounded percentage of the four land cover types were combined to obtain 164 unique combination of land cover percentages (i.e. thermotops). Thus, each element contains a thermotop number between 1 and 164 (**Figure 9.12a**) and a thermotop definition table was generated having the information on the percentage of the four land cover classes for each thermotop. As an example, a detail on the thermotop classification and the associated thermotop definition table is shown in **Figure 9.12b**.

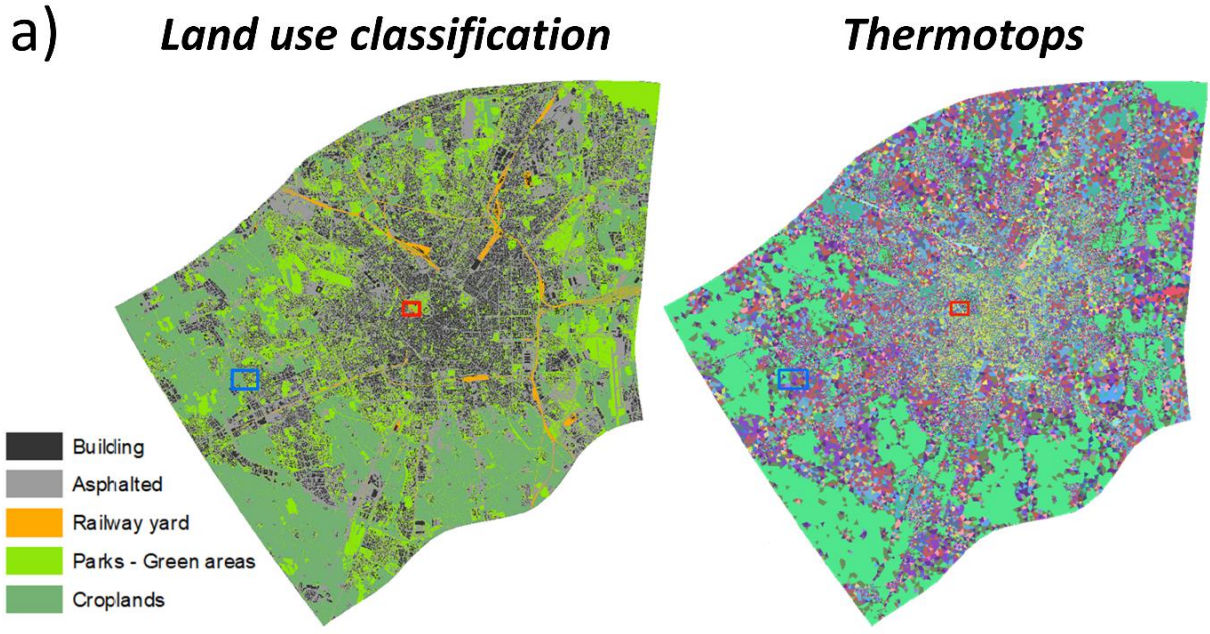


b)

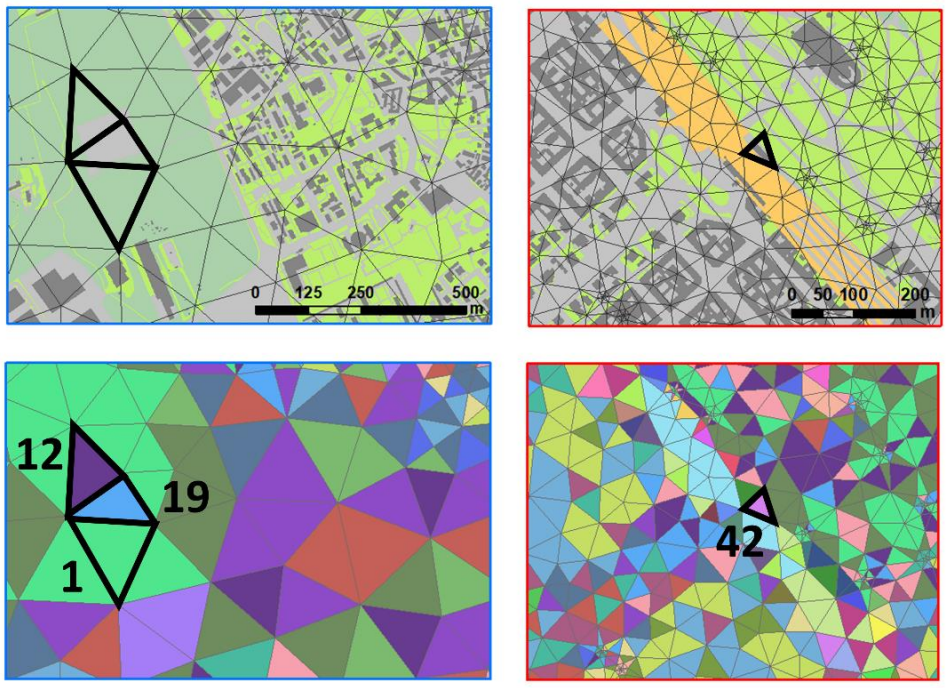


| Thermotop | % Building | % Asphalt | % Railway | % Green |
|---|---|---|---|---|
| **1** | 0 | 0 | 0 | 100 |
| **12** | 0 | 40 | 0 | 60 |
| **19** | 0 | 80 | 0 | 20 |
| **42** | 40 | 20 | 20 | 20 |

***Figure 9.12*** *– (a) maps of the model domain showing the spatial distribution of the land use classification and the 164 unique combinations of land cover class percentage inside the elements (thermotops). (b) Map details (see (a) for the extent and location) showing the thermotop classification of the mesh elements and an example of the associated thermotop definition table for four thermotops (1, 12, 19 and 42)*

#### *9.4.6.3. Surface waters*

In the study area, a dense hydrographic network consisting of rivers, canals and irrigation systems exists. In this study, only the main rivers (Lambro, Seveso and Olona) and canals (Martesana, Pavese and Grande) were considered, whereas the irrigation network was neglected as it covers only a limited part of the area (**Figure 9.1**). The fluid losses and gains from the surface water network were estimated by a 3rd kind BC through the equation:

$$Q_{fluid} = A * \phi * (H_{ex} - H_{in}) \quad \textit{(Eq. 9.3)}$$

The fluid budget $Q_{fluid}$ [$m^3\ s^{-1}$] is proportional to the infiltration area $A$ [$m^2$], the difference between the river/canal water level $H_{ex}$ [m], and $H_{in}$ [m], which for draining conditions (i.e. groundwater level higher than the river/canal water level) is the water table, while for losing conditions (i.e. the river/canal water level is higher than the groundwater) is the riverbed elevation, and the riverbed conductance $\phi$ (also referred to as "fluid transfer rate"), which was calibrated in transient state against groundwater levels measured close to rivers/canals (in particular at OW 6, 12 and 13; **Figure 5.3**).

Similarly, the heat inflow/outflow from river/canal boundaries was calculated by means of a 3rd kind BC:

$$Q_{heat} = A * \phi * (T_{ex} - T_{in}) \quad \textit{(Eq. 9.4)}$$

where $T_{ex}$ [K] is the river/canal temperature and $T_{in}$ [K] the ground/groundwater temperature. Water levels and temperature time series for the 6 rivers/canals considered in this study (**Figure 9.1**) were obtained from the regional environmental monitoring agency database (ARPA Lombardia, 2021). **Figure 9.13a** and **b** show the water level fluctuations (m above the riverbed) of rivers (Seveso, Lambro, Olona) and canals (i.e. "Navigli", Martesana, Pavese, Grande) included in the model. Opening, closing and low discharge periods due to the periodic canals cleaning are clearly visible from the hydrographs. **Figure 9.13c** shows the water temperature time series obtained by interpolating the available river/canal temperature data from 2015 to 2019 with a sine function (measures every 3 months). The water temperature time-series were repeated periodically to cover the entire modeling period.

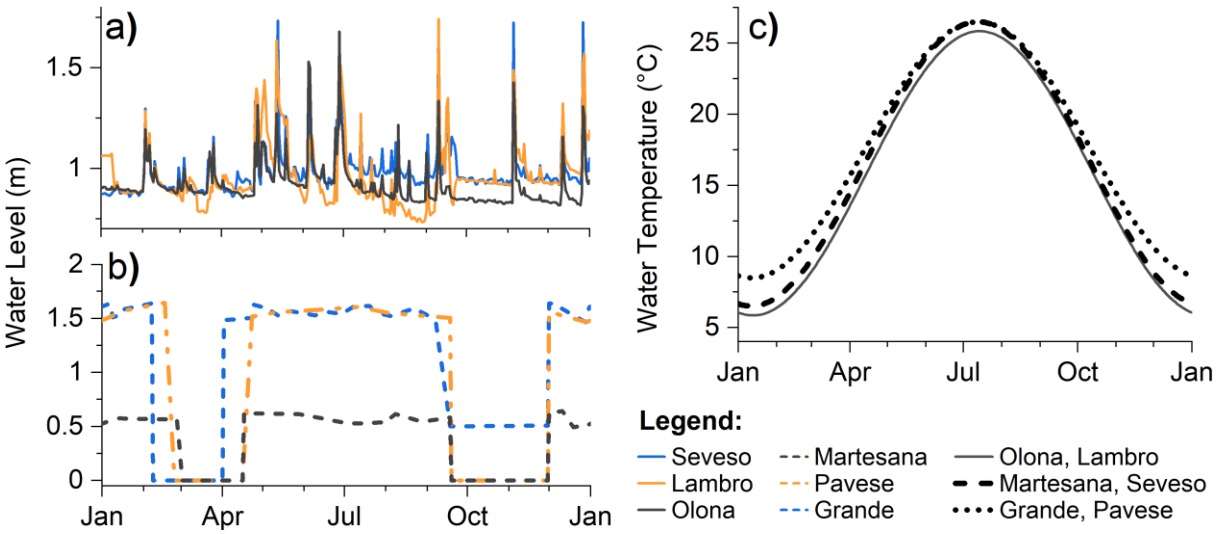


***Figure 9.13*** *– Water level fluctuations (m above the riverbed) for (a) rivers and (b) canals (i.e. Navigli) in 2019 and (c) water temperature periodic time series.*

#### *9.4.6.4. Water supply and geothermal wells*

The fluid outflow via the water supply wells was calculated with a specific 4$^{th}$ kind BC "Multilayer-Well" which is a flux BC implemented in FEFLOW® to automatically distribute the outflow between the nodes located inside the screened depth intervals of the wells proportionally to the transmissivity of the layers crossed by each node (Diersch, 2014). Estimated daily discharge rates were available for the pumping wells located in the Milan municipality, whereas outside this area only the total annual discharge of 2016 was available. Thus, the estimated total annual withdrawal from the supply wells in the model area is about $2.6*10^8$ $m^3/y$. The fluid and heat out-/in-flow through geothermal wells was calculated by means of the specific "Open-Loop" plug-in according to the energy demand curve and on the existing legal thresholds on the maximum temperature difference between extracted and reinjected fluid. According to the regional regulation (Regione Lombardia, 2017), a maximum temperature change of 5 °C is allowed and a upper constraint for reinjection of warm water of 21 and 23 °C is set for natural and urbanized areas, respectively. The location (**Figure 9.7**) of 545 geothermal wells (abstraction and injection) was retrieved from the regional wells database (Città Metropolitana di Milano and CAP, 2021). By means of a proximity analysis based on their mutual distance and the surrounding building boundaries, the wells were grouped into clusters representing 185 single plants. The daily power demand was calculated assuming that, according to typical geothermal installations in the Milan area showed in

section 6, a single well would serve a total residential space of 500 $m^2$ (i.e. 1 to 5 typical residential units). From the available air temperature time series, daily degree days were calculated assuming the reference temperature of 18.3 °C and 23.8 °C for heating and cooling mode, respectively (Banks, 2009a). Typical walls (0.35 W/$m^2$K) and roof (0.16 W/$m^2$K) thermal transmittances (BRE, 2012) were adopted to derive the daily power demand for the representative unit served by each well (**Figure 9.14a**). Thus, at locations with multiple wells, the assumed power demand of the typical residential unit served by a single well was multiplied by the total number of wells.

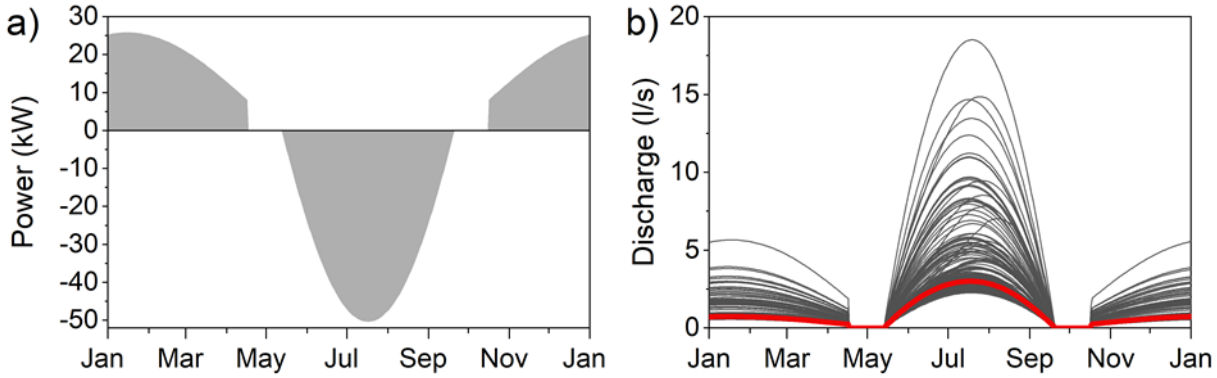


***Figure 9.14*** *- (a) Thermal energy demand calculated for the reference geothermal plant (1 well, 500 m2). (b) GWHP discharge calculated by the Open-Loop plug-in according to (Eq. 9.5) for the 185 plants (the discharge is proportional to the number of wells in each plant). Mean discharge of single-well-plants is highlighted in red.*

Finally, the heat abstraction/injection rate $H$ was calculated (neglecting the efficiency of the heat pump) through the following equation:

$$H = \frac{P}{\rho c_{fluid} * (T_{abs} - T_{inj})} \qquad \textit{(Eq. 9.5)}$$

where $P$ is the daily power demand [W], $T_{abs}$ and $T_{inj}$ [K] are the abstraction and injection groundwater temperature (note that, according to the local regulation, $T_{abs} - T_{inj} \leq 5\ °C$ and, in cooling mode $T_{inj} \leq 21\ °C$). **Figure 9.14b** shows the abstraction/injection discharge of GWHP calculated by the Open-Loop plug-in for the 185 geothermal plants according to (Eq. 9.5) (the discharge is proportional to the number of wells in each plant).

#### *9.4.6.5. Tunnels*

Six subway and underground railway lines cross the Milan city area through the shallow phreatic aquifer (P) for a total length of about 88 km (**Figure 9.7**). The tunnels have been built

over a period of about 60 years starting in 1957 and various construction methods have been adopted showing differences in terms of depth and type of excavation (De Caro et al., 2020a). **Table 9.4** summarizes the construction period starting from the first to the actual configuration and the main characteristics of the tunnels such as the diameter, the length, the depth of the tunnel axis and the percentage below the water table as of March 2016. Apart from line M1, most of the tunnels are submerged up to 15 m below the water table. The line M4 was still under construction during the first years of the modeled period and was further implemented by turning on the BC on the representative date of September 1st 2019, according to the end of the excavations of the main section.

***Table 9.4*** *– Main characteristics of the underground metro and railway lines in the study area. The tunnel depth was obtained as the distance between the ground surface and the tunnel axis. The percentage of tunnel length below the water table (WT) is obtained from groundwater levels as of March 2016. Construction periods include the entire time spans over which the present-day configuration was completed, including the successive extension of the lines. See* ***Figure 9.7*** *for the path of each line.*

| *Line* | *Construction period* | *Diameter (m)* | *Length (km)* | *Depth (m)* | | | *% Below WT* |
|---|---|---|---|---|---|---|---|
| | | | | *Mean* | *Max* | *Min* | |
| *M1* | *1957-1992* | *6.5* | *27* | *10.7* | *15.2* | *7.3* | *4.9* |
| *M2* | *1964-1994* | *7* | *39.4* | *26.5* | *32.1* | *7.4* | *98.1* |
| *M3* | *1981-1990* | *8* | *17.1* | *17.1* | *27.4* | *9.5* | *76.9* |
| *M4* | *2012-2022* | *8.5* | *15.2* | *16.4* | *26.8* | *9.6* | *100* |
| *M5* | *2007-2013* | *8.5* | *16* | *18.3* | *25.1* | *12.8* | *70.4* |
| *M6* | *1984-2004* | *8.5* | *16* | *16.6* | *23.6* | *5.2* | *64.8* |

The tunnels were implemented within the 3D numerical model according to their size and altimetric profile as provided by the designer MM Spa and their shape was simplified and adapted to the 3D layered mesh by selecting the elements intersected by the tunnel geometry (**Figure 9.15a**). To adequately reproduce the 3D shape of the tunnels, the mesh geometry was previously refined along the tunnel axes to have the horizontal dimension of the elements between 10 and 20 m and the vertical around 2 m. **Figure 9.15b** shows a detail of the adopted shape for the tunnel M3. For the fluid flow, the selected elements were considered quasi-impervious ($K = 1*10^{-6}$ m/d), while the heat outflow/inflow was simulated with a 3rd kind BC as described by (Eq. 9.4). The heat flow from/to the tunnels depends on the temperature inside the tunnel and the thermal conductivity of the walls. The terms of (Eq. 9.4) were

adapted so $T_{ex}$ is the temperature inside the tunnel, $T_{in}$ the ground/groundwater temperature, $A$ the relevant area and $\phi$ the thermal conductance (also referred to as "thermal transfer rate") of the walls given by:

$$\phi = \lambda / d \qquad \textit{(Eq. 9.6)}$$

where $\lambda$ and $d$ are the thermal conductivity and the thickness of the tunnel wall, respectively.

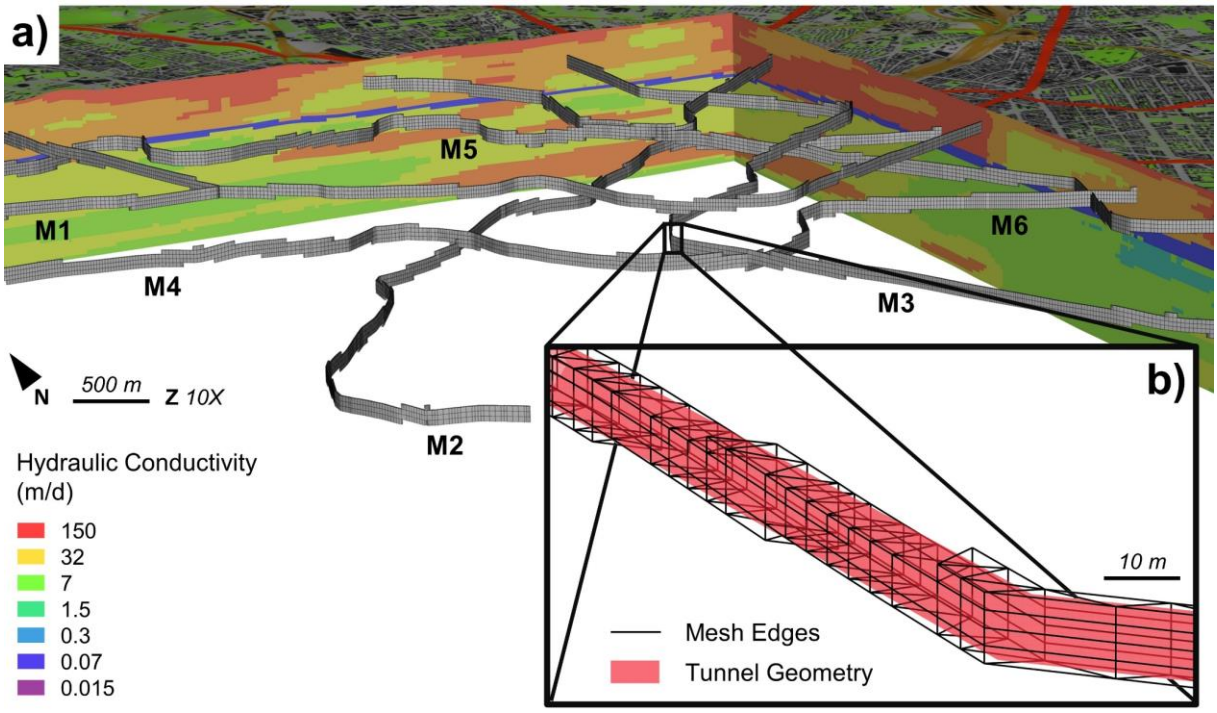


***Figure 9.15*** *– (a) 3D view (vertical exaggeration 10x) of the model domain showing the six underground tunnels (M1 to M6) and (b) mesh discretization of the tunnel geometry (in red the outer tunnel wall, black edges represent the simplified shape adopted in the model).*

### 9.4.7. Initial conditions

The hydraulic head distribution from a first steady-state run representing March 2016 was used as initial condition and to check for the consistency of all the fluid budget terms. Heat transport transient modeling requires appropriate initial conditions in terms of temperature distribution and, thus, energy stored in the subsurface. Since the thermal equilibrium in the subsurface results as the superimposition of different thermal processes that occur at different time scales (that could be significantly longer than the total simulation time), the definition of initial conditions is essential to consider the thermal energy already stored during the past decades. The subsurface can be considered a heat tank where the thermal energy

released/extracted from different heat sources/sinks located at the surface and in the subsurface propagates downwards as a thermal perturbation with different velocities according to the bulk thermal diffusivity, the temperature gradient and the advective velocity. Thus, the subsurface temperature distribution at a certain time is the snapshot of a thermal equilibrium that is difficult to reproduce with a relatively short simulation time (assuming temperature data are available for sufficient previous years). For this reason, the initial temperature distribution was estimated by means of the 3D interpolation of the mean annual groundwater temperature obtained from 61 temperature-depth profiles with a RMS between observed and interpolated temperature of about 0.3°C. This allowed defining the initial amount of thermal energy stored at different depth levels. Moreover, to each transient simulation a "thermal recharge" period of three years was added before the observations to remove the effects of initial conditions in the shallow subsurface where seasonal fluctuations are observed.

### 9.4.8. Thermal potential

The thermal energy stored within groundwater bodies depends essentially on their thermal regime (i.e. mean annual groundwater temperature and seasonal fluctuations) but the amount of energy that could be released/extracted into/from the subsurface depends on several aspects and is commonly referred to as the shallow geothermal potential. Bayer et al. (2019) distinguished between the amount of total heat stored/storable in the subsurface (theoretical potential) and its recoverable fraction (technical potential) upon realistic conditions such as the aquifer thermal properties, the required energy, the operative mode, the allowable groundwater temperature drop, and other variables related to the type of installation and the system configuration. In this study, we evaluated the thermal exchange technical potential of the aquifer P considering the thermal properties of the subsurface, such as the flow velocity and the bulk thermal conductivity, the maximum permitted temperature change (5°C) and thresholds (21°C) for groundwater reinjection (Regione Lombardia, 2017).
First, the theoretical geothermal potential ($P_T$) was assessed evaluating the heat out-/in-flow rate for a unit temperature variation, considering both the advective and conductive heat transport processes. Following (Eq. 4.2) the total injectable/removable heat ($P_T$) was derived

assuming stationary conditions ($\rho c_{bulk} \frac{\partial T}{\partial t} = 0$) and ignoring external positive/negative heat sources ($s = 0$) through the following equation:

$$P_T = \boldsymbol{q}\, \rho c_{fluid} * \nabla T - \lambda_{bulk} * \nabla^2 T \qquad \textit{(Eq. 9.7)}$$

Then, by imposing the maximum allowable temperature drop to 5 °C and the highest and lowest reinjection thresholds ($T_{lim}$) of 21 and 10 °C for cooling and heating mode, respectively, and the aquifer thickness (B) the effective thermal potential ($P_E$) was obtained:

$$P_E = P_T * \Delta T * B \qquad \Delta T = \begin{cases} 5, & |T_{GW} - T_{lim}| \geq 5 \\ |T_{GW} - T_{lim}|, & |T_{GW} - T_{lim}| < 5 \end{cases} \qquad \textit{(Eq. 9.8)}$$

## 9.5. Results and discussion

### 9.5.1. Calibration

The composite sensitivity values obtained for the hydraulic and thermal parameters as the quadratic mean of the sensitivity of all the model-generated observations contained in the Jacobian matrix are shown in **Figure 9.16**. Changeable parameters were chosen according to their composite sensitivity and on their effective range of variation. A list of all the parameters used in the model (with a distinction between calibrated and non-calibrated) and their sensitivity are summarized in **Table 9.5**.

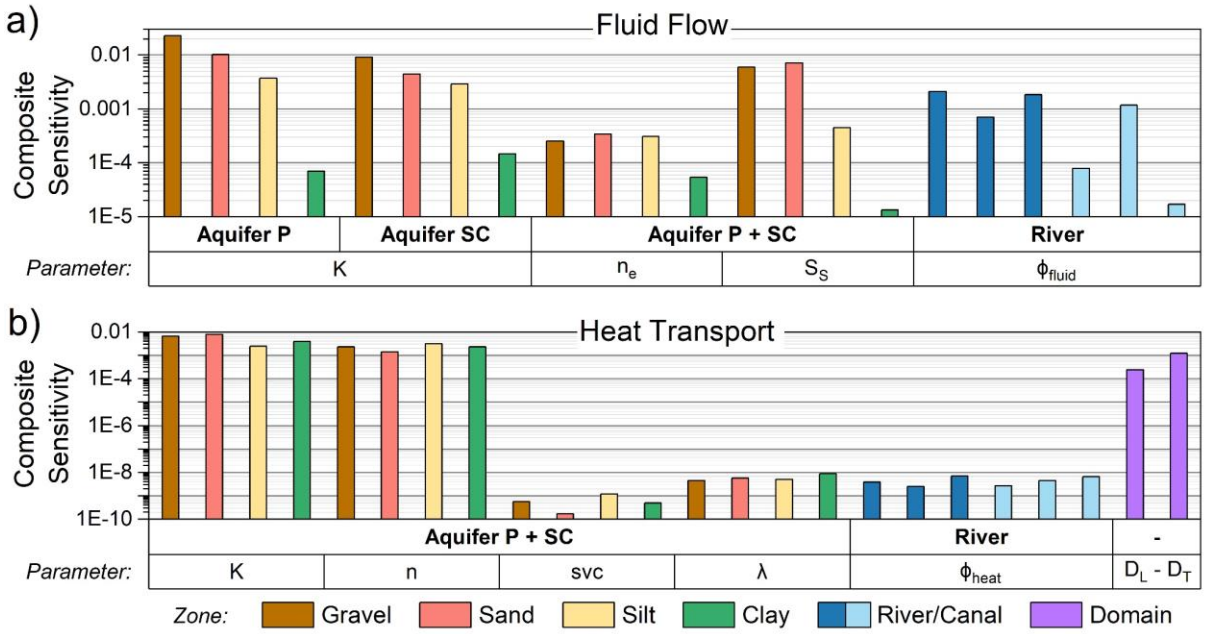


***Figure 9.16*** *– Composite sensitivity of hydraulic and thermal parameters. K: hydraulic conductivity, n and $n_e$: total and effective porosity, $S_S$: specific storage, $\phi_{fluid}$ and $\phi_{heat}$: fluid and heat transfer rate, svc: specific volumetric heat capacity, λ: thermal conductivity, $D_L$ and $D_T$: longitudinal and transversal dispersivity. Structural regularization zones are given by different colors. The parameters selected for calibration are listed in* ***Table 9.5****.*

***Table 9.5*** *– Summary of the fluid and thermal parameters adopted in the model and composite parameter sensitivity. Calibrated parameter values are highlighted bold.*

| Parameter | Aquifer | Zone | Calibrated Value | | Composite Sensitivity | |
|---|---|---|---|---|---|---|
| | | | *Fluid* | *Heat* | *Head* | *Temp* |
| Hydraulic Conductivity (m/d) | P | Gravel | **116.9** | | 2.3E-02 | 6.7E-03 |
| | SC | | **74.2** | | 9.1E-03 | |
| | P | Sand | **48.3** | | 1.0E-02 | 8.1E-03 |
| | SC | | **27.8** | | 4.4E-03 | |
| | P | Silt | **17.3** | | 3.7E-03 | 2.4E-03 |
| | SC | | **13.8** | | 2.9E-03 | |
| | P | Clay | **1.5** | | 6.9E-05 | 3.9E-03 |
| | SC | | **1.1** | | 1.5E-04 | |
| Porosity: Effective (Fluid), Total (Heat) | P + SC | Gravel | 0.26 | 0.29 | 6.0E-03 | 2.3E-03 |
| | | Sand | 0.21 | 0.33 | 7.2E-03 | 1.4E-03 |
| | | Silt | 0.19 | 0.38 | 4.5E-04 | 3.1E-03 |
| | | Clay | 0.11 | 0.44 | 1.3E-07 | 2.3E-03 |
| Specific Storage (1/m) | P + SC | Gravel | 1E-04 | | 2.5E-04 | |
| | | Sand | | | 3.4E-04 | |
| | | Silt | | | 3.1E-04 | |
| | | Clay | | | 5.4E-05 | |
| Thermal Conductivity (W/mK) | Gravel | P + SC | | 2.12 | | 4.5E-09 |
| | Sand | | | 2.17 | | 5.9E-09 |
| | Silt | | | 2.02 | | 5.2E-09 |
| | Clay | | | 1.72 | | 8.8E-09 |
| Volumetric Heat Capacity of Solid ($10^6$ J/m$^3$K) | Gravel | P + SC | | 2.45 | | 5.6E-10 |
| | Sand | | | 2.49 | | 1.7E-10 |
| | Silt | | | 2.51 | | 1.2E-09 |
| | Clay | | | 2.50 | | 5.0E-10 |
| Fluid (1/d) and Heat (W/m$^2$K) Transfer Rate | River | Lambro | **0.4** | **1** | 2.1E-03 | 3.9E-09 |
| | | Seveso | **0.5** | | 7.1E-04 | 2.5E-09 |
| | | Olona | **0.3** | | 1.8E-03 | 7.1E-09 |
| | | Nv. Martesana | **0.5** | | 7.9E-05 | 2.7E-09 |
| | | Nv. Pavese | **0.2** | | 1.2E-03 | 4.5E-09 |
| | | Nv. Grande | **0.1** | | 1.7E-08 | 6.5E-09 |
| Longitudinal Dispersivity (m) | Domain | Domain | | **30** | | 2.4E-04 |
| Transverse Dispersivity (m) | | | | **3** | | 1.2E-03 |

The calibrated horizontal hydraulic conductivity values (**Table 9.5**) range from 1.73*10$^{-5}$ to 1.35*10$^{-3}$ (mean 9.89*10$^{-4}$) m/s and from 8.62*10$^{-6}$ to 8.58*10$^{-4}$ (mean 2.87*10$^{-4}$) m/s for the P and SC aquifer, respectively, with strong vertical and horizontal spatial variability due to lenses or alternate layers (**Figure 9.6c**). As shown, the spatial distribution of regional-scale aquifer heterogeneities is considered by this approach representing the succession of different permeability layers and the occurrence of low permeability lenses by different grain-size classes.

**Figure 9.17a** and **b** show an example of simulated temperature-depth profiles and temperature time series, respectively, for three different dispersivity values at OW3 (refer to **Figure 5.3** for the location). According to the sensitivity analysis shown in **Figure 9.17c**, the values of $D_L$=30 m and $D_T/D_L$=0.1 were chosen as best global estimates showing the highest mean Spearman's correlation of 0.19 with some local exceptions at OW 10 and 9, where the amplitude of the measured temperature time series is low due to the high thermal disturbance in the city center, and at OW 5 and 3 where anomalous lag times (about 4 months less than at other OWs located nearby with similar characteristics) were already identified in this area (Previati and Crosta, 2021a).

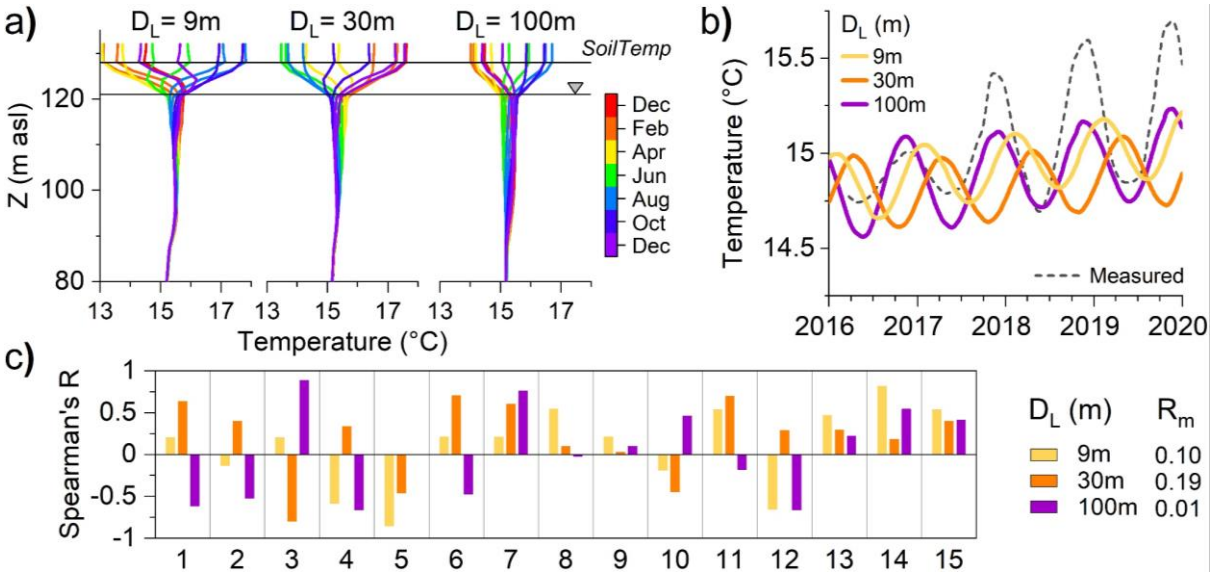


***Figure 9.17*** *– Simulated vertical groundwater temperature profiles (a) and temperature time series (b) 4 m below the water table for three values of thermal dispersivity (DL = 9, 30 and 100 m) at OW3. The line "SoilTemp" in (a) shows the interface depth below which the heat transport computation switches from SoilTemp to FEFLOW®. The dashed line in (b) shows the measured groundwater temperature at OW3. c) Spearman's correlation indexes between the daily increment of the simulated and the measured temperature time series (mean R = 0.1, 0.19 and 0.01 for 9, 30 and 100 m of dispersivity, respectively) for the 15 observation wells, see* ***Figure 5.3*** *for locations.*

The quality of the calibration results is shown in **Figure 9.18** by plotting the daily residuals between simulated and observed head and temperature values at the 15 continuously monitored OWs (see **Figure 5.3** for their location) and the mean of all residuals. The mean error between simulated and observed groundwater head values is around zero during the simulation years meaning that the fluid BCs and parameters are appropriately defined in space (the error is both positive and negative and shows no significant spatial distribution) and in

time (the error remains constant during the simulation time under changing fluid and heat budget components). The mean error between simulated and observed groundwater temperature is almost constant for the simulation time (between 0 and -1 °C) with a little decreasing trend (~ -0.1 °C/y) and clear seasonal oscillations. The error is lower during winter months and higher in summer months possibly due to underestimated thermal sources at the surface and misrepresented phasing of the temperature signal in the subsurface due to thermal parameters. Specific investigations on the unsaturated zone thermal properties and assessments on the thermal dispersivity of different thermofacies are also needed to minimize the error and phase shifting between the simulated and observed groundwater temperature. The increasing difference between simulated and measured groundwater temperatures (on average the mean error decreases by ~ -0.1 °C/y) could be due to an underestimation of the warming trend of the subsurface (i.e. the warming is not fully represented by the simulation and, thus, the difference increases). Longer simulations introducing progressive urbanization and development of heating sources such as tunnels and GWHP could help to reproduce the subsurface warming trend observed from 2016 to 2021.

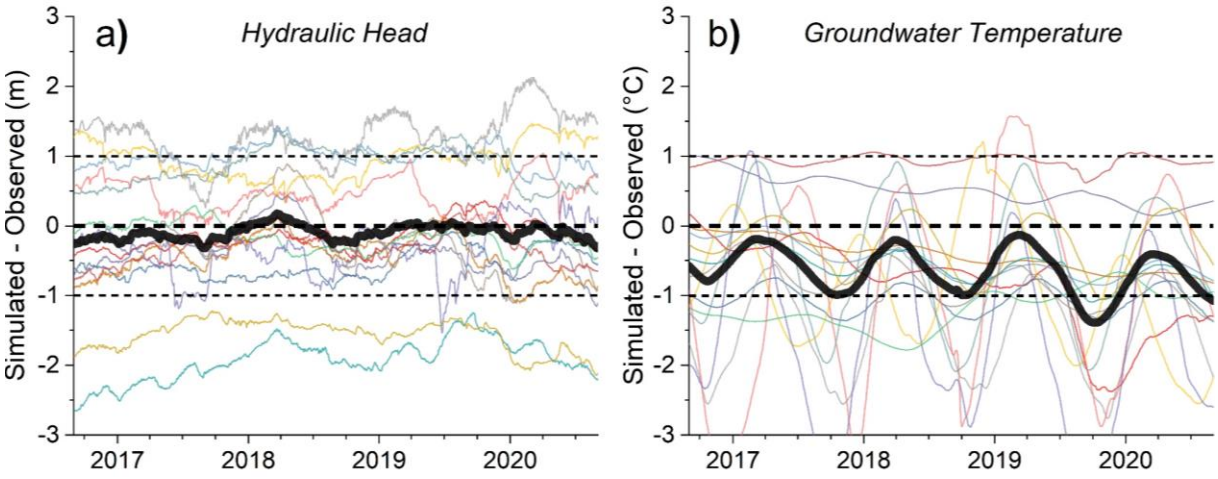


***Figure 9.18*** *– Daily residuals between the simulated and measured hydraulic head (a) and groundwater temperature (b) at the 15 OWs (the thick line represents the mean of all residuals).*

### 9.5.2. Validation

The simulated groundwater temperature regime was validated both in space and time comparing the model results with temperature measurements from time-lapse vertical profiles at 40 OWs (see **Figure 5.3** for their location) beyond the 15 used for calibration and

considering seven measuring campaigns carried out from 2019 to part of 2021, and not included in the calibration. The validation scatterplots between measured and calculated temperature are shown in **Figure 9.19**.

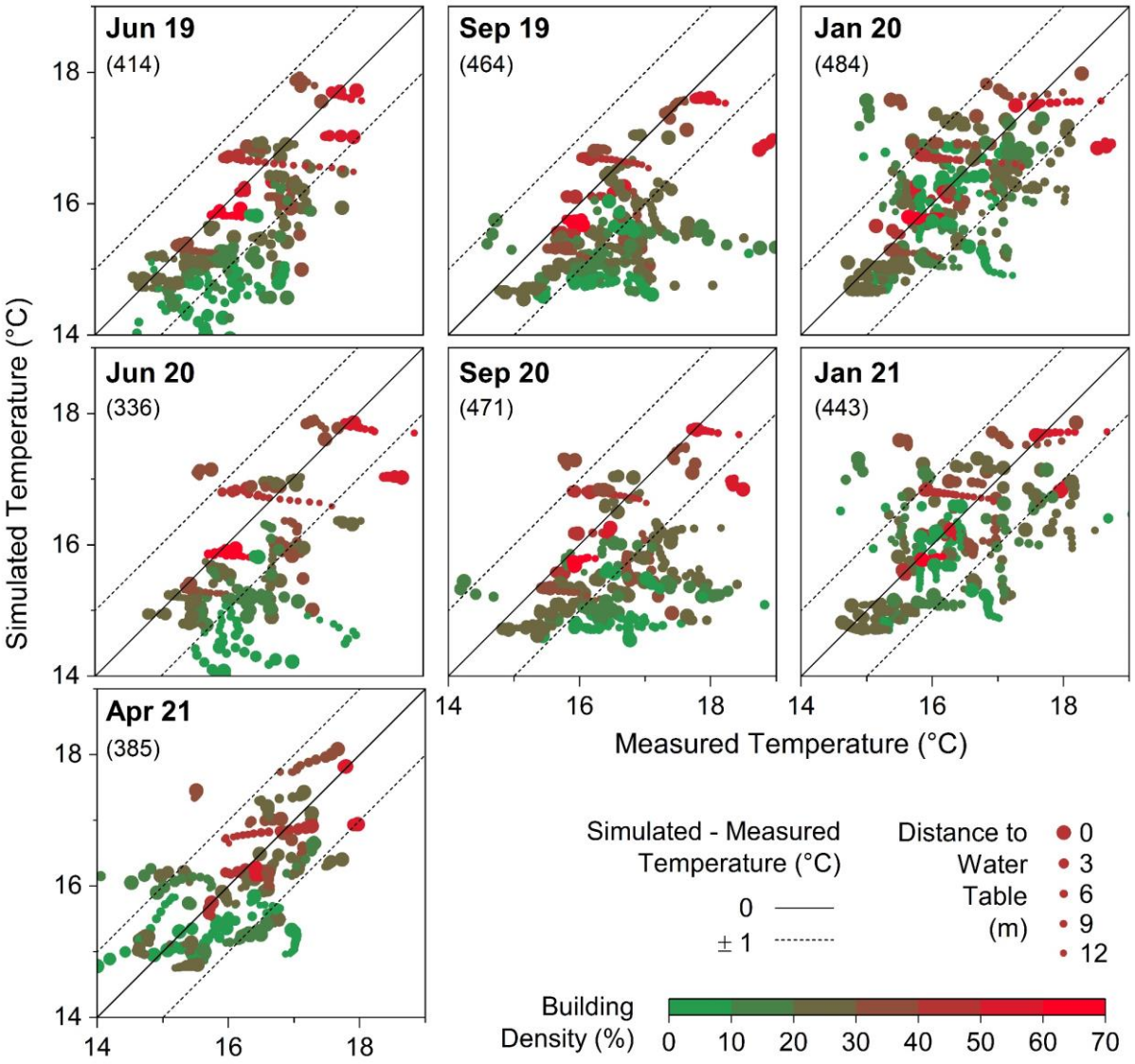


***Figure 9.19*** *– Validation scatter plots for 7 time-lapse groundwater temperature measurements at 55 locations (between brackets the total number of measurements) from June 2019 to April 2021. For each location, 1-m-spaced vertical temperature profiles were compared to the simulated temperature at each depth. The size of the dots represents the distance of the validation point from the water table and the colors show the percentage of area covered by buildings around 500 m from each OW. The total number of observations varies in each measurement campaign due to the OW accessibility and the total water column depth.*

**Figure 9.20** summarizes the time variation of the root mean square error (RMSE) between the measured and simulated groundwater temperature at different depths along the validation temperature-depth profiles. At most of the locations, the difference between the simulated

and calculated temperature is lower than 1 °C (**Figure 9.19**) but some temperatures are underestimated by the model, especially during summer months (**Figure 9.20**) and at medium-low building density locations (**Figure 9.19**). This could be due to: (i) underestimated initial temperature at specific locations (total initial energy content underestimated), (ii) underestimated (or neglected) thermal energy released in the subsurface by specific sources and (iii) wrongly estimated hydraulic or thermal parameters that could prevent heat accumulation in the aquifer. Due to the lack of temperature measurements in the unsaturated zone and too sparse measures downgradient specific heat sources, it is difficult and out of the scope of this work to disentangle which heat source is underestimated or parameter wrongly estimated.

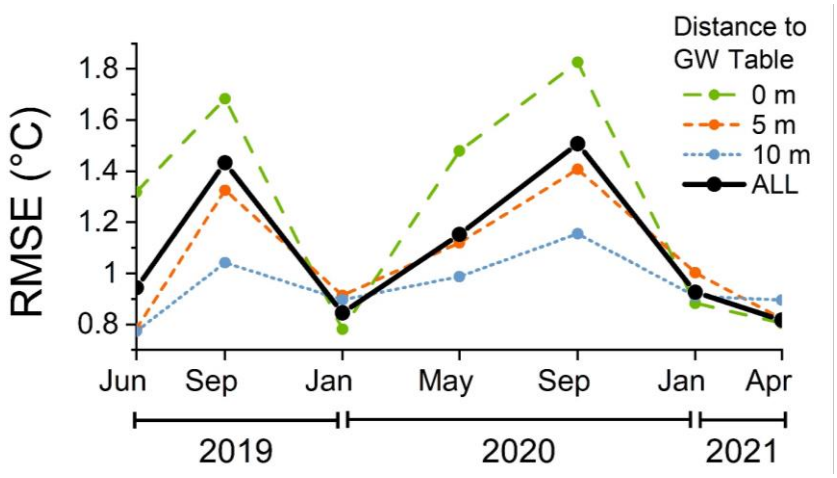


***Figure 9.20*** *– RMSE between simulated and measured temperatures by 7 time-lapse groundwater temperature measurements from June 2019 to April 2021. The thick line represents the RMSE for all the measures, while green, orange and blue lines represent the RMSE calculated at specific depth below the water table (0, 5 and 10 m, respectively).*

### 9.5.3. Simulated groundwater thermal regime

**Figure 9.21a** and **b** show the spatial distribution of the mean annual groundwater temperature and the annual temperature range at three depths below the water table (i.e., 0, 10 and 40 m, respectively). The extent of the SUHI at depth and the relation between the groundwater depth and the range of the annual temperature fluctuations is clearly visible. The simulated vertical temperature profiles at six locations, respectively north (upgradient), in the center and south (downgradient) of the SUHI (#1, 2 and 3), and close to specific heat sources such as

surface water bodies (#4), tunnels (#5) and existing geothermal wells (#6) are shown in **Figure 9.21c**.

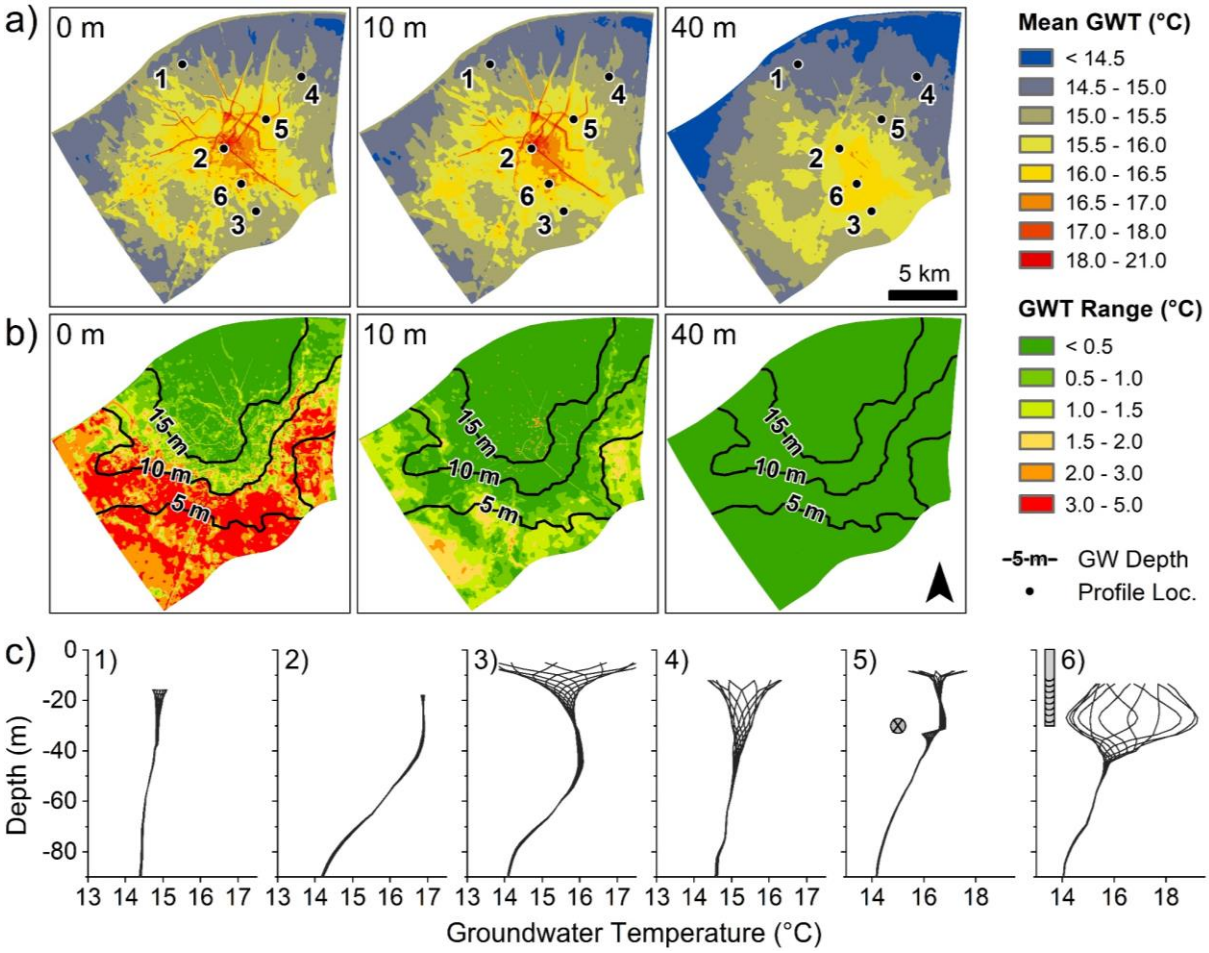


***Figure 9.21*** *– Maps showing the simulated mean annual groundwater temperature (GWT) (a) and the annual temperature fluctuation (b) at three depths below the water table: 0, 10 and 40 m. (c) Simulated temperature-depth profiles for three representative locations (#1, 2 and 3), 100 m downgradient to the Lambro River (#4), close to the underground tunnel "M6" (#5) and at a geothermal reinjection well (#6). Depth of the tunnel and bottom of the reinjection well are illustrated by sketches next to profiles #5 and 6. See (a) for profile locations (Loc.).*

The simulated mean annual subsurface temperature distribution obtained by averaging weekly temperature distributions of the year 2019 is shown in the city-wide cross-section in **Figure 9.22a**. The simulated SUHI extends southward for few kilometers from the center along with the groundwater flow but in the vertical direction it remains mostly confined to the phreatic aquifer due to the permeability contrast between the phreatic and semi-confined units and the aquitard separation. Fluid arrival time from the ground surface to the semi-confined aquifer (e.g. recharge from infiltration, surface water bodies) was estimated by the

model between 3 to 20 years, respectively in the northern and southern portions of the domain. The probability distribution functions (PDF) of the element-volume-weighted mean annual temperature in the two aquifer units (P and SC) and in the unsaturated zone (**Figure 9.22b**) show that 5 ‰ of the unsaturated layer and 2 ‰ of the phreatic aquifer has a temperature above 18 °C. Considering a 2km-radius circle centered in the city center, the aquifer volume percentages above 18 °C become 3.5 % and 2 %, respectively. The median of the simulated mean annual temperature over the entire model is 14.4, 15.3 and 15.5 °C for the semi-confined, phreatic and unsaturated units, respectively. Considering a 2km-radius circle centered in the city center, the median of the simulated mean annual temperature becomes 14.7, 16.2 and 16.4 °C for the semi-confined, phreatic and unsaturated units, respectively. Thus, the semi-confined aquifer can be considered poorly thermally affected by anthropogenic activities. Few exceptions exist near the deep water abstraction wells due to enhanced vertical advective heat transport caused by local vertical component of groundwater flow (i.e. the drawdown cone due to pumping).

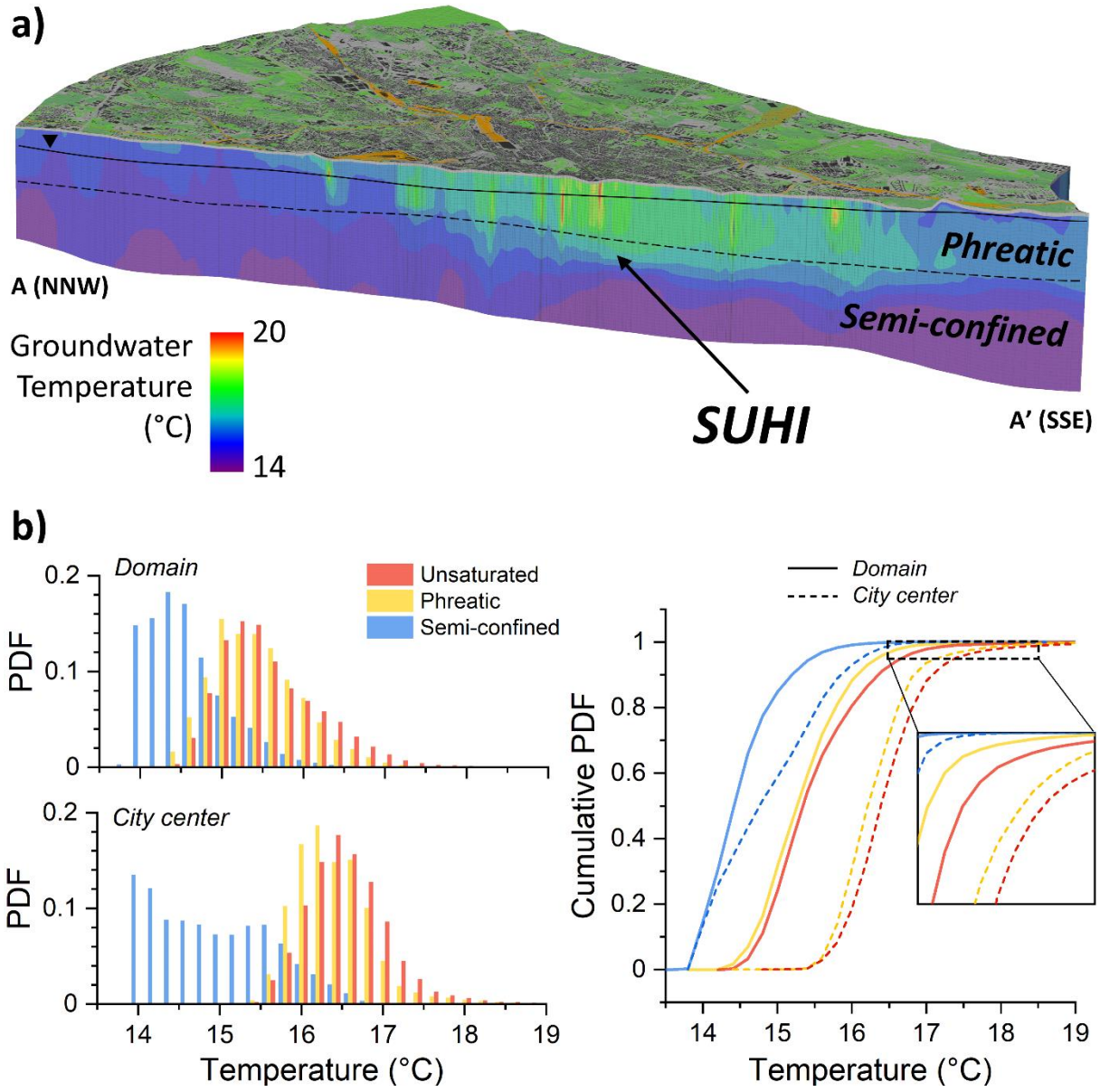


***Figure 9.22*** *– (a) Cross-section (NNW-SSE) across the model showing the simulated mean annual subsurface temperature distribution where the 3D extent and intensity of the subsurface urban heat island (SUHI) is clearly visible. (b) Probability distribution function (PDF) and cumulative PDF of the mean annual element-volume-weighted temperature calculated for the unsaturated zone, and the phreatic and semi-confined aquifers. Continuous lines refer to the entire model, dashed ones were evaluated inside a 2km-radius circle centered in the city center.*

Local strong thermal effects are visible up to 300 m downstream to tunnels and GWHP reinjection wells and their superimposition inside the 2km-radius circle centered in the city center contribute to define the extent and intensity of the SUHI.

Examples of the extent and intensity of the thermal perturbation caused by tunnels and GWHPs are shown in **Figure 9.23** and **Figure 9.24**, respectively.

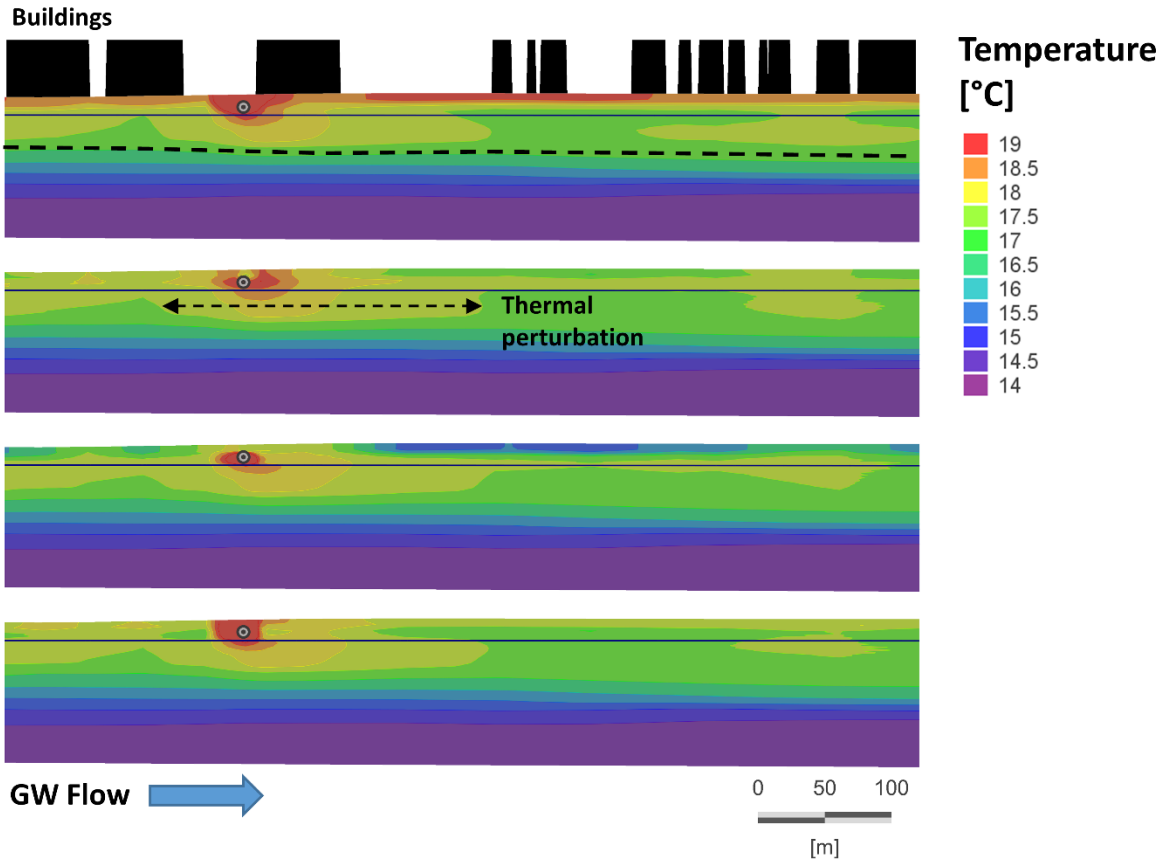


***Figure 9.23*** *– Cross-sections perpendicular to tunnel M1 (parallel to groundwater flow) showing the subsurface temperature distribution in summer, autumn, winter and spring. The 200m-long thermally affected zone is highlighted by arrows. The dashed line in the first section represents the aquitard between P and SC aquifers.*

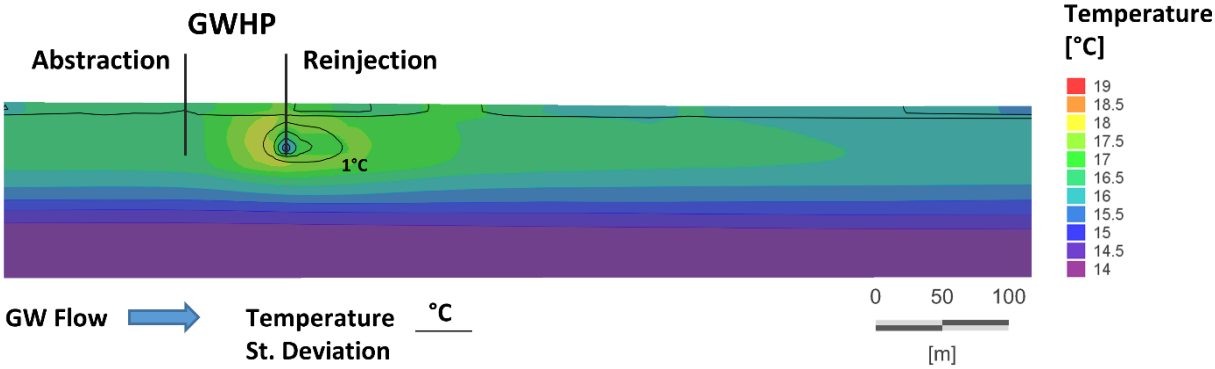


***Figure 9.24*** *– Cross-section showing the mean annual temperature distribution and the temperature standard deviation near a groundwater heat pump system (GWHP). Note the positive thermal perturbation 100 m around the reinjection well, which is higher between the abstraction and reinjection wells due to stagnation.*

### 9.5.4. Fluid and thermal budgets

To assess the most relevant fluid and heat sources in the model area, the rate (i.e. the fluid and heat storage rates for each computing time-step) and period (i.e. the cumulative storage

of fluid and heat during the simulation period) budgets were extracted for the simulation period 2015 to 2021. **Figure 9.25a** shows the components of the daily fluid budget and **Figure 9.25b** shows the cumulated fluid budget expressed in terms of fluid volume change respect to the initial total fluid content of $5.1*10^9$ $m^3$. The short-term fluctuations of the fluid volume (±0.2 % of the initial fluid volume) are due to the precipitation input (recharge) while the long-term variations (reflected in the global minimum in mid-2019; -2 % of the initial fluid volume stored in the SC and P groundwater bodies) are mainly due to the reduced upgradient groundwater inflow and lower cumulative precipitations in 2017 and 2018 (respectively, 50 and 70% of the total precipitation of 2020).

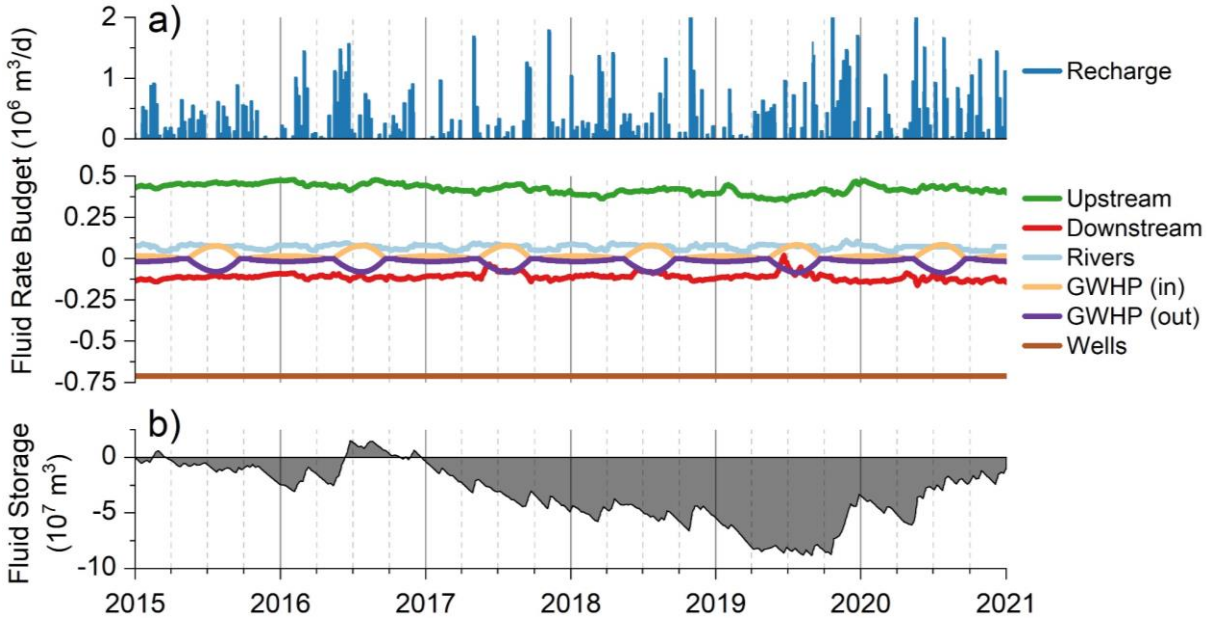


***Figure 9.25*** *– (a) Daily budget for all the fluid sinks and sources considered in the model and (b) total cumulative fluid storage in relation to the initial fluid content in 2015 ($5.1*10^9$ $m^3$).*

Similarly, **Figure 9.26a** shows the components of the daily heat budget rates with respect to a reference temperature of 14.3 °C (mean annual temperature of the air temperature time series of the last 10 years). The highest daily heat budget rates can be related to the upper thermal and rainfall BCs. **Figure 9.26b** shows the cumulative heat budget for the simulated period with respect to the estimated initial energy content of about 100 PJ. The thermal energy content increases at a rate of +1.4 PJ/y (+1 % of the initial energy content) with seasonal fluctuations of ±4.3 PJ (±5 % of the initial energy content) due to the net surface thermal sources contribution.

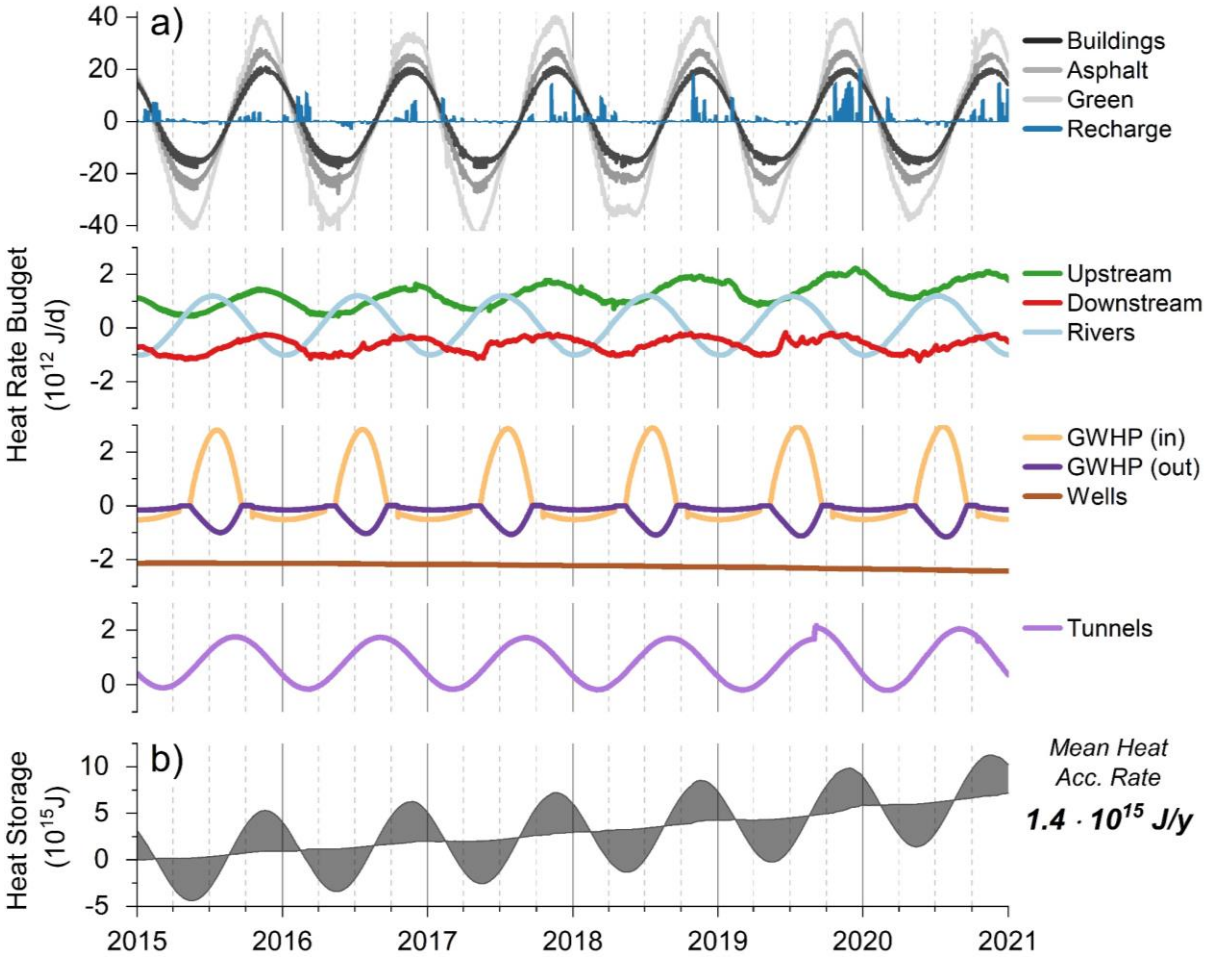


***Figure 9.26*** *– (a) Daily budget for all the heat sinks and sources considered in the model and (b) total cumulative heat storage respect to the initial thermal energy content in 2015 (100 PJ) and mean accumulation rate. The step of the tunnel rate budget in September 2019 is due to the implementation of the sixth line M4.*

Finally, the fluid and heat storage rates were computed for each component by dividing the period budget of each component by the simulated years (**Figure 9.27**). The total fluid storage from all the boundary conditions and sink/source terms is around zero which means that the fluid volume after 5 years is almost the same as the initial volume. The heat storage was divided between the heat entering/leaving the model via the fluid in-/out-flow BCs (e.g. through rainfall, rivers) and by heat conduction (e.g. through the top surface and tunnel walls). Even if single heat sources through the fluid BCs show the greatest absolute values, the total heat storage rate by conduction is an order of magnitude larger (1.2 PJ/y) than that by the fluid BCs (0.15 PJ/y). In fact, the heat in/outflow via fluid in/outflow is calculated with equation:

$$Q_{heat} = Q_{fluid} * \left(T_{fluid} - T_{ref}\right) * svc \qquad \textit{(Eq. 9.9)}$$

where $Q_{fluid}$ is the fluid in/outflow discharge, $T_{fluid}$ is the temperature of the fluid entering/leaving the model, $T_{ref}$ is the reference temperature (i.e. 14.3 °C) and $svc$ is the volumetric heat capacity of fluid. Thus, considering that the positive and negative fluid sources add up to zero, the sum of the fluid-dependent heat sources add up to zero too and the most relevant sources that contribute to store heat in the subsurface are those related to heat conduction from heated surface/subsurface structures and infrastructures. Among these, the most relevant ones are the building foundations, tunnels and asphalted surfaces with contributions of 0.50, 0.35 and 0.31 PJ/y, respectively, which total to 1.17 PJ/y (85% of the net annual heat accumulation in the subsurface). These values are very similar to previous quantitative studies, e.g. Benz et al. (2015) estimated analytically a total heat accumulation of 2.1 and 1.0 PJ/y for the Karlsruhe and Cologne aquifers in Germany, with buildings and elevated ground surface temperature contributing to 88 and 70%, respectively. Given the assumed heating and cooling thermal power of geothermal installations, the net annual thermal contribution of shallow geothermic is low (0.08 PJ/y) compared to other sources since they are used both for heating and cooling.

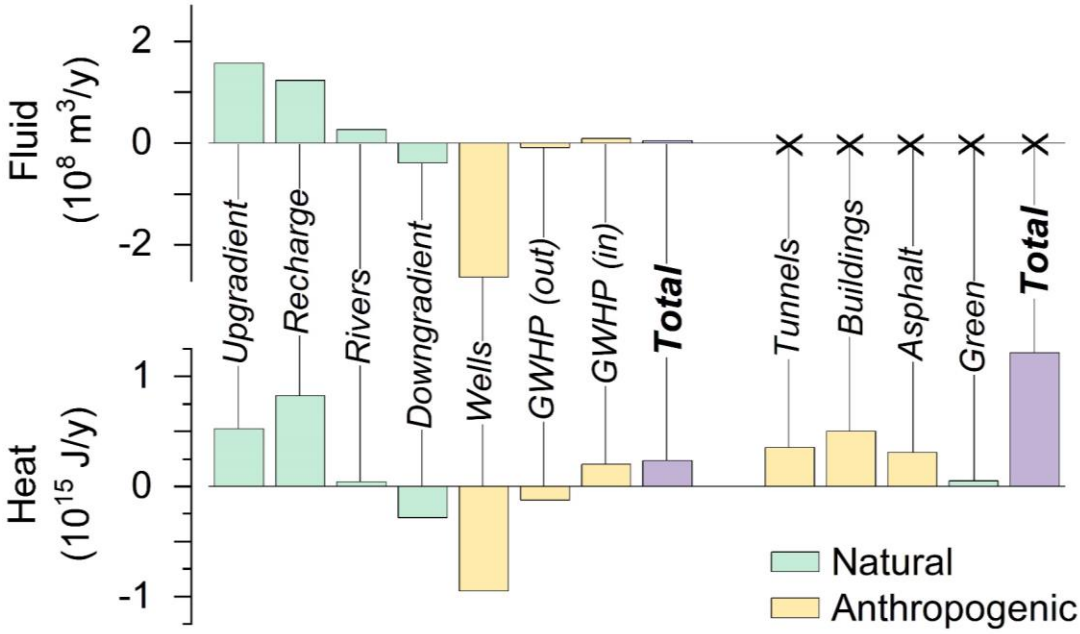


***Figure 9.27*** *– Aquifer fluid and heat storage rates for the natural and anthropogenic sources considered in the model. On the right-hand side the contribution of thermal sources by conduction is shown, while those related sources related to fluid in-/out-flow are on the left-hand side.*

### 9.5.5. Thermal potential assessment

The calculated Darcy flow velocity ($\boldsymbol{q}$), the bulk thermal conductivity ($\lambda_{bulk}$) and the groundwater temperature ($T_{GW}$) were substituted into (Eq. 9.7) and (Eq. 9.8) to obtain the theoretical ($P_T$) and the effective ($P_E$) thermal exchange potentials, respectively. **Figure 9.28a** shows the theoretical exchange potential ($P_T$) calculated using depth averaged values of the phreatic aquifer (P). The highest exchange potential is found in the northern part of the domain due to higher flow velocities and, moving southward, a lower advective heat transport component, due to the finer grain-size of the unconsolidated deposits, leads to a lower exchange potential. Thus, in this area, the sizing of GWHPs, as well as the installation costs and the extent of the thermally impacted area, could be greater and therefore requires more detailed investigation. The more promising development area is represented by the north-eastern sector of the domain where a high theoretical potential (i.e. > 20 W/m$^3$K) is observed together with a high urban density (**Figure 9.3a**) that could take advantage of the high energy capacity of the area.

The effective thermal potential $P_E$ (**Figure 9.28b** and **c** for heating and cooling mode, respectively), obtained according to (Eq. 9.8) ranges between 0.3 and 3 kW/m$^2$ and well agrees with previous analytical estimations at regional scale by Previati and Crosta (2021b) (from 1.1 to 2.5 kW considering heat exchangers deep as the phreatic aquifer). Despite the lower thickness of the phreatic aquifer in the north-eastern sector of the domain, this area is however the most attractive due to the high groundwater flow velocity and low mean annual groundwater temperature.

Although the difference between heating and cooling thermal potential in the study area is poorly appreciable (**Figure 9.28b** and **c**), the SUHI effect leads to a lower cooling thermal potential since in the city center the term $|T_{GW} - T_{lim}|$ of (Eq. 9.8) is significantly lower than the maximum permitted change of 5°C as $T_{GW}$ is higher and closer to the reinjection threshold of 21°C. Since the city center shows the highest density of geothermal installations (**Figure 9.28a**) and the net annual thermal demand in the city center is negative (i.e. the annual cooling demand is larger than the heating one) further investigations on the evolution of the thermal

regime in the city center due to natural and anthropogenic factors are needed to assess future cooling and heating thermal potential changes.

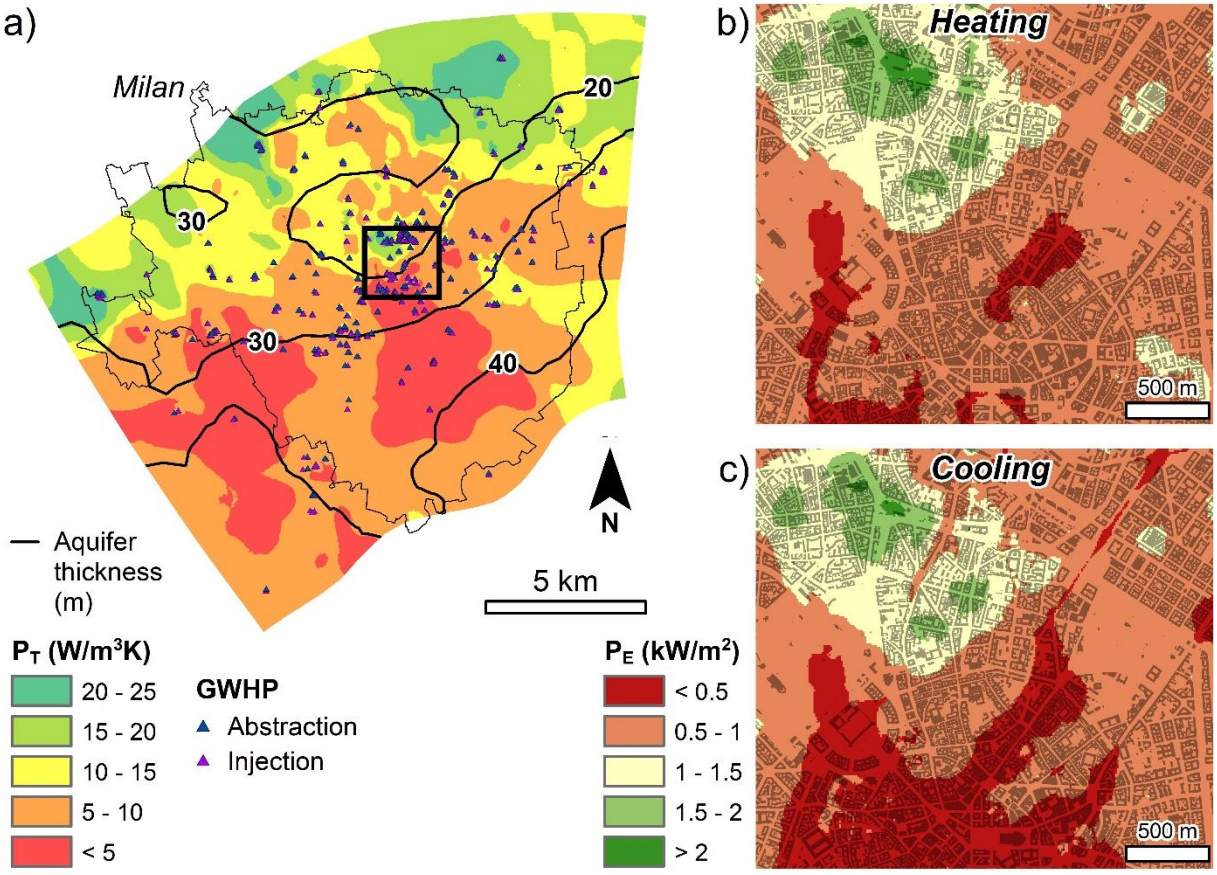


***Figure 9.28*** *– Maps showing: the theoretical exchange potential (PT) calculated for the shallow aquifer, the aquifer thickness and the location of installed GWHP (a), and the effective thermal potential (PE) for heating (b) and cooling (c) mode.*

In-depth investigations on the groundwater flow velocity and thermal regime can be conducted by extracting simulated temperature-depth and Darcy velocity profiles (**Figure 9.29**). The variation of the Péclet number with depth, obtained combining the model parameters and outputs, shows where advection prevails on conduction and, thus, where a more efficient heat exchange is expected. Note that to the north (profile #1) advection is relevant along the entire aquifer vertical profile, whereas in the center and to the south the lower flow velocity (due to lower hydraulic conductivities and hydraulic gradient) leads to an almost balanced equilibrium between advection and conduction in the semi-confined aquifer and prevailing advection only locally in the phreatic aquifer. The effects of the thickness of the unsaturated zone and local disturbances (e.g. tunnel in profile #5) on the yearly fluctuations is clear by comparing the four proposed profiles.

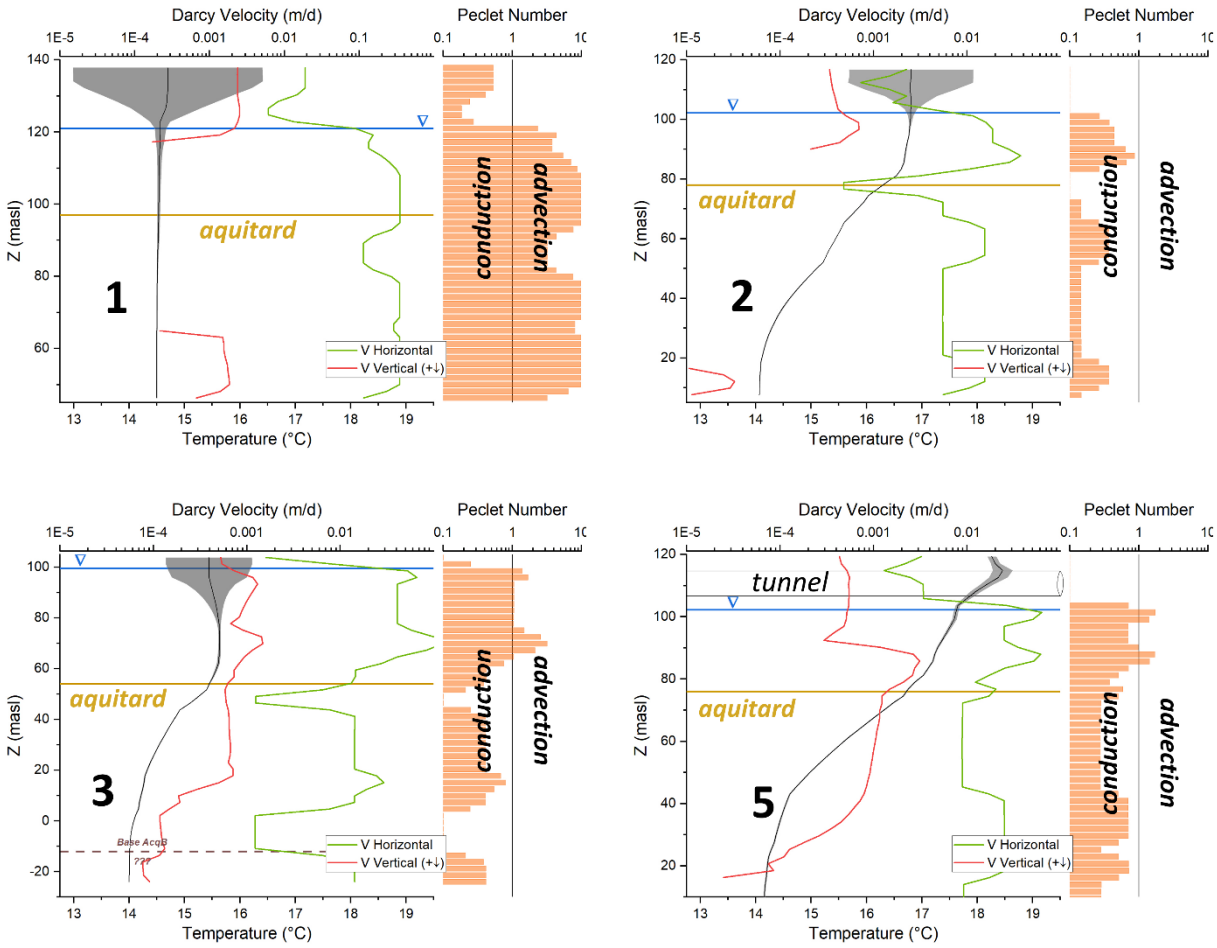


***Figure 9.29*** *– Vertical profiles showing the yearly envelope (grey) and the mean annual (black line) simulated groundwater temperature, the horizontal (green) and vertical (red) groundwater flow velocities, and the Péclet number. The depth of the water table and the bottom of the phreatic aquifer are also shown. For their location refer to* ***Figure 9.21****.*

### *9.5.5.1. Comparison with the ASHRAE analytical solution (chapter 6)*

The equations used to estimate the geothermal potential from the numerical results consider both the conduction and advection heat transport mechanisms (see Section 9.4.8). Since in the study area a high groundwater flow exists, the thermal potential is strongly related to the flow velocity which has a wide variability in the study area (5 order of magnitude) due to the logarithmic distribution of the hydraulic conductivity. For the same reason, the effects of the initial groundwater temperature on the effective thermal potential ($P_E$) are less relevant and poorly visible: the groundwater temperature ranges between 14 and 18.5 °C, while the Darcy flow velocity between $5*10^{-5}$ and 5 m/d.

In chapter 6 the geothermal potential for GCHP was estimated analytically considering only the thermal conduction and the average annual groundwater temperature interpolated at regional scale from available measurements. Although the spacing of the available groundwater measurements is not enough to catch the contribution of individual heat sources, the spatial resolution is adequate for the scale of analysis. In fact, the depth-averaged temperature distribution used for the estimation reflects the degree of urbanization and depth of the aquifer (**Figure 6.3**) which are the main controlling factors on the groundwater temperatures.

A comparison between the two solutions is presented in **Figure 9.30** showing the spatial distribution of the depth averaged mean annual groundwater temperature calculated numerically **(a)** and interpolated from direct measurements **(b)**, and the heating **(c-d)** and cooling **(e-f)** potentials calculated by means of the ASHRAE equation (Eq. 6.10) using both the simulated **(c-e)** and interpolated **(d-f)** groundwater temperature distributions. Although the heat exchange by advection is not considered by the ASHRAE analytical model, the combination with the simulated groundwater temperature distribution better represents the effects on the geothermal potentials induced by anthropogenic warming and it is more accurate in complex environments such as the urban subsurface.

Finally, future developments could consider the estimation of the thermal potential during different seasons from transient simulations instead of using an average annual groundwater temperature distribution. Simulating the evolution of the groundwater temperature will be essential to estimate the variation of the geothermal under different scenarios.

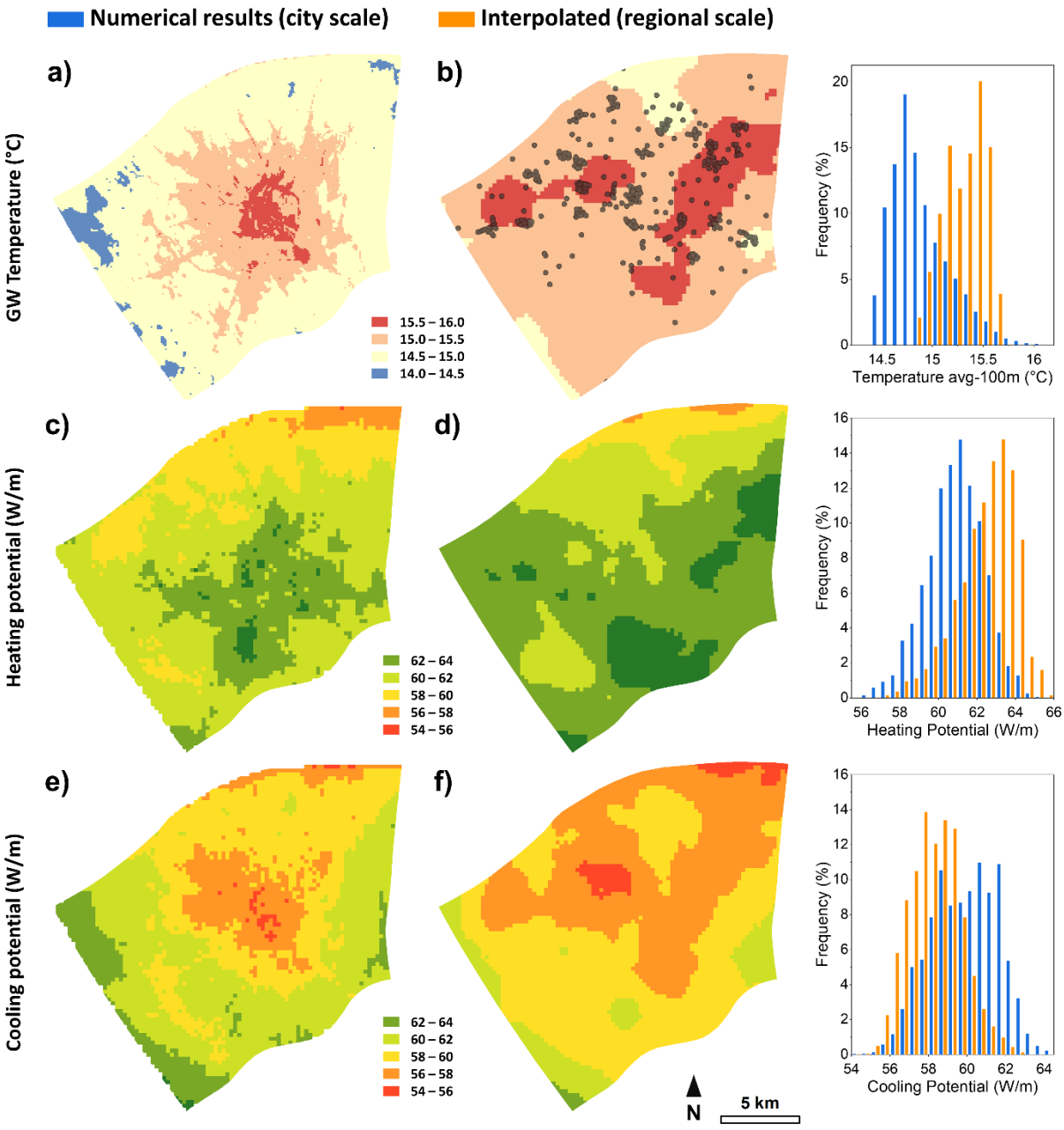


***Figure 9.30*** *– Maps showing the spatial distribution of the mean annual depth averaged groundwater temperature from the numerical simulation (a) and interpolated from available temperature data (b). Heating (c and d) and cooling (e and f) thermal potentials for a 100-m-length GCHP using the groundwater temperature distribution in (a) and (b), respectively*

### 9.5.6. Future scenarios

The thermal energy stored in the shallow groundwater bodies due to changes of natural and anthropogenic factors was evaluated by comparing 18 steady state models with different boundary conditions according to climate change, city development and increasing GWHP installations scenarios. First, a steady state reference scenario was generated by adopting the mean annual values of all the time-varying boundary conditions adopted in the transient model for the period 2016 to 2021 for which the consistency between the total energy content of the shallow aquifer in the transient and steady state models was checked. Then, a total of 12 scenarios for the air temperature change in the Milan city area projected by the global coordinated climate modeling experiment CMIP5 (Taylor et al., 2012) were generated. The mean annual air and river temperatures were increased by the temperature change projected by the RCP2.6 (+1.05 to 1.18°C), 4.5 (+1.11 to 2.15°C) and 8.5 (+1.31 to 4.42°C) scenarios from 2040 to 2100. Boxplots in **Figure 9.31a** summarize the statistics of the projected air temperature changes from different climate models for each RCP scenario available on the Climate Change Knowledge Portal (CCKP, 2021). **Figure 9.31b** shows the mean air temperature change time series implemented in this analysis.

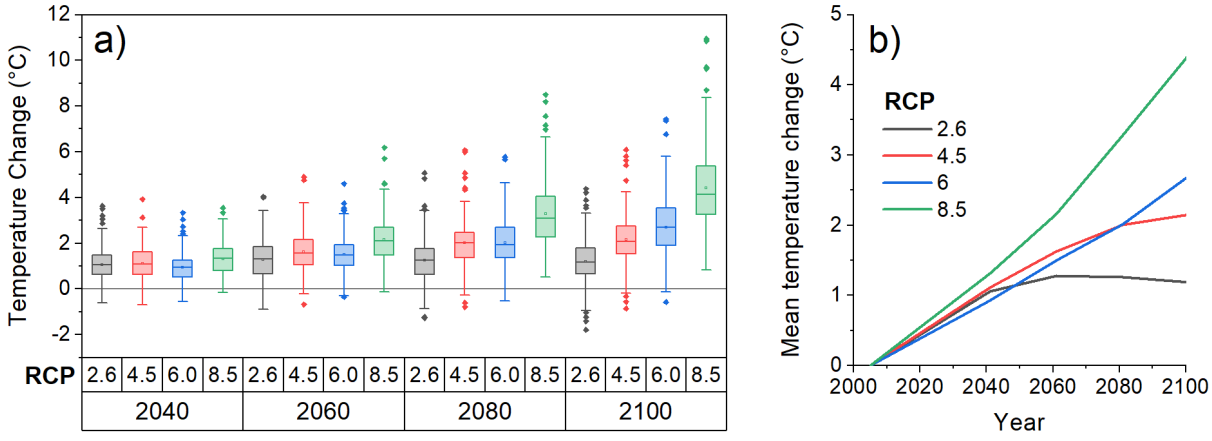


***Figure 9.31*** *– (a) Boxplots showing the statistics of the projected air temperature changes from different climate models for each RCP scenario and (b) the mean values implemented in the scenario-based steady state models. Data from the Climate Change Knowledge Portal (CCKP, 2021)*

Two more scenarios were generated assuming future city expansion according to the concentric classification shown in **Figure 9.3a**. In the first scenario (L1), the percentage of area covered by buildings in zone Z2 (% building = 27.6; 15.25 °C >= mean air temp > 15.50 °C) was

increased to reach the density of zone Z1 (% building = 35.8; mean air temp >= 15.50 °C). In the L2 scenario the percentage of all classes (% building = 15.0 and 13.8 in zone Z3 and Z4, respectively) were increased to reach the building density of zone Z1. **Figure 9.32** shows the percentage of land use classes and the spatial distribution of the building density for the present-day (a), L1 (b) and L2 (c) scenarios.

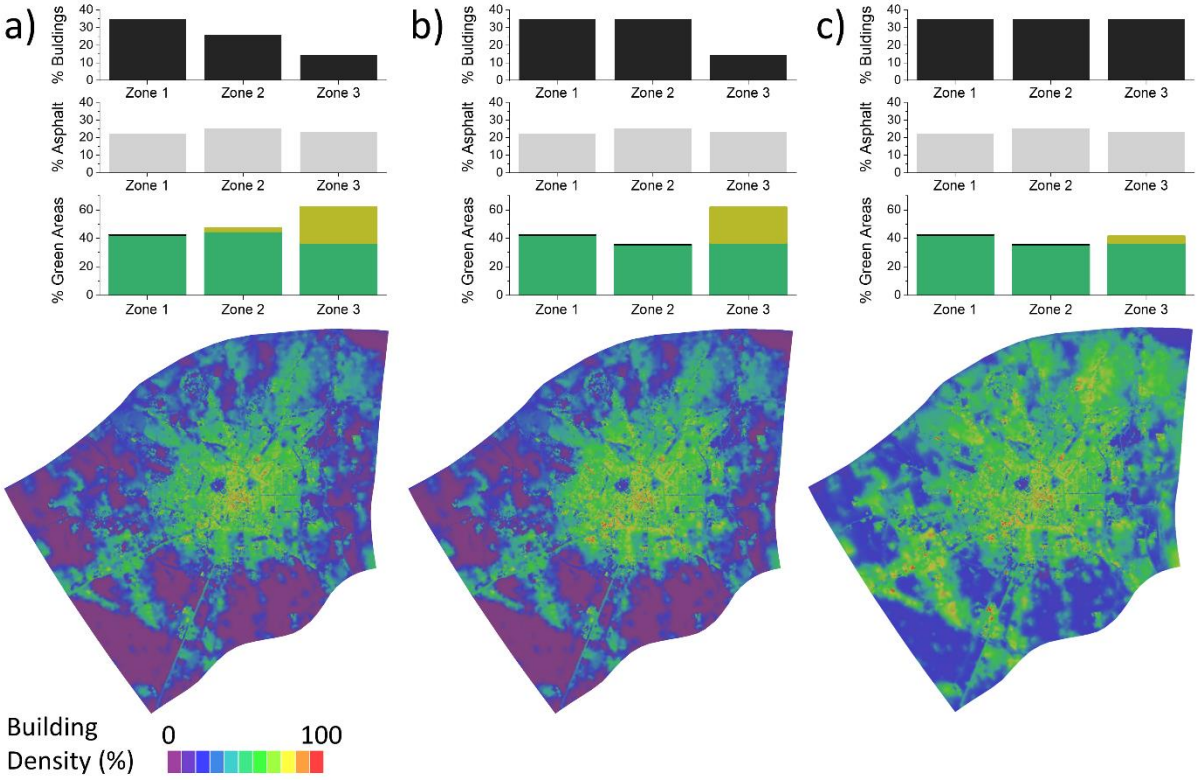


***Figure 9.32*** *– Land use percentages in the three zones of the city (Z1, Z2, Z3+Z4) and spatial distribution of the building density for the present-day (a), L1 (b) and L2 (c) scenarios.*

Finally, three scenarios on the future increase of low enthalpy geothermal installations were generated by increasing the actual total power output by GWHP in the study area by 50, 100 and 200 % as foreseen by Unione Geotermica Italiana (2017) within 2030 (note that this assumption consider only the total number of installations but neglects the change in the thermal demand due to changes in the atmosphere thermal regime). Again, the thermal power output differs from zone Z1 to Z3 (**Figure 9.33**). Thus, the future thermal output by GWHP was calculated multiplying the volumetric power density installed in each zone (i.e. the total power divide by the volume of each zone, **Figure 9.33**) by the percentage raise assumed for each scenario.

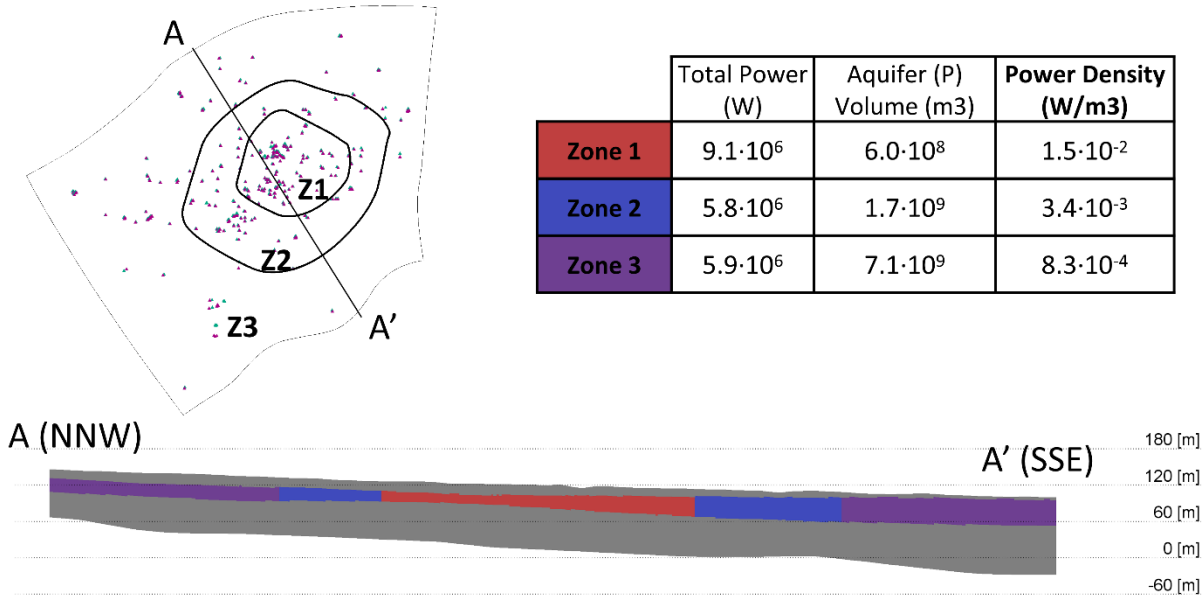


| | Total Power (W) | Aquifer (P) Volume (m3) | **Power Density (W/m3)** |
|---|---|---|---|
| **Zone 1** | $9.1 \cdot 10^{6}$ | $6.0 \cdot 10^{8}$ | $1.5 \cdot 10^{-2}$ |
| **Zone 2** | $5.8 \cdot 10^{6}$ | $1.7 \cdot 10^{9}$ | $3.4 \cdot 10^{-3}$ |
| **Zone 3** | $5.9 \cdot 10^{6}$ | $7.1 \cdot 10^{9}$ | $8.3 \cdot 10^{-4}$ |

***Figure 9.33*** *– Map of the model area showing the spatial distribution of the installed GWHP, and the total installed thermal power and power density in the three concentric zones. The aquifer volume of each zone was obtained as shown in section A-A'.*

Finally, the changes of thermal energy stored in the aquifer P with respect to the reference scenario due to the proposed scenarios were compared by means of a bars plot (**Figure 9.34**, note the logarithmic scale of the y axis). The RCP climate scenarios show the highest energy increment but with significantly different final values (+33, 79 and 189 % for the RCP2.6, 4.5 and 8.5 2100 scenarios, respectively). The land use scenarios consider possible changes in the size of the city (i.e. the increment of the building density outwards the city center) but neglect the associated increase in the surface temperature due to increased UHI, which would lead to even higher thermal energy storage. Hence, the installations of new shallow geothermal systems should be highly supported since their contribution to subsurface heat accumulation is less relevant than estimated changes related to city development and climate change scenarios. However, since at present day, even if the cooling load prevails in the city center, the net thermal budget is almost balanced with little amount of net heat release in the subsurface. Thus, the GWHP scenarios consider only the increase in the total number of installations assuming no changes in the net thermal output and underestimates the potential increase in the cooling load and associated release of heat in the subsurface due to air temperature and UHI increase. Further investigations on the changes in the heating and cooling geothermal potential due to the combination of the proposed scenarios (e.g.

considering different heating/cooling rates because of air temperature changes or changes in the subsurface temperature due to superimposed effects) will be essential to support the future management of shallow geothermal installations.

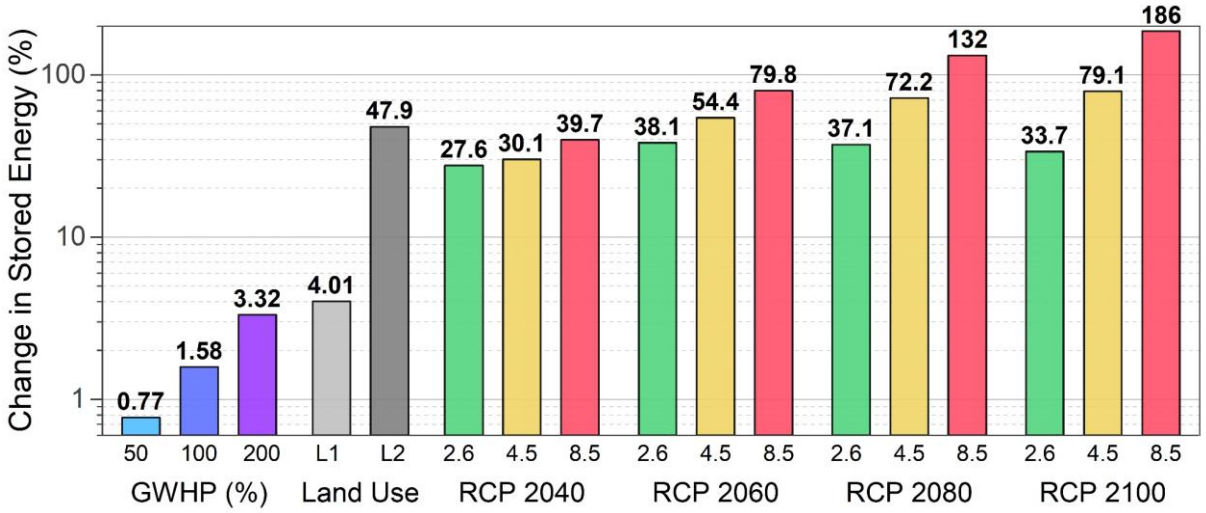


***Figure 9.34*** *– Change of the thermal energy stored by the phreatic aquifer (P) for the calculated scenarios with respect to the reference scenario (average values for the period 2016-2021). GWHP: increase in geothermal installations (%), Land Use: city development scenarios, RCP: climate change scenarios based on projected temperature change for the years 2040, 2060, 2080 and 2100. Please note the logarithmic scale of the y axis.*

# 10. Conclusions

## 10.1. Regional-scale geothermal potential of shallow aquifers

A comprehensive regional assessment of the low enthalpy geothermal potential for both closed- (GCHP) and open-loop (GWHP) systems in a densely urbanized area was presented. The approach is based on the analysis of geological, hydrogeological and climate settings, and includes technical and legislative constraints, together with groundwater quantity and quality conservation principles. The main factors which control the potential of GCHP and GWHP were identified in the water table depth, the transmissivity of the phreatic aquifer, the groundwater temperature, and the aquifer thermal parameters.

The effective thermal potential of closed-loop systems was calculated for both heating and cooling modes combining the mean annual groundwater temperature from direct measurements with site-specific ground thermal parameters averaged on the length of the borehole. On the other hand, the open-loop thermal potential was based mostly on the productivity of the shallow aquifers considering the effects of groundwater extraction and re-injection on the water table fluctuations and preventing the thermal short-circuit.

A 45-kW thermal load was selected as “common residential scenario” according to the typical power of existing installations. The depth to be drilled to deliver such energy with GCHP ranges from 680 to 1200 m and from 720 to 1100 m for heating and cooling mode, respectively. In case of GWHP the depth to be drilled is restricted to the depth of the bottom of the phreatic aquifer and ranges between 10 and 50 m. Considering specific discharge thresholds and temperature differences the thermal potential of GWHP is obtained and compared with the thermal potential of GCHP. Where both solutions are possible from a technical point of view, a long-term cost-benefit analysis is suggested.

The high potential of the study area to host different low enthalpy geothermal systems was demonstrated by maps describing the spatial distribution of specific heat exchange rates with the ground/groundwater. Finally, it was demonstrated that due to the high thermal exchange capacity of the area, at least the amount of thermal energy used in 2019 by non-renewable systems on a municipal basis could be provided only by GCHP and GWHP.

## 10.2. Characterization of the SUHI in the Milan city area

The extent and intensity of the SUHI effect in the Milan City area was investigated and natural and anthropogenic controls on the thermal regime were identified by means of spatial-temporal statistical techniques on high-resolution groundwater temperature data collected by the authors since 2016 and analyzed for the first time. The spatial distribution of the mean annual groundwater temperature and the seasonal fluctuations revealed differences up to 3°C between the City center and the surrounding rural areas located both upstream and laterally to the main groundwater flow direction. Downstream the city center, a superimposition of the effects due to the intense urbanization and the proximity of the water table to the surface is observed leading to higher groundwater temperature and strong seasonal fluctuations in the shallow portion of the aquifer. The impact of natural and anthropogenic factors on the groundwater thermal regime was assessed by means of bivariate, multivariate, and cross-correlation analysis revealing the thickness of the unsaturated zone and the density of surface structures/infrastructures to be the most relevant parameters which control the vertical heat fluxes into the aquifer. Among these, the most relevant anthropogenic heat sources were identified in the building density, the ground sealing by asphalt and concrete structures, underground tunnels, and geothermal installations. Their spatial density varies significantly in the study area but reaches the maximum simultaneously inside a 3km-radius-circle centered in the city center where the SUHI is observed. Inside this area a constant inverse thermal gradient (i.e. heat flux from the ground surface to the aquifer) of about +0.1 °C/m and a warming trend of +0.4 °C/year were observed, leading to a gain of thermal energy by the shallow aquifer beneath the SUHI up to +25 MJ/y/m2.

Insights from this city-scale groundwater temperature analysis, which is original for the Milan city area, were essential to develop the conceptual model for the subsurface thermal regime and the quantitative analysis through the first city-scale numerical model.

## 10.3. Groundwater physical-chemical conditions and microfauna

Investigations on the physical-chemical status and the abundance of microfauna in groundwater revealed the effects of urbanization, hydrological settings, and increased

temperature. It has been observed that the groundwater-atmosphere interactions are essential to microbial growth in terms of oxygen/nutrients input and, thus, land cover modifications such as soil sealing with impervious structures jeopardize the living ecosystems reducing the total number of microbials and, possibly, their diversity. Thus, low urbanized areas with shallow groundwater are prone to sustain healthy groundwater ecosystems, but aquifer characteristics such as the percentage of fine sediments can hinder the replenishment of oxygen in the shallow subsurface leading to reducing conditions and growth of associated communities. The effects of groundwater temperature on the abundance and characteristics of the groundwater fauna are not visible in this study due to the little range of the temperature variation and the prevalence of other mentioned effects. Further investigations on the quality (e.g. type of species) of microbial communities could help understanding the effects of urbanization and groundwater physical-chemical conditions on the groundwater ecosystems and to assess critic areas where the growth of undesired species or the reduction of “good” species is observed or expected in future.

## 10.4. Modeling the SUHI present and future impact on the shallow aquifers

Chapter 7 and 9 revealed that the groundwater thermal regime in the MCA is governed by the complex superimposition in time and space of positive and negative heat flows from many natural and anthropogenic sources. The fluid flow and heat transport 3D FEM numerical model proposed in this study deals with standard modeling techniques and new approaches to consider and quantify the most relevant heat sources and transport processes at the city-scale. The work focused on (I) the reconstruction of large-scale aquifer heterogeneities, essential to define advective dominated heat transport, including the definition of thermofacies from litho- and hydrofacies, (II) the accurate quantification of surface/subsurface thermal interactions defining the upper thermal boundary condition from a high-resolution land use maps and by means of a multilayer heat transfer analytical solution based on heat conduction coupled to the numerical solution, and (III) the integration of many natural and human-related fluid and heat sources as transient boundary conditions.

The results represent the groundwater thermal regime for the period 2015 to 2021 with a RMSE from 0.6 to 1.2 °C, and from 0.8 to 1.4 °C for the calibration and validation datasets,

respectively. As from a fluid and heat budget analysis, the most relevant natural and anthropogenic heat sources are building basements, surface concrete/asphalt structures and underground tunnels which contribute to 85% of the net annual heat accumulation in the subsurface which totals to + 1.4 PJ/y.

Analyzing numerical results such as the thermal and flow regimes and the Péclet number, the north-eastern sector of the domain was identified as the more promising area for low enthalpy geothermal development due to a high exchange potential together with an elevated thermal power demand. The calibrated and validated model allowed to capture the present groundwater and thermal regimes at the city-scale and to investigate the change in thermal energy stored by the groundwater bodies under different climate change, city development and shallow geothermal installations scenarios. It was demonstrated that RCP climate change scenarios and future urban expansions, assuming similar conditions for future urbanization, would contribute the most to the increment of thermal energy in the subsurface (+ 4% to 186% according to the scenario). Thus, the installation of shallow geothermal systems should be highly supported since their contribution to the subsurface heat accumulation is low (+ 0.7% to 3.3%) compared to possible impacts related to city development and climate change. However, the effects of shallow geothermal development could be higher considering that the building cooling demand will grow in future, especially within big cities where a UHI exists, leading to a greater injection of heat in the subsurface by geothermal installations.

Finally, the periodic fluctuations of the average model error (± 0.5 °C) computed for the shallow groundwater temperature suggest that investigations on specific surface thermal sources and assessments on the unsaturated zone thermal properties and the thermal dispersivity of different thermofacies are needed to improve the proposed city-scale model.

## 10.5. Conclusive remarks

It was demonstrated that local anthropogenic alterations at and beneath the surface and elevated air temperatures have a substantial impact on the large-scale distribution of the groundwater temperature in the MCA, leading to the development of a SUHI. This phenomenon was deeply investigated in this thesis through statistical and numerical analysis. In this context, a densely spaced, long-term monitoring network was essential to explore the spatial distribution and the temporal variability of the flow and thermal regimes, revealing the extent and intensity of the SUHI in the MCA. Natural and anthropogenic surface/subsurface changes were linked to the subsurface thermal regime and summarized by a conceptual model for the thermal pollution of the shallow aquifers. For the first time, a city-scale FEM numerical model considering fluid flow and heat transport was developed for the MCA to quantify the contribution from specific sources on the subsurface heat accumulation, reproduce the current-state SUHI and assess the geothermal potential and the future warming of the subsurface according to possible scenarios. This thesis demonstrates the importance of combined monitoring and modeling tools to unravel the anthropogenic disturbances to the subsurface thermal regime: a digital twin is needed in the MCA to support the sustainable development of the groundwater resource and assess the implications of current and future subsurface uses on the thermal regime.

# References


1. A.G.I., 1963. Nomenclatura geotecnica e classifica delle terre (Italian soil classification standard).
2. Al-Khoury, R., 2012. Computational modeling of Shallow Geothermal Systems, Multiphysics Modeling. https://doi.org/10.1037/13620-021
3. Alberti, L., Colombo, L., Formentin, G., 2018. Null-space Monte Carlo particle tracking to assess groundwater PCE (Tetrachloroethene) diffuse pollution in north-eastern Milan functional urban area. Sci. Total Environ. 621, 326–339. https://doi.org/10.1016/j.scitotenv.2017.11.253
4. Allen, R. G., Pereira, L.S., Raes, D., Smith, M., 1998. Crop evapotraspiration guidelines for computing crop water requirements., FAO Irrigation & drainage Paper 56. FAO, Food and Agriculture Organization of the United Nations,Roma.
5. Anderson, M.P., 2005. Heat as a ground water tracer. Ground Water 43, 951–968. https://doi.org/10.1111/j.1745-6584.2005.00052.x
6. Arola, T., Korkka-Niemi, K., 2014. The effect of urban heat islands on geothermal potential: examples from Quaternary aquifers in Finland. Hydrogeol. J. 22, 1953–1967. https://doi.org/10.1007/s10040-014-1174-5
7. ARPA Lombardia, 2021. Agenzia Regionale per la Protezione dell'Ambiente (Regional Environmental Monitoring Agency). URL www.arpalombardia.it/siti/arpalombardia/meteo/richiesta-dati-misurati (accessed 8.17.20).
8. ARPA Lombardia, 2019. Agenzia Regionale per la Protezione dell'Ambiente (Regional Environmental Monitoring Agency). URL www.arpalombardia.it/siti/arpalombardia/meteo/richiesta-dati-misurati (accessed 7.2.19).
9. Attard, G., Rossier, Y., Winiarski, T., Eisenlohr, L., 2016. Deterministic modeling of the impact of underground structures on urban groundwater temperature. Sci. Total Environ. 572, 986–994. https://doi.org/10.1016/j.scitotenv.2016.07.229
10. Bacci, P., Maugeri, M., 1992. The urban heat island of Milan. Nuovo Cim. C 15, 417–424. https://doi.org/10.1007/BF02511742
11. Banks, D., 2009a. An introduction to thermogeology and the exploitation of ground source heat. Q. J. Eng. Geol. Hydrogeol. 42, 283–293.
12. Banks, D., 2009b. Thermogeological assessment of open-loop well-doublet schemes: A review and synthesis of analytical approaches. Hydrogeol. J. 17, 1149–1155. https://doi.org/10.1007/s10040-008-0427-6
13. Bayer, P., Attard, G., Blum, P., Menberg, K., 2019. The geothermal potential of cities. Renew. Sustain. Energy Rev. 106, 17–30. https://doi.org/10.1016/J.RSER.2019.02.019
14. Bayer, P., Saner, D., Bolay, S., Rybach, L., Blum, P., 2012. Greenhouse gas emission savings of ground source heat pump systems in Europe: A review. Renew. Sustain. Energy Rev. 16, 1256–1267. https://doi.org/10.1016/j.rser.2011.09.027
15. Bear, J., 1972. Dynamics of fluids in porous media. New York.
16. Benz, S.A., Bayer, P., Blum, P., Hamamoto, H., Arimoto, H., Taniguchi, M., 2018. Comparing anthropogenic heat input and heat accumulation in the subsurface of Osaka, Japan. Sci. Total Environ. 643, 1127–1136. https://doi.org/10.1016/j.scitotenv.2018.06.253
17. Benz, S.A., Bayer, P., Goettsche, F.M., Olesen, F.S., Blum, P., 2016. Linking Surface Urban Heat Islands with Groundwater Temperatures. Environ. Sci. Technol. 50, 70–78. https://doi.org/10.1021/acs.est.5b03672
18. Benz, S.A., Bayer, P., Menberg, K., Jung, S., Blum, P., 2015. Spatial resolution of anthropogenic heat fluxes into urban aquifers. Sci. Total Environ. 524–525, 427–439. https://doi.org/10.1016/j.scitotenv.2015.04.003
19. Beretta, G. Pietro, Avanzini, M., Pagotto, A., 2004. Managing groundwater rise: Experimental results and modelling of water pumping from a quarry lake in Milan urban area (Italy). Environ. Geol. 45, 600–608.

https://doi.org/10.1007/s00254-003-0918-7

20. Bersezio, R., Bini, A., Giudici, M., 1999. Effects of sedimentary heterogeneity on groundwater flow in a Quaternary pro-glacial delta environment: Joining facies analysis and numerical modelling. Sediment. Geol. 129, 327–344. https://doi.org/10.1016/S0037-0738(98)00145-6

21. Bersezio, R., Cavalli, E., Cantone, M., Cantoni, M., 2010. Aquifer building and apennine tectonics in a quaternary foreland: the southernmost lodi plain of Lombardy. Mem.Descr.Carta Geol.d'It. 21–30.

22. Bertermann, D., Klug, H., Morper-Busch, L., 2015. A pan-European planning basis for estimating the very shallow geothermal energy potentials. Renew. Energy 75, 335–347. https://doi.org/10.1016/j.renene.2014.09.033

23. Bezelgues-courtade, S., Martin, J., Schomburgk, S., Nguyen-the, D., Nguyen, D., Brun, M. Le, Desplan, A., 2010. Geothermal Potential of Shallow Aquifers : Decision-Aid Tool for Heat-Pump Installation.

24. Bidarmaghz, A., Choudhary, R., Soga, K., Kessler, H., Terrington, R.L., Thorpe, S., 2019. Influence of geology and hydrogeology on heat rejection from residential basements in urban areas. Tunn. Undergr. Sp. Technol. 92, 103068. https://doi.org/10.1016/j.tust.2019.103068

25. Bidarmaghz, A., Choudhary, R., Soga, K., Terrington, R.L., Kessler, H., Thorpe, S., 2020. Large-scale urban underground hydro-thermal modelling – A case study of the Royal Borough of Kensington and Chelsea, London. Sci. Total Environ. 700, 134955. https://doi.org/10.1016/j.scitotenv.2019.134955

26. Blum, P., Campillo, G., Kölbel, T., 2011. Techno-economic and spatial analysis of vertical ground source heat pump systems in Germany. Energy 36, 3002–3011. https://doi.org/10.1016/j.energy.2011.02.044

27. Blum, P., Campillo, G., Münch, W., Kölbel, T., 2010. CO2 savings of ground source heat pump systems - A regional analysis. Renew. Energy 35, 122–127. https://doi.org/10.1016/j.renene.2009.03.034

28. Blum, P., Menberg, K., Koch, F., Benz, S.A., Tissen, C., Hemmerle, H., Bayer, P., 2021. Is thermal use of groundwater a pollution? J. Contam. Hydrol. 108947. https://doi.org/10.1016/j.jconhyd.2021.103791

29. Bonte, M., Röling, W.F.M., Zaura, E., Van Der Wielen, P.W.J.J., Stuyfzand, P.J., Van Breukelen, B.M., 2013. Impacts of shallow geothermal energy production on redox processes and microbial communities. Environ. Sci. Technol. 47, 14476–14484. https://doi.org/10.1021/es4030244

30. Böttcher, F., Casasso, A., Götzl, G., Zosseder, K., 2019. TAP - Thermal aquifer Potential: A quantitative method to assess the spatial potential for the thermal use of groundwater. Renew. Energy 142, 85–95. https://doi.org/10.1016/j.renene.2019.04.086

31. BRE, 2012. SAP 2012: The Government's Standard Assessment Procedure for Energy Rating of Dwellings. Watford.

32. Brielmann, H., Griebler, C., Schmidt, S.I., Michel, R., Lueders, T., 2009. Effects of thermal energy discharge on shallow groundwater ecosystems. FEMS Microbiol. Ecol. 68, 273–286. https://doi.org/10.1111/j.1574-6941.2009.00674.x

33. Bundschuh, J., Suarez Arriaga, M., 2010. Introduction to the numerical modeling of groundwater and geothermal systems: fundamentals of mass, energy and solute transport in poroelastic rocks, CRC Press.

34. Busby, J., Lewis, M., Reeves, H., Lawley, R., 2009. Initial geological considerations before installing ground source heat pump systems. Q. J. Eng. Geol. Hydrogeol. 42, 295–306. https://doi.org/10.1144/1470-9236/08-092

35. Carslaw, H.S., Jaeger, J.C., 1959. Conduction of heat in solids. Oxford Clarendon Press. 1959, 2nd ed.

36. Casasso, A., Piga, B., Sethi, R., Prestor, J., Pestotnik, S., Bottig, M., Goetzl, G., Zambelli, P., D'Alonzo, V., Vaccaro, R., Capodaglio, P., Olmedo, M., Baietto, A., Maragna, C., Böttcher, F., Zoesseder, K., 2017. The GRETA project: the contribution of near-surface geothermal energy for the energetic self-sufficiency of Alpine regions. Acque Sotter. - Ital. J. Groundw. 6. https://doi.org/10.7343/as-2017-265

37. Casasso, A., Sethi, R., 2016a. Studio e mappatura delle potenzialità della geotermia a bassa entalpia nella Provincia di Cuneo 1–83.

38. Casasso, A., Sethi, R., 2016b. G.POT: A quantitative method for the assessment and mapping of the shallow geothermal potential. Energy 106, 765–773. https://doi.org/10.1016/j.energy.2016.03.091

39. CCKP, 2021. Climate Change Knowledge Portal. URL https://climateknowledgeportal.worldbank.org/ (accessed 6.1.21).

40. Città Metropolitana di Milano, CAP, 2021. Pozzi e Piezometri nel territorio di Citta' Metropolitana. URL https://ambientecomune.eu/ (accessed 4.1.20).

41. Clauser, C., 2009. Heat transport processes in the earth's crust. Surv. Geophys. 30, 163–191. https://doi.org/10.1007/s10712-009-9058-2

42. Clauser, C., 2006. Geothermal Energy. Springer Verlag. https://doi.org/10.1007/b83039

43. Colombo, L., Gattinoni, P., Scesi, L., 2018. Stochastic modelling of groundwater flow for hazard assessment along the underground infrastructures in Milan (northern Italy). Tunn. Undergr. Sp. Technol. 79, 110–120. https://doi.org/10.1016/j.tust.2018.05.007

44. Crosta, G.B., De Caro, M., 2018. Groundwater Rebound, in: Bobrowsky, P., Marker, B. (Eds.), Encyclopedia of Engineering Geology. Springer International Publishing, Cham, pp. 1–3. https://doi.org/10.1007/978-3-319-12127-7_151-1

45. Cryer, J.D., Chan, K.-S., 2008. Time series analysis: with applications in R, Springer Science & Business Media. https://doi.org/10.1007/BF00746534

46. Danielopol, D.L., Griebler, C., Gunatilaka, A., Notenboom, J., 2003. Present state and future prospects for groundwater ecosystems. Environ. Conserv. 30, 104–130. https://doi.org/10.1017/S0376892903000109

47. Davies, J., 2013. Global map of solid Earth surface heat flow: Global Surface Heat Flow Map. Geochemistry, Geophys. Geosystems. 14.

48. Davis, J.C., Sampson, R.J., 1986. Statistics and data analysis in geology. Wiley New York.

49. De Caro, M., 2018. PhD Thesis: Analysis of groundwater environment change in the Milan Metropolitan area by hydrostratigraphic, groundwater quality and flow modeling.

50. De Caro, M., Crosta, G.B., Frattini, P., 2017. Hydrogeochemical characterization and Natural Background Levels in urbanized areas: Milan Metropolitan area (Northern Italy). J. Hydrol. 547, 455–473. https://doi.org/10.1016/j.jhydrol.2017.02.025

51. De Caro, M., Crosta, G.B., Previati, A., 2020a. Modelling the interference of underground structures with groundwater flow and remedial solutions in Milan. Eng. Geol. 272, 105652. https://doi.org/10.1016/j.enggeo.2020.105652

52. De Caro, M., Perico, R., Crosta, G.B., Frattini, P., Volpi, G., 2020b. A regional-scale conceptual and numerical groundwater flow model in fluvio-glacial sediments for the Milan Metropolitan area (Northern Italy). J. Hydrol. Reg. Stud. 29, 100683. https://doi.org/10.1016/j.ejrh.2020.100683

53. De Luca, D.A., Destefanis, E., Forno, M.G., Lasagna, M., Masciocco, L., 2014. The genesis and the hydrogeological features of the Turin Po Plain fontanili, typical lowland springs in Northern Italy. Bull. Eng. Geol. Environ. 73, 409–427. https://doi.org/10.1007/s10064-013-0527-y

54. De Marsily, G., Delay, F., Gonçalvès, J., Renard, P., Teles, V., Violette, S., 2005. Dealing with spatial heterogeneity. Hydrogeol. J. https://doi.org/10.1007/s10040-004-0432-3

55. De Marsily, G., Delay, F., Teles, V., Schafmeister, M.T., 1998. Some current methods to represent the heterogeneity of natural media in hydrogeology. Hydrogeol. J. 6, 115–130. https://doi.org/10.1007/s100400050138

56. Deming, D., 1994. Fluid flow and heat transport in the upper continental crust. Geol. Soc. London, Spec. Publ. 78, 27–42. https://doi.org/10.1144/GSL.SP.1994.078.01.04

57. DHI-Wasy, 2016. FePEST in FEFLOW 7.0 (FePEST user manual).

58. Di Sipio, E., Galgaro, A., Destro, E., Teza, G., Chiesa, S., Giaretta, A., Manzella, A., 2014. Subsurface thermal conductivity assessment in Calabria (southern Italy): a regional case study. Environ. Earth Sci. 1383–1401. https://doi.org/10.1007/s12665-014-3277-7

59. Diersch, H.-J.G., 2014. FEFLOW: Finite Element Modeling of Flow, Mass and Heat Transport in Porous and Fractured Media.

60. Doherty, J., Brebber, L., Whyte, P., 1994. PEST: Model-independent parameter estimation. Watermark Comput. Corinda, Aust. 122, 336.

61. ENEA, 2018. Rapporto Annuale Efficienza Energetica.

62. Epting, J., García-Gil, A., Huggenberger, P., Vázquez-Suñe, E., Mueller, M.H., 2017a. Development of concepts for the management of thermal resources in urban areas – Assessment of transferability from the Basel (Switzerland) and Zaragoza (Spain) case studies. J. Hydrol. 548, 697–715. https://doi.org/10.1016/j.jhydrol.2017.03.057

63. Epting, J., Händel, F., Huggenberger, P., 2013. Thermal management of an unconsolidated shallow urban groundwater body. Hydrol. Earth Syst. Sci. 17, 1851–1869. https://doi.org/10.5194/hess-17-1851-2013

64. Epting, J., Huggenberger, P., 2013. Unraveling the heat island effect observed in urban groundwater bodies - Definition of a potential natural state. J. Hydrol. 501, 193–204. https://doi.org/10.1016/j.jhydrol.2013.08.002

65. Epting, J., Müller, M.H., Genske, D., Huggenberger, P., 2018. Relating groundwater heat-potential to city-scale heat-demand: A theoretical consideration for urban groundwater resource management. Appl. Energy 228, 1499–1505. https://doi.org/10.1016/j.apenergy.2018.06.154

66. Epting, J., Scheidler, S., Affolter, A., Borer, P., Mueller, M.H., Egli, L., García-Gil, A., Huggenberger, P., 2017b. The thermal impact of subsurface building structures on urban groundwater resources – A paradigmatic example. Sci. Total Environ. 596–597, 87–96. https://doi.org/10.1016/j.scitotenv.2017.03.296

67. EU DIRECTIVE 2006/118, 2006. Directive (EU) 2006/118/EC of the European Parliament and of the Council of 12 December 2006 on the protection of groundwater against pollution and deterioration, Official Journal of the European Union. https://doi.org/10.1007/BF02678785

68. EU DIRECTIVE 2018/2001, 2018. Directive (EU) 2018/2001 of the European Parliament and of the Council on the promotion of the use of energy from renewable sources, Official Journal of the European Union.

69. European Climate Foundation, 2010. Roadmap 2050 A practical guide to a prosperous low-carbon Europe. Technical analysis, Policy. https://doi.org/10.2833/10759

70. EUROSTAT, 2019. Energy statistics - Price of natural gas and electricity. URL https://ec.europa.eu/eurostat/web/energy/data/database (accessed 6.1.19).

71. Farr, G.J., Patton, A.M., Boon, D.P., James, D.R., Williams, B., Schofield, D.I., 2017. Mapping shallow urban groundwater temperatures, a case study from Cardiff, UK. Q. J. Eng. Geol. Hydrogeol. 50, 187–198. https://doi.org/10.1144/qjegh2016-058

72. Ferguson, G., Woodbury, A.D., 2004. Subsurface heat flow in an urban environment. J. Geophys. Res. Solid Earth 109, 1–9. https://doi.org/10.1029/2003jb002715

73. Fogg, G.E., 1996. Transition Probability-Based Indicator Geostatistics. Math. Geol. 28, 453–476. https://doi.org/10.1007/bf02083656

74. Fontana, A., Mozzi, P., Marchetti, M., 2014. Alluvial fans and megafans along the southern side of the Alps. Sediment. Geol. 301, 150–171. https://doi.org/10.1016/j.sedgeo.2013.09.003

75. Foster, S.S.D., 2001. The interdependence of groundwater and urbanisation in rapidly developing cities. Urban Water 3, 185–192. https://doi.org/10.1016/S1462-0758(01)00043-7

76. Francese, R., Giudici, M., Schmitt, D.R., Zaja, A., 2005. Mapping the geometry of an aquifer system with a high-resolution reflection seismic profile. Geophys. Prospect. 53, 817–828.

77. Fridleifsson, I.B., Bertani, R., Huenges, E., Lund, J.W., Ragnarsson, A., Rybach, L., 2008. The possible role and contribution of geothermal energy to the mitigation of climate change, in: IPCC Scoping Meeting on Renewable Energy Sources, Proceedings, Luebeck, Germany.

78. Galgaro, A., Di Sipio, E., Teza, G., Destro, E., De Carli, M., Chiesa, S., Zarrella, A., Emmi, G., Manzella, A., 2015. Empirical modeling of maps of geo-exchange potential for shallow geothermal energy at regional scale. Geothermics 57, 173–184. https://doi.org/10.1016/j.geothermics.2015.06.017

79. García-Gil, A., Vázquez-Suñe, E., Alcaraz, M.M., Juan, A.S., Sánchez-Navarro, J.Á., Montlleó, M., Rodríguez, G., Lao, J., 2015. GIS-supported mapping of low-temperature geothermal potential taking groundwater flow

into account. Renew. Energy 77, 268–278. https://doi.org/10.1016/j.renene.2014.11.096

80. Garzanti, E., Vezzoli, G., Andò, S., 2011. Paleogeographic and paleodrainage changes during Pleistocene glaciations (Po Plain, northern Italy). Earth-Science Rev. 105, 25–48.

81. Gattinoni, P., Scesi, L., 2017. The groundwater rise in the urban area of Milan (Italy) and its interactions with underground structures and infrastructures. Tunn. Undergr. Sp. Technol. 62, 103–114. https://doi.org/10.1016/j.tust.2016.12.001

82. Greswell, R.B., Lloyd, J.W., Lerner, D.N., Knipe, C. V., 1994. Rising groundwater in the Birmingham area. Groundw. Probl. urban areas 330–341. https://doi.org/10.1680/gpiua.19744.0024

83. Griebler, C., Brielmann, H., Haberer, C.M., Kaschuba, S., Kellermann, C., Stumpp, C., Hegler, F., Kuntz, D., Walker-Hertkorn, S., Lueders, T., 2016. Potential impacts of geothermal energy use and storage of heat on groundwater quality, biodiversity, and ecosystem processes. Environ. Earth Sci. 75, 1–18. https://doi.org/10.1007/s12665-016-6207-z

84. GSE, 2018. Gestore dei Servizi Energetici - Rapporto Statistico energia da fonti rinnovabili anno 2017 [2017 statistical report on renewable energy].

85. Günther, S., Hübschmann, T., Rudolf, M., Eschenhagen, M., Röske, I., Harms, H., Müller, S., 2008. Fixation procedures for flow cytometric analysis of environmental bacteria. J. Microbiol. Methods 75, 127–134. https://doi.org/10.1016/j.mimet.2008.05.017

86. Guzzetti, F., Marchetti, M., Reichenbach, P., 1997. Large alluvial fans in the north-central Po Plain (Northern Italy). Geomorphology 18, 119–136. https://doi.org/10.1016/S0169-555X(96)00015-3

87. Händel, F., Liedl, R., Fank, J., Rock, G., 2013. Regional modeling of geothermal energy systems in shallow aquifers: The Leibnitzer Feld case study (Austria). Environ. Earth Sci. 70, 3433–3446. https://doi.org/10.1007/s12665-013-2469-x

88. Hemmerle, H., Hale, S., Dressel, I., Benz, S.A., Attard, G., Blum, P., Bayer, P., 2019. Estimation of Groundwater Temperatures in Paris, France. Geofluids 2019, 1–11. https://doi.org/10.1155/2019/5246307

89. Hepbasli, A., 2004. Ground-Source Heat Pumps, in: Elsevier (Ed.), Encyclopedia of Energy. pp. 97–106.

90. Herbert, A., Arthur, S., Chillingworth, G., 2013. Thermal modelling of large scale exploitation of ground source energy in urban aquifers as a resource management tool. Appl. Energy 109, 94–103. https://doi.org/10.1016/j.apenergy.2013.03.005

91. Huggenberger, P., Epting, J., 2011. Urban geology: process-oriented concepts for adaptive and integrated resource management. Springer Science & Business Media.

92. Ingersoll, L.R., Zobel, O.J., Ingersoll, A.C., 1954. Heat Conduction with Engineering, Geological and Other Applications. Fluid Mech. its Appl. https://doi.org/10.1007/978-3-319-15793-1_9

93. ISPRA, 2015. Modello geologico 3D e geopotenziali della Pianura Padana centrale (Progetto Geomol).

94. ISPRA, Regione Lombardia, 2016. Note Illustrative della Carta Geologica d'Italia - Foglio 118 Milano.

95. ISTAT, 2019. Dati del censimento della popolazione e delle abitazioni 2011 (Italian population census). URL http://datiopen.istat.it/ (accessed 7.2.19).

96. Jolliffe, I.T., 1986. Principal Component Analysis, Springer Series in Statistics, Springer-Verlag. New York.

97. Journel, A.G., Huijbregts, C.J., 1976. Mining geostatistics.

98. Kavanaugh, S.P., Rafferty, K., 2014. Geothermal Heating and Cooling: Design of Ground-Source Heat Pump Systems (ASHRAE).

99. Khatri, N., Tyagi, S., 2015. Influences of natural and anthropogenic factors on surface and groundwater quality in rural and urban areas. Front. Life Sci. 8, 23–39. https://doi.org/10.1080/21553769.2014.933716

100. Koch, F., Menberg, K., Schweikert, S., Spengler, C., Hahn, H.J., Blum, P., 2020. Groundwater fauna in an urban area: natural or affected? Hydrol. Earth Syst. Sci. Discuss. 1–23. https://doi.org/10.5194/hess-2020-151

101. Kottek, M., Grieser, J., Beck, C., Rudolf, B., Rubel, F., 2006. World map of the Köppen-Geiger climate

classification updated. Meteorol. Zeitschrift 15, 259–263. https://doi.org/10.1127/0941-2948/2006/0130

102. Krzanowski, W., 2000. Principles of multivariate analysis. OUP Oxford.

103. Kupfersberger, H., Rock, G., Draxler, J.C., 2017. Inferring near surface soil temperature time series from different land uses to quantify the variation of heat fl1. Kupfersberger H, Rock G, Draxler JC. Inferring near surface soil temperature time series from different land uses to quantify the variation. J. Hydrol. 552, 564–577. https://doi.org/10.1016/j.jhydrol.2017.07.030

104. Kurylyk, B.L., Irvine, D.J., Bense, V.F., 2019. Theory, tools, and multidisciplinary applications for tracing groundwater fluxes from temperature profiles. Wiley Interdiscip. Rev. Water 6, e1329. https://doi.org/10.1002/wat2.1329

105. Kurylyk, B.L., MacQuarrie, K.T.B., Caissie, D., McKenzie, J.M., 2015. Shallow groundwater thermal sensitivity to climate change and land cover disturbances: Derivation of analytical expressions and implications for stream temperature modeling. Hydrol. Earth Syst. Sci. 19, 2469–2489. https://doi.org/10.5194/hess-19-2469-2015

106. Lamarche, L., Kajl, S., Beauchamp, B., 2010. A review of methods to evaluate borehole thermal resistances in geothermal heat-pump systems. Geothermics 39, 187–200. https://doi.org/https://doi.org/10.1016/j.geothermics.2010.03.003

107. Lee, S.Y., Carle, S.F., Fogg, G.E., 2007. Geologic heterogeneity and a comparison of two geostatistical models: Sequential Gaussian and transition probability-based geostatistical simulation. Adv. Water Resour. 30, 1914–1932. https://doi.org/10.1016/j.advwatres.2007.03.005

108. Lindal, B., 1973. Industrial and other applications of geothermal energy. Geotherm. energy 135–148.

109. Lippmann, M.J., 1980. Ground water use for cooling: Associated aquifer temperature changes.

110. Lund, J.W., Boyd, T.L., 2016. Direct utilization of geothermal energy 2015 worldwide review. Geothermics 60, 66–93. https://doi.org/10.1016/j.geothermics.2015.11.004

111. Macey, M.G., 2007. Flow Cytometry, Springer.

112. Martinis, B., Mazzarella, S., 1971. Prima ricerca idrica profonda nella pianura lombarda. Mem. Ist. Geol. e Min. Univ. Padova.

113. Menberg, K., Bayer, P., Zosseder, K., Rumohr, S., Blum, P., 2013a. Subsurface urban heat islands in German cities. Sci. Total Environ. 442, 123–133. https://doi.org/10.1016/j.scitotenv.2012.10.043

114. Menberg, K., Blum, P., Kurylyk, B.L., Bayer, P., 2014. Observed groundwater temperature response to recent climate change. Hydrol. Earth Syst. Sci. 18, 4453–4466. https://doi.org/10.5194/hess-18-4453-2014

115. Menberg, K., Blum, P., Schaffitel, A., Bayer, P., 2013b. Long-term evolution of anthropogenic heat fluxes into a subsurface urban heat island. Environ. Sci. Technol. 47, 9747–9755. https://doi.org/10.1021/es401546u

116. Mueller, M.H., Huggenberger, P., Epting, J., 2018. Combining monitoring and modelling tools as a basis for city-scale concepts for a sustainable thermal management of urban groundwater resources. Sci. Total Environ. 627, 1121–1136. https://doi.org/10.1016/j.scitotenv.2018.01.250

117. Oke, T.R., 1973. City size and the urban heat island. Atmos. Environ. 7, 769–779.

118. Ouellon, T., Lefebvre, R., Marcotte, D., Boutin, A., Blais, V., Parent, M., 2008. Hydraulic conductivity heterogeneity of a local deltaic aquifer system from the kriged 3D distribution of hydrofacies from borehole logs, Valcartier, Canada. J. Hydrol. 351, 71–86. https://doi.org/10.1016/j.jhydrol.2007.11.040

119. Peel, M.C., Finlayson, B.L., McMahon, T.A., 2007. Updated world map of the Köppen-Geiger climate classification. Hydrol. earth Syst. Sci. 11, 1633–1644.

120. Perego, R., Pera, S., Galgaro, A., 2019. Techno-Economic Mapping for the Improvement of Shallow Geothermal Management in Southern Switzerland. Energies 12, 279. https://doi.org/10.3390/en12020279

121. Petrucci, F., Tagliavini, S., 1969. Note Illustrative della Carta Geologica d'Italia, Foglio 61, Cremona.

122. Pichierri, M., Bonafoni, S., Biondi, R., 2012. Satellite air temperature estimation for monitoring the canopy layer heat island of Milan. Remote Sens. Environ. 127, 130–138. https://doi.org/10.1016/j.rse.2012.08.025

123. Previati, A., Crosta, G.B., 2021a. Characterization of the subsurface urban heat island and its sources in the Milan city area, Italy. Hydrogeol. J. https://doi.org/10.1007/s10040-021-02387-z

124. Previati, A., Crosta, G.B., 2021b. Regional-scale assessment of the thermal potential in a shallow alluvial aquifer system in the Po plain (northern Italy). Geothermics 90, 101999. https://doi.org/10.1016/j.geothermics.2020.101999

125. Regione Lombardia, 2021. Registro Regionale Sonde Geotermiche (regional database on closed-loop geothermal applications). URL http://www.rinnovabililombardia.it/rsg (accessed 7.1.21).

126. Regione Lombardia, 2020. Regional Geographic Database. URL https://www.cartografia.servizirl.it/viewer32/index.jsp?config=config_dbt.json (accessed 9.1.20).

127. Regione Lombardia, 2019a. Carta Geoenergetica Regionale. URL http://www.rinnovabililombardia.it/cartageoenergetica (accessed 7.25.19).

128. Regione Lombardia, 2019b. CURIT - Catasto Impianti Termici. URL www.curit.it (accessed 9.20.19).

129. Regione Lombardia, 2017. Deliberazione 6203 (08/02/2017), L.R. 38/2015, D.LGS 152 03/04/2006.

130. Regione Lombardia, 2010. Regolamento Regionale n.7 15/02/2010.

131. Regione Lombardia - CASPITA, 2019. Banca dati geologica del sottosuolo. URL http://www.geoportale.regione.lombardia.it/download-dati (accessed 7.2.19).

132. Regione Lombardia, ENI, 2002. Geologia degli acquiferi padani della Regione Lombardia. SELCA, Firenze.

133. Regione Lombardia, PTUA, 2014. Piezometrie 2014 degli acquiferi superficiali e profondi (2014 piezometric map of the Po plain). URL https://www.geoportale.regione.lombardia.it/download-dati (accessed 11.1.19).

134. Retter, A., Karwautz, C., Griebler, C., 2020. Groundwater Microbial Communities in Times of Climate Change, Climate Change and Microbial Ecology: Current Research and Future Trends (Second Edition). https://doi.org/10.21775/9781913652579.13

135. Rock, G., Kupfersberger, H., 2018. 3D modeling of groundwater heat transport in the shallow Westliches Leibnitzer Feld aquifer, Austria. J. Hydrol. 557, 668–678. https://doi.org/10.1016/j.jhydrol.2017.12.060

136. Rose, S., Long, A., 1988. Monitoring Dissolved Oxygen in Ground Water: Some Basic Considerations. Groundw. Monit. Remediat. https://doi.org/10.1111/j.1745-6592.1988.tb00981.x

137. Rusydi, A.F., 2018. Correlation between conductivity and total dissolved solid in various type of water: A review, in: IOP Conference Series: Earth and Environmental Science. IOP Publishing, p. 12019.

138. Saner, D., Juraske, R., Kübert, M., Blum, P., Hellweg, S., Bayer, P., 2010. Is it only CO 2 that matters? A life cycle perspective on shallow geothermal systems. Renew. Sustain. Energy Rev. 14, 1798–1813. https://doi.org/10.1016/j.rser.2010.04.002

139. Sartirana, D., Rotiroti, M., Zanotti, C., Bonomi, T., Fumagalli, L., Amicis, M. De, 2020. A 3D geodatabase for urban underground infrastructures: implementation and application to groundwater management in milan metropolitan area. ISPRS Int. J. Geo-Information 9. https://doi.org/10.3390/ijgi9100609

140. Scardia, G., Muttoni, G., Sciunnach, D., 2006. Subsurface magnetostratigraphy of Pleistocene sediments from the Po Plain (Italy): Constraints on rates of sedimentation and rock uplift. Bull. Geol. Soc. Am. 118, 1299–1312. https://doi.org/10.1130/B25869.1

141. Self, S.J., Reddy, B. V., Rosen, M.A., 2013. Geothermal heat pump systems: Status review and comparison with other heating options. Appl. Energy 101, 341–348. https://doi.org/10.1016/j.apenergy.2012.01.048

142. Shafiee, S., Topal, E., 2009. When will fossil fuel reserves be diminished? Energy Policy 37, 181–189.

143. Sharp Jr, J.M., Krothe, J.N., Mather, J.D., Gracia-Fresca, B., Stewart, C.A., 2003. Effects of urbanization on groundwater systems, in: Earth Science in the City: A Reader. Wiley Online Library, pp. 257–278.

144. Shonder, J.A., Beck, J. V, 1999. Field test of a new method for determining soil formation thermal conductivity and borehole resistance. ASHRAE Transactions, 106 (1999).

145. Signorelli, S., Kohl, T., 2004. Regional ground surface temperature mapping from meteorological data. Glob. Planet. Change 40, 267–284. https://doi.org/10.1016/j.gloplacha.2003.08.003

146. Smerdon, J.E., Pollack, H.N., Cermak, V., Enz, J.W., Kresl, M., Safanda, J., Wehmiller, J.F., 2006. Daily, seasonal, and annual relationships between air and subsurface temperatures. J. Geophys. Res. Atmos. 111, 1–12. https://doi.org/10.1029/2004JD005578

147. Smith, G.D., Smith, G.D., Smith, G.D.S., 1985. Numerical solution of partial differential equations: finite difference methods. Oxford university press.

148. Solomon, S., Manning, M., Marquis, M., Qin, D., 2007. Climate change 2007-the physical science basis: Working group I contribution to the fourth assessment report of the IPCC. Cambridge university press.

149. Stauffer, F., Bayer, P., Blum, P., Molina-Giraldo, N., Kinzelbach, W., 2013. Thermal use of shallow groundwater, Thermal Use of Shallow Groundwater. https://doi.org/10.1201/b16239

150. Stober, I., Butcher, K., 2017. Geothermal energy, Lecture Notes in Energy. https://doi.org/10.1007/978-3-319-52311-8_9

151. Strebelle, S., 2002. Conditional simulation of complex geological structures using multiple-point statistics. Math. Geol. 34, 1–21.

152. Taniguchi, M., Shimada, J., Tanaka, T., Kayane, I., Sakura, Y., Shimano, Y., Dapaah-Siakwan, S., Kawashima, S., 1999. Disturbances of temperature-depth profiles due to surface climate change and subsurface water flow: 1. An effect of linear increase in surface temperature caused by global warming and urbanization in the Tokyo Metropolitan Area, Japan. Water Resour. Res. 35, 1507–1517. https://doi.org/10.1029/1999WR900009

153. Taniguchi, M., Uemura, T., Jago-on, K., 2007. Combined Effects of Urbanization and Global Warming on Subsurface Temperature in Four Asian Cities. Vadose Zo. J. 6, 591–596. https://doi.org/10.2136/vzj2006.0094

154. Taylor, C.A., Stefan, H.G., 2009. Shallow groundwater temperature response to climate change and urbanization. J. Hydrol. 375, 601–612. https://doi.org/10.1016/j.jhydrol.2009.07.009

155. Taylor, K.E., Stouffer, R.J., Meehl, G.A., 2012. An Overview of CMIP5 and the Experiment Design. Bull. Am. Meteorol. Soc. 93, 485–498. https://doi.org/10.1175/BAMS-D-11-00094.1

156. Trauth, R., Xanthopoulos, C., 1997. Non-point pollution of groundwater in urban areas. Water Res. 31, 2711–2718. https://doi.org/10.1016/S0043-1354(97)00124-3

157. Unione Geotermica Italiana, 2017. Growth forecasts of geothermal energy in Italy 2016-2030, with projections to 2050, UGI.

158. VDI 4640/1, 2000. Thermal Use of the Underground — Fundamentals, Approvals, Environmental Aspects.

159. VDI 4640/2, 2001. Thermal Use of the Underground — Ground source heat pump systems.

160. Viesi, D., Crema, L., Zanetti, A., Galgaro, A., Scotton, P., 2016. Geoscambio Nella Provincia Autonoma Di Trento.

161. Viesi, D., Galgaro, A., Visintainer, P., Crema, L., 2018. GIS-supported evaluation and mapping of the geo-exchange potential for vertical closed-loop systems in an Alpine valley, the case study of Adige Valley (Italy). Geothermics 71, 70–87. https://doi.org/10.1016/j.geothermics.2017.08.008

162. Visser, P.W., Kooi, H., Bense, V., Boerma, E., 2020. Impacts of progressive urban expansion on subsurface temperatures in the city of Amsterdam (The Netherlands). Hydrogeol. J. 28, 1755–1772. https://doi.org/10.1007/s10040-020-02150-w

163. Woodside, W., Messmer, J.H., 1961. Thermal Conductivity of Porous Media I. Unconsolidated Sands. J. Appl. Phys. 32. https://doi.org/10.1063/1.1728419

164. Zhu, K., Bayer, P., Grathwohl, P., Blum, P., 2015. Groundwater temperature evolution in the subsurface urban heat island of Cologne, Germany. Hydrol. Process. 29, 965–978. https://doi.org/10.1002/hyp.10209

165. Zhu, K., Blum, P., Ferguson, G., Balke, K.-D., Bayer, P., 2011. The geothermal potential of urban heat islands. Environ. Res. Lett. 6, 019501. https://doi.org/10.1088/1748-9326/6/1/019501

166. Zienkiewicz, O.C., Taylor, R.L., Nithiarasu, P., Zhu, J.Z., 1977. The finite element method. McGraw-hill London.

# Appendix

***Supporting material*** *– Vertical profiles of groundwater temperature (Temp), dissolved oxygen (DO), pH and electrical conductivity (Cond El). Refer to* ***Figure 5.3*** *for their location.*

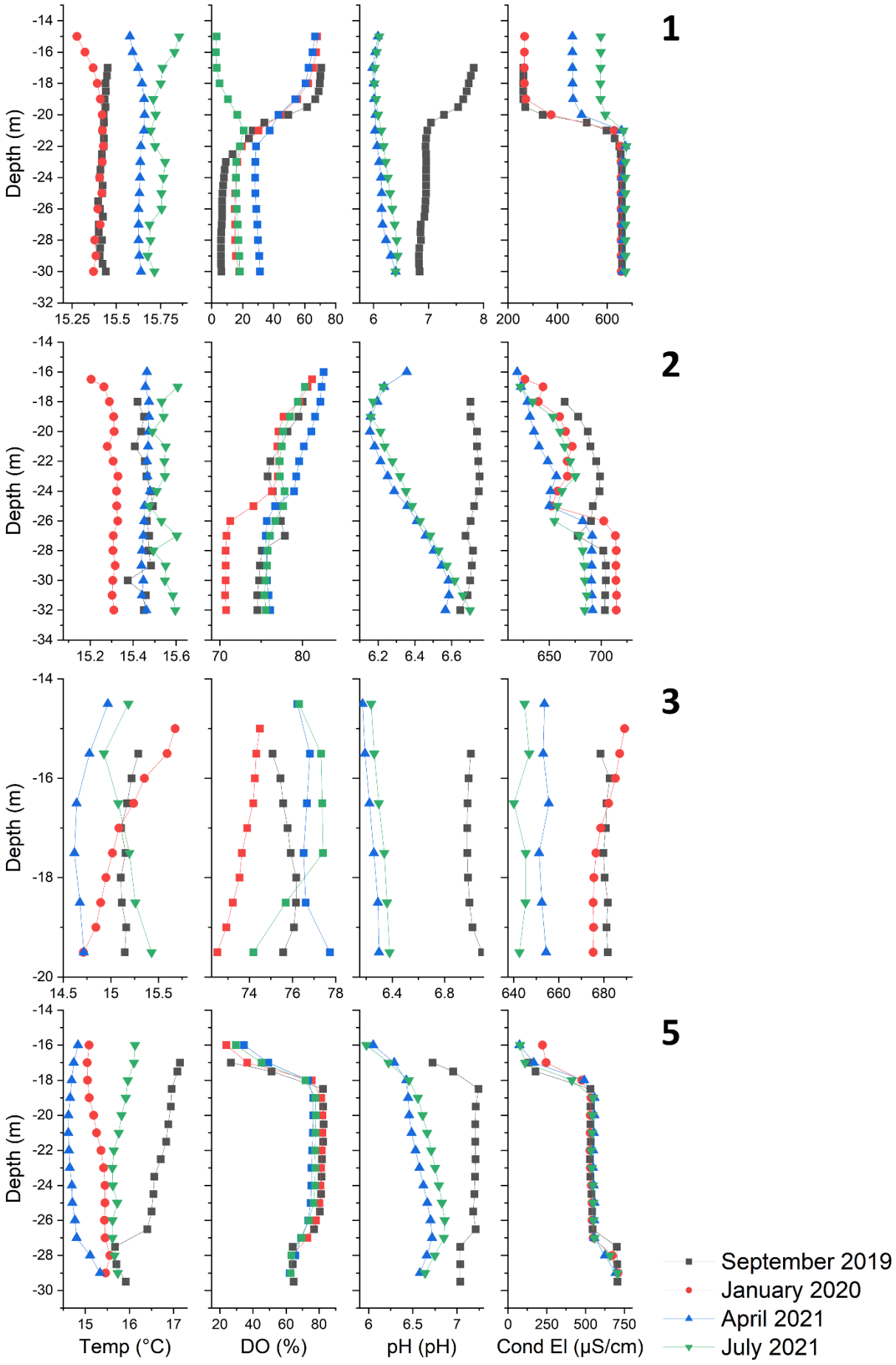
1
2
3
5
Depth (m)
Temp (°C)
DO (%)
pH (pH)
Cond El (µS/cm)
September 2019
January 2020
April 2021
July 2021

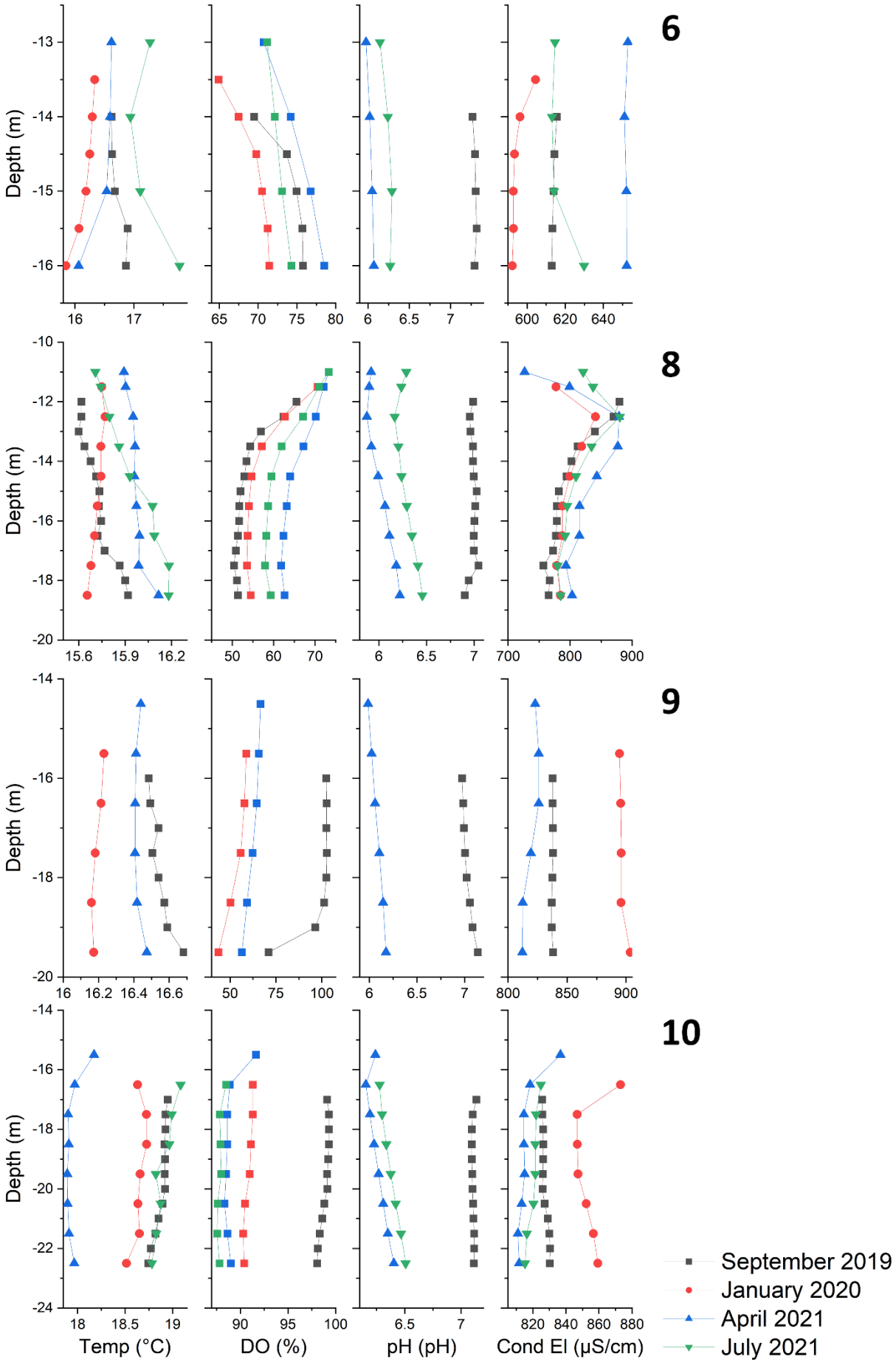
6
8
9
10
Depth (m)
Temp (°C)
DO (%)
pH (pH)
Cond El (µS/cm)
September 2019
January 2020
April 2021
July 2021

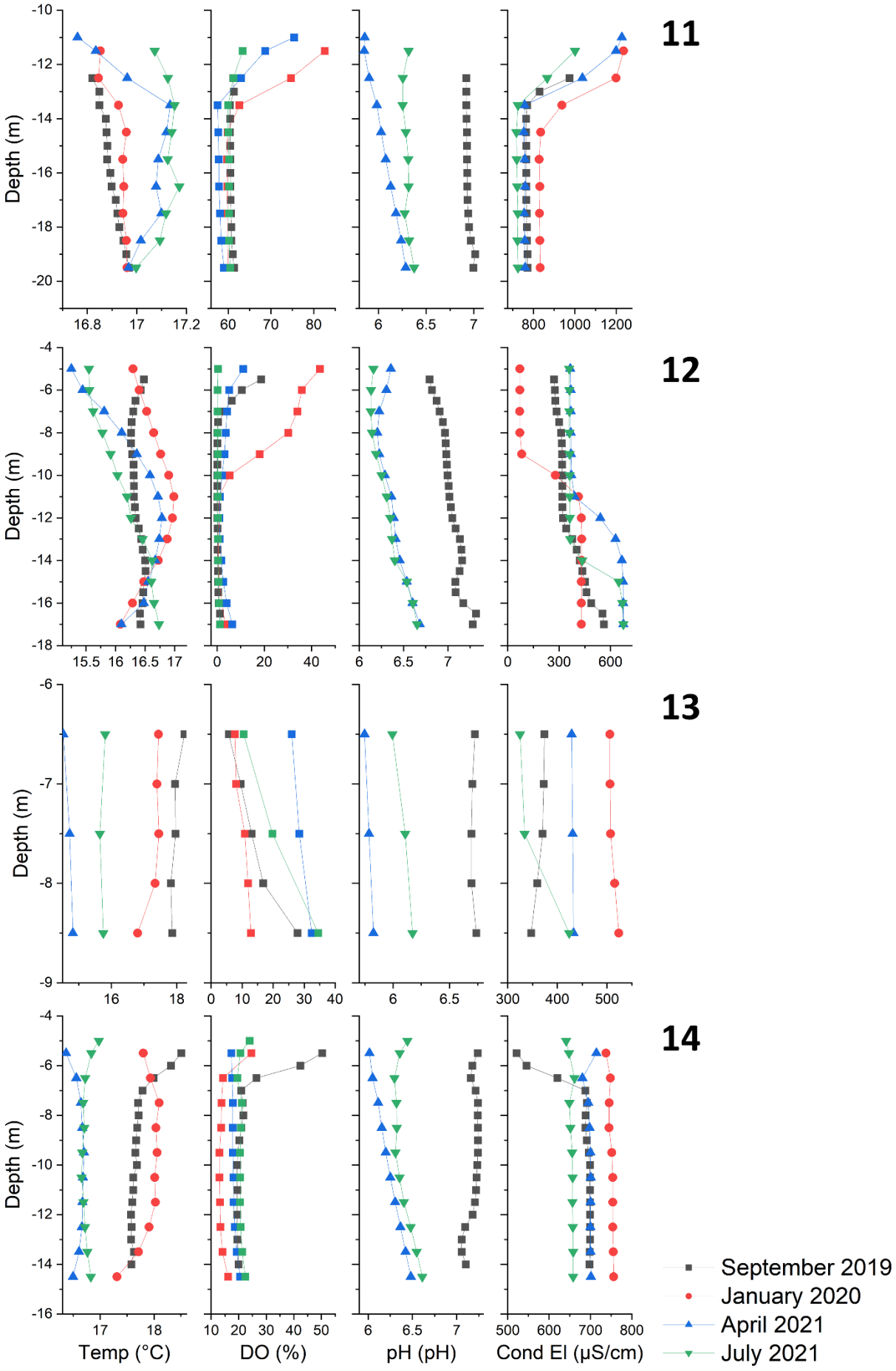
11
12
13
14
Depth (m)
Temp (°C)
DO (%)
pH (pH)
Cond El (µS/cm)
September 2019
January 2020
April 2021
July 2021

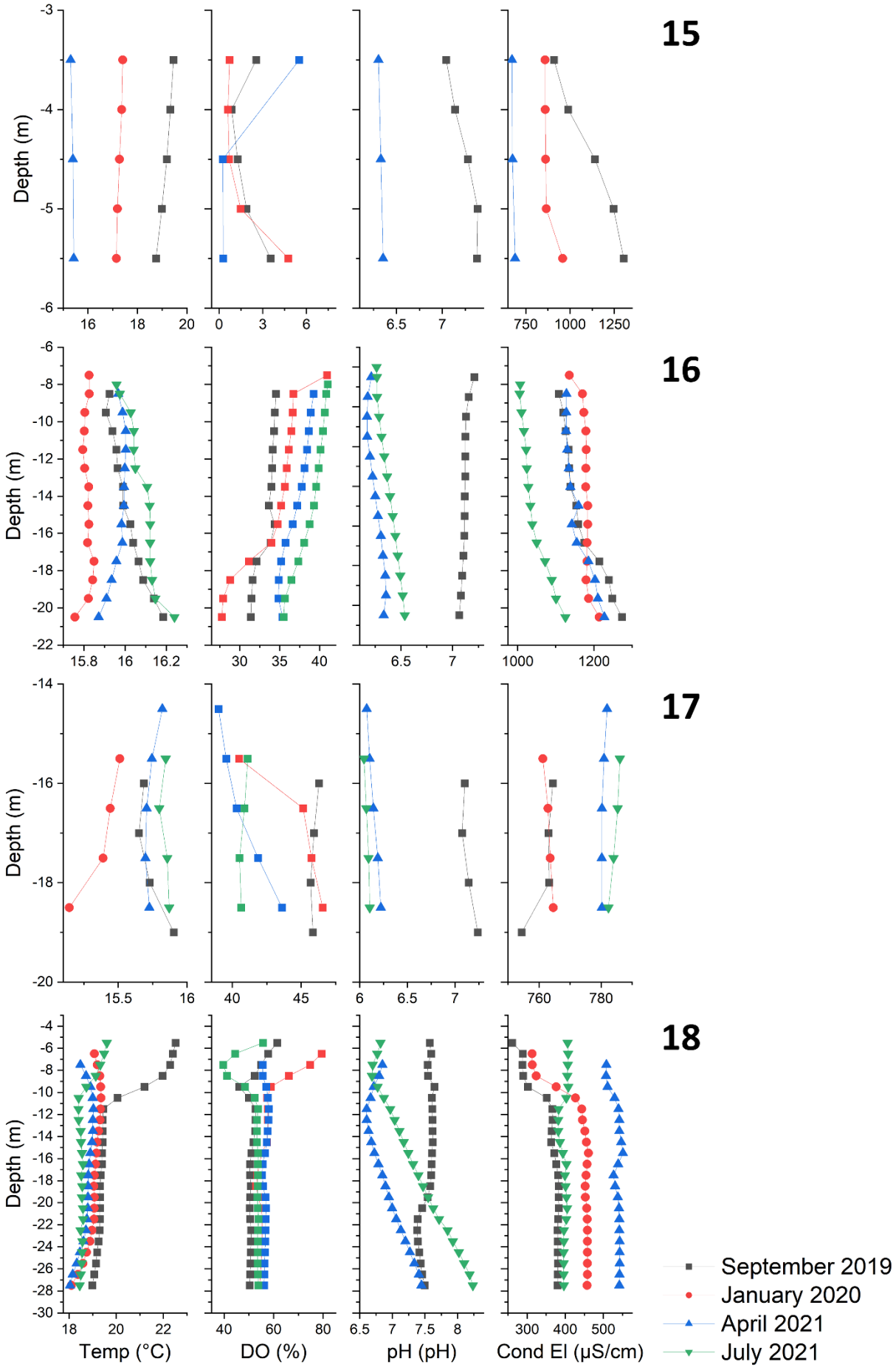
15
16
17
18
Depth (m)
Temp (°C)
DO (%)
pH (pH)
Cond El (µS/cm)
September 2019
January 2020
April 2021
July 2021

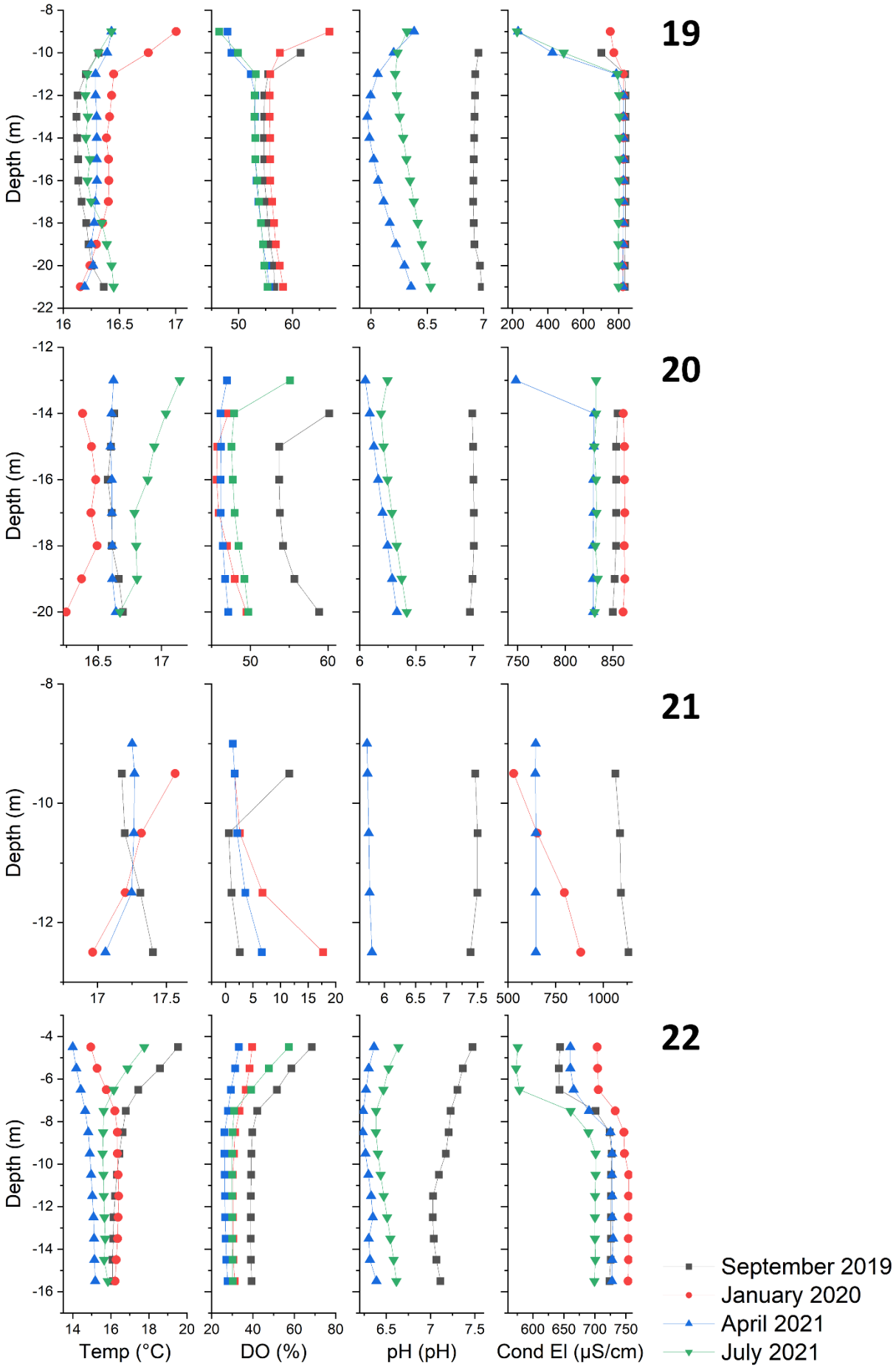
19
20
21
22
Depth (m)
Temp (°C)
DO (%)
pH (pH)
Cond EI (µS/cm)
September 2019
January 2020
April 2021
July 2021